Dynamics of populations in large ecosystems

Félix Roy

université
PARIS-SACLAY

Dynamics of populations in large ecosystems

Thèse de doctorat de l'Université Paris-Saclay

École doctorale n° 564, Physique en Île de France (EDPIF)
Spécialité de doctorat: Physique
Unité de recherche: Université Paris-Saclay, CNRS, CEA
Institut de physique théorique, 91191 Gif-sur-Yvette
Référent: Faculté des sciences d'Orsay

Thèse présentée et soutenue à Paris le 14 décembre 2020, par

Félix ROY

Composition du jury:

Leticia Cugliandolo Sorbonne Université	Présidente
Daniel Fisher Stanford University	Rapporteur
Matteo Marsili SISSA Trieste	Rapporteur
Silvia De Monte École Normale Supérieure	Examinatrice
Kirone Mallick Université Paris Saclay	Examinateur
Giulio Biroli École Normale Supérieure	Directeur
Jean-Philippe Bouchaud CFM	Invité

Thèse de doctorat

NNT: 2020UPASP080

université PARIS-SACLAY

ÉCOLE DOCTORALE
Physique en l'Île-de-France (PIF)

Titre: Les dynamiques de populations dans les écosystèmes diversifiés

Mots clés: Écosystèmes, Systèmes dynamiques non linéaires, Systèmes complexes, Ordre et désordre (physique)

Résumé grand public: Cette thèse est une étude mathématique pour l'écologie. Considérons l'expérience suivante : une parcelle de forêt est délimitée, et les populations des différentes espèces qui s'y trouvent sont référencées. Avec le temps, certaines espèces vont prospérer, d'autres s'éteindre. Le modèle mathématique que nous étudions prédit ces phénomènes : comment les populations changent au cours du temps. Si l'espèce dominante dans la parcelle change constamment, on dit que l'écosystème est chaotique. Il se trouve qu'en écologie, les dynamiques chaotiques sont généralement ignorées dans le cas des écosystèmes isolés. Dans cette étude, à l'aide d'outils mathématiques spécifiques et de simulations sur ordinateurs, nous montrons que le comportement chaotique est bien plus durable que ce qui est attendu.

Title: Dynamics of populations in large ecosystems

Keywords: Ecosystems, Non-linear dynamical systems, Complex systems, Order and disorder (physics)

Mainstream abstract: This thesis is a mathematical study of ecological models. The setup is the following: assume we delimit some forest parcel, and reference the populations of the various species it contains. If we let the ecosystem be, some species will bloom, others will go extinct. Our mathematical model predicts how the populations will change with time. In this PhD, we focus more specifically on the chaotic dynamics. In plain words, if whenever we go back to the forest parcel, the populations are different (sometimes the most abundant species is the rabbits, sometimes the boars), we will call this ecosystem chaotic. Usually in ecology, chaotic dynamics in isolated ecosystems are discarded, because they are unstable. In this work, we try to convey that chaotic dynamics are quite resilient. To do so, we introduce a specific mathematical tool. Then we perform various studies, both from pure mathematics and computer simulations, to show that lasting chaotic behaviour emerges.

Université Paris-Saclay
Espace Technologique / Immeuble Discovery
Route de l'Orme aux Merisiers RD 128 / 91190 Saint-Aubin, France

Thèse financée par la fondation CFM pour la recherche

Institut de Physique Théorique
Commissariat à l'Energie Atomique et
aux Energies Alternatives
Orme des Merisiers bâtiment 774
Point courrier 136
CEA/DRF/IPhT, CEA/Saclay
F-91191 Gif-sur-Yvette Cedex

Laboratoire de Physique de l'Ecole
Normale Supérieure
24 rue Lhomond
75005 Paris

Résumé détaillé

Cette thèse est une étude approfondie des dynamiques de populations hors-équilibre dans les écosystèmes diversifiés. Cette étude théorique est réalisée sur la base de simulations numériques, et de travaux analytiques. Après l'introduction de rigueur, dans laquelle nous présentons le contexte scientifique ainsi que notre modèle et nos méthodes, la thèse se compose de cinq chapitres raisonnablement indépendants les uns des autres. Le Chapitre 2 introduit l'outil théorique principal, à savoir la théorie de champ moyen dynamique. Nous y présentons un nouvel algorithme permettant de résoudre numériquement les équations correspondantes. Le Chapitre 3 est une étude numérique focalisée sur le phénomène de vieillissement dynamique qui se manifeste dans les écosystèmes isolés. Nous montrons que la dynamique des populations y devient marginale à temps longs. D'autre part, nous considérons une méta-dynamique plus simple en termes de sauts entre points fixes. Le Chapitre 4 est une étude analytique dérivant des observations du Chapitre 3. Nous détaillons quelques hypothèses permettant de clôre les équations dynamiques, et nous discutons leur pertinence. Nous présentons également un calcul de type Kac-Rice, qui précise la complexité des points fixes de la dynamique ayant certaines propriétés choisies. A l'aide de cette formule, nous essayons d'inférer les caractéristiques typiques de la dynamique. Dans le Chapitre 5, nous complexifions le modèle initial afin de prendre en compte la structure spatiale des écosystèmes. Nous montrons qu'une organisation spatiale triviale permet déjà d'observer des dynamiques chaotiques sur des temps très longs. Enfin, dans le Chapitre 6, nous oublions la notion d'espace, mais rajoutons au modèle la stochasticité liée au bruit démographique, dans le cas d'interactions symétriques. Nous établissons que la structure de l'espace des phases est complexe. Selon la force du bruit et la diversité des interactions entre espèces, on observe un unique équilibre (replica symmetric), plusieurs équilibres (1RSB) ou alors une structure hierarchique appelée 'phase de Gardner' dans les problèmes de jamming des matériaux amorphes.

Detailed abstract

This thesis consists in a study of the out-of-equilibrium population dynamics that occur in large-ecosystem models, both from a numerical and analytical point of view. After the usual introduction, in which we detail the scientific context and introduce our model and methods, we present five relatively self-contained chapters. Chapter 2 introduces the main analytical tool (Dynamical Mean Field Theory), and a novel algorithm to solve it numerically. Chapter 3 consists in a numerical study of the aging dynamics that arise in isolated ecosystems model. We show that these dynamics become marginal at long times, and propose a simpler meta-dynamics in terms of jumps between fixed points. Chapter 4 presents the analytical study that follows from the previous numerical investigation. We detail a few hypothesis that enable us to close the dynamical equations, and discuss their relevance. We also present a Kac-Rice computation of the fixed-points properties, from which we try to infer the typical behavior of the dynamics. In Chapter 5, we enlarge the initial model to introduce a spatial structure in the simplest possible way. We show that this enables very resilient chaotic dynamics. In Chapter 6, we go back to a single patch dynamics (no spatial structure), but consider the additional stochasticity of demographic noise. We limit the study to the case of symmetric interactions. We show that the structure of the phase space is non-trivial. Depending on the strength of the noise and the variety of interspecies interactions, it goes from a single equilibrium (replica symmetric phase), to a multiple equilibria (1-RSB phase), and finally to a hierarchical structure called a 'Gardner phase' in the context of jamming of amorphous materials.

Dynamique des remerciements

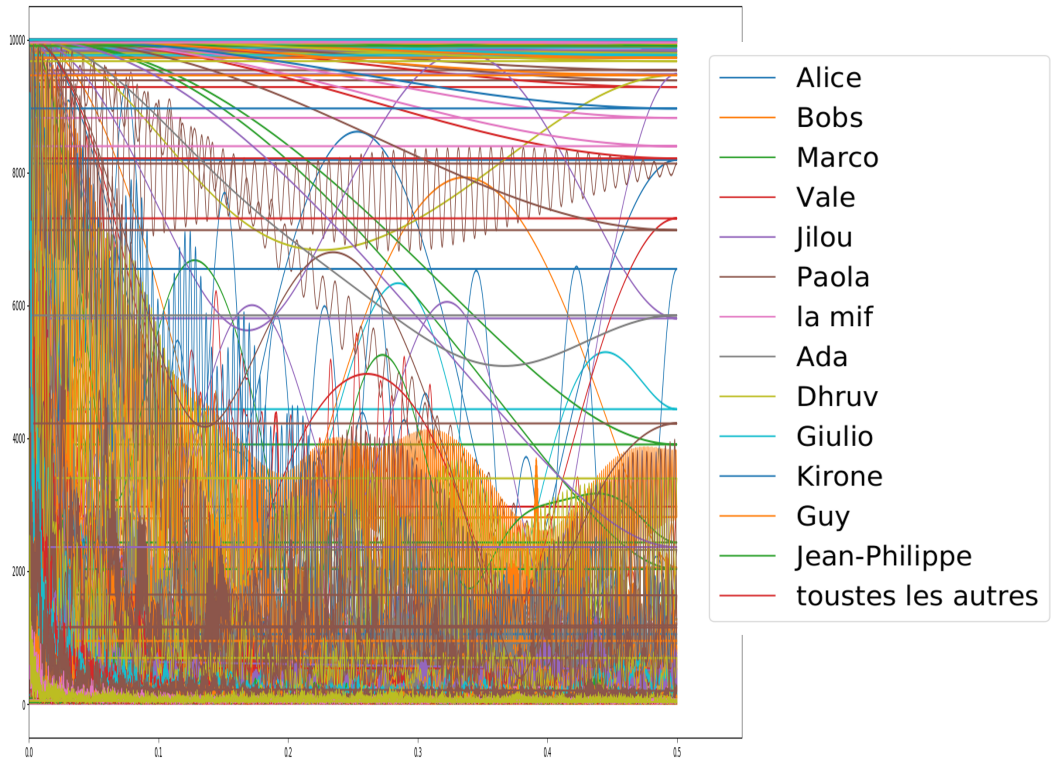

Synthèse en français

Les enjeux

En écologie théorique, l'un des plus gros enjeux actuels consiste à comprendre comment tant d'espèces distinctes peuvent coexister au sein d'un même écosystème. En effet, que l'on considère des exemples aussi différents que le microbiote intestinal ($\sim 10^3$ espèces), le plancton océanique ($\sim 10^5$ espèces), la forêt amazonienne ($\sim 10^6$ espèces) ou la savane brésilienne ($\sim 10^4$ espèces), la diversité des écosystèmes est bien supérieure à ce que les différentes théories permettent d'expliquer [3, 10-14].

Parallèlement à ce problème, les dynamiques chaotiques ne sont généralement pas considérées en écologie théorique. En effet, à partir de données présentant de fortes fluctations temporrelles en termes de populations, il est souvent difficile de faire la différence entre des fluctuations intrinsèques (chaotiques) à l'écosystème, et des perturbations extérieures [17, 18]. De plus, le comportement chaotique d'un écosystème isolé est auto-destructeur : le chaos est dû à la présence de beaucoup d'espèces, il se manifeste par de fortes fluctuations temporelles, qui vont conduire certaines espèces à l'extinction, alimentant ainsi de moins en moins le chaos [22, 23]. Toutefois, le chaos en écologie a été introduit et étudié, notamment pour les écosystèmes de phytoplancton [29-31], et des expériences récentes [32] permettent de valider cette grille d'analyse. En effet, si le mécanisme auto-destructeur du comportement chaotique est avancé pour les écosystèmes simples et isolés, rien n'est encore établi quand au temps nécessaire pour que le chaos disparaisse ainsi. De même, il n'est pas clair que ce comportement soit nécessairement voué à disparaître lorsque l'on considère des modèles d'écosystèmes plus réalistes, tenant compte de la notion d'espace.

Dans ce travail, nous utilisons la diversité importante des écosystèmes comme un atout nous permettant d'utiliser des techniques mathématiques spécifiques (provenant de la physique statistique des systèmes désordonnés). Nous analysons en détails les propriétés du comportement chaotique, dans différentes variantes du même modèle écologique : un écosystème isolé du reste du monde, un modèle insulaire relié à un contient (immigration régulière), un archipel d'îles isolé du reste du monde, ou encore un écosystème isolé où les fluctuations démographiques sont prises en compte. L'idée générale est que le comportement chaotique est généralement bien plus durable que ce qui est attendu.

Le modèle

Dans cette thèse, nous étudions le modèle de Lotka-Volterra généralisé [45]. Les espèces sont dénotées par les indices $i = 1...S$, et les populations par les variables continues $\{N_i\}_{i=1}^{S}$. Les interactions entre espèces sont modélisées par la matrice d'interactions $\{\alpha_{ij}\}_{i,j=1}^{S}$, et les populations suivent alors la dynamique :

$$\forall i = 1, ..., S, \qquad \frac{dN_i}{dt} = \frac{r_i}{K_i} N_i(K_i - N_i) - N_i \sum_{j \neq i} \alpha_{ij} N_j + \lambda_i \tag{1}$$

Dans cette équation, r_i dénote le taux d'accroissement intrinsèque de l'espèce i, et K_i la population que cette espèce atteindrait à temps long si elle était seule. Enfin, le terme λ_i modélise l'immigration régulière de quelques individus de cette espèce dans l'écosystème considéré.

Au cours de mon travail, je considèrerai presque toujours le modèle simplifié, où tous les taux d'accroissement intrinsèques et les populations esseulées sont fixés à 1, et l'immigration est homogène :

$$\forall i = 1, ..., S, \qquad r_i = K_i = 1, \qquad \lambda_i = \lambda$$

Cela revient plus ou moins à adimensionner le temps et les populations. Nous étudions donc le modèle simplifié :

$$\forall i = 1, ..., S, \qquad \frac{dN_i}{dt} = N_i(1 - N_i) - N_i \sum_{j \neq i} \alpha_{ij} N_j + \lambda \tag{2}$$

Dans la limite d'un grand nombre d'espèces $S \to \infty$, on constate une forme d'universalité du modèle : les prédictions que l'on peut réaliser ne dépendent pas de l'ensemble de la matrice d'interaction $\{\alpha_{ij}\}_{i,j=1}^{S}$, mais seulement de quelques paramètres. Nous considérons donc que la matrice d'interaction est échantillonnée à partir d'une distribution de matrices aléatoires donnée, et les paramètres du modèle seront les premiers moments de cette distribution : μ contrôle l'interaction moyenne, σ la diversité des interactions, et γ la symétrie typique des interactions. En termes plus mathématiques, si les moyennes, variances et covariances sont prises par rapport à la distribution de matrices aléatoires, on obtient :

$$\mathrm{E}[\alpha_{ij}] = \mu/S, \qquad \mathrm{Var}[\alpha_{ij}] = \sigma^2/S, \qquad \mathrm{Covar}[\alpha_{ij}, \alpha_{ji}] = \gamma\sigma^2/S$$

Le scaling en $1/S$ de ces moments permet d'avoir une limite $S \to \infty$ bien définie. A l'aide de ces paramètres, on peut reconstruire la typologie grossière des écosystèmes, comme indiqué dans le tableau 1.

En référence [44], il est montré que ce modèle Lotka-Volterra aléatoire permet de reproduire de manière fiable les prédictions de nombreux autres modèles en écologie. Nous nous concentrerons donc sur l'analyse de ce modèle.

Écologie	**Exemples**	**Paramètres**
Proies-prédateurs	Lapin et renards	$\gamma < 0$
Compétition pour les ressources	Plantes pour l'ensoleillement	$\gamma > 0,\ \mu > 0$
Mutualisme	Plantes et pollinisateurs	$\gamma > 0,\ \mu < 0$

Table 1. Formulation mathématique des interactions écologiques

Selon les paramètres d'interactions choisis, l'écosystème peut présenter des comportements très différents :

1. Les populations se stabilisent à temps long, le système atteint un point fixe. Celui-ci est globalement stable, et les populations finales ne dépendent donc pas des conditions initiales.

2. Les populations ne se stabilisent jamais, le système est en perpétuel rééquilibrage. On observe alors un comportement chaotique des populations. Ce comportement est habituellement ignoré en écologie théorique, car il nécessite une petite immigration $\lambda > 0$. Nous montrerons toutefois que de nombreuses situations écologiques peuvent se révéler chaotiques. Il est à noter que selon les implémentations du *cut-off* dans les populations N_c et de l'immigration λ, le comportement est différent : $\lambda > 0$ implique un chaos durable, $\lambda = 0$ et $N_c > 0$ implique un chaos transitoire avant un équilibre statique, $\lambda = N_c = 0$ implique du vieillissement, dont il sera question plus en détails ci-dessous.

3. Un sous-groupe d'espèce voit sa population diverger en temps fini, les autres espèces s'éteignent. Ce comportement est un artefact du modèle, il peut disparaître en changeant par exemple la saturation de l'environnement, mais cela entraîne quelques complications mathématiques. Dans la suite de nos travaux, nous choisirons donc simplement de ne pas utiliser les paramètres d'interaction aboutissant à ce comportement.

Dans la limite d'écosystèmes très diversifiés $S \to \infty$, ces trois différents comportements sont séparés par des limites nettes dans l'espace des paramètres. On peut donc identifier le diagramme de phase en figure 1 [45]. Les comportements y sont respectivement notés 1-'unique equilibriun', 2-'multiple equilibria' et 3-'unbounded growth'.

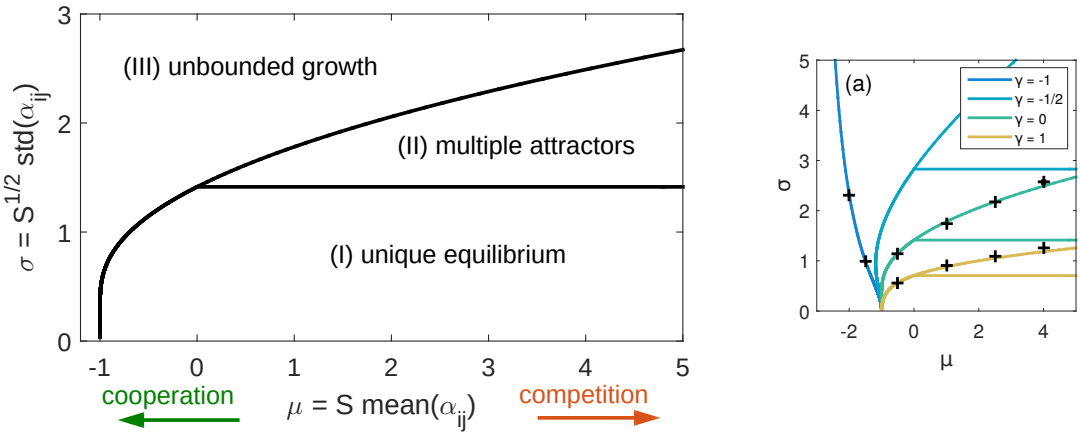

Figure 1. Diagramme de phase [45]. Gauche: Pour $\gamma = 0$, la transition entre *Unique Equilibrium* et *Multiple Attractors* est indépendante de μ et se situe sur la ligne $\sigma = \sqrt{2}$. Droite: Pour γ générique, cette transition se situe sur la ligne $\sigma = \frac{\sqrt{2}}{1+\gamma}$.

La théorie de champ moyen dynamique

Dans le chapitre 2 (inspiré de notre publication [61]) nous introduisons la théorie de champ moyen dynamique qui établit le lien entre le problème initial à S espèces, et un problème stochastique auto-cohérent à une espèce. Lorsque $S \to \infty$, il y a convergence en loi entre les deux processus. La formulation stochastique s'écrit alors :

$$\dot{N} = N\{1 - N - \mu m(t) - \sigma\eta(t) + \gamma\sigma^2 \int_0^t \chi(t,s)N(s)ds + h(t)\} \tag{3}$$

$h(t)$ est un champ introduit pour la définition de la fonction de réponse $\chi(t,s)$. $\eta(t)$ représente un bruit gaussien de moyenne nulle, et de covarance $C(t,s)$. La population moyenne $m(t)$, la corrélation $C(t,s)$ et la fonction de réponse $\chi(t,s)$ sont des fonctions données. Elles sont déterminées de manière auto-cohérentes par les relations :

$$\begin{cases} m(t) = \mathbb{E}[N(t)] \\ C(t,s) = \mathbb{E}[N(t)N(s)] \\ \chi(t,s) = \mathbb{E}[\frac{\delta N(t)}{\delta h(s)}\Big|_{h=0}] \end{cases} \tag{4}$$

Dans ces définitions, les moyennes $\mathbb{E}[.]$ correspondent aux moyennes par rapport aux trajectoires du bruit η, ainsi que par rapport aux conditions initiales $N(0)$.

Dans le chapitre 2, nous présentons la démonstration de la théorie de champ moyen dynamique à l'aide de la méthode de la cavité, pour un ensemble plus général de modèle. Nous proposons également un algorithme afin de résoudre de manière itérative les équations stochastiques obtenues. Nous appliquons cet algorithme au modèle de

Lotka-Volterra généralisé, et montrons que les solutions qu'il produit sont validées par des simulations numériques directes. Nous montrons également que la théorie de champ moyen dynamique et notre algorithme peuvent traiter le problème difficile du vieillissement : dans certains cas[1] les dynamiques de populations sont de plus en plus lentes, à mesure que le système vieillit.

L'étude du vieillissement dans un écosystème isolé

Dans les chapitres suivants, nous étudions ce phénomène de vieillissement plus en détails, d'un point de vue numérique et analytique. Dans le chapitre 3, nous montrons notamment numériquement que la dynamique à temps long devient marginalement stable par rapport aux espèces dominantes, et qu'il est pertinent d'analyser le système en termes de points fixes. Dans le chapitre 4, nous proposons différentes hypothèses simplificatrices permettant de fermer analytiquement les équations de champ moyen dynamique, et étudions leurs conséquences. Nous introduisons également la théorie de Kac-Rice, permettant de compter le nombre typique de points fixes de la dynamique vérifiant certaines propriétés. Nous montrons que lorsque le système passe de la phase *Un Equilibre* à la phase chaotique, on assiste à une transition dans l'espace des phases : initialement, il n'y a qu'un seul point fixe, globalement stable, puis à la transition ce point fixe devient instable selon certaines directions, et d'autres points fixes instables apparaissent (le nombre de points fixes qui apparaissent ainsi est exponentiel en S).

Le comportement chaotique stabilisé par la structure spatiale

Dans le chapitre 5 (inspiré de notre publication [62]), nous complexifions le modèle initial en introduisant la notion d'espace : de nombreuses copies (plus ou moins similaires) du même écosystèmes sont reliées entre elles par des flux de migrations. Ce système est représenté sur la figure 2. On peut visualiser ce modèle comme la description d'un archipel, et les individus de chaque espèce peuvent se déplacer d'une île à l'autre de temps à autres. Dans ce cadre, nous implémentons également un cut-off dans les populations : lorsque la population d'une espèce sur une île devient inférieure à une certaine valeur, nous mettons cette population à zéro et l'espèce est alors éteinte sur cette île.

Les trois paramètres pertinents du modèle sont le nombre M d'îles, σ qui contrôle la diversité des interactions entre espèces, et ρ qui contrôle la similarité des interactions entre les différentes îles.

Nous utilisons la théorie de champ moyen dynamique, qui nous permet d'effectuer certaines prédictions, même si la théorie simplifiée que nous utilisons n'est qu'une approximation. Nous montrons que, dès lors qu'il y a plus d'une île, le système voit coexister beaucoup plus d'espèces, et ce même lorsque les conditions sur les différentes îles deviennent presque identiques. Ce phénomène est appelé l'*effet d'assurance*, puisque pour éradiquer une espèce, il faut le faire sur toutes les îles simultanément. Toutefois,

[1] Lorsqu'il n'y a ni *cut-off* dans les populations, ni immigration.

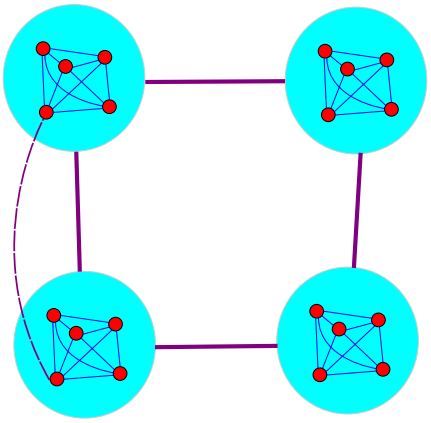

Figure 2. Schéma de la modélisation de l'archipel. Chaque espèce est représentée par un point rouge. Les espèces interagissent de manière habituelle sur chaque île (cercles bleus), où les lignes bleues représentent les interactions entre espèces. Les îles sont connectées par des flux de migrations (lignes violettes). Plus précisément, ces migrations ont lieu au niveau des espèces (ligne violette en pointillés) : les individus migrent depuis les îles où l'espèce est la plus abondante vers les autres.

on pourrait s'attendre à ce que la synchronisation des dynamiques entre les îles vienne tempérer l'effet d'assurance, lorsque les interactions sont quasi-identiques entre îles. Or nous montrons que, grâce à la phase chaotique, cette synchronisation n'a pas lieu[2].

L'étude du bruit démographique dans un écosystème isolé

Dans le chapitre 6 (inspiré de notre article soumis à publication [63]), nous considérons à nouveau le problème des dynamiques de populations sur une seule île avec immigration régulière depuis un continent, toutefois nous intégrons également la description du bruit démographique aléatoire. Le modèle devient alors :

$$\frac{dN_i}{dt} = N_i \left[1 - N_i - \sum_{j,(j\neq i)} \alpha_{ij} N_j \right] + \eta_i(t) \tag{5}$$

$\eta_i(t)$ est un bruit gaussien de moyenne nulle et covariance

$$\langle \eta_i(t)\eta_j(t') \rangle = 2TN_i(t)\delta_{ij}\delta(t-t')$$

[2]Du moins pas avant des temps très longs.

Nous utilisons la convention d'Ito. Ce bruit nous permet de modéliser le bruit démographique dans un modèle continu [117-119] ; plus la population globale est importante, plus la force T du bruit sera réduite. L'immigration est modélisée par une paroi réfléchissante pour la dynamique à $N_i = \lambda$, ce procédé est plus simple à traiter que la version habituelle consistant à rajouter λ au terme de droite de l'équation.

Nous limitons l'analyse à des interactions parfaitement symétriques, et montrons que dans ce cadre, le diagramme de phase présente trois nouvelles phases qui sont détaillées sur la figure 3.

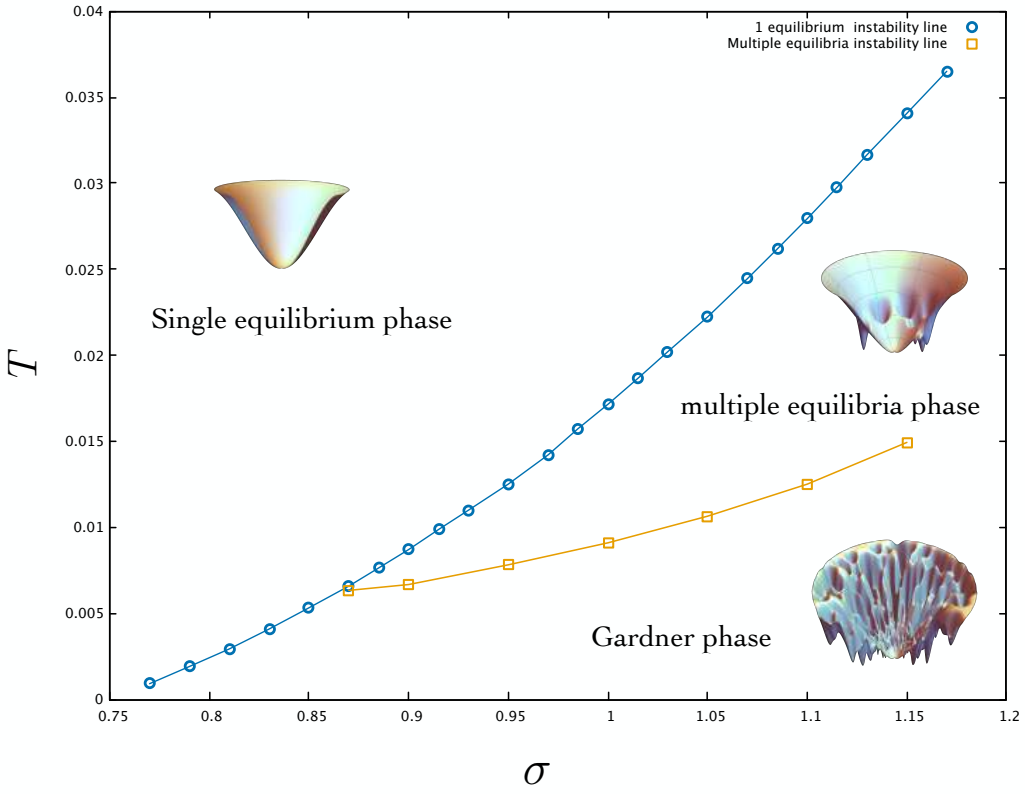

Figure 3. Diagramme de phase en fonction de la force T du bruit démographique, et du degré d'hétérogénéité σ, pour une interaction moyenne $\mu = 10$ et un *cut-off* des populations $N_c = 10^{-2}$. En diminuant le bruit démographique, trois phases distinctes apparaissent : i) une phase avec un seul équilibre ; ii) un régime avec différents équilibres (entre les lignes bleue et orange) ; iii) une *Gardner phase*, caractérisée par l'organisation hierarchique des équilibres dans le paysage d'énergie libre.

Nous introduisons un algorithme permettant de simuler le bruit démographique de façon efficace, avec les conditions aux limites spécifiques. A l'aide de cet algorithme, nous validons les prédictions théoriques établies par la théorie des répliques.

Contents

Notations

Throughout the thesis, we will use the following notations:

- N_i is the population (sometimes called *abundance*) of species i. Species will generically be denoted by indices i or j.
- S is the total number of species.
- λ is the uniform immigration rate into the ecosystem for all species.
- α_{ij} is the interaction matrix.
- μ, σ and γ are the statistical properties of the interaction matrix distribution. They correspond to the rescaled average, standard deviation and symmetry properties.
- ϕ is the diversity of the ecosystem. It corresponds to the proportion of alive species compared to the total number of species.
- $\phi_{marginal}$ (sometimes called $\phi_{MayBound}$) is the marginal diversity. For our model, it is derived in section 3.4.1 and given by:

$$\phi_{marginal} = [\sigma(1+\gamma)]^{-2}$$

- m and q are the statistical properties of the populations' distribution. They correspond respectively to the rescaled first and second moment of the distribution:

$$m = S^{-1}\sum_{i=1}^{S} N_i \qquad \text{and} \qquad q = S^{-1}\sum_{i=1}^{S} N_i^2$$

- $C(t,t')$ denotes generically a correlation function. For instance:

$$C_N(t,t') = S^{-1}\sum_{i=1}^{S} N_i(t)N_i(t')$$

- δ_{ij} is the Kronecker symbol.
- $\delta(t)$ is the Dirac function.

1. Introduction

In this chapter, we start with a context presentation that does not require any scientific background. In the following, we introduce the very basic and general ways to model populations in ecology, and present three fundamental models with associated results: the MacArthur model, the May model and the neutral theory. Then, we underline the recent interest in the study of large ecosystems, and we perform a literature review of the field. Finally, we introduce in more details the model we consider in the rest of the thesis, and the methods we use.

1.1. Non-technical introduction

This thesis focuses on ecology, which here denotes the study of the different species, how they interact with each other, and with their environment.

We deal with theoretical ecology, so we will focus on mathematical models that try to understand the behavior of ecosystems. A mathematical model can be seen as a black box: we provide the model with some input information, and it will output some predictions. In our case, we study how the populations of the different species will change with time. Therefore, our input information is generically which species are present, how they interact with each other and the environment, and what are their respective populations at a given time. From the model, we obtain their populations at any later time.

In simpler words, let's assume we go into a delimited parcel of forest today. We list what are the different species we encounter (foxes, rabbits, etc...), and count their individuals. We feed this to a mathematical model, and it should be able to tell us how many rabbits and foxes we will find in our parcel should we go back in three months, six months or ten years.

Nowadays, the models used in ecology are quite trusted. However, the understanding behind them is still somewhat lacking in some specific aspects. We reckon one of the issues at stake is that many of the common intuitions in ecology are based on studies of models with only **few** species. Using insights from the complementary limit of **infinitely many** species, in this thesis we will mostly focus on two aspects that we deem problematic from a theoretical point of view:

- The global diversity is still badly understood: how can so many species coexist simultaneously?
- Isolated ecosystems are usually considered temporally stable, in the sense that if one waits long-enough, the populations do not change much in time. In other

words, should we go back to the forest parcel, we will always find roughly the same populations for each species.

The logic behind this last point is as follows: if there is some agitation in the population dynamics, at some point some of the species will go extinct, which will lower the source of agitation. Therefore, agitation will eventually die out, and we'll end up with populations that are constant in time. While this argument is valid, our main concern lies in the *eventually*. What is the needed timescale for agitation to disappear?

We reckon that the two points mentioned above are related. More precisely, we think that the chaotic dynamics (the mathematical term for agitation) are relevant for very long timescales: if we come back to the forest within three months, the dominant species will be rabbits, within six months foxes, and within ten years boars maybe. Thanks to this phenomenon, much more species can coexist. Indeed, if there was a subgroup of species that became dominant, the outer species should go extinct. However, if there is a constant change in the equilibrium of the ecosystem, many species are always on the brink of blooming or going extinct.

With our background in statistical physics of disordered systems, we know that *more is different*, in the sense that if you put enough simple parts together, the new group will behave in ways you cannot understand by studying the single parts, or few of them together. Also, chaotic dynamics and scalings lie at the core of this field.

Therefore, this thesis consists in a theoretical study of the **chaotic** dynamics in **diverse**[1] ecosystems.

1.2. Basics for modeling

The general object of the study is an ecosystem, and more precisely the time-dependence of the populations of the species it contains. We label the species with the subscript $i = 1...S$, and denote their respective populations $N_i(t)$ where t stands for time. Depending on models, both time and populations can be either discrete or continuous. Here, we will consider both of them to be continuous, which is equivalent to assuming large populations, and time-scales of observation larger than the typical dynamics of an individual.

Usually, the dynamics of the populations are described by a first-order differential equation of the type:

$$\forall i = 1...S, \qquad \frac{dN_i}{dt} = f_i(N_i) + \sum_{j \neq i} g_{ij}(N_i, N_j) \tag{1.1}$$

There are two distinct phenomena taken into account with that form.

- First, the $f_i(N_i)$ describes the dynamics that would follow the population of species i if it were alone in the environment. This one-species dynamics specifies if the species would strive or disappear on its own (for instance, rabbits would strive

[1] Ecosystems with many different species are called *diverse*.

Ecological interactions	**Examples**	**Mathematical formulation**
Predation-prey (species i preys on species j)	Foxes (i) prey on rabbits (j)	$g_{ij} > 0,\ g_{ji} < 0$
Competition for resources	Plants compete for the sunlight	$g_{ij} < 0,\ g_{ji} < 0$
Mutualism	Plants and pollinators	$g_{ij} > 0,\ g_{ji} > 0$

Table 1.1. Mathematical formulations of ecological interactions

whereas foxes would disappear). There is also the implementation of a kind of environmental saturation, stating that the species cannot become more abundant than a given value of population, because the environment wouldn't be able to sustain more. This value is called the carrying capacity of the species. One should note that it is somewhat artificial to separate species from the environment, but this is only to fix ideas here.

- Then, the $\sum_{j\neq i} g_{ij}(N_i, N_j)$ part takes into account the interactions between distinct species. It is assumed that the global effect on one species can be modelled as a superposition of two-species interactions. More refined models, treating three-species interactions or more can also be used. If the presence of species j is deleterious to the species i, the contribution $g_{ij}(N_i, N_j)$ is negative and tends to reduce the population N_i. The typology of ecological interactions is presented in table 1.1.

The models in ecology tend to be multiplicative ones, in the sense that the impact on population N_i is proportional to N_i itself. This is quite logical, but leads to more mathematical struggles than usual additive models in physics.

This kind of modeling eventually assumes that there is no spatial structure in the ecosystem: all individuals from all species can interact. In particular, the interactions and the presence/absence of a species do not depend on its spatial location. Therefore, it is generically used to describe well-mixed ecosystems, such as the oceanic plankton. This modeling is also deterministic, but it is usually built on probabilistic models. For

instance, the standard Lotka-Volterra model for predation-prey can be seen as the mean-field limit of an individual-based model when the populations become large enough.

In the following sections, we introduce three very influential models in ecology: the MacArthur model for resource competitors, the May bound and the neutral theory.

1.2.1. MacArthur's Consumer Resource model

The first one was proposed around 1970 by Robert MacArthur in [1]. It was designed to model competition between consumer species for non-interacting resources. The species populations are always labelled $\{N_i\}_{i=1...S}$, and they are competing for resources whose abundances are denoted $\{R_l\}_{l=1...m}$, where m is the total number of resources. The species populations follow the dynamics:

$$\frac{1}{N_i}\frac{dN_i}{dt} = b_i\left(\sum_{l=1}^{m} c_{il}\, w_l\, R_l - m_i\right) \tag{1.2}$$

in which w_l is the value of one unit of resource species l to the consumer; c_{il} is the rate at which consumer species i captures resource l per unit abundance of resource l; m_i is the total value of resource that must be harvested per capita for the growth rate to be exactly 0. For species population N_i to grow, it needs to have gathered in total more resources than m_i. b_i is a factor converting the resource excess into the per capita growth rate. In this model, the resources abundances are dynamical variables as well. They follow the dynamics:

$$\frac{1}{R_l}\frac{dR_l}{dt} = r_l\left(1 - \frac{R_l}{K_l}\right) - \sum_{i=1}^{S} c_{il}N_i \tag{1.3}$$

The first part of these dynamics is the usual logistic growth, with an intrinsic growth rate r_l, and a carrying capacity (*i.e.* saturating abundance) K_l. Then the growth rate is reduced by the amount of resources that were captured by the consumer species.

The model was studied initially in [1], in which it is for instance shown that if the resource dynamics are faster than the populations' one, they can be integrated out and the remaining model is the generalized Lotka-Volterra model from Equation (1.7). For more details on the MacArthur model analysis, see the review [2] by Peter Chesson in 1989.

1.2.2. The May bound

In his 1972 work *Will a large complex system be stable?* [3], Robert May starts from generic dynamics such as the ones from Equation (1.1). He then assumes that the analysis can be performed close to a fixed point, and linearizes the equations. He additionally assumes that each species is self-regulating in the absence of the others. Therefore the dynamics for the population of species i around its fixed point value follows:

$$\forall i = 1...S, \qquad \frac{d}{dt}\,\delta N_i = -1 + \sum_{j=1}^{S} a_{ij}\,\delta N_j \tag{1.4}$$

We introduced in this equation the difference $\delta N_i(t) = N_i(t) - N_i^{FP}$ from the population equilibrium value at the fixed point N_i^{FP}. The -1 term comes from the self-regulation, and would induce an exponential relaxation to the fixed point, if it were not for the interactions with other species a_{ij}.

In May's setup, the matrix elements a_{ij} are taken as a independent identically distributed random variables. More precisely, a_{ij} is set to 0 with probability $1 - C$; this models the fact that some species do not interact. Otherwise, a_{ij} is drawn from a distribution of zero mean and variance σ^2. Therefore, in the final model, there are only three parameters: the number of species S, the connectance[2] C of the ecological network, and the strength of interaction σ.

The result of May, rooted in random matrix theory, is that the fixed point is stable if and only if the connectance or the strength of interactions are small enough compared to the number of species. More precisely:

$$\text{stability} \qquad \Longleftrightarrow \qquad S < (\sigma^2 C)^{-1} \tag{1.5}$$

This is usually referred to as the *May bound*: the ecosystem will drive some species to extinction until only a stable community of S_{Mb} species remain, out of the S initial species.

$$S_{Mb} = (\sigma^2 C)^{-1} \tag{1.6}$$

This result is discussed in context in section 1.3.1. We can already say that ecologists have been quite skeptical about this bound because it is very often exceeded in data from real ecosystems. From a theoretical point of view, the main problem is that it uses completely *random* interactions at the fixed point; whereas one could assume that the ecological dynamics would select some kind of structure in the interactions. Nevertheless, the prediction seems quite robust to this aspect (see later on).

1.2.3. Neutral theory

There are traditionally two flavors to model ecosystems: niche and neutral approaches. The **niche** approach states that each surviving species occupies its own ecological niche; it uses specific resources or preys upon species in a specific way. The usual examples are different bird species, that all have a distinct beak which enable each species to have a different diet. In this setup, the individuals from one species compete more strongly with other representatives of the same species than with other species: the intraspecific competition is stronger than the interspecific competition. Most of the usual models in theoretical ecology follow this path. For instance, the MacArthur model and the May model presented above are niche models.

[2]The connectance is the proportion of possible links between species that are realized.

On the other hand, the **neutral** approach in its strong formulation assumes that there is no such concept of species; every individual is competing in the same way with all other individuals. The dynamics, and the assembly of the community is then determined mostly by randomness. It can come from speciation, migration, and demographic noise (birth and death) from the populations. This approach was put forward by Hubbell in 2001 [4] and 2011 [5]. It can be seen as a null model, which yields interesting predictions. Some of them were validated by empirical studies, the most famous one being the Species Abundance Distributions: in neutral theory, the distribution of abundance decays as a power law $P(N) \propto N^{-1}$. For a thorough review and presentation of neutral theory, see [6] released in 2016.

1.3. Literature review

In this section, we review the relevant literature to our research. We mainly focus on two axis: the high diversity puzzle, and the ongoing debate about chaotic dynamics in isolated ecosystems. In this thesis, we develop the old idea that the two axis can merge: chaotic dynamics are quite robust, and they allow for high diversity.

We also review the insights that statistical physics enabled to provide on theoretical ecology, taking advantage of the high-diversity. We highlight that however, to our knowledge a theoretical description of the dynamics is still somewhat missing. This is the context and aim for our research.

1.3.1. The high diversity puzzle

Initially, it was generically considered that ecosystems with a high number of interactions between species would be more stable when facing exterior perturbations, invasions or extinctions [7, 8]. However, early simulations [9] followed by the theoretical work of May [3] (see section 1.2.2) seemed to indicate otherwise: to be stable, an ecological community needs few or only weak links between species. This is at least exact for a *random* community. Along the same lines, theories such as the competitive exclusion principle [10] states that there cannot be more distinct coexisting species than the number of distinct resources. This limits drastically the diversity of ecosystems, theoretically speaking. Nevertheless, field observations show that many important ecological communities – such as tropical forests, coral reefs, freshwater plankton [11, 12], gut microbiota [13] and so on – display high diversity; much more than what the theories can account for. This is true to the point that understanding the maintenance of high biodiversity is considered to be one of the most important modern challenges in science [14].

1.3.2. Can endogenous fluctuations persist in ecology?

While large temporal variations are widespread in natural populations [15, 16], it is difficult to ascertain how much they are caused by external perturbations, or by the ecosystem's internal dynamics; see for instance [17, 18]. In particular, both theoretical tools and empirical results come short of addressing a fundamental question: can we

identify when fluctuations in species abundances arise from complex ecological interactions?

Historically, studies of endogenous fluctuations have focused on single populations or few species [19, 20, 21]. On the other hand, theories of many-species interaction networks often center on ecosystems that return to equilibrium in the absence of perturbations [3]. Some authors have even proposed that fluctuations driven by interactions are generally too rare or short-lived to matter, since they can be self-defeating: dynamics that create large erratic variations lead to extinctions, leaving only species whose interactions are less destabilizing, until an equilibrium is reached [22, 23]. In this thesis, we will go past both the equilibrium [3, 24] or few-species starting points [19, 20, 21], to look directly at the dynamics of high-diversity communities.

Many-species endogenous fluctuations can only persist if they do not induce too many extinctions. Extinction rates depend critically on the amplitude of fluctuations [25, 26], their synchrony [27] and their correlation time [28]. The peculiarity of endogenous fluctuations is that these properties arise from the species dynamics, and therefore feed back on themselves. A theory of these feedbacks is however lacking.

The idea of sustainable chaotic dynamics in ecology is an old one. In 1993, [29] reviews the concept of chaotic dynamics in ecology. It focuses on modeling, analysis of time series, and experiments. Chaos was mostly popularized by the study of plankton dynamics: [30] and [31] perform rough numerical studies of a model close to the MacArthur Consumer Resource one. They show that chaos allows for more diversity, even though they only consider few (around 10) species and resources. In 2008, [32] reports chaotic dynamics in a long term (6 years) experiment for a full planktonic community.

From a mathematical point of view, [33] shows that chaotic behavior is prevalent in high-dimensional dynamics. Along the same line of ideas, but focused on game theory, [34] states that "complex non-equilibrium behavior, exemplified by chaos, is the norm for complicated games with many players".

The empirical high diversity hints that the properties of communities of interacting species can be studied using tools of statistical mechanics, with the role of the thermodynamic limit being played by the large number of species. This thesis is part of this philosophy, and we will now review more specifically this field.

1.3.3. Statistical physics insights on ecology

In a simple generalization of the initial work of May [3] (detailed in section 1.2.2), [35] argued in 2012 that the May bound is dependent on the typology of the ecosystem. The analysis is again based on random matrix theory; and states for instance that predator-prey relations are more stable than mutualism.

MacArthur's Consumer Resource model

Many studies built on the MacArthur's Consumer Resource model [1] (presented in section 1.2.1). In 2017, [36] studied the phase portrait of the model. The authors showed that depending on the number of species and the heterogeneity of resource supply, two

phases can be distinguished: external perturbations in resources from the environment can propagate to the local surroundings, or not. Later on, in 2018, [37] deepens the study by also considering resource dynamics and resource depletion. It confirms that ecosystems shape their environment, and modify the ecological niches. The same year, [38] establishes a direct mapping with a well-known model that describes dynamics in glasses at low-temperature.

Some studies proposed to modify the MacArthur initial model to account for different mechanisms. In [39], the model is enlarged to take into account *cross feeding*[3]. It is validated against microbial communities, and shows that even though species variability seems random, functional families[4] repartition is very predictable. In a later analytical work, [40] tracks the flow of energy in the model, and distinguishes two ecological phases.

General Lotka-Volterra model

This is the model that we focused on in this thesis. It is presented in more details in section 1.4.1 and equation (1.7).

In 2014, [41] shows that there exists a neutral-niche phase transition, varying the diversity of interactions and the strength of demographic noise. All analytics are done on a much simpler model of presence-absence of a species. In 2015, [42] considers a pure competition realization of the model [5] in the mainland-island setting, and studies the phase portrait as a function of the strength of competition and the variance of the interactions. The study is mostly numerical with an individual-based model, so demographic noise is taken into account. The authors identify four distinct dynamical phases. Following, [43] presents a way to count the number of stable and uninvadable communities, and shows that in this regime it is surprisingly sub-exponential in the number of species.

In 2017, [44] shows numerically that the general Lotka-Volterra model is able to reproduce almost all predictions from other models.

[45] presents the first analytical derivation of the exact ecological properties for the equilibrium phase, and pinpoints the chaotic instability onset. It also shows what emerging properties come forward in community assembly, compared to fully random. These properties are presented in more details in [46], along with an experimental validation based on plants. More recently, [47] focuses on the pure-symmetric interactions, and shows that the dynamics are marginally stable using disordered system tools.

In a work that was parallel to ours, [48] derived the dynamical equations (2.9) for random Lotka-Volterra systems from statistical field theory. Also, in a close-related work published in 2020, [49] uses the general Lotka-Volterra model for micro-diversity (different strains of the same species) in ecosystems of microbes and phages. The authors impressively solve the dynamics for pure antisymmetric interactions building on [50], and relax the assumption to weak antisymmetry in the setup of infinitely many islands connected by migration.

[3] When one species feeds on the metabolic waste of another one, it is called *cross feeding*.
[4] *Functional families* contain species that perform the same ecological function.
[5] With a different scaling for the interactions.

Other models and research fields

In a distinct modeling approach, [51] adapts a chemistry kinetics model to multispecies microbial communities. The model is checked against experiments with three species on a spatial lattice.

Random neural network models can be quite close to ecological ones, so the onset of chaotic dynamics that were first described in this field [52, 53] have been influential.

The general Lotka-Volterra model has also been used to model financial markets and complex economic systems [54, 55, 56, 57].

1.4. Our model and methods

1.4.1. The random Lotka-Volterra model

In this section, we introduce the model we will mostly use in this thesis: the random Lotka-Volterra (rLV) model [45]. We present its phase portrait in the limit of a large number of species.

Definition and notations

The ecosystem consists of S species. Each species i is characterized by its population $N_i(t)$ which is a positive continuous variable at all times t. In the absence of interactions each species may grow until saturation (e.g., due to limitations on resources). The impact of other species is modeled through bilinear interactions. A small immigration rate λ_i is added so that new individuals arrive to the ecosystem from the outside. The dynamical equations read:

$$\forall i = 1, ..., S, \quad \frac{dN_i}{dt} = \frac{r_i}{K_i} N_i(K_i - N_i) - N_i \sum_{j \neq i} \alpha_{ij} N_j + \lambda_i \tag{1.7}$$

The different parameters are the intrinsic growth rates r_i of the species, their single-species population sizes (*carrying capacities*) K_i in the environment and the interaction matrix α. Within our convention, a positive coefficient α_{ij} indicates that the presence of species j is deleterious to the species i, due to predation or competition over resources.

For clarity of presentation, in this thesis we mainly discuss the case where all r_i and K_i are set to unity, but the generalization is quite straightforward. We also consider that the immigration rate λ is uniform. The analytical and numerical tools described can be used more generally. Immigration acts as a regularization of the problem, as detailed in appendix A.1. Many of our published results are derived with infinitesimal but finite immigration rate $\lambda > 0$. We will separately discuss the case without immigration, and how the chaotic behavior is aging in chapters 3 and 4. The elements of the interaction matrix α_{ij} [6] are i.i.d. random variables with moments:

$$\overline{\alpha_{ij}} = \mu/S, \qquad \overline{(\alpha_{ij} - \overline{\alpha_{ij}})^2} = \sigma^2/S, \qquad \overline{(\alpha_{ij} - \overline{\alpha_{ij}})(\alpha_{ji} - \overline{\alpha_{ji}})} = \gamma\sigma^2/S$$

[6] Recent works on the inference of the interaction matrix from experiments have been carried out for the gut microbiome in [58, 59].

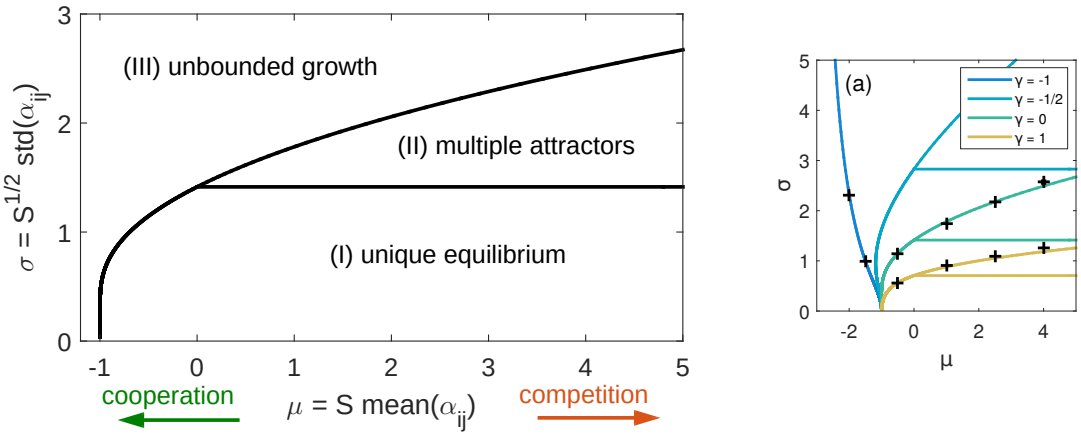

Figure 1.1. Phase diagram, taken from [45]. Left: At $\gamma = 0$, the transition from Unique Equilibrium to Multiple Attractors is independent from μ and lies on the line $\sigma = \sqrt{2}$. Right: For generic γ the previous transition lies on the line $\sigma = \frac{\sqrt{2}}{1+\gamma}$. Increasing the symmetry γ shifts the two transitions towards lower variance and stronger interactions. This result shows how predation-prey relations may stabilize an ecosystem.

where we introduced $\overline{X}$ the average over the distribution of the $\{\alpha_{ij}\}$. The exact distribution of the $\{\alpha_{ij}\}$ does not matter for our results, only the existence and values of the first two cumulants do[7]. The scaling with S of the cumulants ensures a proper large S limit. In this limit, the model becomes characterized by three parameters only: the average strength of interaction μ, the variety of interactions σ, and their symmetry γ. More specifically, γ ranges from -1 (fully antisymmetric case, where all interactions are of predation-prey type) to 1 (fully symmetric case, where an energy can be defined).

For a real ecosystem with given size S, the parameters μ, σ and γ can be statistically computed from the interaction matrix α. Our result then stands for this ecosystem with the relevant parameters values. From numerical simulations, we find that ecosystems with $S > 200$ are well described by results obtained in the "thermodynamic" limit $S \to \infty$.

Phase diagram

In the large-S limit, three different dynamical phases are found [45]; see figure 1.1.

- *Phase I: Unique Equilibrium.* In this regime, corresponding to small σ, the ecosystem displays only one stable equilibrium. Whatever the initial conditions, each

[7] More precisely, what we require is that the distribution of α satisfies:

$$\lim_{S\to\infty} S \log \overline{e^{X\,\alpha}} = X\,S\,\overline{\alpha} + X^2/2\,S\,\overline{(\alpha-\overline{\alpha})^2}$$

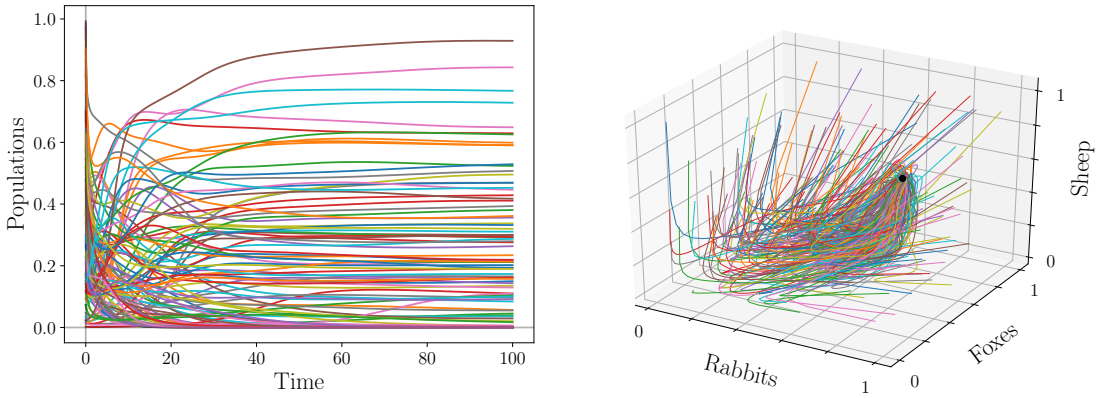

Figure 1.2. Time evolution of 100 species in the Unique Equilibrium phase: $(\mu, \sigma, \gamma, \lambda|S) = (4, 1, 0, 10^{-10}|100)$. Left: After a transient time, each species reaches a final population value which is stable. Right: Dynamical evolution of three species (e.g., 'sheep', 'rabbits' and 'foxes') out of all the species. We show different trajectories obtained starting from different initial conditions. They always converge to the same equilibrium value (black dot) independent of the initial conditions, demonstrating the stability and uniqueness of this equilibrium.

species asymptotically ends up with a given number of individuals which is always the same (it can be zero as some species go extinct). This equilibrium state is stable to local and global perturbations. On figure 1.2 we display the dynamics of an ecosystem in this phase: each line represents the time evolution of the population of one species.

- *Phase II: Multiple Attractors.* When the variability in the interactions σ is increased, the single stable fixed point loses its stability, and the system is left with a huge number of (possibly unstable) equilibria. This phase exhibits a complex dynamics with chaos (or aging dynamics, as for spin-glasses, for $\gamma = 1$ [47]). If there is a positive immigration rate $\lambda > 0$ into the ecosystem, these dynamics are stable in time: they keep on existing indefinitely. However, when the immigration rate λ is set to zero, another kind of aging dynamics appear: the dynamics become slower and slower. We present in section 2.4.3 a preliminary study using numerical DMFT, and later on tackle this aging numerically in chapter 3. An example of lasting chaotic dynamics can be seen on figure 1.3.

- *Phase III: Unbounded Growth.* When the average interaction is negative enough ($\mu < -1$), the interactions are cooperative enough to have a beneficial effect on any given species that overrides the single-species saturation. If we fix a higher μ and increase the standard deviation σ, at some point a small community of species will have cooperative interactions stronger than their own saturation and this subgroup of species will thus grow without bound, even though all the other species will die

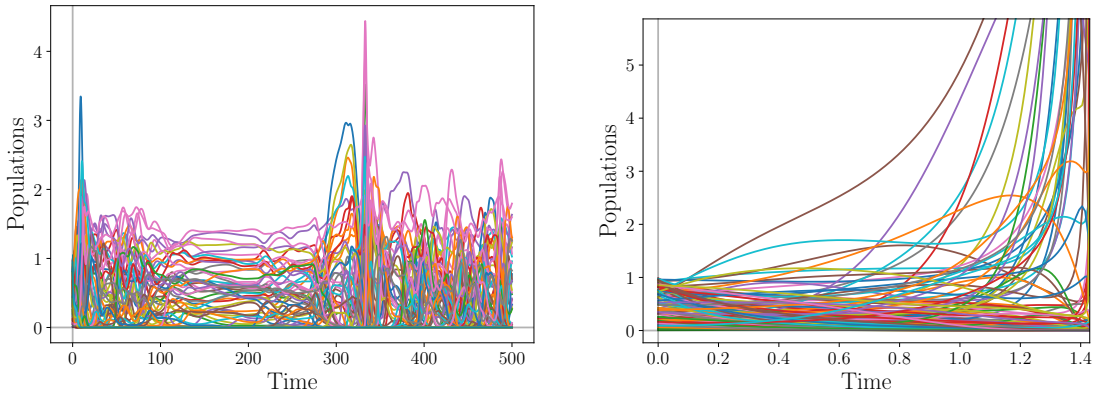

Figure 1.3. Left: Time evolution of 100 species in the Multiple Attractors phase: $(\mu, \sigma, \gamma, \lambda|S) = (4, 2, 0, 10^{-10}|100)$. The trajectories do not display any simple behavior; at some points, the system seems to relax to a fixed point before realizing that it has some unstable directions, and the dynamics starts again. Right: Time evolution of 100 species in the Unbounded Growth phase: $(\mu, \sigma, \gamma, \lambda|S) = (4, 4, 0, 10^{-10}|100)$. A large proportion of species present a divergence of their population, while the other ones die out.

out. This explains the existence of phase III also for $\mu > -1$ for a large-enough σ. An example of such dynamics is displayed in figure 1.3. It should be noted that the divergence occurs as a finite time explosion of the ecosystem. The unbounded growth is a pathology of the model that could be cured by a saturation stronger than quadratic.

The borders between phases can be computed analytically: I/II and I/III are exact, but II/III is only approximate [45]. They are shown on figure 1.1.

The symmetric case $\gamma = 1$ is special in the sense that the Multiple Attractor phase is not a chaotic one, but rather a spin glass one [47]: the dynamics gets slower and slower as the system approaches marginally stable states. In this case, a kind of physical energy can be defined and serves as a Lyapunov function. The dynamics corresponds to a gradient descent in a rough energy landscape. We study this phase (enriched with demographic noise) in more details in chapter 6. The antisymmetric case $\gamma = -1$ is also special, because another Lyapunov function can be defined. For a thorough study of this setup, see [49].

1.4.2. Methods

In this section, we review briefly the different tools we used: both theoretical ones and numerical ones.

Theory

Most of the theoretical techniques used in this thesis come from the field of statistical physics of disordered system. However, there are two main issues that are specific to ecology.

1. Unlike all common systems that comes from physics, ecological interactions usually are non-symmetric. For instance, rabbits do not have the save impact on foxes as foxes on rabbits. This trivial difference actually represents a considerable theoretical difficulty. Indeed, the symmetry of the interactions simplifies a lot the analysis from a mathematical point of view: a global energy can be defined for the system, and some equilibrium relationships such as Fluctuation-Dissipation Theorem hold. This is not the case in generic ecosystems.

2. The way we model the ecosystems (assuming large continuous populations) is problematic, because in a regular model, a continuous variable can only go to 0 in an infinite time. However, we know that at some point species do become extinct; when the last individuals die out. There are different ways to consider this issue, mainly by adding a cut-off in the dynamics (if the rescaled population gets below say 10^{-4}, the species is withdrawn from the system), or implementing some immigration. It always depends on what we actually want to describe, but for our purposes immigration is often the best mathematical way to regularize the problem. We discuss this point in more details in appendix A.1.

Some tools from disordered systems can still be adapted to our problem. More precisely:

- Our whole analysis relies heavily on dynamical mean field theory. This is a tool that draws a mapping between an S-body mathematical problem, and a 1-body stochastic problem. The theory is presented in more details in chapter 2, along with its derivation for the random Lotka-Volterra model.

- In section 4.6, we use a technique that counts the number of fixed points for a given dynamics. This is referred to as the Kac-Rice method.

- In the case of perfectly symmetric interactions in the ecosystems ($\gamma = 1$), it is possible to define some kind of energy landscape. This enables us to draw an exact mapping to a standard disordered systems problem, and we use replica theory to study it. We refer to [60] for a gentle introduction of this theory.

- We use some standard dynamical system techniques: mostly for linear stability of a given fixed point of the dynamics. This also calls for some random matrix theory, from which we use the typical spectrum distribution for large matrices.

Numerics

We use numerics for two distinct purposes: simulating the dynamical systems, and solving some equations.

For simulations, we always use discrete schemes to approximate the systems: time only takes discrete values. One needs to be careful in doing so, to avoid some numerical problems. For instance, the populations need to stay positive at all times. This is obviously the case in the continuous system of dynamical equations. However, as soon as the system is discretized in time, there is always a non-zero probability that the populations become negative. In order to prevent this, we usually simulate the system using the log-population variables. The case with demographic noise induces a whole new difficulty for simulations, we discuss this in section 6.5 of chapter 6.

To solve simple equations (such as the stationary cavity ones from equation (A.4)) numerically, we use standard numerical methods. However, more involved equations such as the DMFT from equation (2.5) required a specific algorithm, which we detail in section 2.2.3.

Most of the numerical results in this thesis rely on some (usually simple) parallelization on the Kondo cluster of IPhT, CEA Saclay.

1.5. Outline of the work in this thesis

Starting from the random Lotka-Volterra model, we introduce the dynamical mean field theory in chapter 2. We present a simple derivation for a generic class of models, perform a quick theoretical analysis for the field theory applied to the random Lotka-Volterra model, and describe the algorithm we derived to solve it numerically. This work is published in [61].

In the two following chapters (which are still unpublished work), we focus on the chaotic properties and the aging phenomenon of the basic model without immigration. In both chapters, we present finished results and ongoing work; the distinction is made clear in each introduction. In chapter 3, we first explore the dynamics numerically, and show that they are marginally stable. Then in chapter 4, we explore different simplifying analytical approaches to understand the aging phenomenon. We also introduce a way to count the number of fixed points of the dynamics with given properties.

Armed with these initial studies, we then generalize the model by taking into account two other ecological effects. In chapter 5, we enlarge the model to describe spatial heterogeneities in the ecosystem. We show both analytically and numerically that in this case, chaotic dynamics (also known as endogenous fluctuations) can persist for very long times. This work is published in [62].

In chapter 6, we study the impact of demographic noise on the phase portrait of the model. As the treatment becomes quite involved, we restrain ourselves to fully symmetric ecosystems. We derive an analytical study, and introduce a complex numerical scheme for comparison. This work can be seen in [63].

In Appendix G we enclose a few additional results: a Landau-like expansion in the correlation function, and a quick study of the LV model modified with logarithmic or cubic saturation.

2. Dynamical Mean Field Theory

In this chapter, we introduce the dynamical mean field theory. We detail the generic intuitive derivation through the cavity method. Then we apply the theory to the random Lotka-Volterra model, and give some analytical results. Eventually, we present a numerical scheme that we designed to solve the DMFT equation, and we show some results.

Materials from this chapter can be found in [61]. Additional details about computations and numerics are given in Appendix A.

2.1. Introduction[1]

> A growing body of work has demonstrated that the properties of communities of interacting species can be studied using tools of statistical mechanics, with the role of the thermodynamic limit being played by the large number of species. Such high-diversity communities, with tens to thousands of species, are ubiquitous and can be found anywhere from microbes in the gut to plants in a rain forest[13].

Most of the works in ecology have focused on the properties of fixed-points of the dynamics, and much less is known about the dynamics themselves, in particular when they never reach a fixed-point.

Dynamical mean-field theory (DMFT) is a useful theoretical framework which has been often used in the past to study complex stochastic dynamics of interacting degrees of freedom (spins, agents, neurons, ...) [64, 65, 66, 53, 52]. In this work we develop DMFT for models of ecosystems formed by a large number of interacting species [47, 45, 48]. In the limit of large ecosystems, interactions between different species are commonly modeled by taking random interaction strengths [67, 44]. The resulting model consists in generalized Lotka-Volterra equations with random couplings. This leads to interesting problems of statistical physics, similar to ones encountered in the theory of disordered systems. Yet, there are a number of crucial differences; in particular an ecosystem is driven by non-conservative forces, hence its dynamics cannot be mapped in general to the one of a physical system in thermal equilibrium. Therefore ecosystems display complex dynamical regimes which have been discussed in other fields before, mainly in neural networks [52] and game theory [66, 53] (see also [68] and [69] for disordered system-like treatment).

[1] So that each chapter may be read separately, I decided to preserve all specific chapters' full introduction, even though it may overlap with the global and more detailed introduction from section 1. The overlapping parts are presented in the box and can be skipped.

DMFT maps a many-body dynamical problem to a one-body stochastic problem. However, in doing so it introduces specific mathematical complications such as a time-delayed friction or non-linearities. Dues to these complications, solving numerically the equations corresponding to DMFT represents a major difficulty. In the past this obstacle has been solved—actually circumvented—only for simplified (spherical or truncated) spin-glass models for which DMFT equations greatly simplify and reduce to closed integro-differential equations on correlation and response functions of local degrees of freedom [70]. To the best of our knowledge, a procedure to numerically integrate DMFT was still missing when we started our project (with the exception of [71, 72] that were restricted to the case of Ising spins and simple dynamical protocols), especially one able to analyze the complex dynamics relevant for ecosystems. In [61], following ideas developed for DMFT of strongly correlated quantum systems [73], we develop a generic numerical scheme to solve DMFT. Our method lays foundations for the study of high-diversity ecological dynamics, but also provides general tools that can be applied to problems beyond ecology, for example in the fields mentioned above. Our code is available in a public gitHub repository [74].

We focus on the generalized Lotka-Volterra model of ecosystems. We first present a derivation of DMFT based on the dynamical cavity method [75], which is a more intuitive procedure compared to the usual ones based on generating functional formalism, such as Martin-Siggia-Rose-DeDominicis-Janssen [66, 48, 71, 72]. We then detail our numerical approach for solving DMFT, and show concrete examples of its implementation. This allows us to test the method, and illustrate its ability to describe and characterize complex dynamics involving chaos and aging. We finally conclude by discussing further directions and possible future applications.

2.2. The Dynamical Mean Field Theory

In this section, we derive the Dynamical Mean Field Theory (DMFT) using the dynamical cavity method [75]. For simplicity, we first present the derivation in the simplest case of random Lotka-Volterra model, then we extend the result to more general models, and finally we explain a numerical method to solve the DMFT equation. We also checked the relevance of the description by comparing the DMFT results with direct simulations, increasing the size S of the ecosystem.

2.2.1. Derivation via the cavity method

For simplicity, DMFT is first derived with the simplest random Lotka-Volterra model, presented in equation (2.1). Our approach holds in more general cases, we will present its generalization in section 2.2.2. We start from the Lotka-Volterra equations:

$$\forall i = 1, ..., S, \qquad \dot{N}_i = N_i(1 - N_i - \sum_{j \neq i} \alpha_{ij} N_j + h_i(t)) \tag{2.1}$$

where we have added an external field h_i that will be necessary to define the response of the system to a perturbation. The initial conditions are sampled from a product

measure: $P\{N_i(t=0)\} = \prod_{i=1}^{S} P(N_i(t=0))$. For instance, we generally use a uniform distribution in $[0,1]$ for simulation purposes.

The main steps of the derivation are the following:

1. For given parameters μ, σ, γ and system size S, accordingly sample the interaction matrix $\{\alpha_{ij}\}_{i,j=1...S}$ and initial populations $\{N_i(0)\}_{i=1...S}$ species;

2. Obtain the trajectories $\{N_i(t)\}_{i=1...S}$ following the dynamics from equations (2.1);

3. Add a new species N_0, and draw its initial condition $N_0(0)$ and the interactions α_{i0} and α_{0i} for $i = 1, ..., S$;

4. If S is large enough, the impact of this new species on the previous trajectories is a small perturbation and therefore we only consider linear response for the trajectories $\{\tilde{N}_i(t)\}_{i=1...S}$ in the presence of species '0':

$$\tilde{N}_i(t) = N_i(t) - \sum_{j=1,...,S} \int_0^t \left.\frac{\delta N_i(t)}{\delta h_j(s)}\right|_{h=0} \alpha_{j0} N_0(s) ds$$

   The partial derivative are to be understood in a functional sense. We introduce the notation $\chi_{ij}(t,s) = \left.\frac{\delta N_i(t)}{\delta h_j(s)}\right|_{h=0}$

5. We plug these new trajectories in the equation for N_0:

$$\dot{N_0} = N_0(1 - N_0 - \sum_{i\neq 0} \alpha_{0i}\tilde{N}_i + h_0(t))$$

   We introduce the matrix a_{ij}: $\alpha_{ij} = \mu/S + \sigma a_{ij}$, so that a_{ij} is a Gaussian with zero mean and $1/S$ variance, verifying in addition $\overline{a_{ij}a_{ji}} = \gamma/S$. All the sums $\sum_i$ stand for $\sum_{i=1}^{S}$, so the interaction term reads:

$$\begin{aligned}\sum_j \alpha_{0j}\tilde{N}_j = \frac{\mu}{S}\sum_i N_i(t) - \frac{\mu}{S}\sum_{ij}\int_0^t \chi_{ij}(t,s)\left(\frac{\mu}{S} + \sigma a_{j0}\right) N_0(s) ds \\ + \sigma \sum_i a_{0i} N_i(t) - \sigma \sum_{ij} a_{0i} \int_0^t \chi_{ij}(t,s)\left(\frac{\mu}{S} + \sigma a_{j0}\right) N_0(s) ds \end{aligned} \tag{2.2}$$

6. We take the large S limit and analyze the statistical properties of all terms. The main idea is that by construction $\{N_i(t)\}_{i=1,...,S}$ are independent from α_{i0} and α_{0i}, therefore one can use central-limit-like arguments. Henceforth, the notation $\langle . \rangle$ refers to the average over the couplings a_{ij} and initial conditions $N_i(0)$. We will detail the procedure for the response function term as an example. We start from $\sum_{ij} a_{0i}\chi_{ij}(t,s)a_{j0}$. We consider that the different $\chi_{ij}(t,s)$ are random functions that will depend on the initial conditions $N_{i>0}(0)$ and the interaction matrix $a_{ij>0}$, but are otherwise independent from a_{j0} and a_{0i}. We first treat the diagonal part.

According to the central limit theorem and up to second order contribution, the term $\sum_i a_{0i}\chi_{ii}a_{i0}$ will converge towards its average:

$$S\langle\chi_{ii}a_{i0}a_{0i}\rangle = S\langle\chi_{ii}\rangle\langle a_{i0}a_{0i}\rangle = \gamma\langle\chi_{ii}\rangle$$

We now focus on the non-diagonal part. Its average is zero because $\langle a_{0i}a_{j0}\rangle_{i\neq j} = 0$. To determine the scaling of its fluctuations we evaluate the variance of its single components obtaining $\langle\chi_{ij}^2\rangle_{i\neq j}\langle a_{j0}^2 a_{0i}^2\rangle_{i\neq j}$. It can be shown by perturbation theory in the strength of interactions that χ_{ij} is of order $S^{-1/2}$ for $i \neq j$ [75] (see appendix A.2). Regrouping the scalings, we obtain that $\sum_{i\neq j} a_{0i}\chi_{ij}a_{j0}$ behaves as:

$$\begin{aligned} &S(S-1)\langle\chi_{ij}\rangle_{i\neq j}\langle a_{j0}a_{0i}\rangle_{i\neq j} + \sqrt{S(S-1)}\sqrt{\langle\chi_{ij}^2\rangle_{i\neq j}}\sqrt{\langle a_{j0}^2 a_{0i}^2\rangle_{i\neq j}}Z \\ &\sim 0 + S\frac{1}{\sqrt{S}}\frac{1}{S}Z \end{aligned}$$

where Z is a centered standard Gaussian. This shows that the non-diagonal term induces corrections of order $S^{-1/2}$ and can therefore be neglected in the large-S limit. After careful evaluation of all terms in equation 2.2 according to the same procedure, we get:

$$\dot{N_0} = N_0\{1 - N_0 - \mu\langle N_i(t)\rangle - \sigma\eta(t) + \gamma\sigma^2\int_0^t \langle\chi_{ii}(t,s)\rangle N_0(s)ds + h_0(t)\}$$

where $\eta(t)$ is a Gaussian noise with zero mean and covariance $\langle\eta(t)\eta(s)\rangle_\eta = \langle N_i(t)N_i(s)\rangle$.

7. Since nothing differentiates N_0 from any other species, we obtain the self-consistent equation that leads to dynamical mean field theory:

$$\dot{N} = N\{1 - N - \mu m(t) - \sigma\eta(t) + \gamma\sigma^2\int_0^t \chi(t,s)N(s)ds + h(t)\} \tag{2.3}$$

where η is a Gaussian noise with zero mean and correlator $C(t,s)$, and $m(t)$, $C(t,s)$ and $\chi(t,s)$ are given functions. They are self-consistently determined with the relations:

$$\begin{cases} m(t) = \mathbb{E}[N(t)] \\ C(t,s) = \mathbb{E}[N(t)N(s)] \\ \chi(t,s) = \mathbb{E}[\left.\frac{\delta N(t)}{\delta h(s)}\right|_{h=0}] \end{cases} \tag{2.4}$$

In these definitions, the averages $\mathbb{E}[.]$ are now taken with respects to the noise trajectories η and the initial condition $N(0)$. Therefore, the equation is self-consistent in the three following functions: the **average population** $m(t)$, the **correlator** of the noise $C(t,s)$ and the **averaged response function** $\chi(t,s)$.

To sum up, we started from an S-body deterministic system of differential equations, and ended up with a one-body stochastic self-consistent differential equation [2]. It has been mathematically proven [77] for spin glasses that when $S \to \infty$, there is a convergence in law between the statistics of the two descriptions. We expect that this holds true for our class of models as well, due to the similarity of both the equations and the method.

An important additional remark is that the DMFT is valid as long as we consider times that do not diverge with system size S. Otherwise, one cannot neglect terms vanishing with S as we did.

2.2.2. DMFT equation for a general class of models

The derivation above can be performed almost identically in more general cases. The only additional subtlety is that we use the fact that the correlation $\langle N_i(t)N_j(t)\rangle$ scales as $S^{-1/2}$ for $i \neq j$, as can be shown by perturbation theory in the strength of interactions [75] (see appendix A.2). Below, we just present the result for a general class of dynamics with a generic and species-dependent response function $R_i(N_i)$, non-linear p-body interactions due to $I_i(N_i)$, $J(N_j)$ and a species scaled thermal noise $f_i(N_i)\xi_i(t)$.

$$\dot{N}_i = R_i(N_i) + I_i(N_i)\left(\sum_{1\leq j_2<\ldots<j_p\leq S} \alpha^i_{j_2\ldots j_p} J(N_{j_2})\ldots J(N_{j_p}) + h_i(t)\right) + f_i(N_i)\xi_i(t) \quad (2.5)$$

where ξ_i is a Gaussian white noise, with variance $2\omega^2$. The i-dependence of the functions denotes the possible presence of random parameters for each species. For instance, in the general Lotka Volterra case, $R_i(N_i) = (r_i/K_i)(K_i - N_i)$ where the r_i and K_i respectively correspond to species-dependent growth rates and carrying capacities, that we will treat as random variables sampled from given distributions. The coupling tensor satisfies $\alpha^i_{j_1\ldots j_p} = 0$ if there exists k such that $i = j_k$, so as not to interfere with the self-interaction $R_i(N_i)$. Otherwise, its cumulants are taken as:

$$\overline{\alpha^i_{j_1\ldots j_p}} = \mu\frac{p!}{2S^{p-1}} \qquad \overline{(\alpha^i_{j_1\ldots j_p})^2}_{con} = \sigma^2\frac{p!}{2S^{p-1}} \qquad \overline{\alpha^i_{j_1\ldots j_p}\alpha^{j_k}_{j_1\ldots i\ldots j_{k-1}j_{k+1}\ldots j_p}}_{con} = \gamma\sigma^2\frac{p!}{2S^{p-1}}$$

where the notation $\overline{X}_{con}$ denotes the connected average of X, *i.e.* when subtracting their average to the elements. Because of the constraint $1 \leq j_1 < \ldots < j_p \leq S$, when considering the cross correlation, there is only one place for the upper index i to go down.

Within this setup, the DMFT equation for a given species reads:

$$\dot{N} = R(N) + I(N)\left(\mu m + \sigma\eta + \gamma\sigma^2\frac{p(p-1)}{2}\int_0^t \chi(t,s)C(t,s)^{p-2}J(N(s))ds + h\right) + f(N)\xi \quad (2.6)$$

[2] The derivation is similar to the one of the Langevin equation from Newtonian dynamics [76], with the extra-ingredient that the bath corresponds to the rest of the system whose behavior can be self-consistently obtained from the one of N_0.

where η is a Gaussian noise with zero mean and covariance $C_\eta(t,s) = \frac{p}{2}C(t,s)^{p-1}$, and ξ is a Gaussian white noise, with variance $2\omega^2$. The species-dependent parameters R, I and f are random variables to be sampled according to their statistical distribution. The self-consistent average is over the thermal noise and these parameters. For example, in the Lotka-Volterra case, the growth rate r and carrying capacity K should be sampled at each realization of the process. Using subscripts for the different times, we obtain the self-consistent closure:

$$\begin{cases} m(t) = \mathbb{E}[J(N_t)]^{p-1} \\ C(t,s) = \mathbb{E}[J(N_t)J(N_s)] \\ \chi(t,s) = \mathbb{E}[J'(N_t)\left.\dfrac{\delta N_t}{\delta h_s}\right|_{h=0}] \end{cases} \tag{2.7}$$

where the average $\mathbb{E}[.]$ is now taken with respects to the initial condition distribution, the distribution of species-dependent parameters in the functions R, I and f , the noise trajectory η and the thermal noise ξ.

It should be stated that the DMFT we derived with the dynamical cavity technique can also be obtained using generating functional technique of Martin-Siggia-Rose-DeDominicis-Janssen [66, 48, 71, 72] .

2.2.3. Solving numerically the DMFT equation

It is difficult to solve numerically a self-consistent equation where the self-consistency applies to functions. We focus on DMFT generic equations (2.6) and (2.7). We implemented a strategy which works as pictured in figure 2.1. In this section, we write down in details the methodology of the algorithm. More details are presented in appendix A.8. We always work with discrete time. The different steps of the program are the following:

1. We start from initial guesses for the correlator $C(t,s)$, the average population $m(t)$, and the response function $\chi(t,s)$. The results are found to be independent on the initial guesses.

2. Using the correlator, we can sample a Gaussian path as a simple multivariate Gaussian random variable with covariance matrix $C_\eta(t,s) = (p/2)\,C(t,s)^{p-1}$. We draw many ($\#_{traj}$) such Gaussian paths.

3. For each path, we use our guesses $m(t)$ and $\chi(t,s)$ to numerically integrate the DMFT equation where the initial condition is sampled according to the wanted distribution. We used the uniform measure on $[0,1]$ for example. For each Gaussian path, we get a different population trajectory.

4. From these trajectories, we compute the updated values of the average population vector, the correlator matrix and the response matrix (see below), using the self-consistent closure:

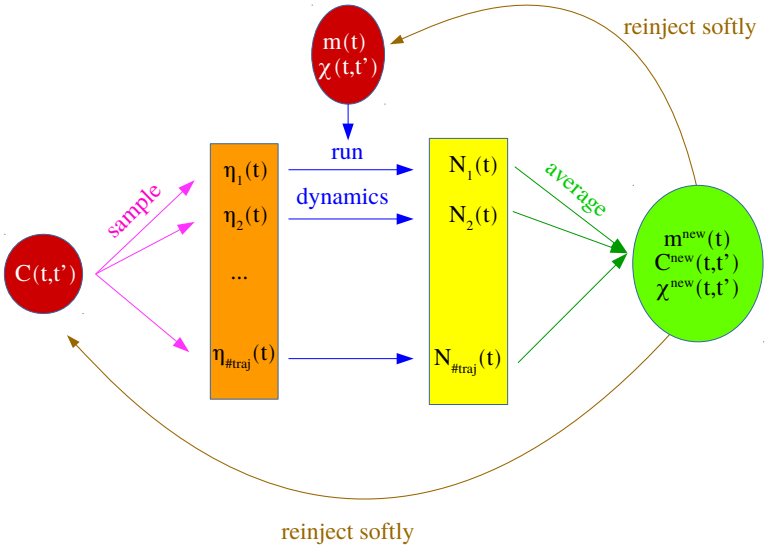

Figure 2.1. Sketch of the numerical scheme for solving the DMFT equation.

$$\begin{cases} m^{new}(t) = \mathbb{E}_{paths}\left[J(N_t)\right]^{p-1} \\ C^{new}(t,t') = \mathbb{E}_{paths}\left[J(N_t)J(N_t')\right] \\ \chi^{new}(t,t') = \mathbb{E}_{paths}\left[J(N_t)\int ds\; C_\eta^{-1}(t',s)\;\eta(s)\right] \textbf{ or } \mathbb{E}_{paths}\left[\chi_i(t,t')\right] \end{cases}$$

5. We update softly the set of functions: $X^{updated} = (1-a)X + aX^{new}$ with X being respectively m, C and χ. The soft reinjection is necessary for the algorithm to converge, and not jump erratically from functions to functions.

6. We start a new iteration of the loop, with the updated set of functions.

The convergence of the algorithm is of exponential form in the number of iterations, and is independent of the initial set of functions. On figure 2.2, we show an example of such a convergence.

Now, let us explain the above point (4) in more detail. Obtaining the average population vector, and the correlator matrix from the trajectories is a trivial procedure: one just needs to average. Evaluating the response function χ is instead more tricky. We studied two different complementary, or alternative, procedures. The first one consists in using Novikov's theorem [78] (or Stein's lemma) in the statistical field formulation in order to obtain:

$$\chi(t,s) = \sigma^{-1}\mathbb{E}[J(N_t)\int dx\; C_\eta^{-1}(s,x)\;\eta(x)] \tag{2.8}$$

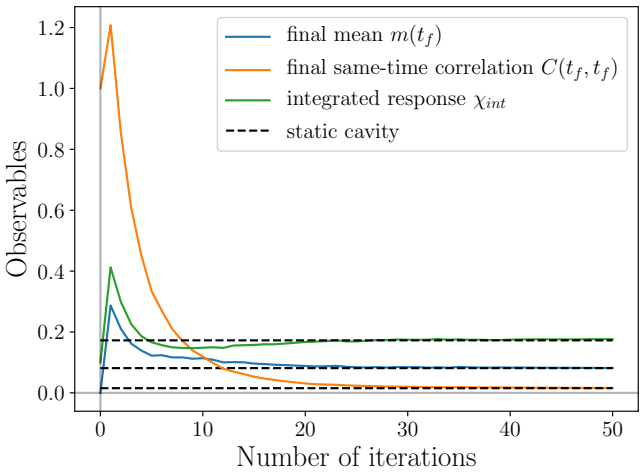

Figure 2.2. We show the convergence of different observables as a function of the number of iterations: the final mean abundance $m(t_f)$, the final same-time correlation $C(t_f, t_f)$ and the integrated response kernel $\chi_{int} = \int_0^{t_f} ds\, \chi(t_f, s)$. For comparison, dotted black lines represent the analytic stationary cavity solutions. The relative errors to the stationary cavity solutions are below 2%. As the DMFT observables are computed from a finite number of trajectories $\#_{traj}$, there is always some residual fluctuations. The solver was run with rLV DMFT with parameters $(\mu, \sigma, \gamma, \lambda) = (10, 1/2, -1, 10^{-4})$ in the Unique Equilibrium phase. The parameters of the program are: reinjection rate $a = 0.3$, final time $t_f = 40$, discrete time steps $\tau = 0.1$, final number of trajectories to average upon $\#_{traj} = 10^5$.

In this formulation, C_η^{-1} denotes the matrix inverse of C_η. The detailed derivation is presented in appendix A.3. This expression is easy to implement, however it is sometimes too greedy for numerics. For instance, in our problem with multiplicative noise, the number of DMFT trajectories to average upon in order to obtain a satisfactory estimate for the response function is too high. We thus derive another relation, by directly applying $\frac{\delta}{\delta h(t')}$ to equation 2.6. In this way, for each trajectory i, we can compute the response function $\chi_i(t,t')$ *via* temporal integration, and eventually average over trajectories to obtain $\chi(t,t')$. This procedure is less greedy in terms of needed trajectories, and is of the same numerical complexity. However, it is not fully parallelizable. The details are given in appendix A.4. In appendix A.5, we sum up and compare the adequacy of the two methods.

The algorithm we presented here can still be improved in several ways. More specifically, when the response function is needed (when $\gamma \neq 0$), the above algorithm is quite expensive numerically.

The details of the numerical implementation are in appendix A.8, and a public gitHub repository with the corresponding Python programs is available [74].

2.2.4. Numerical check of the results

We checked that the numerical solution of DMFT is consistent with the one from direct simulations. More specifically, we sample $\#_{instances} = 200$ interaction matrices and initial conditions for an ecosystem of size S, run the deterministic dynamics, and aggregate the observables by averaging over the S species and $\#_{instances}$ realizations. This is what we call direct simulations. In the Unique Equilibrium phase, the agreement is excellent. In figure 2.3, we show the comparison between DMFT and direct numerical simulations in the Multiple Attractors phase. As S increases the direct simulations observables converge at all times to the one from DMFT. It is surprising however that the direct simulations are so different from DMFT for $S = 200$. We reckon it is related to the fact that at finite S, when sampling the interaction matrix with parameters in the Multiple Attractor phase, there is a non-zero probability to get an interaction matrix that describes an Unbounded Growth ecosystem. This problem makes it difficult to have clean data using direct simulations, and underlines the relevance of DMFT analysis.

2.3. Application to the random Lotka-Volterra model

From the general model in equation 2.5, we recover the random Lotka-Volterra model by taking:

$$\begin{cases} R_i(x) = x(1-x) + \lambda \\ I_i(x) = -x \\ J(x) = x \\ f_i(x) = 0 \end{cases}$$

Note that there is no species-dependent parameters in these functions, as we consider the simplified case where all parameters r_i and K_i are set to unity, and the immigration

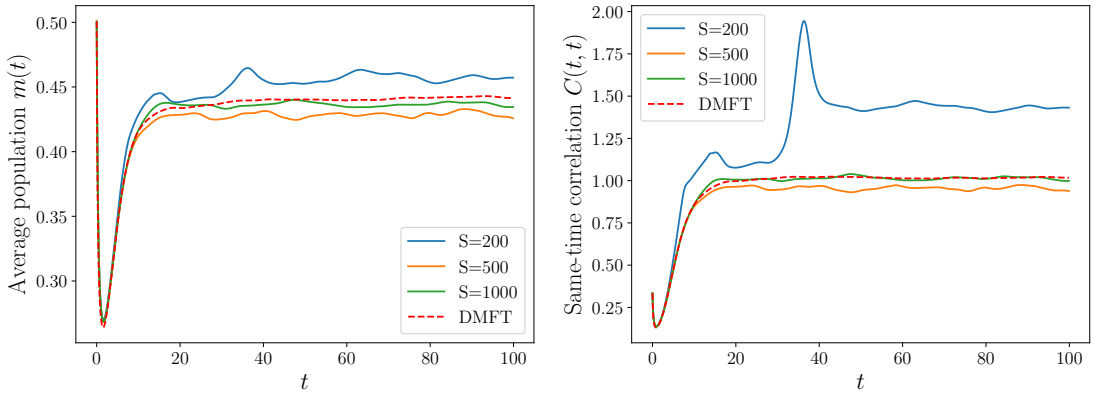

Figure 2.3. Comparison of the observables $m(t)$ (Left) and $C(t,t)$ (Right) between direct simulations varying the ecosystem size S, and DMFT predictions in dotted red line. It shows the convergence in law towards DMFT as S increases. The parameters of the simulations are $(\mu, \sigma, \gamma, \lambda) = (4, 2, 0, 10^{-4})$, in the Multiple Attractors phase.

rate λ is uniform. We then apply the general result of equation 2.6, and we obtain the DMFT:

$$\dot{N} = N\{1 - N - \mu m(t) - \sigma\eta(t) + \gamma\sigma^2 \int_0^t \chi(t,s)N(s)ds + h(t)\} + \lambda \tag{2.9}$$

The self-consistent closure is that of equation 2.4. In this section, we show how to get back the stationary results [45] from DMFT, and we study the stability of such stationary solution. All the following results are valid for $\lambda > 0$ where the limit $\lambda \to 0$ is subsequently taken. The reason for this regularization is detailed in appendix A.1.

2.3.1. How to recover the stationary results

If the ecosystem parameters belong to the Unique Equilibrium phase, each species will eventually reach a final population value and stop changing. We describe this final state using DMFT. The one-species stochastic process becomes time-independent, so the derivative is zero, the average $m(t)$ converges to a number $m(\infty)$, the population $N(t)$ and the Gaussian noise $\eta(t)$ converge to random variables $N(\infty)$ and $\eta(\infty)$. As the process is stationary, we treat the memory kernel as time-translational invariant $\chi(t,s) = \chi(t-s)$ and therefore:

$$\int_0^t \chi(t,s)N(s)ds = \int_0^t \chi(u)N(t-u)du \to_{t\to\infty} \int_0^\infty \chi(u)duN(\infty)$$

Introducing the integrated memory kernel $\chi_{int} = \int_0^\infty du\ \chi(u)$, the DMFT equation 2.9 finally converges to:

$$0 = N_\infty\{1 - N_\infty - \mu m_\infty - \sigma\eta_\infty + \gamma\sigma^2\chi_{int}N_\infty + h\} \tag{2.10}$$

$$\begin{cases} m_\infty = \mathbb{E}[N_\infty] \\ \chi_{int} = \mathbb{E}[\frac{\delta N_\infty}{\delta h}] \\ \mathbb{E}[\eta_\infty^2] = \mathbb{E}[N_\infty^2] \end{cases} \tag{2.11}$$

From equation 2.10, N_∞ can either be 0 or $(1-\gamma\sigma^2\chi_{int})^{-1}(1-\mu m_\infty - \sigma\eta_\infty)$. By a simple linear stability analysis performed on the real system of S species (see appendix A.6.1), it can be shown that the 0 solution is linearly unstable when the other solution is positive. Therefore, we obtain:

$$N_\infty = \max\left(0, \frac{1-\mu m_\infty - \sigma\eta_\infty}{1-\gamma\sigma^2\chi_{int}}\right) \tag{2.12}$$

so the random variable N_∞ follows a Gaussian distribution, truncated for negative abundances. We write the closed system of equations in appendix A.6.1, and show that we end up with the same system as the one from [45]. From it, all observables can be computed numerically as a function of the parameters (μ, σ, γ): the fraction of species coexisting at the fixed-point, the mean abundance N of species that survive and the mean response function. Some further analytical results can be derived as well, such as identifying in parameter space the boundary between the Unique Equilibrium phase and the Unbounded Growth phase. However, this analysis is only exact when we are in the Unique Equilibrium phase. It becomes approximate in the Multiple Attractors phase.

2.3.2. Dynamical stability and the transition line to Multiple Attractors

We now describe the loss of stability of the Unique Equilibrium solution when increasing the variability σ of interactions: a dynamical phase transition takes place. The setup follows the one of [53]: starting in the Unique Equilibrium phase, we let the system reach an equilibrium point, then add some small field $h(t)$ which we will take as a Gaussian white noise with covariance $\overline{h(t)h(s)} = \sigma_h^2\delta(t-s)$, and see how the system responds in perturbation theory. In order to do so, we consider the DMFT equation 2.9, linearize it around a stationary solution, and perform a Fourier analysis [53]. The detailed calculations are presented in appendix A.7. Introducing $\tilde{X}$ the Fourier transform of X, we obtain the small frequency expansions for both the connected correlator $C_c(t,t') = \mathbb{E}[\eta(t)\eta(t')] - \mathbb{E}[\eta_\infty^2]$ and the response function:

$$\tilde{C}_c(\omega)/\sigma_h^2 = \chi_{int}^2 \left(\phi - \sigma^2\chi_{int}^2 + \omega\, \tfrac{\chi_{int}}{\phi}\tfrac{\pi}{2}\, p_+(0)\right)^{-1} \tag{2.13}$$

$$\tilde{\chi}(\omega) = \chi_{int} + i\omega\log(\omega)\tfrac{p_+(0)\,\chi_{int}^2/\phi}{\phi-\gamma\sigma^2\chi_{int}^2} \tag{2.14}$$

.

where ϕ, χ_{int} and $p_+(0)$ are properties of the Unique Equilibrium we started from. They correspond respectively to the fraction of surviving species, the integrated response to perturbations, and the value in 0^+ of the surviving species' distribution. They can be computed using the Unique Equilibrium distribution detailed in appendix A.6.1.

Different things should be noted about these expansions. First, it can be checked that we obtain the same zeroth order condition for the response function as in the stationary cavity study: $\tilde{\chi}(\omega = 0) = \chi_{int}$. Secondly, the correlator initially behaves as $(a + b\,\omega)^{-1}$ which corresponds to a temporal decay as $1/t^2$. But a change of behavior is displayed when zeroth order term a goes to zero: we observe a $1/\omega$ correlation spectrum, which is an indicator of the chaotic transition [53]. Indeed, with this criterion we find the same transition in parameter space as the one from random matrix theory (the line $\sigma_c = \frac{\sqrt{2}}{1+\gamma}$ in the phase portrait in figure 1.1). Surprisingly, the response function instead does not exhibit a transition at σ_c, except for $\gamma = 1$ where the fluctuation-dissipation theorem establishes a direct link between the correlation function and the response function. More complex response functions might be needed to locate the transition in the general case.

2.4. Numerical solution for the random Lotka-Volterra model

In this section, we present some numerical results for the random Lotka-Volterra DMFT, and show the consistency of both analytics and numerics. The aim is to illustrate the quality of the DMFT results, and present a first description of the dynamical phases (a more complete one will be presented elsewhere).

2.4.1. Results in the Unique Equilibrium phase

We focus on the correlator $C(t, t') = \mathbb{E}[N(t)N(t')]$. In the Unique Equilibrium phase, it reaches a plateau as each trajectory converges to a random constant. Moreover, the value of the plateau coincides with the stationary cavity observable q. This is indeed the case, as pictured on figure 2.4. The convergence to the stationary solution is a good check of the validity of our numerical strategy. It is shown more precisely on figure 2.2.

2.4.2. Results in the Multiple Attractors phase

In the Multiple Attractor phase we expect a different behavior. The system does reach a time-translational invariant (TTI) chaotic state. This means that the one-time observables (the mean population $m(t)$, the proportion of alive species $\phi(t)$, or the equal-time correlation $C_\sigma(t, t)$) converge to a constant, and the two-time observables become functions of the time difference: $C_\sigma(t, t') = C_\sigma(t - t')$. If we focus on large times, we expect a relaxing behavior for the correlator, as the trajectory decorrelates from itself when it explores the phase space along the chaotic attractor. We observe this phenomenon in the numerical solutions. Moreover, the TTI state depends on how deep in the Multiple Attractors phase the system is. On figure 2.5, we show the dependence on σ of the TTI correlation $C_\sigma(t - t')$, rescaled as follows. These functions $C_\sigma(\tau)$ starts at a TTI value for the equal-time correlation $C_\sigma(0)$, then as the trajectories decorrelate from themselves $C_\sigma(\tau)$ relaxes towards a TTI final value $C_\sigma(\infty)$ over a timescale a_σ. We therefore plot $\frac{C_\sigma(t-t') - C_\sigma(\infty)}{C_\sigma(0) - C_\sigma(\infty)}$. We also denote $Q_\sigma = C_\sigma(0) - C_\sigma(\infty)$ the amplitude of the decorrelation. It is representative of the chaos strength, and this is an order parameter for the

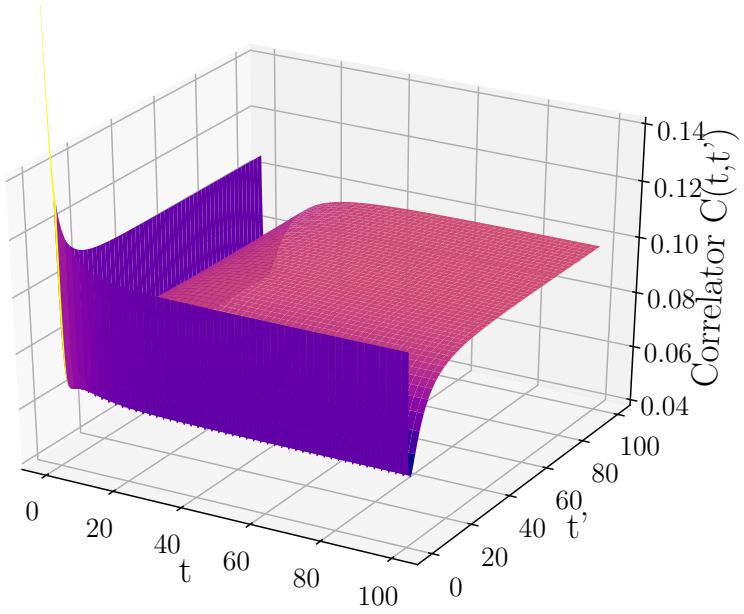

Figure 2.4. Numerical correlator of plateau type, for rLV DMFT with parameters $(\mu, \sigma, \gamma, \lambda) = (4, 1, 0, 10^{-4})$ below the onset of chaos. The parameters of the program are the same as in figure 2.2.

chaotic transition. Indeed, $Q_\sigma = 0$ in the One Equilibrium phase as the TTI $C_\sigma(t)$ is a constant in this phase, and $Q_\sigma > 0$ in the Multiple Attractors phase as there is some persistent dynamics. It is easier to compute numerically than other order parameters such as the Lyapunov exponent. On figure 2.6 we show the dependence of both the chaos strength Q_σ and the time scale a_σ as a function of the chaotic depth $\sigma - \sigma_c$. As expected, the chaos strength Q_σ increases and the chaos time scale a_σ decreases with the chaotic depth. Our results show that chaos emerges through a *second-order out of equilibrium dynamical phase transition*. A first attempt to obtain critical exponents is shown in figure 2.6.

We recall that we have considered small but finite immigration. Dynamics without immigration is different, as we discuss below.

2.4.3. Aging dynamics without immigration

We now consider the effect of the absence of immigration on the chaotic dynamics. The main issue is that chaos induces fluctuations that can drive species to extinction in absence of immigration and, hence, potentially kill chaos itself. The sustainability of chaotic dynamics without immigration is therefore far from being granted, actually a very different dynamical behavior can be present when $\lambda = 0$. Here we show that this is indeed the case for $\gamma = 0$. In figure 2.7 we compare the correlation functions, normalized by its equal time value, obtained by DMFT for $\gamma = 0$ with and without immigration. In

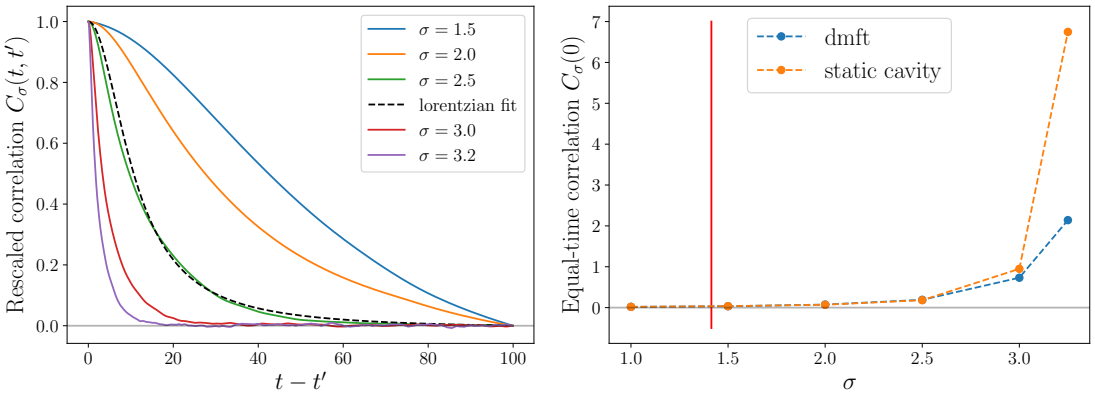

Figure 2.5. Left: Time evolution of the TTI correlation $C_\sigma(t-t')$ varying σ. Those are DMFT numerical results with parameters $(\mu, \gamma, \lambda) = (10, 0, 10^{-4})$. We checked that the system indeed reaches TTI, $t' = 200$ is enough here. More precisely, we show the rescaled TTI correlator $\frac{C_\sigma(t-t')-C_\sigma(\infty)}{C_\sigma(0)-C_\sigma(\infty)}$, in order to see the dependence of the chaotic time scale a_σ with σ. This time scale decreases with σ. In order to have a quantitative approximation for a_σ, we use a Lorentzian fit; an example of such is the dotted black curve. Right: σ dependence of the TTI equal-time correlator $C_\sigma(0)$. The red line indicates the chaotic transition. In orange dots, we show for comparison the analytical static cavity results. In the Unique Equilibrium phase, the DMFT and static cavity results coincide (to a non-zero but small value). In the Multiple Attractors phase, they diverge from each other, but the static cavity remains a good approximation for a relevant chaos depth. Note that $C_\sigma(0) > 0$ for all σ.

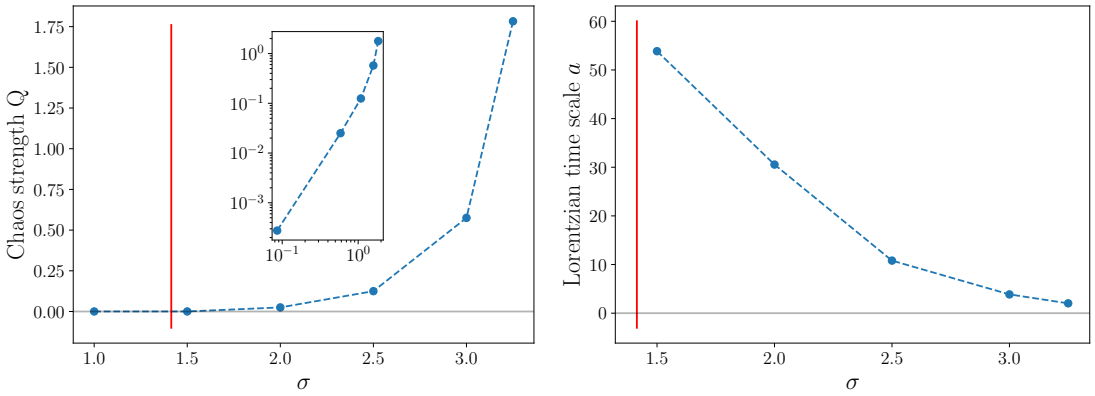

Figure 2.6. Left: Chaos strength $Q_\sigma = C_\sigma(0) - C_\sigma(\infty)$ as a function of σ. It is zero in the Unique Equilibrium phase, and non-zero in the Multiple Attractors phase. The red line corresponds to the chaotic transition $\sigma = \sigma_c$. The inset is a log-log plot $Q(\sigma - \sigma_c)$. The behavior seems to agree with a critical exponent around 2.4: $Q \sim (\sigma - \sigma_c)^{2.4}$. Right: Chaos time scale a_σ as a function of σ. It is non-zero in the Multiple Attractors phase, and should diverge as we approach the chaotic transition. The red line corresponds to the chaotic transition $\sigma = \sigma_c$. These values are only approximate, based on basic Lorentzian fit from figure 2.5. They do not allow us to extract a critical exponent.

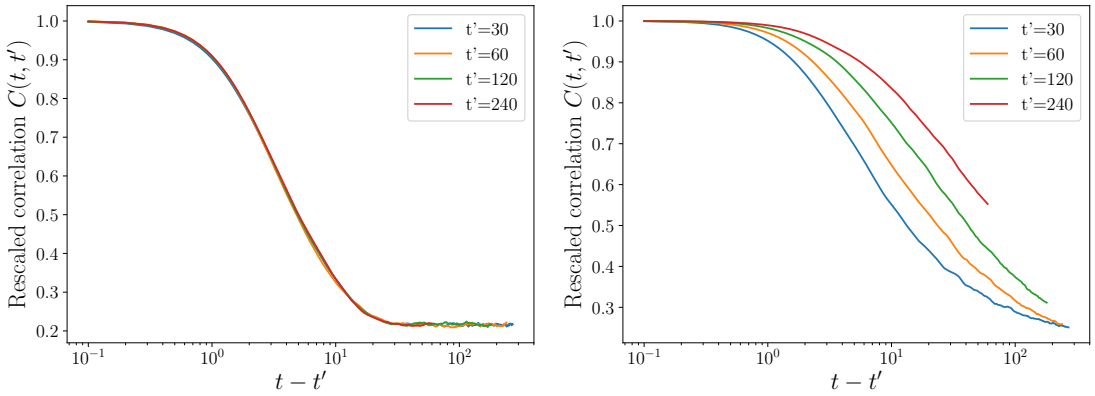

Figure 2.7. Aging phenomenon without immigration in DMFT. In the chaotic phase, we show the decay of the rescaled correlation $C(t,t')/C(t',t')$ as a function of $(t-t')$, varying t'. The parameters are $(\mu,\sigma,\gamma)=(10,3,0)$ Left: With immigration $\lambda=10^{-4}$, the system reaches a TTI state, there is no dependence on the age of the system t'. Right: Without immigration $\lambda=0$, the relaxation of the correlation does depend on the age of the system t'; the older the system, the longer it takes to relax. The parameters of the program are the same as in figure 2.2.

the former case (left panel), it is clear that a stationary chaotic state establishes as $C(t,t')$ becomes a function of $(t-t')$ at large times. On the contrary, without immigration (right panel), $C(t,t')$ shows the aging behavior characteristic of glassy system: the correlation function is not a function of $t-t'$ and displays a relaxation that is slower the older is the system. This is a nice illustration of how our numerical implementation of DMFT allows to unveil the existence of different and complex dynamical behaviors.
A more detailed study of the aging chaotic behavior shown in figure 2.7, and an analysis of how and when chaos fades away is presented later on in chapters 4 and 4.6.

2.5. Conclusion

In summary, we have presented a general derivation of DMFT for models of ecosystems based on the dynamical cavity method. We have implemented and tested our numerical method for generalized Lotka-Volterra models of ecosystems and showed that it can capture complex dynamics such as chaos and aging. Future works will be devoted to a thorough analysis of these complex dynamical regimes, and also to improvements of our algorithm along the ways discussed in this chapter.
The main contribution of our work is the development of a numerical method to solve DMFT that can be used for many different systems characterized by stochastic dynamics and by a large number of degrees of freedom. One important potential application is to the dynamics of interacting particle glassy systems in the limit of infinite dimensions

for which mean-field dynamical equations were derived recently [79, 80]. A collaborator [81] presented numerical results for this system, after our initial work [61].

3. Numerical investigation of the aging dynamics

In this chapter, we focus on the Lotka-Volterra dynamics without the immigration regularization. This aim of the study is to shed light at how and why chaos is killed, and to give insights on related models from economy for example.

First, we present the most obvious and intuitive manifestations of aging in the numerics. Then we detail the mathematical tools for fixed points (FP) and stability, that we use later on to investigate numerically the marginal stability of the dynamics.

This chapter consists in unpublished results and ongoing work, we make the clear distinction between both here. The numerical study of the aging phenomenon establishes the marginal stability of the dynamics as a result. Starting from section 3.5, the Fixed Point picture which we propose is only tentative, and involves ongoing work.

Throughout the chapter, we use a slightly misleading vocabulary for convenience. We will refer to a species being 'dead'/'alive' instead of 'extinct'/'present'. We will also say that it is 'invadable' if it can invade the system.

3.1. Introduction[1]

Historically, studies of endogenous fluctuations have focused on single populations or few species [19, 20, 21]. On the other hand, theories of many-species interaction networks often center on ecosystems that return to equilibrium in the absence of perturbations [3]. Some authors have even proposed that fluctuations driven by interactions are generally too rare or short-lived to matter, since they can be self-defeating: dynamics that create large erratic variations lead to extinctions, leaving only species whose interactions are less destabilizing, until an equilibrium is reached [22, 23]. In this thesis, we will go past both the equilibrium [3, 24] or few-species starting points [19, 20, 21], to look directly at the dynamics of high-diversity communities.

Without immigration, we observe that the chaotic dynamics[2] displayed by the ecosystem in the Multiple Equilibria phase are no longer stable: the dynamics become slower and slower as the time goes on. The fact that the dynamics depend on the time at which we look at them is called *aging* phenomenon: because indeed the observations depend on the *age* of the system. It is quite studied in the context of spin-glasses and disordered systems [82, 83, 65, 84]. The mathematical analysis is generically more involved

[1] So that each chapter may be read separately, I decided to preserve all specific chapters' full introduction, even though it may overlap with the global and more detailed introduction from section 1. The overlapping parts are presented in the box and can be skipped.

[2] Such dynamics can be seen on figure 1.3.

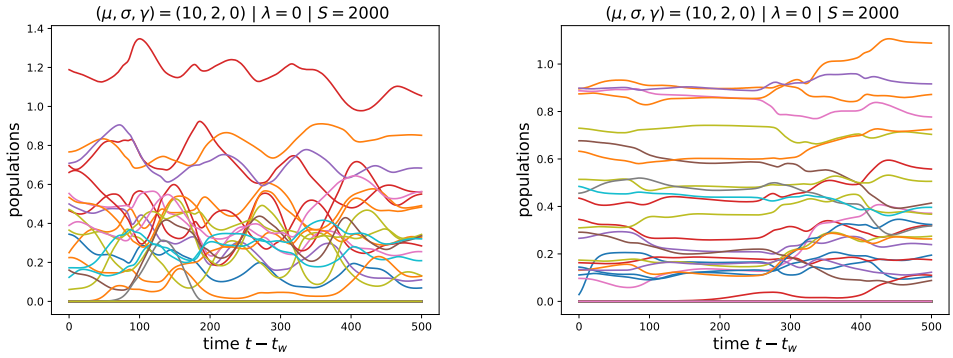

(a) Age of the system $t_w = 10^4$ **(b)** Age of the system $t_w = 10^5$

Figure 3.1. We consider one given ecosystem, sampled in the chaotic phase, and run the dynamics without immigration. We show the time evolution of the populations of a few species (the same set for both plots). We perform this plot with the same time window, but after different waiting times. We clearly see that the dynamics become slower as the system gets older: the dynamics are slower on figure 3.1b than on figure 3.1a.

than for usual systems that lie in an equilibrium state. In disordered systems, aging is associated with trapped dynamics and a general slowing down: the energy landscape displays many local minima that effectively trap the system for longer and longer times. In the case of ecology, there is generically no energy landscape to simplify the analysis. In this chapter, we detail a brief analysis of the ecological fixed points, followed by the numerical investigation of the aging behavior in this context.

3.2. Preliminary numerical investigation

The first obvious proof of aging appears when plotting the populations as a function of time, on figure 3.1. We can see that the dynamics gets slower as the ecosystem gets older.

To quantify more precisely the slowing down of the dynamics, we consider the correlation function $\langle N(t)N(t')\rangle$, averaged over the species [82] . The typical time it takes for the species population to decorrelate is linked to the timescale of the dynamics. We show on figure 3.2 that this timescale increases with time, and that this phenomenon is robust to different values of the symmetry parameter γ. This is important, because we know that perfect symmetry $\gamma = 1$ or antisymmetry $\gamma = -1$ are two special cases (of which we have a better understanding). In this thesis, we study perfect asymmetry $\gamma = 0$, and interpolate between perfect symmetry or antisymmetry. For $\gamma = 0$, we see on figure 3.2 that the timescale for decorrelation is roughly proportional to the age of the system:

$$\tau_{decorrel}(t) \sim t \tag{3.1}$$

Eventually, the aging phenomenon in the correlation function can also be seen numerically with the DMFT formalism, as detailed in section 2.4.3 (figure 2.7).

3.3. Stability considerations for fixed points

In order to study the dynamics, a crucial aspect is the linear stability of the fixed points of the dynamics. Indeed, a good understanding of the dynamical flow in phase space can be achieved by such a study. In this section, we detail the stability theoretical analysis of the fixed points, that we use later on for the numerical investigation.

3.3.1. Set up

From the dynamics, it is possible to define many stability conditions. In this section we will focus on two of them: the stability with respect to perturbation in the environment, and the dynamical linear stability. We start from the general Lotka-Volterra equations:

$$\forall i \in \{1...S\}, \qquad \dot{N}_i = N_i \left(K_i - N_i - \sum_j \alpha_{ij} N_j \right)$$

We introduce the population vector $\vec{N}$, with coordinates the species populations $N_{i=1...S}$. We look for a fixed point: $\dot{\vec{N}} = 0$. Then, for each species we can either choose $N_i = 0$, or $N_i = K_i - \sum_j \alpha_{ij} N_j$. We will refer to this as the '(dead/alive) choice'. Therefore, there are always 2^S possible fixed points, but some of them are dynamically unreachable because they have negative coordinates.

We consider a given fixed point, so each (dead/alive) choice has already been made. We relabel the species so that the alive ones correspond to $i = 1...\phi S$. We introduce the notation X^a that corresponds to vectors and matrices restricted to alive species $i \leq \phi S$. We introduce the corresponding notation X^d for vectors and matrices restricted to dead species $i > \phi S$. The population values of the fixed point are then given by:

$$\begin{cases} \vec{N}^a = \left(\underline{\underline{\tilde{\alpha}}}^a\right)^{-1} . \vec{K}^a \\ \vec{N}^d = \vec{0}^d \end{cases} \tag{3.2}$$

where we denote a matrix by the two underlines $\underline{\underline{\alpha}}$, and we used the matrix . product. We introduced the matrix $\underline{\underline{\tilde{\alpha}}} = \underline{\underline{Id}} + \underline{\underline{\alpha}}$. We assumed that $\underline{\underline{\tilde{\alpha}}}^a$ is invertible, which is generically the case.

We now derive the two distinct stabilities that we consider: the environmental one, and the dynamical one.

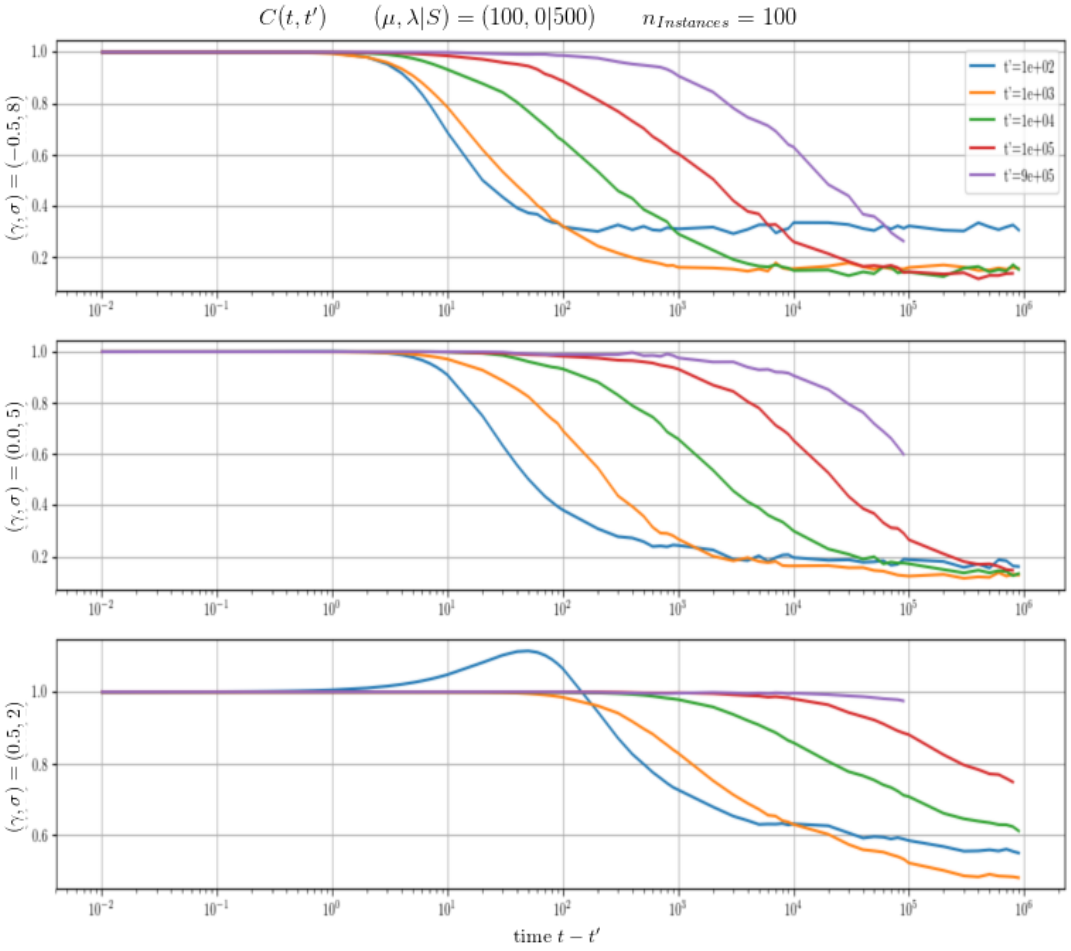

Figure 3.2. Correlation function showing aging phenomenon in the chaotic phase without immigration. This is robust to different values of the symmetry parameter γ, from top to bottom $\gamma = -0.5$, 0, 0.5. More precisely, what is shown is the rescaled correlation $C(t,t')/C(t',t')$ as a function of $t-t'$, varying t'. This data corresponds to $n_{instance} = 100$ realizations of ecosystems with parameters $S = 500$, $\mu = 100$, varying γ and σ to stay in the chaotic phase.

3.3.2. Environmental stability

A perturbation in the environment of the ecosystem can be modelled as a perturbation in the carrying capacities $\{K_i\}_{i=1...S}$. Now we wonder whether the alive species populations at the fixed point are stable with respects to infinitesimal environmental fluctuations. We define: $(\chi_K^a)_{ij} = \frac{\partial N_i^a}{\partial K_j^a}$. From equation 3.2, we obtain directly the environmental stability matrix:

$$\underline{\underline{\chi_K^a}} = \left(\underline{\underline{\tilde{\alpha}}}^a\right)^{-1} \tag{3.3}$$

The only instability that can occur in this case comes from the largest eigenvalue of $\underline{\underline{\chi_K^a}}$. Indeed, from random matrix theory [85], we know that the typical spectrum of the matrix $\underline{\underline{\tilde{\alpha}}}^a$ is a dense ellipse in the complex plane, centered in the Cartesian coordinates $(1, 0)$. Therefore, if the spectrum has some eigenvalues with negative real part, it will also have eigenvalues very close to zero (by density, and connectedness of the ellipse). Then, the corresponding eigenvalue for the inverse matrix $\underline{\underline{\chi_K^a}}$ will be diverging.

Eventually, we will consider that the ecosystem is stable with respect to perturbation in the environment iif all the eigenvalues of the interaction matrix $\underline{\underline{\tilde{\alpha}}}^a$ have a strictly positive real part.

3.3.3. Dynamical stability

We linearize the dynamics around the above fixed point. Remember that it is given by (3.2). We introduce the lower left submatrix $\underline{\underline{\alpha}}^{da}$, such that $\underline{\underline{\alpha}}^{da}_{ji} = \underline{\underline{\alpha}}_{j>\phi S,\, i\leq\phi S}$. With these conventions, the linearization yields:

$$\begin{cases} \delta\dot{N}_i = -N_i^a \left(\underline{\underline{\tilde{\alpha}}} \,.\delta\vec{N}\right)_i & \text{for alive species } i \leq \phi S \\ \delta\dot{N}_j = e_j \; \delta N_j & \text{for dead species } j > \phi S \end{cases} \tag{3.4}$$

where we introduced the growth rates:

$$\vec{e}^d = \vec{K}^d - \underline{\underline{\tilde{\alpha}}}^{da}.\, \left(\underline{\underline{\tilde{\alpha}}}^a\right)^{-1} . \vec{K}^a \tag{3.5}$$

that quantifies whether a dead species j can establish in the ecosystem after a small immigration ($e_j \geq 0$) or not ($e_j < 0$).

There are three questions to answer for the above fixed point to be both physical and dynamically stable:

1. Is this fixed point physical? By this we mean that all populations have to be positive:
$$\vec{N}^a = \left(\underline{\underline{\tilde{\alpha}}}^a\right)^{-1} . \vec{K}^a \geq 0$$

2. Are the dynamics stable, when considering only the alive community of species? *I.e.* does the ecosystem remain close to the fixed point, or does it escape quickly

from it? To define this, we use equation (3.4) and we introduce the dynamical stability matrix:

$$\underline{\underline{\chi_D^a}} = \underline{\underline{diag}}(\vec{N}^a).\,\underline{\underline{\tilde{\alpha}}}^a \tag{3.6}$$

so that the linear dynamics restrained to alive species writes $\dot{\vec{\delta N}}^a = -\underline{\underline{\chi_D^a}}.\,\vec{\delta N}^a$. Then, the dynamical stability condition amounts to the positive definition of the dynamical stability matrix $\underline{\underline{\chi_D^a}}$: all its eigenvalues need to have a strictly positive real part.

$$\underline{\underline{\chi_D^a}} > 0 \qquad \text{(in the positive definite sense)}$$

3. Do the dead remain dead? More precisely, for all dead species, if a few individuals of the species are introduced in the ecosystem at the fixed point, does the species go extinct quickly? This is quantified by the condition:

$$\vec{c}^d = \vec{K}^d - \underline{\underline{\tilde{\alpha}}}^{da} \left(\underline{\underline{\tilde{\alpha}}}^a\right)^{-1} \vec{K}^a < 0$$

3.3.4. Summary of the fixed point properties

We present in table 3.1 the different mathematical formulations of the ecological properties of the fixed points. We abusively used the *positive* notation. For vectors, we mean it for each coordinates:

$$\text{"}\vec{X} > 0\text{"} \qquad \Leftrightarrow \qquad \text{"}\forall i,\ X_i > 0\text{"}$$

And for matrices, in the positive definite sense. If we denote λ_i^M the eigenvalues of a matrix $\underline{\underline{M}}$, then:

$$\text{"}\underline{\underline{M}} > 0\text{"} \qquad \Leftrightarrow \qquad \text{"}\forall i,\ \lambda_i^M > 0\text{"}$$

3.3.5. Relation between the two stability matrices

We recall the two different stability matrices (restrained to alive species) that we introduced:

- the environmental stability matrix: $\underline{\underline{\chi_K^a}} = \left(\underline{\underline{\tilde{\alpha}}}^a\right)^{-1}$
- the dynamical stability matrix:$\underline{\underline{\chi_D^a}} = \underline{\underline{diag}}(\vec{N}^a).\,\underline{\underline{\tilde{\alpha}}}^a$

We are interested only in definite-positivity for these two matrices. A very interesting result from [86] states that in our setup, for large ecological communities $\phi S \gg 1$, environmental stability is equivalent to dynamical stability (provided the fixed point is feasible):

$$\text{"}\underline{\underline{\chi_K^a}} > 0\text{"} \qquad \Leftrightarrow \qquad \text{"}\underline{\underline{\chi_D^a}} > 0\text{"}$$

Fixed point property	**Mathematical object to consider**	**Mathematical condition**
Feasibility	$\vec{N}^a = \left(\underline{\tilde{\alpha}}^a\right)^{-1} . \vec{K}^a$	$\vec{N}^a \geq 0$
Uninvadability	$\vec{e}^d = \vec{K}^d - \underline{\tilde{\alpha}}^{da} \left(\underline{\tilde{\alpha}}^a\right)^{-1} \vec{K}^a$	$\vec{e}^d < 0$
Environmental stability	$\underline{\underline{\chi^a_K}} = \left(\underline{\tilde{\alpha}}^a\right)^{-1}$	$\underline{\tilde{\alpha}}^a > 0$
Dynamical stability	$\underline{\underline{\chi^a_D}} = \underline{\underline{diag}}(\vec{N}^a).\underline{\tilde{\alpha}}^a$	$\underline{\underline{\chi^a_D}} > 0$

Table 3.1. Mathematical formulation of the ecological properties of the fixed points

3.4. Marginality of numerical simulations

In this section, we will argue that at long times, the chaotic dynamics without immigration become marginally stable. This behavior is quite standard in disordered systems [82]. Indeed, in the context of spin-glasses the situation is the following. The system explores the vicinity of different fixed points, which are initially dynamically unstable, so it evades quickly from them. However, as time goes on, the fixed points that the system explore become marginally stable: they have directions in phase space that are neither stable nor unstable. As a consequence, it takes a long time for the system to evade from these fixed points. The analysis is generally performed by studying the energy function (whose extrema correspond to the fixed points of the dynamics). In the case of ecology, there is no energy (or Lyapunov) function, we thus have to come up with a distinct procedure to study the dynamics. Still, the idea of marginal stability has been around in this field for a long time as well. Indeed, the May bound (presented in more details in section 1.2.2) corresponds exactly to the ecosystem being in a marginally stable equilibrium.

3.4.1. Our protocol to study marginality

In order to study the dynamics, our idea is to identify which fixed points the system visits as time goes on, and examine their properties. Identifying which fixed point the system feels is not an easy task. The most intuitive way to find the corresponding fixed

point $\vec{N}_F P(t)$ to the dynamical $\vec{N}(t)$ would be to stop the dynamics, define some other dynamics[3] that can find the fixed point, and look at how these specific dynamics end at long times. This is quite tedious, and numerically heavy.

We follow a different approach here. We will use the fact that, once we have identified which species are dead or alive, there is an obvious fixed point: the one defined from equations (3.2) that we recall here when all carrying capacities are set to unity.

$$\begin{cases} \vec{N}^a = \left(\underline{\underline{\tilde{\alpha}}}^a\right)^{-1} . \vec{1}^a \\ \vec{N}^d = \vec{0}^d \end{cases} \tag{3.7}$$

It should be stated that there is no *a priori* reason for this fixed point to be the closest, nor the most influential for the dynamics. However, it is an easy choice, and we will check in the following that it is indeed relevant for the dynamics.

Therefore, the initial step of our study is to define at each time step which species are dead, and which ones are alive. There is actually another interest quantifying the global diversity[4] of the ecosystem at each time. This follows the same line as the May bound argument (in section 1.2.2), but we present it in more details here:

1. From [87], we know that the dynamics from Lotka-Volterra do not modify the obvious statistical properties of the interaction matrix. In particular, the interactions restrained to the alive communities that are formed still retain the same variance and symmetry compared to the initial pool of species.

2. Thanks to this and classical random matrix theory [85], we know the typical spectrum of eigenvalues of the modified interaction matrix $\underline{\underline{\tilde{\alpha}}}^a$ of the alive species: the spectrum forms a dense ellipse in the complex plane whose geometrical properties directly follows from the statistics. We recall the properties of the initial interaction matrix (see section 1.4.1):

$$\overline{\alpha_{ij}} = \mu/S, \qquad \overline{(\alpha_{ij} - \overline{\alpha_{ij}})^2} = \sigma^2/S, \qquad \overline{(\alpha_{ij} - \overline{\alpha_{ij}})(\alpha_{ji} - \overline{\alpha_{ji}})} = \gamma\sigma^2/S$$

   Then, the ellipse is centered in $(1, 0)$ in Cartesian coordinates, with horizontal semi-axis $b = \phi^{1/2}\sigma(1+\gamma)$ and vertical semi-axis $b = \phi^{1/2}\sigma(1-\gamma)$. We introduced the diversity ϕ at the fixed point.

3. Thanks to the work of [86], we know that the dynamical stability of a fixed point is equivalent[5] to the definite positivity of the modified interaction matrix of the alive species:

$$\text{"}\underline{\underline{\tilde{\alpha}}}^a > 0\text{"} \qquad \Leftrightarrow \qquad \text{"}\underline{\underline{\underline{\underline{\chi_D^a}}}} > 0\text{"}$$

[3] A gradient descent minimizing the derivative norm for instance.
[4] The *diversity* is the proportion of alive species.
[5] Provided its feasibility.

4. Combining all previous results, we derive that the dynamical stability of a fixed point can be directly inferred from its diversity (and the statistical properties of interactions, but these do not change with time):

$$\text{"}\underline{\underline{\chi^a_D}} > 0\text{"} \qquad \Leftrightarrow \qquad \text{"}\phi < \phi_{marginal}\text{"} \tag{3.8}$$

where we introduced the marginal diversity (*i.e.* the May bound):

$$\phi_{marginal} = [\sigma(1+\gamma)]^{-2} \tag{3.9}$$

We explain a bit more the above points 1 and 2. It should be noted that when we use the random matrix spectrum, we implicitly assume that the interaction matrix restricted to alive species is statistically equivalent to a random matrix with *i.i.d.* elements. One could have imagined that the matrix element become correlated because they are conditioned on the alive species. Even though it is shown in [46] that the conditioning does introduce some correlation, this cannot be seen if considering simple statistical observables [87]. In particular, Ref [47] shows that for the typical spectrum of the matrix, the approximation is valid.

We just showed that the marginal stability of the dynamics is equivalent to $\phi(t) = \phi_{marginal}$. We now detail the different methods we use to infer diversity.

3.4.2. Inference of diversity from the dynamics

The determination of diversity from simulations is slightly ill-defined. Indeed, the populations are continuous variable in the general Lotka-Volterra model, it takes therefore an infinite time for a species abundance to be exactly zero.

Counting cut-off

The most intuitive way to infer diversity is then to use a counting cut-off N_{cut}: for each species, we will consider that it is extinct at a given time t iif $N_i(t) < N_{cut}$. One needs to remember that according to this criterion and our dynamics, a species can be extinct at a given time, but alive later on.

Assuming truncated Gaussian distribution of abundances

We present here an alternative way to infer diversity. In the One-Equilibrium phase, the abundances $\{N_i\}_{i=1...S}$ have a truncated Gaussian distribution. In the dynamical phase, it is only an approximation. Indeed, species can fluctuate around their typical populations (what we call their bias N^* in chapter 4), so the truncated Gaussian distribution is wrong at low abundances $N \ll 1$. Still, we can use this approximation to infer the global diversity of the system from simple observables.

What we have access to easily is (m, q), the first and second moments of the full abundance distribution. Assuming truncated Gaussian distribution, we can define a

corresponding diversity $\phi(m, q)$:

$$\phi(m, q) = w_0 \circ \left(w_2/w_1^2\right)^{-1} [q/m^2]$$

where we used the static cavity functions $w_k(\Delta) = \int_{-\infty}^{\Delta} (\Delta - s)^k Ds$, with Ds the standard Gaussian measure.

With this method, we can infer the diversity, but not which species are dead or alive.

Evidence of marginality from simulations

We now use the distinct methods to compute the diversity at all time, and compare it to the marginal stability one from (3.9). On figure 3.3, we see that the dynamics get quite close to $\phi_{marginal}$ up to numerical precision, whatever the criterion used to define dead/alive. This is the first evidence that the ecosystem becomes marginally stable at long times, and that this phenomenon is responsible for the slowing down of the dynamics.

3.4.3. Fixed points analysis

We now identify marginality more thoroughly. We use an effective cut-off to distinguish dead/alive species. In the following study, we always checked that the results do not depend on the value of this cut-off $N_{cut} = 10^{-5}, 10^{-10}, 10^{-100}...$ First, we check that the fixed point defined by this cut-off (all populations below the cut-off are put to zero, all above are determined by inverting the alive interaction matrix) is relevant for the dynamics. This is done on figure 3.4. For each time, we plot the distance between the dynamical point $\vec{N}(t)$ and the corresponding fixed point $\vec{N}_{FP}(t)$. More precisely, we plot the rescaled distance as a function of time:

$$d(t) = \left(\frac{1}{S} \sum_{i=1}^{S} (N_i(t) - N_{i,FP}(t))^2 \right)^{1/2}$$

We see that as time increases, the distance decreases and goes towards 10^{-3} or lower, so the corresponding fixed point is a good approximation of the dynamics. Therefore we can use its corresponding stability analysis.

Second, we use the corresponding fixed points and study their stability. To do this, we compute the spectrum of their environmental and dynamical stability matrices, and plot them on figure 3.5. It can be seen that they both become marginal: all eigenvalues are positive at long times, but the smallest one touches zero. This means that the dynamics become slower and slower.

3.4.4. Comparison with immigration

For comparison, we now use results from simulations with immigration ($\lambda = 10^{-10}$). The one-time observable are very similar, and there is no aging as expected. On figure 3.6a, we show the distance to the corresponding fixed points. The dynamics cannot get

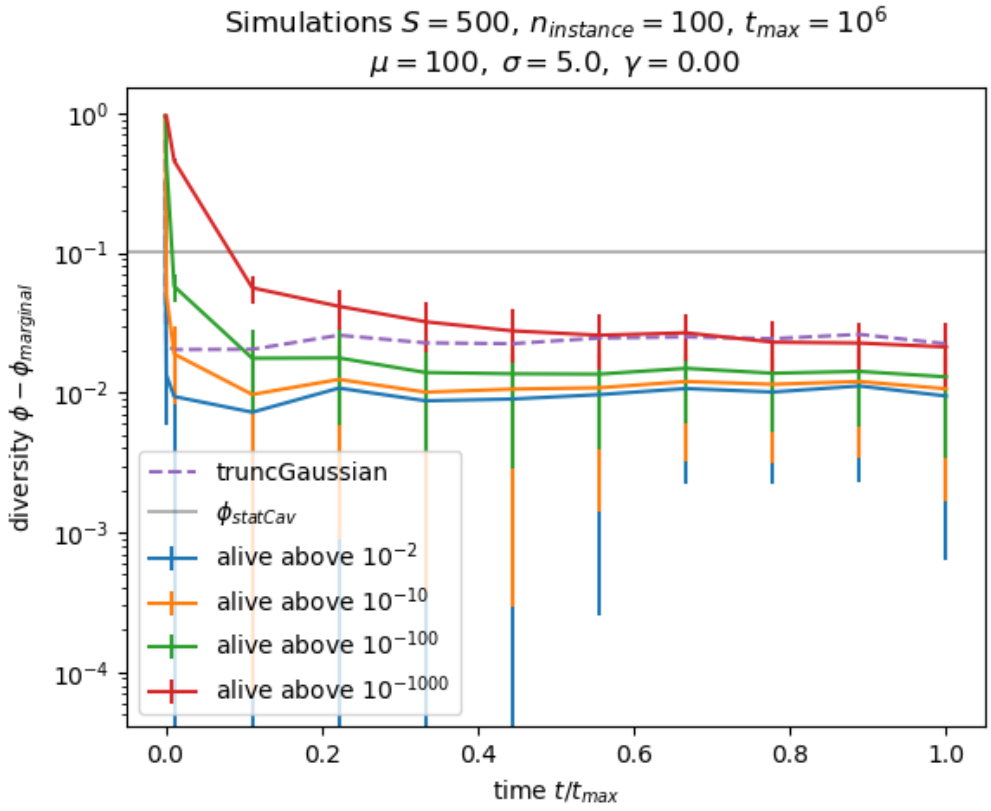

Figure 3.3. We plot the diversity difference to the marginal one as a function of time, for different criterions. The parameters for this particular data set are $n_{instance} = 100$ realizations (from which the error bars are computed). Results are robust to distinct parameter choices. In purple dotted line we plot the diversity inferred using the truncated Gaussian assumption. In full colored lines, the diversity is computed using different N_{cut}. Whatever the criterion, we see that the numerical diversity tends to the marginal one: it is eventually only higher by 10^{-2}). The static cavity diversity is shown in grey line, for comparison. It overestimates diversity, which confirms that the static cavity predictions are not valid in this phase.

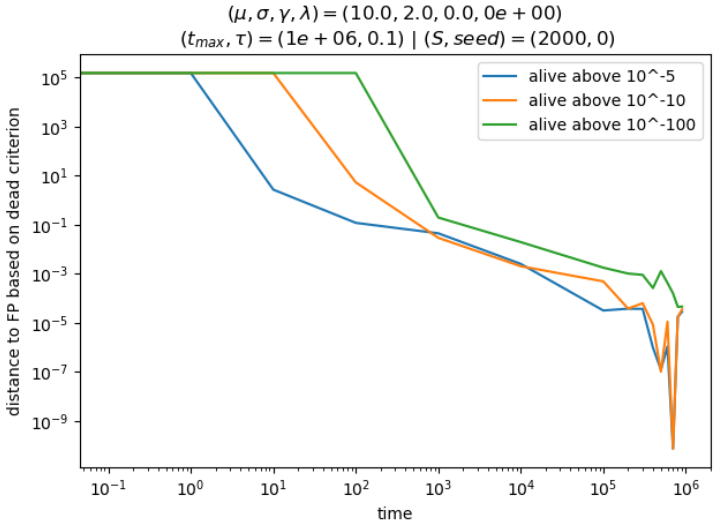

Figure 3.4. Distance to the corresponding fixed point across time, for different alive criterions. The rescaled distance decreases with time, and goes towards 10^{-3} or lower, indicating that the FP at long times are a good approximation of the dynamics.

as close to the fixed points as in the isolated case, because immigration acts as a barrier. Therefore the stability analysis of the fixed points is not so relevant for the dynamics. However, it can also be seen on figure 3.6b that the fixed points are no longer marginally stable, but rather unstable.

Basically, immigration prevents aging with the following mechanism: around the unstable fixed points, it builds an unreachable sphere of radius λ if the fixed point has dead species; and therefore makes the exit from this fixed points influence much quicker.

For this analysis, we assumed that for small immigration, we could still apply equations (3.2) to compute the fixed point populations.

3.5. Slowing down of the dynamics, fixed point picture

We established that at long times, the corresponding fixed points (FPs) are good approximations of the configurations visited by the real dynamics. We will use this in order to study the dynamics, by considering some simpler metadynamics: we will assume that the system jumps between FPs. We will analyze these metadynamics in the following: how does the system chooses which FP to jump to, and how much time does it spend in one FP.

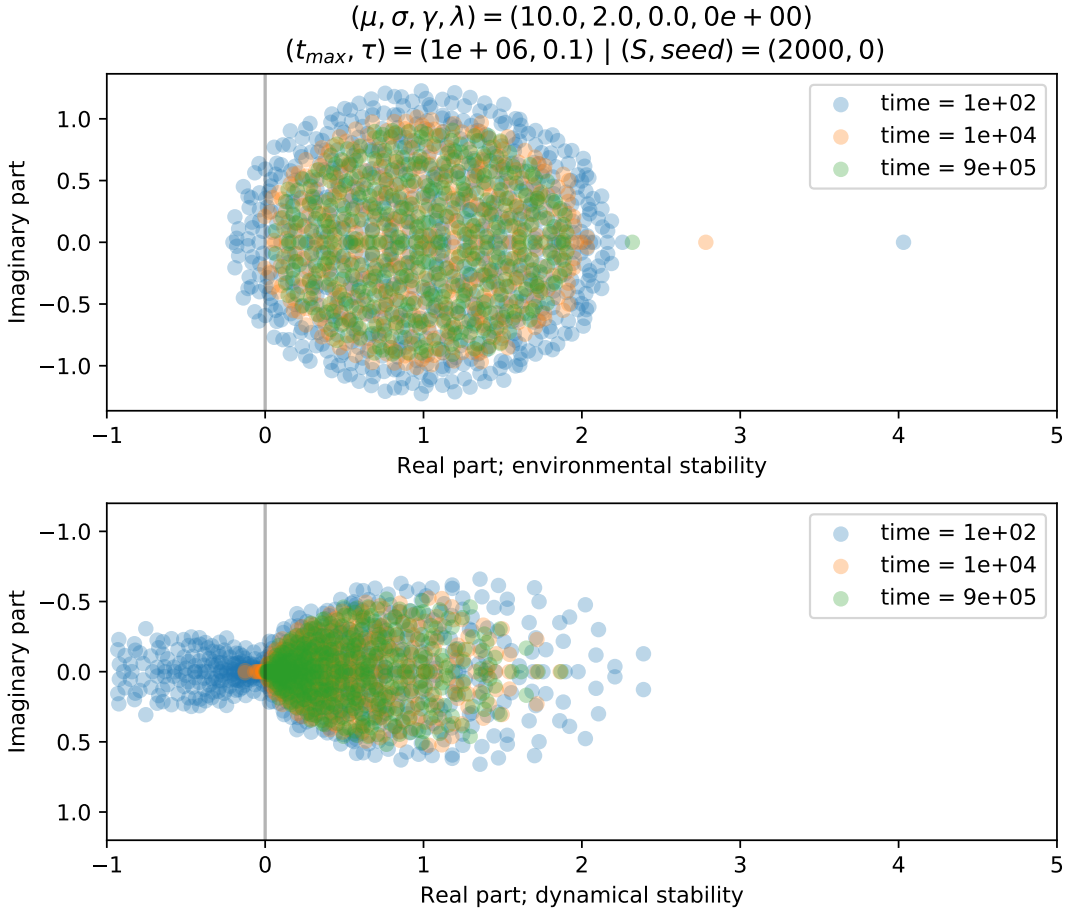

Figure 3.5. Stability spectra. At different times, we compute the corresponding FP of the dynamics, and evaluate the spectrum of its matrix stabilities. We then plot the distribution of complex eigenvalues, both for the environmental (*top* plot) and dynamical (*bottom* plot) stability. For the environmental stability, we actually plot the spectrum of the inverse $\tilde{\underline{\underline{\alpha}}}^a$ of the environmental stability matrix. For its spectrum, we expect the usual ellipse [85] in complex plane, shrunk by diversity until it reaches marginality: the left edge of the ellipse touches zero. This is indeed the case. For the dynamical stability, the structure is less clear (somehow fish-like [86]), but the same marginality can be seen for large times.

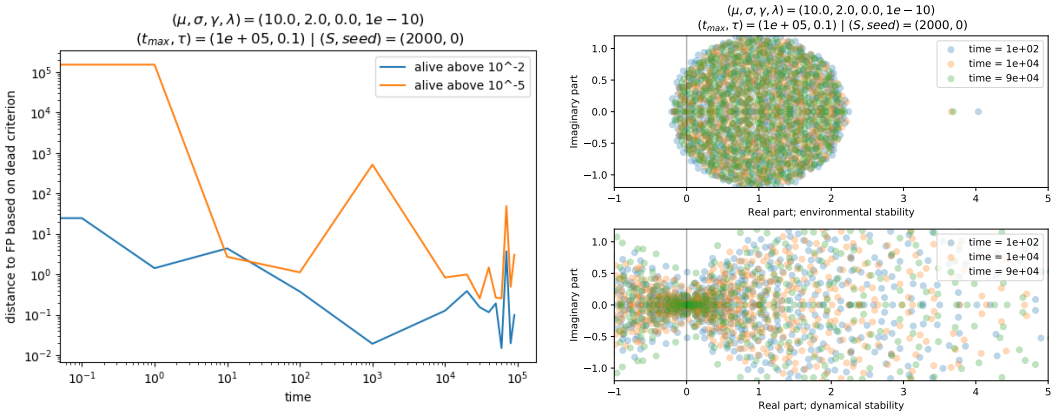

(a) Distance to FP

(b) Spectrum with immigration

Figure 3.6. Stability spectra and distance to the corresponding fixed points, with immigration. These are the equivalents of figures 3.3 and 3.5. On figure 3.6a, we see that whatever the alive criterion, the dynamical point stays quite far from its corresponding FP ($d \sim 10^{-1}$). This means that the analysis in terms of fixed points is not so relevant here. Anyway, on figure 3.6b we show that these fixed points are not marginal but rather unstable: there are many eigenvalues with negative real parts.

3.5.1. Metadynamics

We consider a naive picture: the system jumps from FP to FP because none of them are stable. Each FP is characterized by the dead/alive choice for species. From this state vector, all population values and stabilities can be computed, as stated in section 3.3.3. More precisely, one should check for each FP:

1. the feasibility of the FP: positivity of the alive species populations;
2. the stability of the dynamics restrained to the alive species;
3. the uninvadability of the FP from dead species.

If those conditions are not matched, the system should jump to another FP by changing the choice of 'dead/alive' consequently. In particular, if condition 1) is not matched, the system should kill negative alive species. And if condition 3) is not matched, it should introduce invadable dead species. Condition 2) is usually verified at long times, as the dynamics become marginally stable. In the new FP, the new populations and stability are computed again based on the new 'dead/alive' choice. We then iterate the procedure.

We now analyze real dynamics, keeping in mind this naive picture.

In this section, we consider a long ($t_{max} = 10^6$) and detailed simulation of a big chaotic isolated ecosystem $S = 2000$, $(\mu, \sigma, \gamma, \lambda) = (10, 2, 0, 0)$. This chaos is not stable: it will

age. Again, defining a cut-off abundance (say $N_{cut} = 10^{-5}$) [6] , at each time step we can define which species are alive (*i.e.* with population $N_i(t) > N_{cut}$), and which ones are dead. From this information, we can compute the corresponding fixed point and its properties: what are the alive populations, their stability, the invadability from the dead species...

3.5.2. Quantified properties of the fixed points

On figure 3.7, we show the simple properties of the FPs varying time. More precisely, for each FP, we count the fraction of species that are respectively alive with positive population, alive with negative population, dead and non-invadable, or dead and invadable. We can see that there is stabilization in time: these diversities become roughly constant. The wrong classification 'negative alive' disappears, which is what we expected: the system becomes marginal, and is only driven by invasions. Indeed, a huge fraction of species (around 10%) stay invadable. Arguably, this might be an indicator of the chaos strength. The marginality can be seen as the positive alive diversity reaches the marginal one.

Through the simulation (after the transient), we check that almost all events are consistent with the corresponding FP categorization. For instance, an invasion of species 554 occurred, and we check afterwards that for the corresponding FP, species 554 was indeed invadable. Or species 33 went extinct, and it was indeed alive negative in the corresponding FP. However, at this stage we cannot predict what FP the system will typically jump to, given the FP it jumps from. We expect it to be a balance between the classification and the real dynamical population distribution. This is still ongoing investigation.

3.5.3. Timescales analysis

In this section, we study a different indicator of the slowing down of the dynamics, based on diversity rather than correlations.

Rate of events

Given a counting cut-off N_{cut}, we consider that an *event* occurred at time t if there has been an "invasion" or an "extinction": if a species population has crossed the cut-off. We first investigate on figure 3.8 the rate of these events (the number of events divided by the time of the observation window), and how it evolves with time. Because of the dynamical slowing down, the rates decrease with time. We expected a typical slow down $rate_{events}(t) \sim t^{-1}$, based on the numerical scaling of the decorrelation time $\tau_{decorrel}(t) \sim t$ (computation in the next paragraph). Data is more or less consistent with this scaling. Numerically, the fit rather shows $rate_{events}(t) = At^{-0.85}$, but we reckon this might be a finite size effect.

[6] Then we check that the analysis is robust to change of N_{cut}. Generically, we check $N_{cut} = 10^{-5,-10,-100}$. Lowering N_{cut} only seems to delay the results in time, because it takes more time for species to reach it. However, all the *quantitative* results seem to hold.

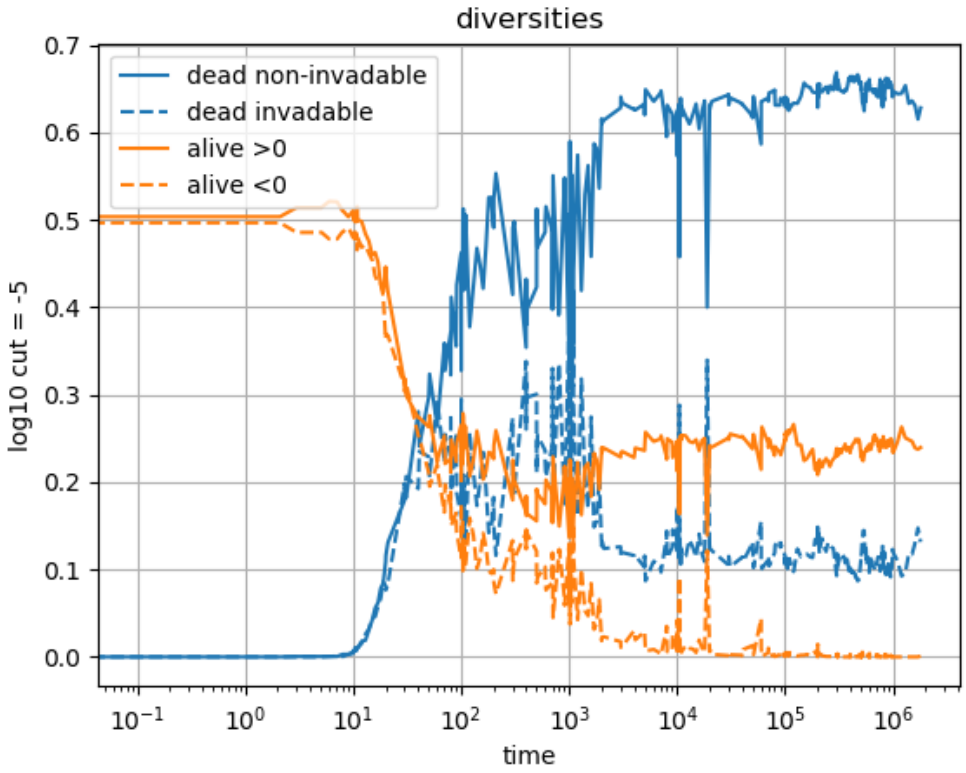

Figure 3.7. Classification proportions of the corresponding FP species as a function of time. Proportions stabilize with time. We can see that the positive alive species (orange full line) reach the marginal diversity (25% here), while the wrongly classified negative alive species (orange dotted line) almost disappear. However, the wrongly classified invadable dead species (blue dotted line) stabilize around a non-zero value (roughly 10%).

We want the typical scaling $\tau_{FP}(t)$ of the time for which the system stays in one given FP at time t. We use:

$$\int_{t}^{t+\tau_{FP}(t)} rate_{events}(t)\, dt \sim 1 \tag{3.10}$$

Then, assuming $rate_{events}(t) = At^{-1}$, it follows:

$$\tau_{FP}(t)/t = e^{A^{-1}} - 1 \tag{3.11}$$

With this scaling of $rate_{events}(t)$, $\tau_{FP}(t)$ is then proportional to t, as $\tau_{decorrel}(t)$. However, if we use numerical estimates for $A \sim e^5$, this yields $\tau_{FP}(t) \sim 10^{-2}\, t$, whereas from simulations $\tau_{decorrel}(t) \sim t$. This would indicate that to actually lose correlation, the system would need to go through many (100) FPs.

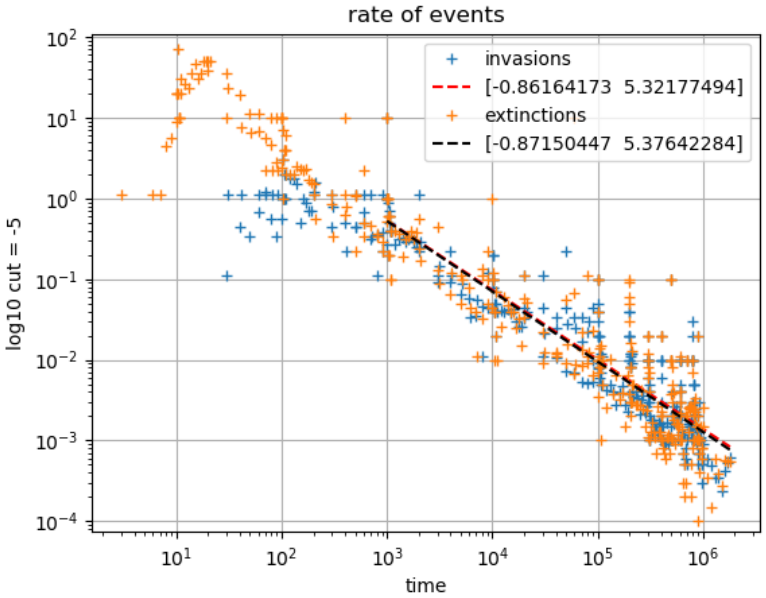

Figure 3.8. Rate of events ("invasions" and "extinctions") as a function of time, respectively in orange and blue. At the beginning of the simulation, there are more extinctions than invasions, as the system reduces its diversity. After this transient state, the two rate become comparable as the diversity is stabilized. However, the rates still decrease as the system ages, because of the dynamical slow down. The decay is roughly consistent with t^{-1} scaling. In dotted lines we show the log-log fits of the rate decays, with coefficients in the legend (the first one is the slope, the second one the intercept).

Turn-over of alive species

In this section, we wonder how important is the turn-over in the species: are they always the same species that contribute to the dynamics (*i.e.* alive or invadable)? On figure 3.9, we show an estimate for redundancy. For each species, we compute during how much time it was alive across the simulation. Then we plot the distribution across species of these times.

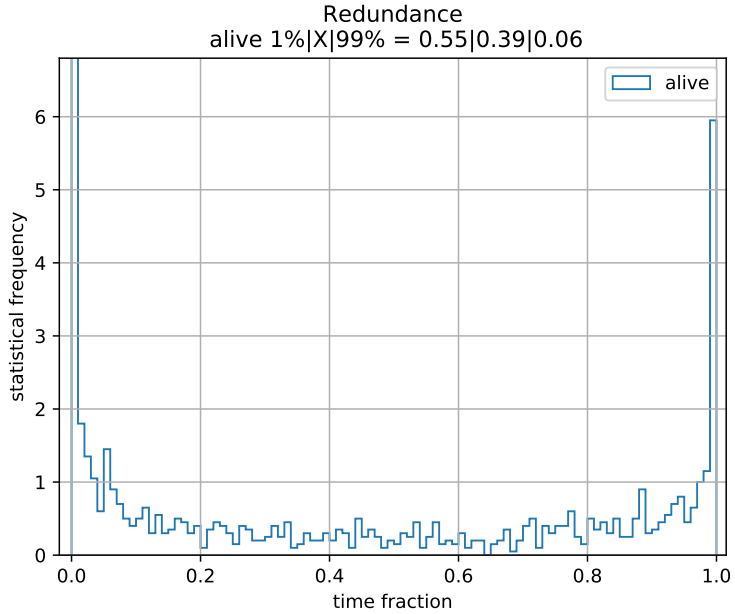

Figure 3.9. Time distribution of the alive time fraction for species. In the vertical axis is shown the statistical frequency. The distribution is very roughly uniform, with two peaks around 0 and 1. The two peaks mean that some species keep their status across the whole simulation: 55% stay permanently dead, and 6% permanently alive. However, the uniform distribution states that the remaining 40% are switching between dead and alive, with varying levels of success.

We see that the distribution presents two peaks at 0 and 1, which stand respectively for the species that are always dead and alive. However, the fraction of species corresponding to the alive peak is much lower than the real diversity of the system ($0.06 \ll 0.25 = \phi_{marginal}$). It follows that a great part of the diversity of the system consists of species that flickers from alive to dead. We reckon that these species are responsible for the slowing down on the dynamics, according to the following picture:

1. When the ecosystem is around a given FP, some species i should go extinct;
2. However, as the population variables are continuous, it only dives towards 0 but does not reach it;

3. Then, due to some other invasion or extinction, the ecosystem jumps to another FP, in which species i is favored;

4. At this point, species i needs to come back up from its very low population in order to relaunch the dynamics by causing a new invasion;

5. This takes a long time, during which the ecosystem stays in the same FP, where another species j should go extinct;

6. As the ecosystem stays for a long time in this FP, it has the time to make species j reach even lower population values than what species i had reached;

7. Therefore, it will take even longer for species j to come up again afterwards.

We are still investigating this idea, both numerically and analytically (see section C).

4. Analytics: DMFT closures and Kac-Rice complexity

In this chapter, we provide some analytical analysis of the Lotka-Volterra system of equations (2.1). More precisely, we detail different theoretical approaches to study the dynamics.

First, we assume time-translational invariance and integrability of the correlation, and we close the DMFT equation (2.9) for the stationary process. However, for the closure to be self-consistent, we need to solve the dynamics as well. We then introduce some further approximations, that enable us to do so, and investigate whether the chaotic solution is self-consistent. Nevertheless, the numerical study from chapter 3 showed us that the chaotic state is not stable. Our aim was to show an inconsistency such as an infinite temperature in the chaotic phase, in order to prove that a stable chaotic phase is impossible. This is not what we found, other instabilities may be responsible for the unreachability of a chaotic steady state. Eventually, we present an alternative way to look at the dynamics, using the Kac-Rice complexity of fixed points.

This chapter consists in unpublished results and ongoing work, we make the clear distinction between both here. The results are the following:

- The analytical closure of the TTI chaotic state is finished for all potential approximations we tried, and yields a finite temperature in the Multiple Equilibria phase;
- The annealed Kac-Rice computation of the number of fixed point is finished. It shows that at the onset of the Multiple Equilibria phase, the number of fixed points goes from one to an exponential number in the number of species S of the system. Similarly to what was found recently in [88], none of these fixed points are stable, a feature likely linked to the complex dynamics observed in this regime.

The ongoing work consist in:

- Understanding why the TTI chaotic state found within our approximation seems consistent. This might be due to a dynamical instability: this state exists, but the system would not be able to reach it.
- From the Kac-Rice computation, and following section 3.5, we tried but so far failed to match the numerical dynamics with our fixed point picture for the aging behavior.
- In Appendix C, we propose a toy model that might be able to catch the aging phenomenon.

4.1. Introduction[1]

Historically, studies of endogenous fluctuations have focused on single populations or few species [19, 20, 21]. On the other hand, theories of many-species interaction networks often center on ecosystems that return to equilibrium in the absence of perturbations [3]. Some authors have even proposed that fluctuations driven by interactions are generally too rare or short-lived to matter, since they can be self-defeating: dynamics that create large erratic variations lead to extinctions, leaving only species whose interactions are less destabilizing, until an equilibrium is reached [22, 23]. In this thesis, we will go past both the equilibrium [3, 24] or few-species starting points [19, 20, 21], to look directly at the dynamics of high-diversity communities.

Without immigration, we observe that the chaotic dynamics displayed by the ecosystem in the Multiple Equilibria phase are no longer stable: the dynamics become slower and slower as the time goes on. The fact that the dynamics depend on the time at which we look at them is called *aging* phenomenon: because indeed the observations depend on the *age* of the system. It is quite studied in the context of spin-glasses and disordered systems [82, 83, 65, 84]. The mathematical analysis is generically more involved than for usual systems that lie in an equilibrium state. In disordered systems, aging is associated with trapped dynamics and a general slowing down: the energy landscape displays many local minima that effectively trap the system for longer and longer times. In the case of ecology, there is generically no energy landscape to simplify the analysis.

4.2. General assumptions

In this chapter, we will focus on the DMFT equation (2.9), that we recall here in the case of purely asymmetric interactions ($\gamma = 0$ which removes the memory kernel χ) and no immigration:

$$\dot{N} = N\{1 - N - \mu m(t) - \sigma\eta(t)\} \tag{4.1}$$

where η is a Gaussian noise with zero mean and correlator $C_\eta(t,s)$; $m(t)$ and $C_\eta(t,s)$ are given functions. They are self-consistently determined with the relations:

$$\begin{cases} m(t) &= \mathbb{E}[N(t)] \\ C_\eta(t,s) &= \mathbb{E}[N(t)N(s)] \end{cases} \tag{4.2}$$

Here, $\mathbb{E}[.]$ denotes the average over the process: the initial condition $N(t=0)$ and the Gaussian noise.

To investigate the possibility of a self-consistent chaotic solution, we assume the existence of **time translational invariance** (TTI). This implies: $m(t) = m$ and $C_\eta(t,t') = C_\eta(t-t')$. From the numerics (such as figure 3.2 for instance), we know that the correlation has a non-vanishing residual part at long times: $C_\eta(+\infty) > 0$. Therefore, we separate the noise into a static part, and a dynamical part: $\sigma\eta(t) = z + \xi(t)$. In this setup, z and $\xi(t)$ are independent zero-mean Gaussian variables, with second moment:

[1] So that each chapter may be read separately, I decided to preserve all specific chapters' full introduction, even though it may overlap with the global and more detailed introduction from section 1. The overlapping parts are presented in the box and can be skipped.

$$\begin{cases} \mathrm{Var}[z] &= \sigma^2 C_\eta(+\infty) \\ \mathrm{Cov}[\xi(t)\,\xi(t')] &= \sigma^2\left[C_\eta(t-t') - C_\eta(+\infty)\right] \end{cases} \tag{4.3}$$

Now that the noise η has been separated, we will refer to the correlation $C_N(t,t') = C_\eta(t,t')$ in the following, for clarity's sake. We label $C_\xi(t-t') = \mathrm{Cov}[\xi(t)\,\xi(t')]$ the dynamical correlation. We also introduce the species-dependent bias $N^* = 1 - \mu m - \sigma z$, and write the DMFT equation in terms of the more natural variable $x(t) = \log N(t)$:

$$\dot{x} = -V'(x) + \xi(t)$$

with $V(x) = -N^* x + \exp(x)$. As ξ is not a white noise, there is no Ito term within the change of variables. We denote by $\overline{X}$ the ensemble average over the noise $\xi(t)$. Assuming **ergodicity**, we assimilate this average to the time average: $\overline{X} = T^{-1}\int_t^{t+T} ds\, X_s$. The species for which $N^* < 0$ will simply be extinct in the TTI state, we will forget about them in what follows. Within the TTI state (for alive species), the average of a one-time observable is a constant, therefore:

$$\overline{\mathrm{d}_t\, x(t)} = \mathrm{d}_t\, \overline{x(t)} = 0 \qquad \Rightarrow \qquad \overline{N} = N^* \tag{4.4}$$

This is already an interesting result: the time average of the population of a species is equal to its bias.

At this stage, let's recall the three different averages:

- $\overline{X}$ the ensemble average over $\xi(t)$ the dynamical noise, identified with the time average;
- $\mathbb{E}_{z+}$ the average over the static noise z for alive species, *i.e.* species with positive bias $N^* > 0$;
- $\mathbb{E}_{IC}$ the average over the initial condition (IC) $N(t=0)$.

The closure equations rely on the average over the whole process: $\mathbb{E}[X] = \mathbb{E}_{IC,\,z}[\overline{X}]$. Another simplification comes from the ergodicity assumption: within this hypothesis we can forget $\mathbb{E}_{IC}$. The TTI assumption implies that the distribution $\mathbb{P}(N(t)|N^*)$ is stationary. In order to compute dynamical correlations, we will sample the initial condition for the TTI process from this distribution, and denote the average over this distribution by $\mathbb{E}_{ICTTI}$. Eventually, we write down the simplified (TTI + ergodicity) process:

$$\begin{cases} \dot{x} &= -V'(x) + \xi(t) \\ V(x) &= -N^* x + \exp(x) \end{cases} \tag{4.5}$$

With the closures in the bias and dynamical noise:

$$\begin{cases} C_N(t) &= \mathbb{E}_{z,\,ICTTI}[\overline{\exp(x_t + x_0)}] \\ \mathrm{Mean}[N^*] &= 1 - \mu\, \mathbb{E}_{z,\,ICTTI}[\overline{\exp(x_t)}] \\ \mathrm{Var}[N^*] &= \sigma^2 C_N(+\infty) \\ C_\xi(t) &= \sigma^2\left[C_N(t) - C_N(+\infty)\right] \end{cases} \tag{4.6}$$

We can already say a few things about this set of equations. We introduce two quantities at given bias: the average population $m_{N^*} = \mathbb{E}_{ICTTI}[\overline{\exp(x_t)}]$, and the left-over correlation $q_{N^*} = \lim_{t\to\infty} \mathbb{E}_{ICTTI}[\overline{\exp(x_t + x_0)}]$. Given equation 4.4, we know that for a given bias, $\overline{N} = m_{N^*} = \max(N^*, 0)$. In addition, for an ergodic state, it is safe to assume that the variables N_t and N_0 decorrelate at long times. Therefore the left-over correlation is simply $q_{N^*} = m^2_{N^*} = \max\left((N^*)^2, 0\right)$. The closure on the Gaussian distribution of bias N^* then becomes:

$$\begin{cases} \text{Mean}[N^*] &= 1 - \mu\, \mathbb{E}_{N^*}[\max(N^*, 0)] \\ \text{Var}[N^*] &= \sigma^2 \mathbb{E}_{N^*}[\max\left((N^*)^2, 0\right)] \end{cases} \tag{4.7}$$

This is exactly the static cavity closure, detailed in section 2.3.1. So N^* follows the static cavity Gaussian distribution, if a chaotic state exists (without immigration). This is also an interesting result. Even though we know that the static cavity result is only an approximation in the chaotic phase, we see that the time averaged populations is exactly given by this result. Eventually we only have to deal with the closure on the dynamical noise ξ.

We summarize again the intended procedure:

1. Assume a stable chaotic state (TTI and ergodicity);
2. Make simplifying assumptions for the correlation C_ξ and the potential, in order to solve the dynamics;
3. Make predictions, and check if these assumptions are self-consistent or not.

4.3. Stationary distribution with the real potential

The first usual approximation that we make is to assume that the noise is white. This implicitly assumes **the existence of a temperature** T, which amounts to the integrability of the dynamical correlation:

$$T = \int_0^{+\infty} dt\; C_\xi(t) < +\infty \tag{4.8}$$

Therefore, in this section we will consider that the correlation simplifies to:

$$C_\xi(t, t') = 2T\delta(t - t') \tag{4.9}$$

The details of the computations are in Appendix B.1. Under this assumption, we can compute the stationary distribution for abundances, at given bias N^*:

$$\mathbb{P}_{t=\infty}(N|N^*) = \frac{\beta^{\beta N^*}}{\Gamma(\beta N^*)} N^{-1+\beta N^*} e^{-\beta N}\, \mathbf{1}_{N^*>0} + \delta(N)\mathbb{P}(N^* < 0) \tag{4.10}$$

which is a usual Gamma distribution. We introduced $\beta = T^{-1}$. It can be shown with Large Deviation Theory (in Appendix B.1) that the white noise assumption can

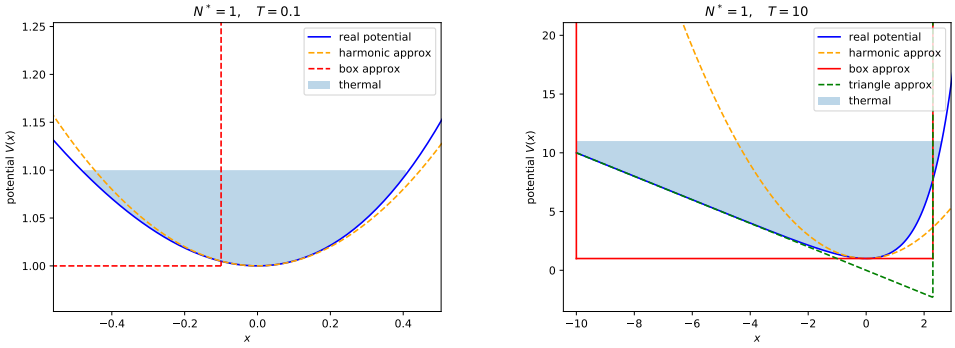

(a) $T \ll N^*$ **(b)** $T \gg N^*$

Figure 4.1. In blue line, we show the real potential, and in filled blue the part of the x-space that is typically reachable with thermal agitation. We show our approximations for the potential: the harmonic one in dotted orange, the box one in red, and the triangular one in dotted green. (Left) The box approximation is obviously wrong at $T \ll N^*$, but the harmonic one is a good one. (Right) When $T \gg N^*$, the harmonic approximation fails, but the box approximation holds better, and the triangular one even more so.

be relaxed, and the conditional distribution stays the same for $N \ll 1$. However, the temperature still needs to be finite: $\int_0^\infty dt\, C_\xi(t) = T < \infty$.

We also obtain the consequent small-population expansion for the stationary distribution on N, by averaging equation (4.10) over the bias N^*:

$$P_{alive}(0 < N \ll 1) \simeq \frac{1}{N \log(N)^2}$$

which is barely integrable at low abundances. This interestingly gives back the inverse distribution from neutral theory, up to log corrections.

All we have done so far does not yield tractable dynamics, so we cannot check the self consistency of the TTI assumption. Indeed, we would like to close the equation on the correlation C_ξ to check the finite temperature crucial assumption. In order to do this, we need to simplify the potential. Different simplified potentials can be used: harmonic, box, triangle... We present on figure 4.1 the approximations we will use (harmonic, box and triangle), and their validity domains.

4.4. Dynamics with the approximate potentials

4.4.1. Harmonic potential

The usual simplest approximation from physics is the harmonic (or Gaussian) one. We first look at the true potential $V(x) = -N^* x + e^x$. It has its minimum at $x_{min} = \log N^*$.

There, $V(x_{min}) = N^*(1 - \log N^*)$, and the curvature is $V''(x_{min}) = N^*$. The harmonic approximation then becomes:

$$V_h(x) = \frac{N^*}{2}(x - x_{min})^2 \tag{4.11}$$

This approximation should be valid when the system cannot explore far from the minimum x_{min}, so when $T \ll N^*$. With the harmonic potential, the dynamics become linear in log space. The full solution is given in appendix B.2.

We present now a few interesting aspects of this solution (for a positive bias $N^* > 0$). The time-averaged population is no longer $\overline{N} = m_{N^*} = N^*$. Indeed, we changed the potential, so equation (4.4) no longer holds. It is given by:

$$m_{N^*} = N^* e^{\frac{T}{2N^*}} > N^* \tag{4.12}$$

The x variable is confined symmetrically around its minimum, which then translates into an overestimation in N variable. However, the populations do decorrelate (as follows from ergodicity), and therefore $q_{N^*} = m_{N^*}^2$ still holds. We see that it does satisfy $m_{N^*} \sim N^*$, for $T \ll N^*$ which is the validity domain of the harmonic approximation. It is then diverging exponentially when $T \gg N^*$.

We compute the self-consistent temperature:

$$\boxed{T_{N^*}^{harm}(T)/\sigma^2 = N^* \exp(T/N^*) \int_0^{T/N^*} \frac{e^x - 1}{x} dx} \tag{4.13}$$

The self-consistent temperature is logically an increasing function of T/N^*, because the log variable can explore a larger space.

4.4.2. Box potential

In this section, we investigate the other limit $T \gg N^*$. In this regime, the harmonic approximation is no longer valid. We consider more carefully the true potential $V(x) = -N^*x + e^x$. Indeed, in this case the x variable can explore much further on the left (weak confinement) than on the right. We will treat both the exponential and linear saturation by hard walls, so that the potential becomes box-like. We determine the position x_{left} and x_{right} of the walls by thermal reachability. Then, we use the linear approximation on the left, and the exponential one on the right.

More precisely, we use:

$$\begin{cases} V(x_{boundary}) - V(x_{min}) \sim T \\ V(x_{left}) \sim -N^* x_{left} \\ V(x_{right}) \sim e^{x_{right}} \end{cases}$$

in order to obtain:

$$\begin{cases} x_{left} &= -\frac{T}{N^*} - (1 - \log N^*) \\ x_{right} &= \log T + \log\left(1 + \frac{N^*}{T}(1 - \log N^*)\right) \end{cases}$$

Keeping in mind that we are interested in the regime $T \gg N^*$, we will only keep the dependence:

$$\begin{cases} x_{left} &= -\frac{T}{N^*} \\ x_{right} &= \log T \end{cases} \tag{4.14}$$

Then the box potential is fully determined:

$$V_{box}(x) = \begin{cases} 0 & \text{if} \quad x \in [x_{left}, x_{right}] \\ +\infty & \text{otherwise} \end{cases} \tag{4.15}$$

And so is the stationary distribution, if we introduce $L = x_{right} - x_{left}$:

$$\mathbb{P}_{t=\infty}(x|N^*) = L^{-1}\,\mathbf{1}\,(x \in [x_{left}, x_{right}]) \tag{4.16}$$

The problem eventually consists in solving the diffusion equation in a box. This can be done by standard techniques, and we obtain the probability distribution at all times. From this we perform the closure relation in temperature (still conditioned on N^* via L). See Appendix B.3 for all details. We can deduce the average population at given positive bias:

$$m_{N^*} = N^* \left(1 - e^{-\frac{T}{N^*}}\right) < N^* \tag{4.17}$$

Compared to equation (4.12), the average population is now underestimated, because the x log variable can explore much further on the left. The ergodic relation $q_{N^*} = m_{N^*}^2$ is again fulfilled. And we still recover $m_{N^*} \sim N^*$ from equation (4.4) when $T \gg N^*$ which is the validity domain of the box approximation.

Finally, the self-consistent temperature is:

$$\boxed{T_{N^*}^{box}(T)/\sigma^2 = \frac{1}{3}T - \frac{3N^*}{2} + \frac{2(N^*)^2}{T} + \mathcal{O}_{T/N^* \to \infty}(T\,e^{-T/N^*})} \tag{4.18}$$

4.4.3. Triangular potential

In this section, we investigate again the other limit $T \gg N^*$. Indeed, the box potential can be considered as a rather crude approximation, so we improve it by considering a triangular potential. This one fits snuggly the real potential at high negative values, and models the exponential saturation with the same hard wall on the right side as the box potential. Just as was done in section 4.4.2, we fix the location of the right wall by thermal reachability, yielding $x_{right} = \log T$.

We solve the whole dynamics using Laplace transforms; the full computation is presented in Appendix B.4. We deduce the average population at given positive bias:

$$m_{N^*} = N^* \frac{T}{T + N^*} < N^* \tag{4.19}$$

The same comments as for the box potential still holds here. Compared to equation (4.12), the average population is again underestimated, because the x log variable can

Approximate potential	**Harmonic**	**Box**	**Triangle**
Validity domain	$T < N^*$	$T > N^*$	$T > N^*$
Stationary distribution $P(N\|N^*)$	Log-normal	Bounded power-law N^{-1}	Power-law N^{-1}, with exponential cut at low populations
Average population m_{N^*}	$N^* e^{\frac{T}{2N^*}} > N^*$	$N^* \left(1 - e^{-\frac{T}{N^*}}\right) < N^*$	$N^* \frac{T}{T+N^*} < N^*$
Self-consistent temperature T_{N^*}/σ^2	$N^* E(T/N^*)$	$\simeq \frac{1}{3}T - \frac{3N^*}{2} + \frac{2(N^*)^2}{T}$	$\frac{2\,T}{(1+\frac{N^*}{T})^3(2+\frac{N^*}{T})}$

Table 4.1. Comparison of the results for the potential approximations

explore much further on the left. The ergodic relation $q_{N^*} = m_{N^*}^2$ is again fulfilled. And we still recover $m_{N^*} \sim N^*$ from equation (4.4) when $T \gg N^*$ which is the validity domain of the triangular approximation.

The self-consistent temperature is:

$$\boxed{T_{N^*}^{tri}(T)/\sigma^2 = \frac{2\,T}{(1+\frac{N^*}{T})^3(2+\frac{N^*}{T})}} \tag{4.20}$$

4.4.4. Summarizing results

In table 4.1, we summarize the results from the dynamics with white noise and the three approximations for the potential: the harmonic one, the box one, and the triangular one. We introduced the function:

$$E(y) = \exp(y) \int_0^y \frac{e^x - 1}{x} dx$$

4.5. Closure in temperature

In order to solve the dynamical closure in temperature, we still have to perform the z-average, *i.e.* the average over the bias N^*. To do this, we need to use both potential approximations, in their respective validity domain: the box potential for low bias $N^* < T$, and the harmonic potential for high bias $N^* > T$. More precisely:

$$T = \int_0^T dN^* \rho(N^*)\, T_{N^*}^{box}(T) + \int_T^\infty dN^* \rho(N^*)\, T_{N^*}^{harmonic}(T) \tag{4.21}$$

where we recall that $\rho(N^*)$ is the Gaussian distribution from the static cavity.

We perform the low and high temperature expansion for the *rhs* of equation (4.21). The behavior is dominated by the harmonic contribution at low temperature, and by the box contribution at high temperature:

$$T_{rhs}(T)\,\sigma^{-2} \sim \begin{cases} \phi T - \frac{5}{4}T^2 \log T & \text{when } T \to 0 \\ \frac{\phi}{3} T & \text{when } T \to \infty \end{cases} \tag{4.22}$$

where we introduced the proportion of alive species $\phi = \int_0^{+\infty} dN^*\, \rho(N^*)$. From the static cavity, ϕ depends only on σ and not on μ, just like the transition to chaos (and unlike the average population m for instance). So first, we'll consider only the σ-dependence.

On figure 4.2, we plot T_{rhs} as a function of T in a log-log plot, varying σ. There are three different regimes. More precisely, we show on figure 4.3 the self-consistent temperature solutions of equation (4.21) as a function of σ.

$T = 0$ is always a solution. At low $\sigma < \sigma_1$, it is the only solution. This makes sense, because in the One Equilibrium phase there are no dynamics. Surprisingly, increasing σ but still in the One Equilibrium phase, two other solutions appear (as a first-order transition). From the expansion in equation (4.22), we can show that the lower solution merges with 0 exactly at the chaotic transition $\sigma = \sigma_{chaos} = \sqrt{2}$ (the condition writes $\sigma^2\phi = 1$). For $\sigma > \sigma_{chaos}$, there is then only one non-zero solution. This makes sense as well, as this is the Multiple Equilibria phase, a possible chaotic state. This self-consistent temperature is an increasing function of σ, which is logical as the higher σ, the stronger the chaos.

There might be additional transitions, for instance when $\sigma^2\phi > 3$. But this occurs for quite high σ, that usually lie in the Unbounded Growth phase so we do not consider them here.

We can also perform a stability analysis of the temperature solutions, if we consider the closure from equation (4.21) in the following sense: we start from a given long time chaotic state of the system with temperature T, then the dynamics perform the closure from the *rhs* $T_{rhs}(T)$, and the system settles in a new long time chaotic state with temperature $T_{rhs}(T)$. With this kind of *ad hoc* iteration, we can show that the $T = 0$ solution is stable in the One Equilibrium phase, and unstable in the Chaotic phase. We represent instability with dashed lines on figure 4.3.

We were a bit surprised by the results. Indeed, from numerical simulations we expected:

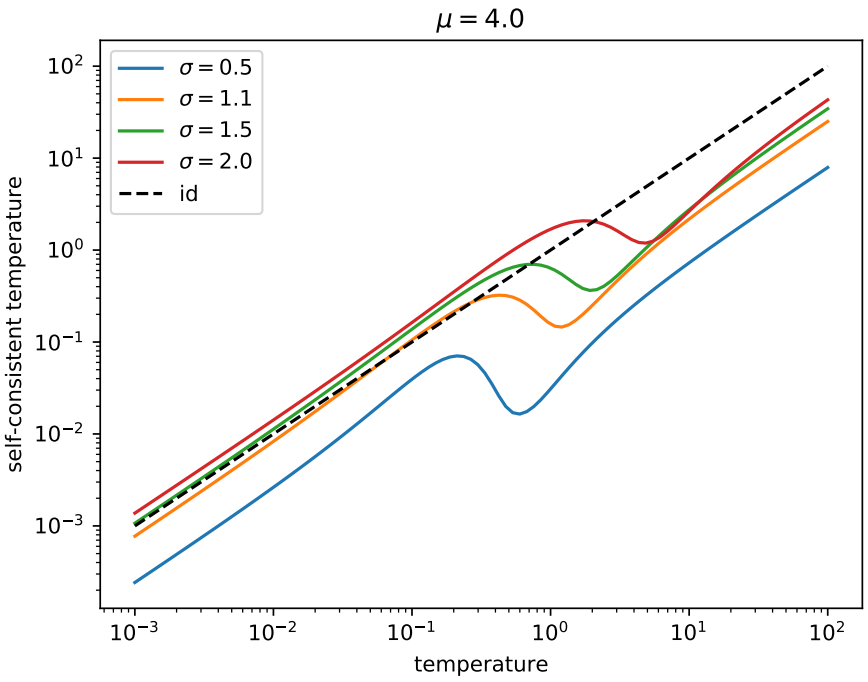

Figure 4.2. Log-log plot of T_{rhs} as a function of T, varying σ. The self-consistent temperature lies at the intersection between the dashed black line (identity function) and the colored lines. There are three different regimes. At low σ, T_{rhs} is below T for all T. Then increasing $\sigma \in [\sigma_1, \sigma_{chaos}]$, the two curves intersect twice. Eventually, for $\sigma > \sigma_{chaos} = \sqrt{2}$ there is only one intersection.

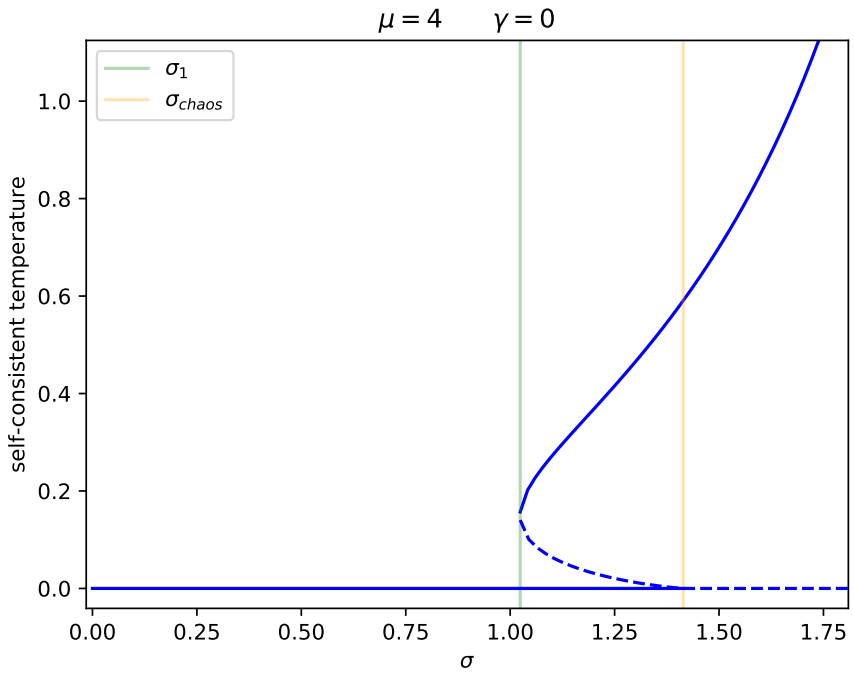

Figure 4.3. Self-consistent temperature solution, as a function of σ. Increasing from $\sigma = 0$, there is initially only the $T = 0$ solution. Then, at $\sigma = \sigma_1$ (green line), two other solutions appear discontinuously. The lower one merges with 0 exactly at $\sigma = \sigma_{chaos}$ (orange line). The dashed lines represent unstable solutions.

- A self-consistent zero temperature $T = 0$ for all the One Equilibrium phase;
- Something indicating that there was no self-consistent solution in the Chaotic phase, which would have shown that our assumptions were wrong. We know that without immigration, there is no stable TTI chaotic state.

This is still ongoing work. A solution to the above points might be in a possible dynamical instability of the different branches of temperature solutions. We also expect the intermediate phase with three solutions to be a consequence of the rough modeling. Indeed, the mixed model predictions are quite sensitive to the precise location of the walls in the box potential for instance. It seems doable to solve the dynamics with a triangular potential, *i.e.* drifted diffusion with a wall. We assume that this would get rid of the three-solution phase issue, and maybe also of the non-inconsistence of the TTI chaotic phase[2]. Based on numerical simulations, we expect a stable $T = 0$ solution in all the One Equilibrium phase, and an unstable or infinite solution in the Multiple Equilibria phase.

We know from simulations that the chaotic state is unstable, and the system displays aging dynamics. In Appendix C, we propose a model to analyze the aging behavior that slows down the chaotic dynamics. We do not have results for this model yet, this is also ongoing work.

4.6. Analysis based on complexity and properties of the typical fixed points

In this section, we present an alternative to DMFT in order to study the dynamical Lotka-Volterra system. We introduce a way to count the number of fixed points (FP) of the dynamics, with given properties such as average population, species diversity and uninvadability. We perform the Kac-Rice computation of this number of FP, and try to use this to shed a new light on the dynamics.

4.6.1. Context

We recall here the general Lotka Volterra dynamics from equation (1.7), without immigration:

$$\forall i \in \{1...S\}, \qquad \dot{N}_i = N_i \left(1 - N_i - \sum_j \alpha_{ij} N_j \right) \tag{4.23}$$

These dynamics allow a huge number of FPs. Indeed, when putting the derivative to zero, we can decide for each species whether it is dead ($N_i = 0$) or alive ($N_i =$

[2] After computation, the self-consistent closure with the triangular potential yields almost the expected behavior, but it still requires more analysis. More precisely, the small and high temperature expansions in this case predict that $T = 0$ is a stable solution for $\sigma < \sigma_{chaos}$, and that $T = \infty$ is a stable solution for $\sigma > \sigma_{chaos}$. However, the behavior of $T_{rhs}(T)$ at intermediate values of T is still problematic.

$1 - \sum_j \alpha_{ij} N_j$) in this FP. This amounts to exactly 2^S possible FPs[3]. However, for the FP to be interesting for the dynamics, it needs to satisfy other conditions. For instance, all populations have to be positive. This leads to the specific question of how many FPs with given properties do exist. We focus in this chapter on the following properties:

1. The FP needs to be feasible, so all alive species should have a positive population;
2. The FP has a given proportion of alive species, which we denote ϕ;
3. The FP populations have their first moments specified by $m = S^{-1} \sum_{i=1}^{S} N_i$ and $q = S^{-1} \sum_{i=1}^{S} N_i^2$;
4. The FP should be stable with respects to the invasions of dead species: any dead species that is injected in small quantity into the ecosystem at the FP should not establish.

Summarizing, we want to count how many FPs do the dynamics allow, imposing their feasibility (positive populations) and uninvadability, and specifying their properties (ϕ, m, q). Naively, we expect this number of FPs to scale exponentially with S; we recall that the total number of unspecified FPs is 2^S. In order to solve quantitatively this problem, we introduce in the next section the Kac-Rice method (see [89] for the first introduction of the method, and [90] for detailed lectures notes).

The goal of this procedure is the following. Once we know the total number of FPs with given properties $\#_{FP}(\phi, m, q)$, we might be able to predict some of the properties by imposing other ones and optimizing the complexity. More precisely, we know that at long times in the Multiple Equilibria phase, the dynamics become marginally stable. This imposes as a direct consequence that the diversity has a specific value $\phi = \phi_{marginal}$. At this stage, the dynamics visit different feasible FPs that all share the marginal property $\phi = \phi_{marginal}$. We assume that this set of visited FPs is stable in time, and form a given ensemble $\mathcal{E}$. If the system is simple enough, we can make some kind of ergodic assumption, stating that the dynamical observables correspond to an average over $\mathcal{E}$. For instance, we expect the mean abundance to be given by:

$$m = \mathbb{E}_{FP \in \mathcal{E}} \left[m_{FP} \right] \tag{4.24}$$

Eventually, if the number of FPs with given properties is indeed exponential in S, we expect that the average in equation (4.24) is dominated by the most abundant properties:

$$m = \mathrm{argmax_m} \left[\, \#_{FP}(\phi = \phi_{marginal}, m, q) \, \right] \tag{4.25}$$

Therefore, we could predict the mean abundance imposing only the marginality of the fixed points.

[3] Up to invertibility of a modified interaction matrix, which is generically the case.

4.6.2. Kac-Rice complexity of Lotka-Volterra system

What we call the (annealed) complexity $\Sigma(\phi, m, q)$ here is the average log-number of non-invadable feasible FPs with given value of (ϕ, m, q), which are respectively the proportion of alive species, the first and second moment of the population distribution. More precisely, if we call $\#_{FP}(\phi, m, q)$ the number of FPs with properties (ϕ, m, q), the complexity is defined as:

$$\Sigma(\phi, m, q) = S^{-1} \log \#_{FP}(\phi, m, q) \tag{4.26}$$

As we defined it so far, the number of FPs $\#_{FP}(\phi, m, q)$ is specific to a given interaction matrix α_{ij}. However, in the large S limit, we expect that this number typically does not depend on the specific realization of the interaction matrix. Therefore, we will compute it as:

$$\Sigma(\phi, m, q) = S^{-1} \log \mathbb{E}_\alpha \left[\#_{FP}(\phi, m, q)\right] \tag{4.27}$$

where $\mathbb{E}_\alpha [X]$ is the average over the distribution of random interaction matrices introduced in section 1.4.1; we recall it here. The elements of the interaction matrix α_{ij} are i.i.d. Gaussian random variables with moments:

$$\mathbb{E}_\alpha [\alpha_{ij}] = \mu/S, \qquad \mathrm{Var}_\alpha [\alpha_{ij}] = \sigma^2/S, \qquad \mathrm{Cov}_\alpha [\alpha_{ij}, \alpha_{ji}] = \gamma\sigma^2/S$$

Equation (4.27) corresponds to what we call the annealed complexity. However, so as not to give too much importance to very rare realizations of the matrix, the right complexity to consider would be the quenched one, defined by:

$$\Sigma_{quenched}(\phi, m, q) = S^{-1} \mathbb{E}_\alpha \left[\log \#_{FP}(\phi, m, q)\right] \tag{4.28}$$

This last computation is much more involved, and in this thesis we only present the annealed one, which should already give relevant insights. The quenched computation is still ongoing work.

It should be noted that at some point we might want to relax the uninvadability condition for the FPs. Indeed, we know that at some point the dynamics become susceptible to invasions from the dead species. In case of ambiguity, we will denote Σ_{free} the complexity without imposing uninvadability.

4.6.3. Sketch of the Kac-Rice computation

In this section, we sketch briefly how the computation is performed in the simplest setup. The details are in Appendix D. From equation (4.27), we want to compute:

$$\mathbb{E}_\alpha \left[\#_{FP}(\phi)\right] \sim \int D\alpha \; \mathbf{1} \left[N_{i \leq \phi S} > 0; N_{i > \phi S} = 0\right] \tag{4.29}$$

But once we have specified which species are alive, the abundances are completely determined by the interaction matrix, as detailed in equation (3.2). If we denote $\vec{N}$ the vector of alive species with components $N_{i=1 \ldots \phi S}$, this vector is a simple function of the

interactions: $\vec{N} = \vec{f}(\alpha)$. We inject this information into equation (4.29) in the following way:

$$\mathbb{E}_\alpha \left[\#_{FP}(\phi)\right] \sim \int D\alpha \int_0^{+\infty} d\vec{N}\, \delta\left(\vec{N} - \vec{f}(\alpha)\right) \tag{4.30}$$

where we used the Dirac function $\delta(X)$. Switching the integrals, we obtain:

$$\mathbb{E}_\alpha \left[\#_{FP}(\phi)\right] \sim \int_0^{+\infty} d\vec{N}\, \mathbb{P}_\alpha\left(\vec{N} = \vec{f}(\alpha)\right) \tag{4.31}$$

which can be computed using standard Gaussian integrals. In the above sketch, we did not care about uninvadability of the FP, permutation of species, nor the Jacobian from the change of variables.

4.6.4. Mathematical formulas for complexity

The derivations are presented in Appendix D. Putting all together, we obtain the final complexity:

$$\Sigma(\phi, m, q) = \mathcal{C}(\phi) + \mathcal{D}_{\gamma,\sigma}(\phi) - \mathcal{P}_{\mu,\gamma,\sigma}(\phi, m, q) + \mathcal{V}(\phi, m, q) \qquad [+\mathcal{U}_{\mu,\sigma}(\phi, m, q)]$$

Combinatorial term

$$\mathcal{C}(\phi) = S^{-1} \log \binom{S}{\phi S} = -\left[\phi \log \phi + (1-\phi)\log(1-\phi)\right]$$

Determinant term

$$\mathcal{D}_{\gamma,\sigma}(\phi) = \frac{\phi}{\pi} \int_{-1}^{1} dx \int_0^{\sqrt{1-x^2}} dy\, \log\left[(1+ax)^2 + (by)^2\right]$$

with $a = \sigma\sqrt{\phi}(1+\gamma)$ and $b = \sigma\sqrt{\phi}(1-\gamma)$.

Probability term

$$\mathcal{P} = \frac{\phi}{2}\log(2\pi\sigma^2 q) + \frac{1}{2\sigma^2 q}\left((1-\mu m)^2\left[\phi - \frac{\gamma}{1+\gamma}\frac{m^2}{q}\right] + \frac{q - 2m(1-\mu m)}{1+\gamma}\right)$$

Uninvadability term

$$\mathcal{U}(\phi, m, q) = (1-\phi)\log cdf\left(-\frac{1-\mu m}{\sqrt{\sigma^2 q}}\right)$$

We introduced *cdf* (and later on *pdf*) the cumulative distribution function (and probability distribution function) of the standard Gaussian.

Volume term

$$\mathcal{V}(\phi, m, q) = \frac{\phi}{2}\log(2\pi) + \phi \max_{x,y}\left\{ \frac{m}{\phi}xy + \frac{q}{\phi}\frac{y^2}{2} - \log(y) + \frac{1}{2}x^2 + \log cdf(-x)\right\}$$

The $(\log cdf)$ term comes from the $\{N_i \geq 0\}$ boundaries. Taking the derivatives of the function $\mathcal{H}$ in the max, the saddle point values are given by:

$$\begin{cases} \frac{\alpha}{2}\left(\sqrt{x_{SP}^2 + 4/\alpha} - x_{SP}\right) = -x_{SP} + \frac{pdf}{cdf}(-x_{SP}) \\ y_{SP} = \frac{\phi}{m}\frac{\alpha}{2}\left(\sqrt{x_{SP}^2 + 4/\alpha} - x_{SP}\right) \end{cases}$$

where we introduced $\alpha = \frac{m^2}{q\phi}$. To find an non-subdominant volume term, it is necessary to have $1/2 < \alpha < 1$. This is discussed in appendix D.3.3.

4.6.5. Check of the complexity formula in the One Equilibrium phase

Before trying to predict anything with the mathematical formulas, we wanted to perform a few basic checks. The first simple one corresponds to the One Equilibrium phase of the ecosystems. Indeed, for interaction matrix parameters in this domain, we know that the system has only one FP which is a globally stable and unique equilibrium. Therefore, we expect a zero complexity in this phase. In addition, we know the properties of this FP, they are given by the static cavity equations (A.4).

We check this in two steps. First we compute the complexity evaluated at the static cavity values $\Sigma(\phi_{sc}, m_{sc}, q_{sc})$. We plot this as a function of σ in figure 4.4. We show that the complexity evaluated at the static cavity values is indeed 0 in the One Equilibrium phase. Then, we checked numerically that in the One Equilibrium phase, the complexity is maximal at the static cavity values:

$$\text{argmax}\ \Sigma(\phi, m, q) = (\phi_{sc}, m_{sc}, q_{sc}) \tag{4.32}$$

It should be possible to prove equation (4.32): this would amount to obtaining the static cavity set of equations (A.4) by optimizing the complexity. However, it is quite tedious and we did not spend enough time on this derivation.

4.6.6. Complexity in the chaotic phase

On figure 4.4, we see that in the chaotic phase, the complexity becomes strictly positive, and increasing with the chaos strength (related to σ). This also corresponds to the intuition: entering the chaotic phase, the previously unique and stable FP loses its stability and many other FPs appear (an exponential number in S). Even without considering invadability, the vast majority of these FPs is unstable with respect to the alive species dynamics. Indeed, this condition directly amounts to $\phi_{FP} > \phi_{marginal}$, and we show on figure 4.5 that the complexity is actually higher when allowing for higher diversities $\phi > \phi_{statCav}$ $(> \phi_{marginal})$.

The behavior of the complexity in the chaotic phase is shown in more details on the following figures, where we optimize in (m, q) the complexity Σ at given diversity ϕ. In

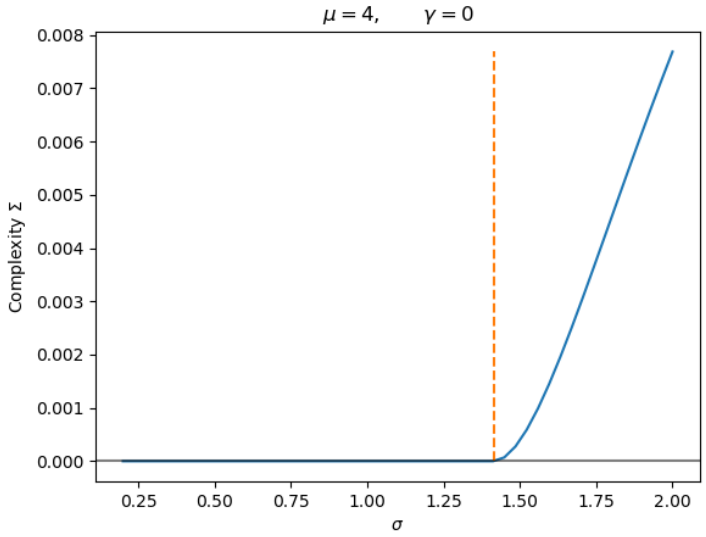

Figure 4.4. Complexity computed at the static cavity values. It is exactly zero in the One Equilibrium phase, as there is only one valid FP. Above the chaotic transition (orange dotted line), the complexity increases but all the FPs are unstable.

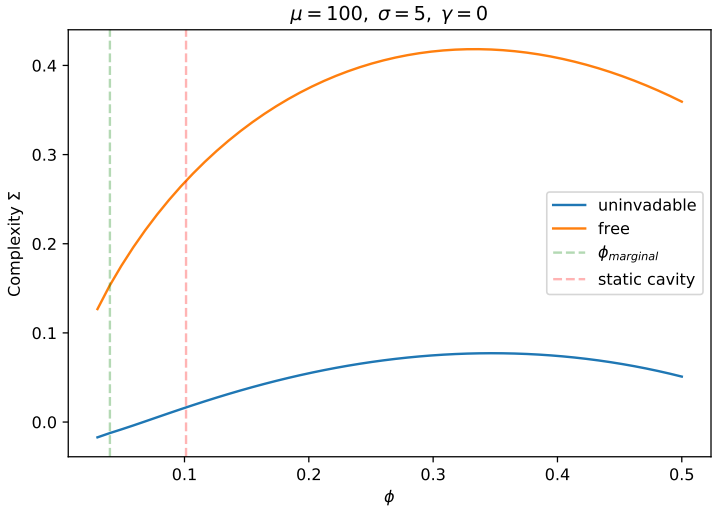

Figure 4.5. Optimization of complexity in the chaotic phase with respect to (m, q), varying ϕ. We show that the maximal complexity is reached for higher diversities $\phi > \phi_{statCav}$ $(> \phi_{marginal})$. This is true imposing uninvadability (blue line) or not (orange line).

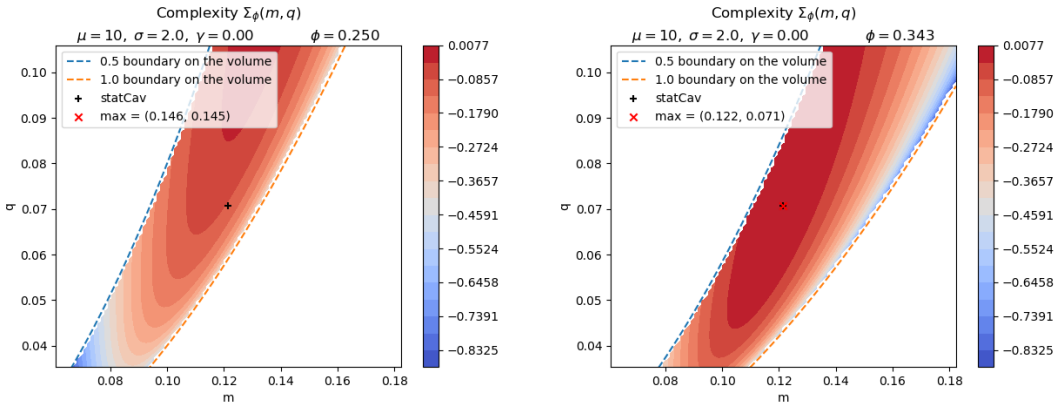

(a) Marginal ϕ **(b)** Static cavity ϕ

Figure 4.6. Complexity $\Sigma(\phi, m, q)$ varying (m, q) in the chaotic phase, for two different diversities ϕ: on the *left* the marginal diversity, and on the *right* the static cavity one. The black cross corresponds to the static cavity values for (m, q), while the red one is the argmax of the complexity. The argmax coincides with the static cavity value, when constraining the diversity at the static cavity result, but not otherwise. The two dotted lines indicate the analytical bounds from the volume term.

figure 4.6b, we show that optimizing at the static cavity diversity yields the static cavity (m, q).

On figure 4.7, we show that the number of fixed points goes from one to an exponential number in the number S of species, right at the Unique Equilibrium / Multiple Equilibria transition. In addition, we show that although the unique fixed point was stable in the Unique Equilibrium phase, in the Multiple Equilibria phase all the numerous fixed points are unstable. The exact complexity would be the quenched one; however, as the annealed complexity is always an upper bound for the quenched one, our result shows that indeed all fixed points are unstable.

4.6.7. The complexity cannot predict chaotic dynamical observables so far

We had the following picture in mind. In the chaotic phase, the dynamics starts to move around FPs with high diversity. Then the system realizes that these FPs are unstable, so it will move away from them. From long simulations, we saw in section 3.4 that the system moves towards marginal stability (the May bound). In this case, it might be possible to follow the (m, q) observables by comparing them with the typical FP properties (argmax of the complexity), at fixed $\phi = \phi_{marginal}$. The argument is more detailed in section 4.6.1.

On figure 4.8, we show the results for uninvadable complexity. We inferred the diversity from simulations $\phi(t)$, then computed the argmax of the complexity evaluated at this

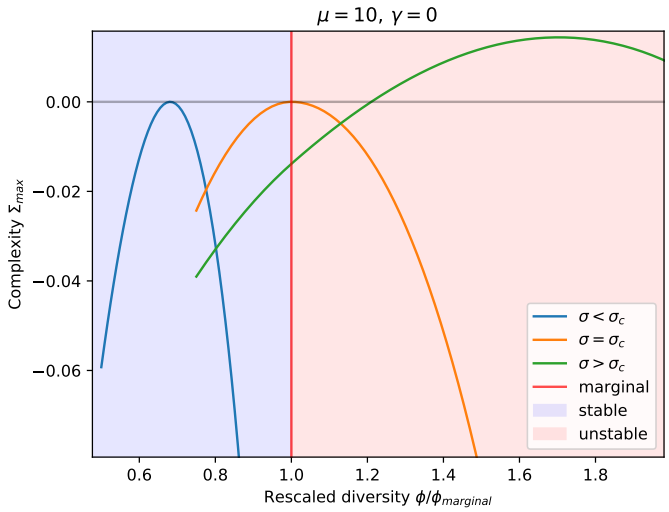

Figure 4.7. Optimized uninvadable complexity in the chaotic phase with respect to (m, q), varying ϕ and σ. We rescale diversity ϕ so that the marginal stability diversity does not depend on σ (red line). The fixed points with a lower diversity, if they exist, are stable (blue zone), while a higher diversity indicates instability (red zone). In the One Equilibrium phase (blue line), there is only one fixed point (the complexity is zero), and it is stable. Exactly at the transition (orange line), this fixed point becomes marginally stable. In the Multiple Equilibria phase (green line), there are many fixed points but they are all unstable: indeed, the complexity is always negative for the stable fixed points.

diversity:

$$(m_{KC}, q_{KC}) = \text{argmax}_{m,q} \Sigma \left(\phi = \phi(t), m, q\right)$$

where KC stands for Kac-Rice. Then we compare the argmax (m_{KC}, q_{KC}) to the corresponding numerical observables $(m(t), q(t))$. On figure 4.8, we see that the argmax is not a good prediction. Still, this makes sense because we know that the FPs explored by the dynamics are invadable.

However, on the same figure 4.8 we see that results for non-uninvadable complexity are non-conclusive either. This is surprising, it means that either our intuition with typical FP dynamics is wrong, or the marginal diversity information is not enough to capture the behavior. It could also be that the quenched computation of complexity is needed, instead of the annealed one we performed here.

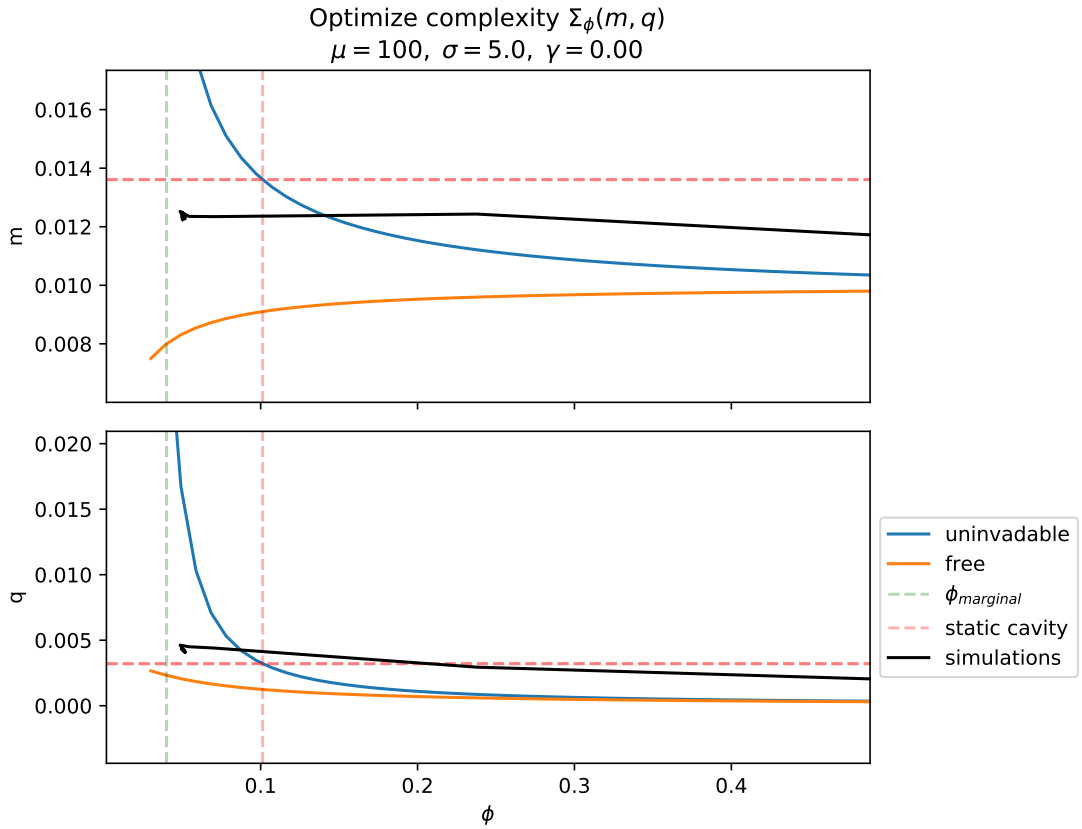

Figure 4.8. Optimization of complexity in the chaotic phase with respect to (m, q), varying ϕ. We use this optimization to plot the $argmax(\Sigma)$, that we hoped would be a good prediction. We show the corresponding m and q predictions, imposing uninvadability (blue line) or not (orange line). We compare them with the simulation data (black line): for each time of simulation, we infer the diversity of the system and plot the corresponding observables (m, q). The optimal complexity is actually worse than the static cavity (dotted red lines) as a prediction.

5. Stabilization of chaos by a spatial structure

In this chapter, we add a simple spatial structure to the initial model presented in section 1.4.1. We show that high-diversity metacommunities can persist in dynamically-fluctuating states for extremely long periods of time without extinctions, and with a diversity well above that attained at equilibrium. We describe the quantitative conditions for these endogenous fluctuations, and the key fingerprints which would distinguish them from external perturbations. We establish a theoretical framework for the many-species dynamics, derived from statistical physics of out-of-equilibrium systems. These settings present unique challenges, and observed behaviors may be counter-intuitive, making specialized theoretical techniques an indispensable tool. Our theory exactly maps the many-species problem to that of a single representative species (metapopulation). This allows us to draw connections with existing theory on perturbed metapopulations, while accounting for unique properties of endogenous feedbacks at high diversity.

Materials from this chapter can be found in [62]. Additional details about computations and numerics are given in Appendix E.

My contribution to this work was to perform the DMFT derivation detailed in section 5.3, redo the computation of the theory from section 5.4.1, and perform numerical simulations for both "real" ecosystems and DMFT.

5.1. Introduction[1]

While large temporal variations are widespread in natural populations [15, 16], it is difficult to ascertain how much they are caused by external perturbations, or by the ecosystem's internal dynamics, see e.g. [17, 18]. In particular, both theoretical tools and empirical results come short of addressing a fundamental question: can we identify when fluctuations in species abundances arise from complex ecological interactions?

Our focus here is on high-diversity communities. Historically, studies of endogenous fluctuations have focused on single populations or few species [19, 20, 21]. On the other hand, theories of many-species interaction networks often center on ecosystems that return to equilibrium in the absence of perturbations [3]. Some authors have even proposed that fluctuations driven by interactions are generally too rare or short-lived to matter, since they can be self-defeating: dynamics that create large erratic variations lead to extinctions, leaving only species whose interactions are less destabilizing, until an equilibrium is reached [22, 23]. Here we go past both the equilibrium [3, 24] or few-species starting points [19, 20, 21], to look directly at the dynamics of high-diversity communities in a spatially extended systems.

Many-species endogenous fluctuations can only persist if they do not induce too many extinctions (Fig. 5.2). Extinction rates depend critically on the amplitude of fluctuations [25, 26], their synchrony [27] and their correlation time [28]. The peculiarity of endogenous fluctuations is that these properties arise from the species dynamics, and therefore feed back on themselves. A theory of these feedbacks is however lacking.

We propose a novel quantitative approach, and show that many-species endogenous fluctuations can persist for extremely long times. Furthermore, they can be realized in experimental conditions, and identified in these experiments by multiple characteristic features. Crucially, we show that states with higher species diversity have stronger fluctuations, and vice versa. We also offer reasons why they may not have been observed in previous studies, and directions in which to search. An important factor in maintaining a dynamically fluctuating state is the spatial extension of the ecosystem, here modeled as a metacommunity: multiple patches (locations in space) that are coupled by migration. Such as setup is pictured in figure 5.1.

While equilibria are bound by linear stability, beyond that diversity there exist dynamically fluctuating states, with abundance fluctuations that grow continuously with the diversity. This places equilibria within a broader continuum which also includes non-equilibrium states. And as equilibria at high diversity have a unique phenomenology and require dedicated tools [3, 24], so do these high-diversity, dynamically fluctuating states.

Our strategy is the following. We first propose and simulate experiments to show that persistent fluctuations can be very elusive in a single well-mixed community, yet attainable in a metacommunity via three main ingredients: the existence of multiple patches, moderate migration fluxes coupling them, and differences in conditions between patches. These three ingredients can dramatically reduce the likelihood that large fluctuations within a patch will lead to overall extinctions (see Fig. 5.2), and make it possible for species to persist in highly fluctuating states. We then offer a quantitative understanding of this phenomenon. We build on the analytical framework developed in [61] (dynamical

[1] So that each chapter may be read separately, I decided to preserve all specific chapters' full introduction, even though it may overlap with the global and more detailed introduction from section 1. The overlapping parts are presented in the box and can be skipped.

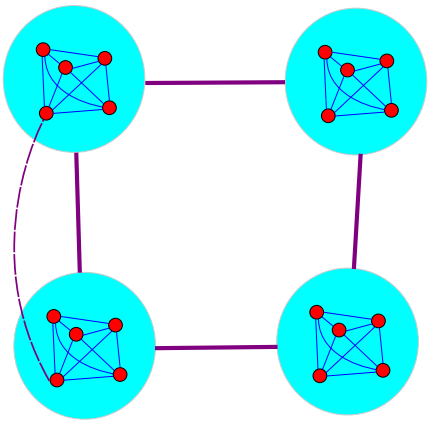

Figure 5.1. Picture of the metacommunity setup. Each species is represented by a red circle. The species form locally distinct well-mixed communities (blue circles), where the blue lines stand for the interaction between species. Eventually, communities are coupled by migration fluxes (large purple lines). Specifically, this migration acts at the level of the species (dotted thin purple line), flowing individuals from the most abundant community to the less abundant one.

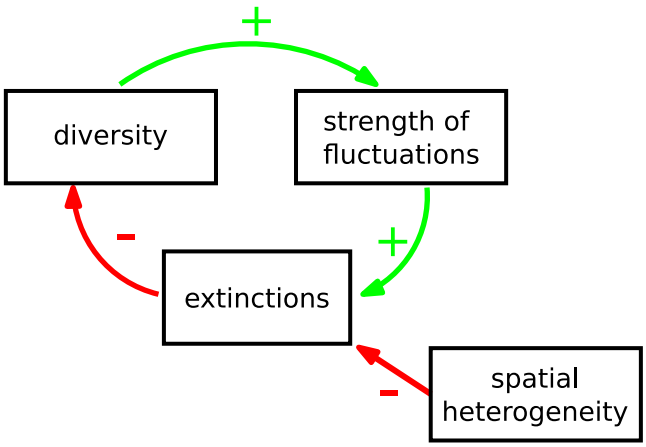

Figure 5.2. The fluctuation-diversity feedback cycle. Species diversity is required to maintain endogenous fluctuations. But these fluctuations cause extinctions, which reduce diversity. This negative feedback cycle can lead to the disappearance of endogenous fluctuations, especially in a well-mixed community. However, if spatial heterogeneity can limit extinctions, this negative feedback loop may slow down and create a fluctuating state that persists for very long times.

mean-field theory, see also [53, 66, 49]) that allows us to investigate, in a quantitative and predictive way, the conditions under which robust fluctuations can arise from complex interactions. This theory exactly maps a deterministic metacommunity (many-species dynamics over multiple spatial locations) to a *stochastic representative metapopulation* (single-species dynamics over multiple spatial locations). It predicts the distribution of abundance, survival and variability for a species subjected to "noise" that results from other species in the same community, rather than external perturbations. Dynamical mean-field theory allows us to analyze these fluctuations, and show that the effective stochasticity of species dynamics is a manifestation of high-dimensional chaos.

The intuitive picture that emerges from our analysis is the following: the persistence of endogenous fluctuations involves a balance between competing phenomena, see Fig. 5.2. On the one hand, the system needs to preserve a high diversity (both in terms of species number and interaction heterogeneity), as it is known [3, 24] that lower diversity leads to a stable equilibrium. On the other hand, the system also has to limit excursions towards very low abundances. This requires weeding out species that induce unsustainable fluctuations, and rescuing the others from sudden drops.

To accomplish that, the system relies on asynchronous dynamics between different spatial locations, and finite strength and correlation time of the abundance fluctuations. Even though all species show large fluctuations (so that interactions in a patch often switch between being favorable and unfavorable to a given species), long-lasting "sources" emerge for some of the species, i.e. patches where these species are, on average, more likely to remain away from extinction. Rare dynamical fluctuations leading to extinction in a given patch are hampered by migration from the other patches, which keeps the system in a non-equilibrium state. We show that, with moderate migration and some spatial heterogeneity, high-diversity dynamical states can be reached where species populations fluctuate over orders of magnitude, yet remain bounded for very long times above their extinction threshold.

In a parallel work, Pearce et. al. [49] study a similar model for micro-diversity (different strains of the same species) in ecosystems of microbes and phages. They impressively solve the dynamics for pure antisymmetric interactions, and relax the assumption to weak antisymmetry in the setup of infinitely many islands connected by migration. They also find that spatial structure enables endogenous fluctuations to persist for very long times.

Our findings allow us to paint a more precise picture of when persistent endogenous fluctuations can arise. We conclude with a discussion of the implications for biodiversity and ecosystem stability, and predictions for future experiments on community dynamics.

5.2. Proposed experiments

In the following, we introduce our results via a set of proposed experiments, realized in simulations, see Fig. 5.3. These results are later explained in the theoretical analysis. All parameters for simulations are detailed in Appendix E.1.

We focus on a meta-community which consists of M patches (well-mixed systems)

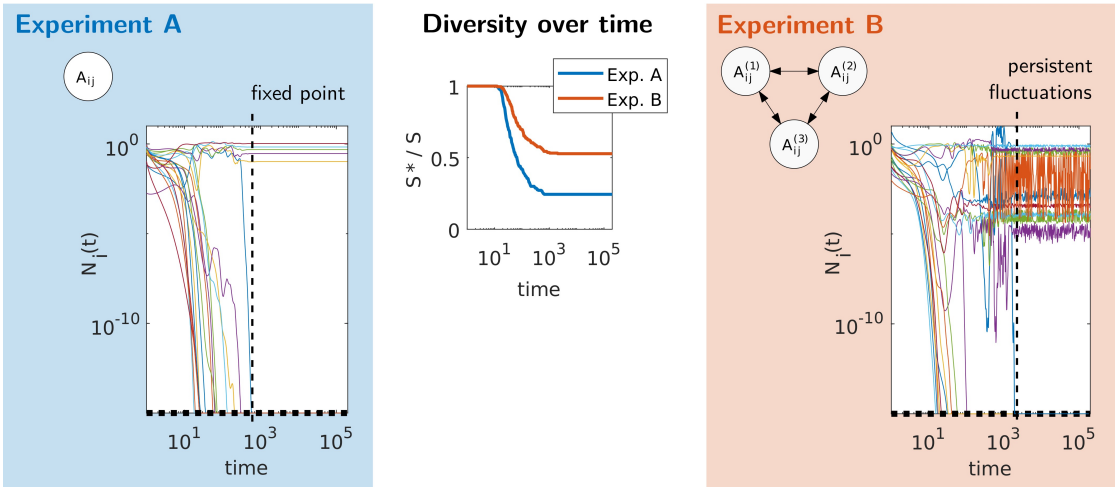

Figure 5.3. Numerical realization of the proposed experiments, illustrating conditions that lead to a fixed point or persistent fluctuations. (A) A single patch (well-mixed community) with an interaction matrix A_{ij}. (B) Multiple patches connected by migration, with slightly different conditions (e.g. temperature or resources) in each patch, represented here by location-dependent parameters such as $A_{ij,u}$. In the right and left panels we show the time evolution of a few representative species abundances $N_i(t)$: Experiment A, with a single patch ($M = 1$) reaches a fixed point, while in experiment B a meta-community with $M = 8$ patches reaches a stationary chaotic state ($S = 250$). Middle panel: Fraction of persistent species (S^* out of a pool of $S = 250$ species) as a function of time. Parameters and values for running the simulations are given in Appendix E.1.

connected by migration, and isolated from the external world. As an archetype of complex ecological dynamics, we consider generalized Lotka-Volterra equations with random interactions, which have been the focus of many recent theoretical advances [91, 42, 92]. The dynamics of the abundance $N_{i,u}$ of species i in patch u read:

$$\frac{d}{dt}N_{i,u} = N_{i,u}\left[B_{i,u} - N_{i,u} - \sum_j A_{ij,u}\,N_{j,u}\right] + \sum_v D_{i,uv}\,\left(N_{i,v} - N_{i,u}\right)\ . \tag{5.1}$$

where $A_{ij,u}$ are the interactions coupling the species, $B_{i,u}$ represents the equilibrium abundance in absence of interactions and migration (known as the carrying capacity), and $D_{i,uv}$ are the migration rates between patches u and v. In addition, an extinction threshold is implemented as follows: when a species' abundance goes below a cutoff N_c in *all* patches, the species is removed from the metacommunity and cannot return[2]. This threshold corresponds to the minimum sustainable number of individuals, hence $1/N_c$ sets the scale for the absolute population size (P) of the species. This recipe combines differential equations, which applies when populations are large, while still allowing for extinctions. For simplicity, we take $D_{i,uv} = d/\left(M-1\right)$ and N_c identical for all species and patches.

The species are assumed to have unstructured interactions (e.g. they belong to the same trophic level), meaning that $A_{ij,u}$ are sampled independently [3] and identically for different (i,j). (Our results also hold when $A_{ij,u}$ and $A_{ji,u}$ are correlated, see Appendix E.5.) For a given species pair, its interactions $A_{ij,u}$ vary somewhat with u; this variability corresponds to small differences in the conditions between the patches [93]. In the simulation examples we set all carrying capacities $B_{i,u} = 1$; the phenomena described below are also found if $B_{i,u}$ vary between patches in addition to, or instead of the interaction coefficients.

Our proposed experiments, illustrated by dynamical simulations, are the following:

(A) First, we model a single patch, $M = 1$ initially containing $S = 250$ species. Each interaction coefficient is non-zero with probability $c = 1/8$, and the non-zero interactions are Gaussian with mean $\left(A_{ij,u}\right) = 0.3$, std $\left(A_{ij,u}\right) = 0.45$. We find that species go extinct until the system relaxes to a fixed point (stable equilibrium), see left panel of Fig. 5.3.

(B) We now take $M = 8$ patches with the same initial diversity $S = 250$ and interaction statistics as in (A). For each pair of interacting species, $A_{ij,u}$ varies slightly with location u, with a correlation coefficient $\rho = 0.95$ between patches. The abundances now fluctuate

[2] We are interested in the regime where recolonization by migration between patches is fast compared to the rate of extinction events. In this regime, we expect (and checked in a few cases) that other implementations of the cut-off N_c will lead to the same qualitative phenomena. For instance, we implemented patch-wise extinctions when the abundance goes below the threshold in one particular patch, while still allowing migrations in.

[3] In the main text we focus on the asymmetric case in which $A_{ij,u}$ and $A_{ji,u}$ are uncorrelated. We show in Appendix E.5 that our results also hold when correlations are present.

without reaching a fixed point, see right panel of Fig. 5.3. At first the diversity decreases as species go extinct, but this process dramatically slows down, and the diversity is unchanged at times on the order of 10^5, see middle panel of Fig. 5.3. This result is robustly reproducible: repeating the experiment three times, with interaction and initial conditions sampled anew each time, dynamical fluctuations are reached and at a similar long-time diversity, see Fig. 5.4(top).

Three essential observations emerge from simulating these experiments, and repeating them for different parameters. First, species diversity and the strength of endogenous fluctuations are tightly bound, each contributing to the other's maintenance. Second, as shown in Fig. 5.3, species trajectories first go through a transient phase where they fluctuate over many orders of magnitude, causing numerous extinctions which lead to a reduction of variability, until a fixed point (for $M = 1$) or non-equilibrium state (for $M = 8$) with weaker fluctuations is reached. Third, the qualitative difference between experiments A and B is robust to changes in parameter values. Changes in N_c and d affect only quantitatively the states that are reached in experiment B, see Fig. 5.4(top). For instance, by increasing the population size $P = 1/N_c$, we can reach dynamically fluctuating states with higher long-time diversities, as shown in Fig. 5.4(bottom). When the population size is reduced by increasing N_c, the long-time diversity decreases, but remains high until $N_c \sim 10^{-2} - 10^{-1}$, where it decreases dramatically. For example, the diversity shown in Fig. 5.3(right) is $80\%_{\pm 13\%}$ higher than that reached for fixed-points[4] with precisely the same number of patches, interactions and migration. Similarly, as long as the migration coefficient is in the range $d \lesssim 0.1$ the main qualitative results remain unaltered.

5.3. Dynamical Mean Field Theory

We now aim to understand which conditions allow a fluctuating state to be reached and maintained without loss of species.

We use the Dynamical Mean Field Theory (DMFT), already presented in more details in chapter 2. It exactly maps the deterministic meta-community problem (many species in multiple patches) to a stochastic meta-population problem (single species in multiple patches). When species traits and interactions are disordered, e.g. drawn at random from some probability distributions, all species can be treated as statistically equivalent [44]. We can then describe the whole system by following the trajectory of a single species, randomly sampled from the community, and studying its statistics. In the DMFT framework, the effect of all other species on that single species is encapsulated by an "ecological noise" term generated by their fluctuations. This is analogous to the use, in physics, of thermal noise to represent interactions between an open system and its environment. Since species are statistically equivalent, the properties of this ecological noise can be self-consistently obtained from the dynamics of the single species.

[4]Fixed points were found by removing species after the dynamical state has stabilized, by increasing N_c until a fixed point was obtained.

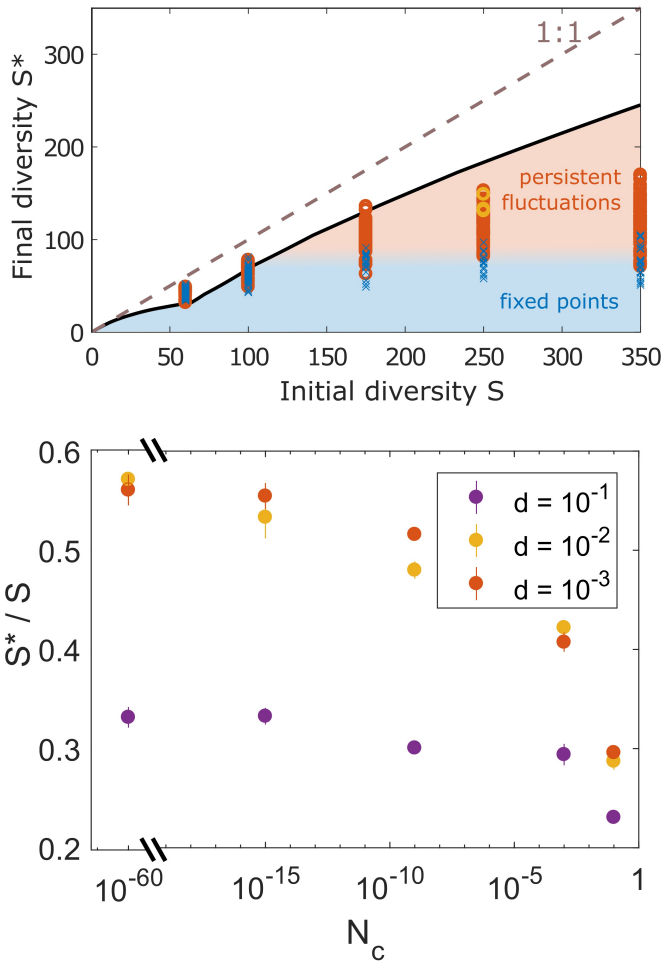

Figure 5.4. (Top) Species diversity at long times, compared to the theoretical bound obtained in Appendix E.3 for large S (solid line). The bound depends on the distribution of interactions, carrying capacities and initial pool size S. Each symbol represents the state at the end of one simulation run, with different values of the migration rate d and the abundance cut-off N_c, with fluctuating states (circles) and fixed points (crosses). Three yellow circles (two of which are overlaid) show the diversity in three runs with the same conditions as in Fig. 5.3(B), all reaching dynamically-fluctuating states and similar diversities. States closer to the theoretical bound (with higher diversity) also exhibit larger fluctuations and are more difficult to reach due to extinctions in the transient dynamics (see Fig.5.3). The dashed line represents full survival ($S^* = S$). (Bottom) The final diversity is set by the transient dynamics, which is affected by factors such as the migration strength and the total population size ($1/N_c$).

We now present the sketch of the mathematical derivation of DMFT in this case. We consider as a starting point equation Eq. (5.1). For the sake of clarity, we derive DMFT under simplifying assumptions, but the result is much more robust and could be applied to different ecology models as well as real data [44]. DMFT for ecological models has a double valency analogous to the one of mean-field theories in physics: it is at the same time an exact theory for some simple models, and a powerful approximation largely applicable to a broad range of systems. For the sake of clarity, the derivation assumes a fully connected model (all interactions are non-zero), but the results hold for any connectivity C as long as $C \gg 1$, see remark at the end of this Appendix.

The assumptions which make DMFT exact are the following: all constants $N_{i,u}(0)$, $B_{i,u}$, $D_{i,uv}$ and $A_{ij,u}$ are random variables, sampled from known distributions. More precisely:

- In each patch u and for all species i, the parameters $X^u = \{N_{i,u}(0),\, B_{i,u},\, D_{i,uv}\}_{i=1}^{S}$ are drawn from a probability distribution $\mathbb{P}$ which is a product measure $\mathbb{P}_u(X^u) = \prod_{i=1}^{S} \mathbb{P}(X_i^u)$;
- The interaction matrix can be decomposed as $A_{ij,u} = \mu/S + \sigma/\sqrt{S}\; a_{ij,u}$. $a_{ij,u}$ are standard random variables with mean zero, variance one, and correlation:

$$\mathbb{E}\left[a_{ij,u}\, a_{kl,v}\right] = \delta_{ik}\, \delta_{jl}\, \rho_{uv}$$

  where we used the Kronecker symbol δ_{ik}, and $\rho_{uv} = \rho + (1-\rho)\delta_{uv}$ is a uniform correlation ρ between patches.

With these conventions, we rewrite Eq. (1) in the following way:

$$\frac{d}{dt} N_{i,u} = N_{i,u}\left[B_{i,u} - N_{i,u} - \mu\, m_u(t) + \eta_{i,u}(t)\right] + \sum_v D_{i,uv}\left(N_{i,v} - N_{i,u}\right)$$

where $m_u(t) = S^{-1} \sum_{i=1}^{S} N_{i,u}(t)$ is the mean abundance in patch u, and $\eta_{i,u}(t) = -\sigma S^{-1/2} \sum_{j=1}^{S} a_{ij,u}\, N_{j,u}(t)$ is a species-and-patch-dependent noise.

The DMFT equation can be obtained by following Ref. [61]: in the large-S limit, it can be shown that the statistics of this multi-species deterministic process corresponds to the following one-species stochastic process, for each patch.

$$\frac{d}{dt} N_u = N_u\left[B_u - N_u - \mu\, m_u(t) + \eta_u(t)\right] + \sum_v D_{uv}\left(N_v - N_u\right) \tag{5.2}$$

where $\{N_u(0),\, B_u,\, D_{uv}\}$ are sampled from the distribution $\mathbb{P}(X^u)$, $m_u(t)$ is a deterministic function, and $\eta_u(t)$ is a zero-mean Gaussian noise. The variability from one species to another becomes in the DMFT setting the randomness contained in $\{N_u(0),\, B_u,\, D_{uv}\}$ and $\eta_u(t)$.

To make this point clearer, let us introduce two different averages:

- $\overline{Y}$ averages over the stochastic process in Eq. (5.2): over the stochastic noise η_u and over the distribution $\mathbb{P}(X^u)$;

- $\mathbb{E}_S(Y)$ denotes the statistical average over the deterministic multi-species system. $\mathbb{E}_S(Y) = \sum_{i=1}^{S} Y_i$, and therefore also includes sampling of X_i^u.

DMFT represents in terms of a stochastic process the deterministic dynamical system governing the dynamics of the S species in the ecosystem. In consequence, averages over the stochastic process coincide with average over species [75, 61, 94]: for a given observable Y: $\overline{Y} = \lim_{S\to\infty} \mathbb{E}_S(Y)$. This is analogous to the representation of the environment of an open physical system in terms of thermal noise, as it is done e.g. in the case of the Langevin equation.

The second important aspect of DMFT is *self-consistency*. This is related to the fact that the noise is induced by the dynamics of the species themselves, so its properties can be obtained from dynamical averages:

$$\begin{cases} m_u(t) = \overline{N_u(t)} \\ \langle \eta_u(t)\eta_v(t')\rangle = \sigma^2\, \rho_{uv}\, \overline{N_u(t)\, N_v(t')} \end{cases}$$

where we used a last average $\langle\cdot\rangle$ over the stochastic noise only, in order to define its covariance. Henceforth we use the notation $C^N_{uv}(t,t') = \rho_{uv}\, \overline{N_u(t)\, N_v(t')}$. These relations exactly take into account the correlations that emerge between the abundances and the interactions.

We now show how DMFT equations simplify for a time-translationally-invariant state of the system, which is in general reached after some transient time. In this state, all one-time observables become constant in time, and two-time observables become functions of the time difference only.

$$\begin{cases} m_u = \overline{N_u(t)} \\ C^N_{uv}(t,t') = C^N_{uv}(t-t') \end{cases}$$

The correlation $C^N_{uv}(t-t')$ decays at large time differences to a non-zero constant, leading to a static contribution to the noise term. In order to disentangle the static part and the time-fluctuating part of the noise, we perform the decomposition $\eta_u(t) = z_u + \xi_u(t)$ such that z_u and $\xi_u(t)$ are independent zero-mean Gaussian variables and processes verifying:

$$\langle z_u z_v\rangle = \sigma^2 \lim_{t-t'\to\infty} C^N_{uv}(t-t')$$

and subsequently $\langle \xi_u(t)\xi_v(t')\rangle = \sigma^2\, C^N_{uv}(t-t') - \sigma^2 \lim_{t-t'\to\infty} C^N_{uv}(t-t')$ which vanishes for $t-t' \to \infty$.

Substituting this decomposition into Eq. (5.2), we obtain:

$$\boxed{\frac{d}{dt}N_u = N_u\left[N_u^* - N_u + \xi_u(t)\right] + \sum_v D_{uv}\,(N_v - N_u)} \tag{5.3}$$

where $N_u^* = 1 - \mu\, m_u + z_u$ is a Gaussian variable, whose statistics is described in section 5.4.1. We checked numerically that for small migration D, the noise is only correlated

between patches through its static part: for $u \neq v$, $\langle \xi_u(t)\, \xi_v(t') \rangle \ll z_u\, z_v$, as presented in Fig. 5.5. In this case, we can write the self-consistent closure as follows:

$$\begin{cases} m_u = \lim\limits_{t' \gg 1} \overline{N_u(t')} \\ \langle z_u z_v \rangle = \sigma^2 \lim\limits_{t \gg t' \gg 1} C^N_{uv}(t,t') \\ \langle \xi_u(t) \xi_v(t') \rangle = \delta_{uv}\, \sigma^2 \left[C^N_{uv}(t,t') - \lim\limits_{t \gg t' \gg 1} C^N_{uv}(t,t') \right] \end{cases} \tag{5.4}$$

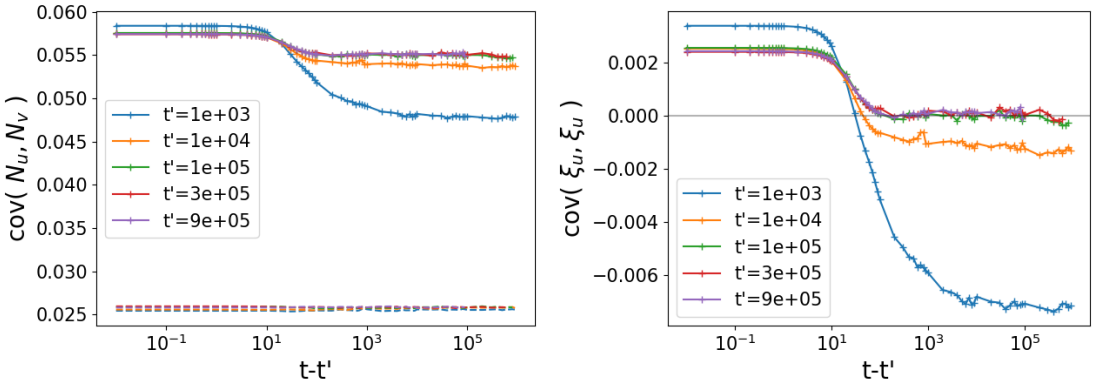

Figure 5.5. Covariance of the abundances in distinct patches. We use the general notation $\mathrm{cov}(Y_u, Y_v) = \mathbb{E}_S[Y^c_u(t)\, Y^c_v(t')]$ and $Y^c_u(t) = Y_u(t) - \mathbb{E}_S[Y_u(t)]$. Left: In full lines we show the abundance covariance within a patch $u = v$, and across patches $u \neq v$ in dotted lines. The correlation in abundances across patches is mainly static: dotted lines are reasonably flat. In other words, the correlation of ξ_u with ξ_v for $u \neq v$ is very small. Right: The covariance in ξ is shown to reach a TTI state. It only depends on $t - t'$ after $t' = 10^5$: the colored curves collapse. In this data, 100 distinct simulations were averaged, with parameters $(S, \mu, \sigma \,|\, M, \rho, d, N_c) = (400, 10, 2 \,|\, 8, 0.95, 10^{-10}, 10^{-15})$.

We detail in Appendix E.2 that even though it is outside of the scope of this chapter, the DMFT equations are valid in more general settings such as complex spatial structures, or random graphs of interactions.

5.4. Diversity predictions at low migration rates, and numerical validation

In this section, we use DMFT to predict some ecological properties, which we then compare to numerical simulations. In order to compute the analytical predictions, we

use the static cavity method (see section 2.3.1). This method is exact in the Unique Equilibrium phase, but is only approximate in the chaotic phase.

5.4.1. Predictions

We now focus on what the theory can predict. More precisely, we derive in Appendix E.3 that the distribution of $\{N_u^*\}_{u=i\ldots M}$ satisfies the following closure in the limit of large populations and small migration $N_c \ll D \ll 1$:

$$\begin{cases} \text{mean}\,[N_u^*] = 1 - \mu \left\langle N_{i,u}^* \right\rangle_+ \\ \text{covariance}\,[N_u^*, N_v^*] = \sigma^2 \rho_{uv} \left\langle N_{i,u}^* N_{i,v}^* \right\rangle_+ \end{cases} \tag{5.5}$$

where we introduced the average $\langle X_{i,u} \rangle_+$ over alive species ($N_{i,u}^* > 0$) only.

When $u = v$, as $\rho_{uu} = 1$, we find the expected single community result. In particular, mean $[N_u^*]$ and variance $[N_u^*]$ do not depend on the patch u.

Given covariance $[N_u^*, N_v^*]$, the distribution of $N_{i,u}^*$ is completely specified: it is a multivariate Gaussian in u, has the single-patch statistics of a single community, and a known covariance between patches. The solution can then also give the distribution of the number of sourcing patches.

In addition, we can compute the correlation coefficient ρ_{N^*} of the N_u^*'s. We use here our simple case of a uniform correlation ρ_a between patches $\rho_{uv} = \rho_a + (1 - \rho_a)\delta_{uv}$. We introduce the notation ρ_a instead of 'ρ' in this section in order to avoid confusion with ρ_{N^*}.

$$\rho_{N^*} \equiv \frac{\text{covariance}\,[N_u^*, N_v^*]}{\text{variance}\,[N_u^*]} = \rho_a \frac{\left\langle N_{i,u}^* N_{i,v}^* \right\rangle_+}{\left\langle N_{i,u}^{*\,2} \right\rangle_+}$$

The results are surprising: even when the different patches' conditions tend to be identical ($\rho_a \to 1$), the overlap between communities is not perfect ($\rho_{N^*} < 1$), so the total diversity is larger than the one in each patch. This happens *exactly at* the transition to chaos at $\sigma_c = \sqrt{2}$, see Fig. 5.6.

5.4.2. Numerical checks

On Fig. 5.7, we compare the theory predictions to simulations. In terms of diversity, the theory appears to give an upper bound to the simulations. The difference becomes larger at higher values of σ, and for ρ_a closer to one. To look further into this difference, it is useful to study diversity as a function of the value of the space-averaged $N_{\text{eff}}^* = M^{-1} \sum_{u=1}^{M} N_u^*$ of each species. Most of the difference in diversity is due to low values of N_{eff}^*, which are precisely the species that are more likely to go extinct, with good agreement with theory at higher values of N_{eff}^*. This is demonstrated in Fig. 5.9, which shows that the theoretical prediction for the number of species with $N_{\text{eff}}^* > 0.2$ is closer to simulation results than the predictions for total diversity. At the moment we do not know if remaining differences are because the theoretical argument is only approximate,

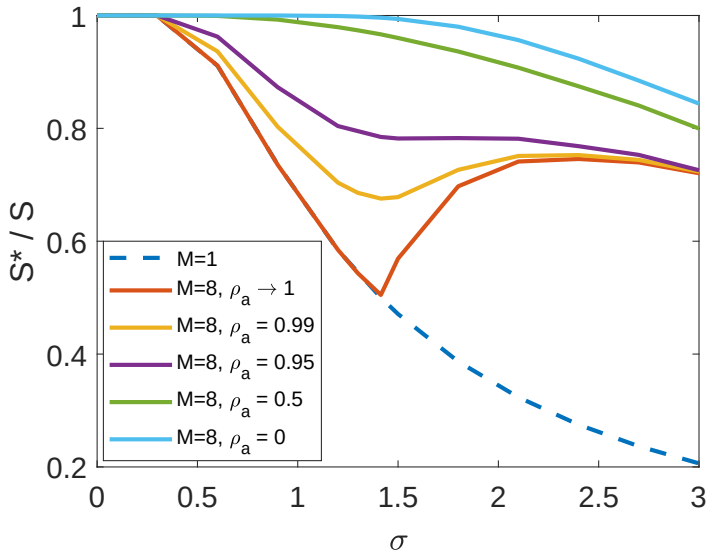

Figure 5.6. Theoretical predictions for the diversity as a function of σ for $M = 1, 8$ patches, $\rho_a = 0, 0.5, 0.95$ and $\rho_a \to 1$.

or whether in principle, with exceedingly low values of N_c and D, it could be approached by simulations for any σ.

In addition, the analysis of the DMFT equations clarifies the main effect of coupling patches by migration: patches with higher N_u^* tend to act as sources, i.e. the species most often grows there, and migrates out to sites where it cannot grow (sinks). We show directly from simulations of the Lotka-Volterra equations in Fig. 5.8 that species have particular patches which tend to act as sources consistently over long times. This fact is counter-intuitive, as the abundances of all species may be fluctuating over orders of magnitude in any given patch, yet this patch will retain its identity as a source (or sink) when averaging over long time periods. The variability of the N_u^*s between patches thus leads to an insurance effect, since it is enough to have one patch acting as a source to avoid extinction of the species in the others.

5.4.3. Limitations of the theory

We do know however that the argument (in the derivation of Appendix E.3 for instance) relies heavily on the fact that the time-averaged abundance of a species equals its local bias:

$$\overline{N_{i,u}(t)} = N_{i,u}^* \tag{5.6}$$

and that this condition is only approximate for low biases $|N_{i,u}^*| \ll 1$. Also, the fact that the theory does not explicitly depend on the migration implementation is somewhat problematic. For instance, we could invert the flow of migrations and still get the same

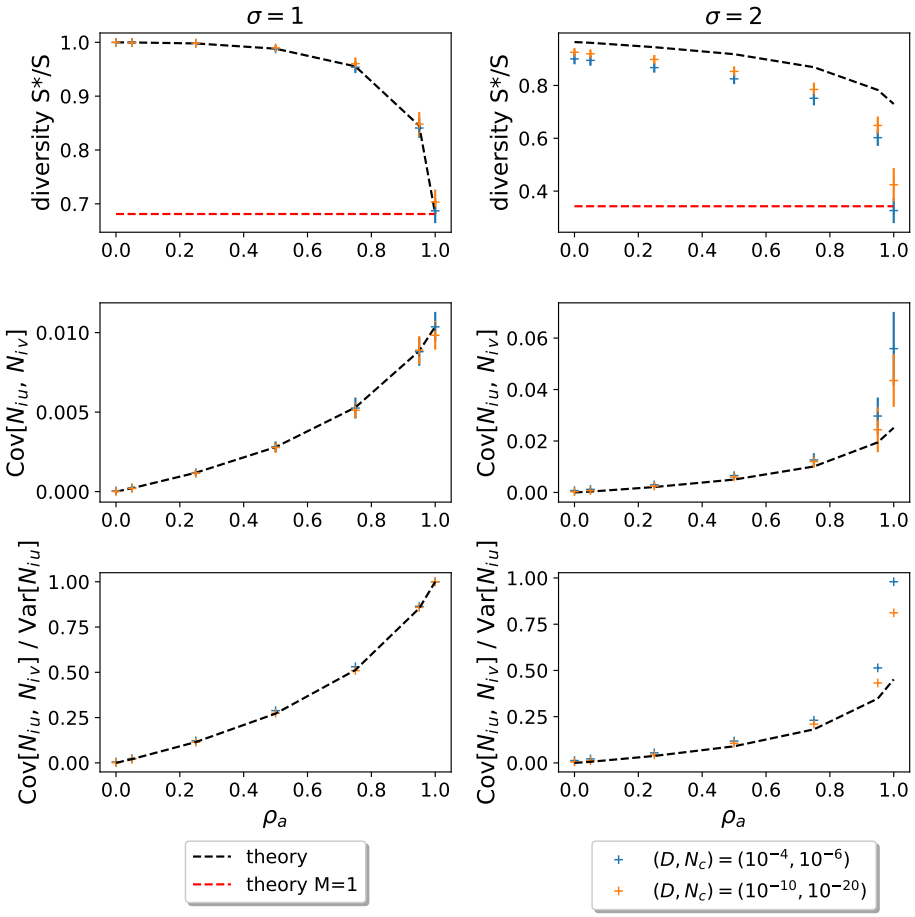

Figure 5.7. Numerical checks of the theoretical predictions. From top to bottom, we consider three different observables: the diversity, the covariance in the abundances across distinct patches, and this covariance rescaled by the one patch variance. By varying σ, we can control the state of the system: on the left ($\sigma = 1$), we show the results for fixed points; on the right ($\sigma = 2 > \sqrt{2}$), we show the results for persistent dynamical fluctuations. In dotted lines, we plot the theory predictions, as functions of the correlation between patches' interactions ρ_a. We compare them to simulations with parameters $(S, M, \mu) = (400, 8, 10)$, and obtained by simulations run until final time $t_f = 10^4$. We eventually vary the couple (D, N_c). We use 50 distinct samples of the simulations for each combination of parameters, in order to get error bars and relevant statistics. The cut-off is implemented via patch-wise extinctions when the abundance goes below the threshold in each particular patch, in which case migration out of the patch is turned off while still allowing inward migrations.

On the left side, we can see that the theory is exact in the fixed point regime. In this regime, as $\rho_a \to 1$, the predictions are equivalent to the one patch $M = 1$ theory, as all patches are the same. In the persistent fluctuation state, the theory is only a good approximation. More precisely, the predictions become more accurate as D and N_c go to zero, as expected. In addition, the agreement gets worse when $\rho_a \to 1$, because synchronization can occur.

In the top right figure, we show that the prediction for diversity is an upper bound. In the bottom right figure, we see that indeed the prediction for ρ_n is still far from 1 when $\rho_a \to 1$, for the values of D, N_c used in the simulations.

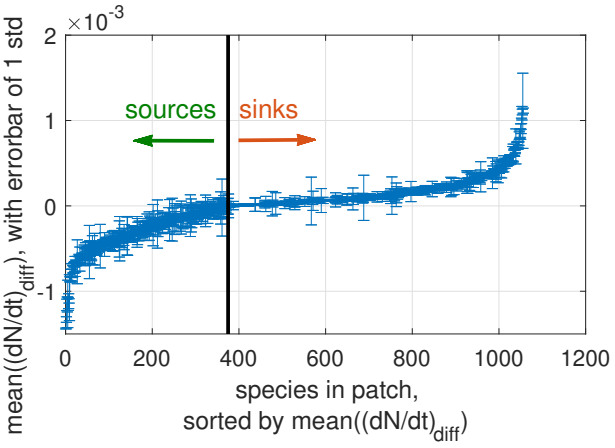

Figure 5.8. Sources maintain their identity over time. The degree to which a patch is a source for a given species is measured by $(dN/dt)_{\text{diff}}$, the contribution of diffusion to the change of $N(t)$, which is negative for sources and positive for sinks. We show all species-patch pairs ordered by the average of this quantity over long times, with error bars giving its standard deviation. For 94% of sources, and 85% of all species-patch pairs, this quantity $(dN/dt)_{\text{diff}}$ retains its sign most of the time, being at least one standard deviation away from zero.

(wrong in this case) theory. However, the agreement with numerical experiments is surprisingly good as shown in figure 5.7, given the limitations.

To find the boundary of parameter space where fixed points loose their stability and the system becomes chaotic, we look at the linear stability of persistent species. When D is small, the species that are not sourced in each patch do not affect the stability, and so the question simplifies to single patch stability, which when $\text{corr}\left[A_{ij}, A_{ji}\right] = 0$, results in $\sigma_c = \sqrt{2}$ and with 1/2 of the species being sourced in each patch [45].

5.5. Reaching and maintaining a dynamical state

Let us first consider a single community ($M = 1$). For a species to survive for long periods of time, it follows from DMFT that it must have positive N^*, or else $N\left(t\right)$ decays exponentially until the species goes extinct. Even if $N^* > 0$, there is still a probability (per unit time) of extinction, which depends on N^*, N_c and on the strength of the noise $\xi\left(t\right)$. Following extinctions, a remaining species interacts with fewer fluctuating other species, causing the strength of the noise to decrease, see Fig. 5.10(a), and with it the probability for extinction, see feedback loop in Fig. 5.10. To generate Fig. 5.10(a), abundance fluctuations were measured in simulations at precisely the same conditions but with fewer surviving species. Since extinctions become very rare at long times, this

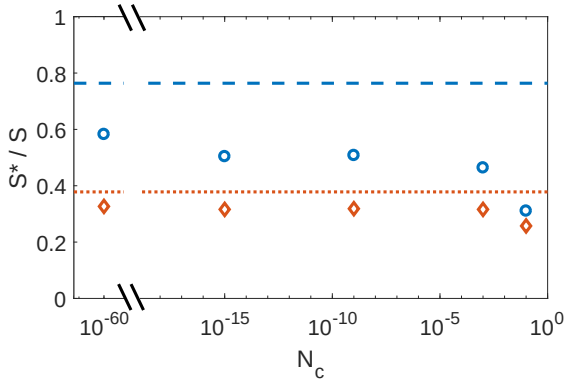

Figure 5.9. The fraction of persistent species S^*/S (circles) is compared to theoretical bound (blue dashed line), for different values of N_c. Also shown is the fraction of species above $N^*_{\text{eff}} > 0.2$, compared to the theoretical bound for that (red dotted line), showing better agreement than for the full diversity. In this case, N^*_{eff} has a slightly different definition.

could not be done by running the simulations for longer times. Instead, species where removed from the simulation, starting with those that have the highest probability for extinction, see Appendix E.1 for details. Results are averaged over 3 runs.

We can develop an analytical treatment for very small cut-off N_c (large population size). In this case there is a large difference in time-scales between the short-term dynamics induced by endogenous fluctuations, and the long-term noise-diversity feedback cycle discussed above. In fact, the extinctions driving this feedback are due to rare events in which the abundance of species with a positive N^* decreases below the (very small) cut-off N_c. For a species in an isolated patch ($M = 1$), the time-scale for such an event is known [25, 26] to be of order of $\tau\,(1/N_c)^a$ where τ is a characteristic time of the endogenous fluctuations, and $a = 2N^*/W$ is independent[5] of N_c, with W the amplitude of the endogenous fluctuations,

$$W \equiv \int dt\, C_\xi\left(t, t'\right) \tag{5.7}$$

The important point here is that, although endogenous fluctuations disappear eventually, there is a clear *separation of time-scales* between typical endogenous fluctuations, that are fast and lead to a quasi-stationary dynamical state, and rare extreme fluctuations that cause extinctions and push the ecosystem into a different state.

While a single community might in principle achieve long-lasting endogenous fluctuations, this however requires unrealistically large population sizes and species number,

[5]The expression of the time scale is analogous to the Arrhenius law for activated processes in physics and chemistry: in this case, the counterpart of the energy barrier is $-[N^* \ln N_c]$ and fluctuation amplitude W plays the role of the temperature.

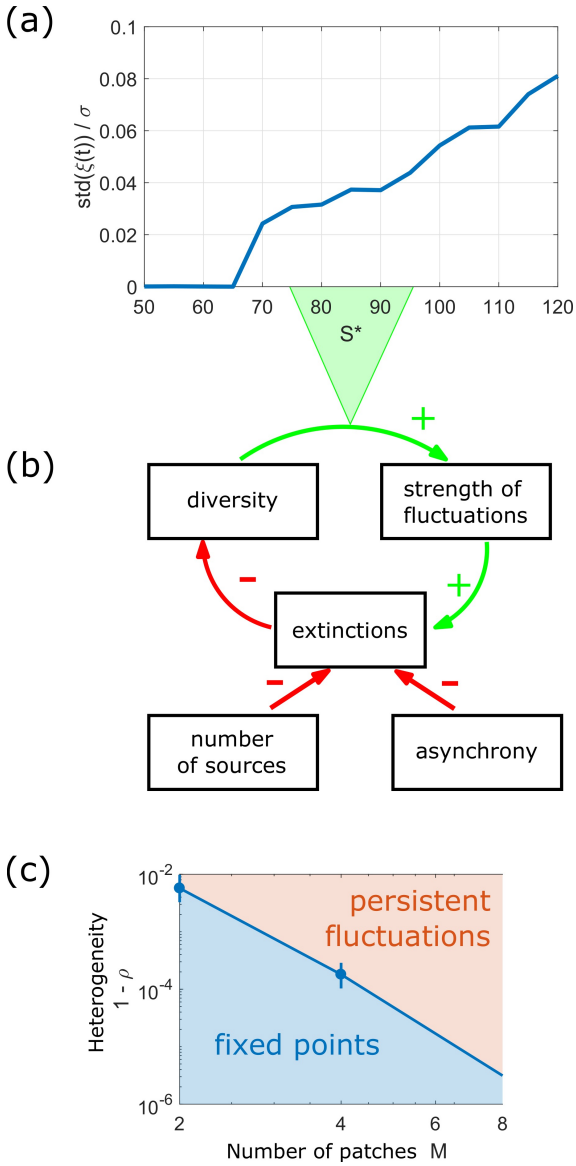

Figure 5.10. Revisiting the noise-diversity feedback cycle in the light of our theoretical framework. (a) Quantitative relationship between species diversity S^*, i.e. the number of coexisting species, and strength of fluctuations std(ξ) for $M = 8$ (rescaled by interaction heterogeneity σ). (c) Patch number M and heterogeneity $1 - \rho$ (defined from the correlation coefficient ρ between interactions $A_{ij,u}$ in different patches u) both contribute to the persistence of endogenous fluctuations by two means, shown in (b): they create source patches where a given species will tend to grow (see Fig.5.8), and allow the asynchrony of fluctuations in different patches. These two factors mitigate the likelihood that endogenous fluctuations will induce species extinctions and cause their own suppression.

see Appendix E.4. Migration between multiple patches substantially enhances persistence due to the spatial insurance effect [27]: species are more unlikely to go extinct because they need to disappear everywhere at once. The time scale for such an event is intuitively expected to scale as $\tau\,(1/N_c)^{Ma_{\text{eff}}}$ with $a_{\text{eff}} = 2N^*_{\text{eff}}/W$ where N^*_{eff} is an effective value for N^* of a species across patches. This result is thus similar to the one identified above for one patch, raised to the power M. The exact dependency should still be worked out, this is ongoing work. These results assume that W is finite, and that the noise acting on a species is independent between patches (asynchrony). Indeed, for moderate values of D and ρ not too close to one, simulations show that $C_\xi\,(t,t')$ is a well-behaved function of t so that W is finite, and the correlation between patches is found to be very small, see Fig. 5.5.

These expressions provide a quantitative description of the feedback cycle in Fig. 5.10. Endogenous fluctuations disappear on the time scale at which species with characteristic abundance N^*_{eff} of order one would go extinct. We must further account for the vanishing strength of the noise W as species disappear. This is shown in Fig. 5.10(a), where the strength of the fluctuations is tightly linked to species diversity, and is zero at the diversity of fixed points. Hence, extinctions significantly increase a_{eff}, reducing the chance for further extinctions.

As stressed above, the asynchrony of fluctuations in different patches is crucial: it allows some species to survive with positive characteristic abundance N^*_i in at least one of the patches. This leads to a higher total number of long-term persisting species, decreases the likelihood of fluctuations to small abundances, and hence increases the stability of a dynamically fluctuating state. If the migration rate D is too strong or ρ very close to one, dynamics in the different patches synchronize, quickly annulling the insurance effect. However, minor (few percent) changes in interaction coefficients or carrying capacities between patches are enough to maintain this effect, see Fig. 5.10(bottom); we don't need to impose coexistence artificially, e.g. by requiring that every species has at least one refuge (a patch so favorable to it that it always dominates there). These little variations in the interaction coefficients are highly plausible, as interaction strength can vary with many factors, including resource availability [95], or temperature and its influence on metabolism [96]. The heterogeneity ρ required to reach a fluctuating state decreases with M, see Fig. 5.10(bottom).

In practice, maintaining a dynamical state seems unfeasible for only one patch, at least for reasonable values of population size $P = 1/N_c$ and species number S, see discussion in Appendix E.4. Yet the combined effect of the two phenomena described above allows for very long-lived endogenous fluctuations in metacommunities, already for $M = 2$ patches.

5.6. Discussion

Complex ecological interactions can give rise to long-lasting fluctuating states, which both require and allow the maintenance of high species diversity. This can happen under a wide range of conditions, which we have illustrated in simulated experiments,

and identified through an analytical treatment based on Dynamical Mean-Field Theory. These results are robust to various modeling assumptions: our work puts forward the role of spatial extension in persistent endogenous fluctuations. In a close-related study, Pearce et al. [49] start from a slightly different ecological setting[6] and reach a similar conclusion. It should be noted that their analytical treatment is much more developed than ours. In particular, they were able to derive the precise expression for the typical timescale of extinctions.

While we have drawn parallels with the theory of stability and coexistence in externally-perturbed ecosystems [27, 25, 26, 20], our approach also highlights essential differences between environmentally-driven and endogenous fluctuations. We show that many-species dynamics induce feedback loops between perturbation and response, and in particular a tight relationship between fluctuation strength and species diversity, which are absent from externally-perturbed ecosystems. Moreover, while similar species can display correlated responses to environmental stochasticity [97], we expect here that their trajectories will be starkly different and unpredictable, due to high-dimensional interactions which lead to complex dynamics. The resulting picture from DMFT is that the abundance of any given species undergoes stochastic dynamics with a finite correlation time. This means that the trajectory of the species abundance cannot be predicted after a time that is large compared to the correlation time–a hallmark of chaos, also found in other models of high-dimensional systems [52]. Our theory paves the way for quantitative testing of these fingerprints of diversity-driven fluctuations in data.

In a counterpoint to classic results [3], we have shown that, while highly diverse ecosystems are unstable, they might still persist: extinctions can be avoided and biodiversity maintained, despite species abundances fluctuating over multiple orders of magnitude. We do observe a negative feedback loop, in which endogenous fluctuations cause extinctions, and eventually lead to their own disappearance as the ecosystem reaches a lower-diversity stable equilibrium. But this self-suppression of fluctuations can be mitigated by a number of factors, among which space is particularly important.

In a single well-mixed community, we expect that persistent fluctuations might not be observed in practice: while theoretically possible, they may require unrealistic population sizes and species numbers. But spatial extension and heterogeneity can dramatically reduce these requirements, in a way that parallels the insurance effect against exogenous perturbations. When fluctuations are not synchronized across space, some patches can act as sources, from which failing populations will be rescued through migration [20, 27]. Here, we find that the existence of sources is surprisingly robust: even if there is no location where the environment is favorable to a given species, source patches can arise from interactions, and endure for long times despite the large fluctuations in species abundances. By allowing fluctuations without extinctions, spatial heterogeneity helps maintain species diversity, and thus the fluctuations themselves. This result is robust over a wide range of parameters, as it only calls for moderate values of inter-patch

[6] The two studies focus on complementary examples (antisymmetric interactions instead of asymmetric, without self-regulation). In our setting, a single species pair would attain a stable equilibrium, while in [49], it would exhibit predator-prey oscillations. Both cases lead to many-species chaotic fluctuations.

migration [98]: the rate D must be such that, over the typical time scale of abundance fluctuations, many individuals can migrate out of a patch (allowing recolonization in the absence of global extinction), while representing only a small fraction of the population in that patch.

A crucial result is that this condition suffices to ensure that synchronization between patches is absent, and that the total strength and correlation time of the noise within patches (W above) remain bounded for finite populations and finite migration rates between patches. This is in contrast to alternative scenarios where noise correlations decay slowly with time [99]. This result is non-trivial for endogenous fluctuations, as the existence of feedbacks (encoded in the self-consistent equations of the DMFT framework) can potentially lead to synchronization and long-time correlations in the noise. Yet we demonstrate that synchrony is avoided, both through direct simulations, and by building an analytical theory based on these assumptions, whose predictions match simulations quantitatively.

The work raises many interesting directions for future work, including the role of finite-dimensional space, where patches are only connected to their neighbors, and comparison with experiments, for example on the role of asynchrony [100].

In conclusion, non-equilibrium fluctuating states might be much more common than suggested by experiments and theory for well-mixed communities. And since these fluctuations permit the persistence of more species than could coexist at equilibrium, we might also expect significantly higher biodiversity in natural environments.

6. Impact of demographic noise

In this chapter, we forget about the spatial structure of the ecosystem, but we add the stochasticity of demographic noise for symmetric interactions. Our theoretical analysis, which takes advantage of a mapping to an equilibrium disordered system, proves that for sufficiently heterogeneous interactions and low demographic noise the system displays a multiple equilibria phase, which we fully characterize. In particular, we show that in this phase the number of stable equilibria is exponential in the number of species. Upon further decreasing the demographic noise, we unveil a *Gardner* transition to a marginally stable phase, similar to that observed in jamming of amorphous materials. We confirm and complement our analytical results by numerical simulations. Furthermore, we extend their relevance by showing that they hold for others interacting random dynamical systems, such as the Random Replicant Model. Finally, we discuss their extension to the case of asymmetric couplings.

Materials from this chapter can be found in [63]. In particular, all details about the analytical computations are in the Appendix of [63]. Additional details about numerics are given in Appendix F.

My main contribution to this work lies in the numerical simulations. I designed the numerical scheme, and performed the numerical study; which is a complex issue in presence of demographic noise (see section 6.5). I also checked the basic analytical computations.

6.1. Introduction[1]

Lotka-Volterra equations describing the dynamics of interacting species are key to theoretical studies in ecology, genetics, evolution and economy [67, 13, 58, 54, 42, 101]. Cases in which the number of species is very large are becoming of general interest in disparate fields, such as in ecology and biology, *e.g.* for bacteria communities [102, 103], and economy where many agents trade and interact simultaneously both in financial markets and in complex economic systems [55, 56].
The theoretical framework used in the past for a small number of species is mainly based on the theory of dynamical systems [104, 1, 105, 106, 107, 108]. When the number of ordinary differential equations associated with the Lotka-Volterra (LV) model becomes very large, *i.e.* for many species, methods based on statistical physics are ideally suited. Indeed, several authors have recently investigated different aspects of community ecology, such as properties of equilibria, endogenous dynamical fluctuations, biodiversity, using ideas and concepts rooted in statistical physics of disordered systems [42, 41, 109, 45, 47, 36, 38, 49, 62, 110, 111, 112]. Similar investigations have been also performed for economic systems [57]. Dealing with a large number of interacting species can actually become a welcome new ingredient both conceptually and methodologically. In fact, qualitatively new collective behaviors, classified into *phases*, can emerge. Also, as it happens in physics, such phases are not tied to the specific model they come from, instead they characterize whole classes of systems in a generic way, potentially including natural systems[2]. From this perspective, it is very interesting to ask which kind of different collective behaviors arise for LV models in the limit of many interacting species and what are their main properties [45, 47]. These questions, which have started to attract a lot of attention recently, tie in with the analysis of the properties of their equilibria [113, 114, 115].

Here, we focus on the usual disordered Lotka-Volterra system from section 1.4.1, but we add demographic noise. We consider the case of symmetric interactions and small immigration and work out the phase diagram as a function of the degree of heterogeneity in the interactions and of the strength of the demographic noise. Compared to previous works [42, 116, 45, 47] adding demographic noise not only allows us to obtain a more general picture, but also to fully characterize the phases and connect their properties to the ones of equilibria. In particular, we show that the number of stable equilibria in the LV model is exponential in the system size and their organization in configuration space follows general principles found for models of mean-field spin-glasses. Our findings, which are obtained for symmetric interactions, provide a useful starting point to analyze the non-symmetric case, as we shall demonstrate by drawing general conclusions on properties of equilibria in the case of small asymmetry.

[1] So that each chapter may be read separately, I decided to preserve all specific chapters' full introduction, even though it may overlap with the global and more detailed introduction from section 1. The overlapping parts are presented in the box and can be skipped.

6.2. Model

Henceforth we focus on the disordered Lotka-Volterra model for ecological communities [42, 45] defined by the equations:

$$\frac{dN_i}{dt} = N_i \left[1 - N_i - \sum_{j,(j\neq i)} \alpha_{ij} N_j \right] + \eta_i(t) \tag{6.1}$$

where $N_i(t)$ is the relative abundance of species i at time t ($i = 1, \dots S$), and $\eta_i(t)$ is a Gaussian noise with zero mean and covariance $\langle \eta_i(t)\eta_j(t')\rangle = 2TN_i(t)\delta_{ij}\delta(t-t')$ (we follow Ito's convention). This noise term allows us to include the effect of demographic noise in a continuous setting [117, 118, 119]; the larger the global population, the smaller the strength T of the demographic noise. Immigration from the mainland is modeled by a reflecting wall for the dynamics at $N_i = \lambda$, since this is more practical for simulations than the usual way of adding a λ in the RHS of Eq. (6.1) (see the Appendix for more details).

The elements of the interaction matrix α_{ij} are again independent and identically distributed variables such that:

$$\text{mean}[\alpha_{ij}] = \mu/S \quad \text{var}[\alpha_{ij}] = \sigma^2/S \tag{6.2}$$

We consider the interactions in the symmetric case with $\alpha_{ij} = \alpha_{ji}$. As shown in [47], the stochastic process induced by eq. (6.1) admits an equilibrium-like stationary Boltzmann distribution:

$$P(\{N_i\}) = \exp\left(-\frac{H(\{N_i\}}{T} \right) \tag{6.3}$$

where

$$H = -\sum_i \left(N_i - \frac{N_i^2}{2} \right) + \sum_{i<j} \alpha_{ij} N_i N_j + \sum_i [T \ln N_i - \ln \theta(N_i - \lambda)] \tag{6.4}$$

The before-last term is due to the demographic noise and the last one to the reflecting wall, which leads to a lower-immigration cut-off, at $N_i = \lambda$ ($\theta(x)$ is the Heaviside function). By taking advantage of this mapping to an equilibrium statistical mechanics problem and by using theoretical methods developed for disordered systems, we obtain the properties of the stationary states and the equilibria of the LV-model from the analysis of the equilibrium states and the local minima of the energy function H. Our theoretical framework is standard and based on the replica method [75]; the computation is described in full details in the Appendix of [63]. Here, we present directly the results.

6.3. Analytical Results

Among the most important ones is the existence of three distinct phases for the LV-model in presence of demographic noise and small but non-zero immigration, as shown

in Fig. 6.1 (we focus on $\lambda = 10^{-2}$, similar results are obtained for smaller values of λ). We find no sensitive dependence on the average interaction parameter, so the phase diagram has been obtained at fixed value $\mu = 10$.

For large enough demographic noise (corresponding to high-temperature) we find that there is a single equilibrium phase, *i.e.* the noise is so strong that the interactions within species do not play an important role: for any initial condition the system relaxes toward a unique dynamically fluctuating stationary state. When the strength of the demographic noise decreases, multiple states emerge. We can study this transition by analyzing the stability of the thermodynamic high-temperature phase. This is performed by analyzing its free-energy Hessian matrix $\mathcal{H}$. The point at which the lowest eigenvalue of $\mathcal{H}$ reaches zero signals the limit of stability of the high-temperature phase and the emergence of multiple equilibria.

Within the replica method that we used here, this corresponds to the breaking of replica symmetry and to the requirement of having a zero replicon eigenvalue. This leads to an equation for the transition line corresponding to the blue curve in Fig. 6.1:

$$\lambda_{\mathrm{R}} = (\beta\sigma)^2 \left[1 - (\beta\sigma)^2 \overline{\left(\langle N_i^2\rangle - \langle N_i\rangle^2\right)^2}\right] = 0 \ , \tag{6.5}$$

where $\beta = 1/T$. The average $\langle X\rangle$ is the thermodynamics average taken over the effective Hamiltonian (6.4), while $\overline{X}$ denotes the average over the quenched disorder associated to the random interactions (i is a dummy index since statistically all species are equivalent after average over the interactions). Physically, the condition above can be shown to correspond to a diverging response function [45, 47], and is a signature of the system being at the edge of stability, namely at a *critical point* in the parameter space.

Below the blue curve there exist multiple states—which one is reached dynamically depends on the initial condition. Such states correspond to dynamically fluctuating equilibria that are stable to perturbations and that have typically an overlap in configuration space given by

$$q_0 = \frac{1}{S}\sum_i \langle N_i\rangle_\alpha \langle N_i\rangle_\beta \tag{6.6}$$

where α and β denote the average within two generic states α and β. One can similarly define the intra-state overlap $q_1 = \frac{1}{S}\sum_i \langle N_i\rangle_\alpha^2$. See Fig. 6.2 for a pictorial representation of these two quantities and the organization of equilibria in phase space. This is (in the replica jargon) the so-called one-step replica symmetry breaking phase (1RSB) [60]. In order to characterize the properties of this phase of the LV-model, we have computed the number of states, and hence of equilibria, using methods developed for structural glasses [120]. More specifically, we have computed the complexity Σ, which is defined as the logarithm of the number of equilibria with a given free-energy density f normalized by the number of species S. This allows us to show that the number of equilibria below the blue line in Fig. 6.1 is *exponential* in S, *i.e.* there is a strictly positive complexity Σ.

When decreasing further the demographic noise, the heterogeneity in the interactions becomes even more important and a second phase transition takes place. In order to

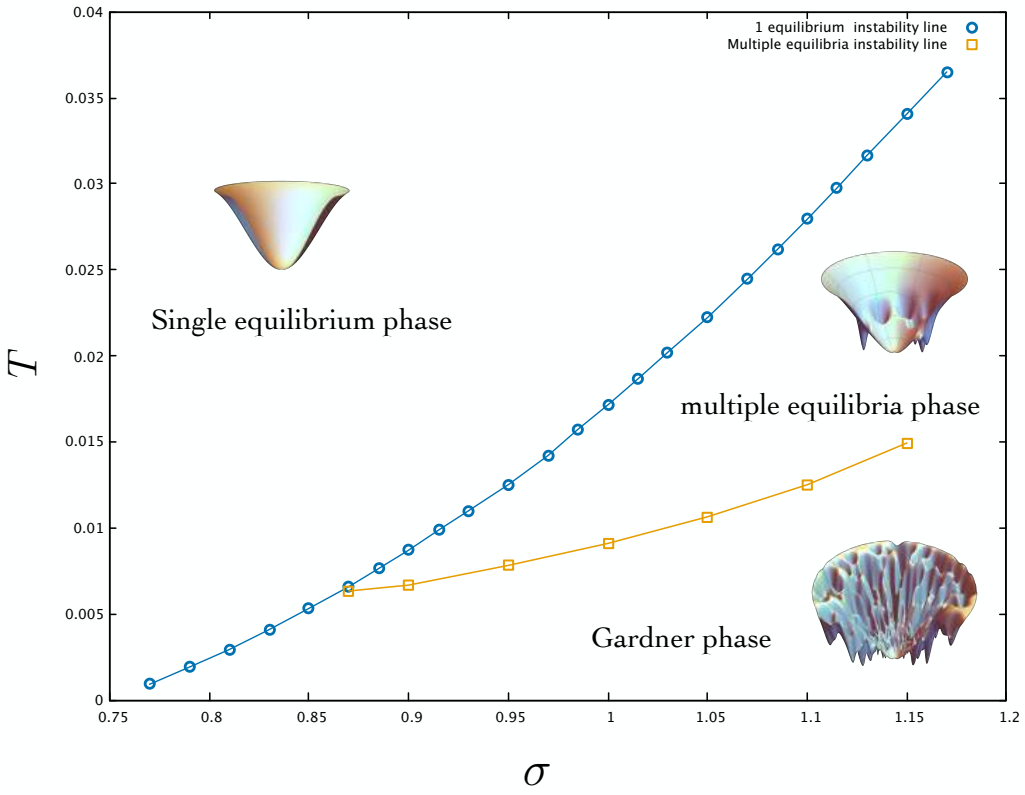

Figure 6.1. Phase diagram showing the strength of the demographic noise, T, as a function of the degree of heterogeneity, σ, at fixed $\mu = 10$ and selected value of the cutoff, $N_c = 10^{-2}$. Upon decreasing the noise three different phases can be detected: i) a single equilibrium phase; ii) a multiple equilibria regime between the light blue and the orange lines; iii) a Gardner phase, which turns out to be characterized by a hierarchical organization of the equilibria in the free-energy landscape.

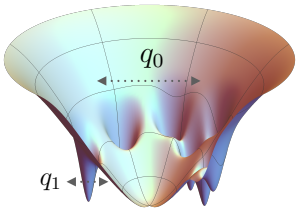

Figure 6.2. Zoom on a pictorial landscape. The parameters q_0 and q_1 denote the size of the largest and the innermost basins respectively within the two-level structure of the 1RSB phase.

locate it, we repeat exactly the same procedure as for the single equilibrium phase but now within one of the typical states with a given free-energy f. The computation is more involved (it corresponds to analyzing the stability of the 1RSB Ansatz) and leads to the condition:

$$\lambda_{\mathrm{R}}^{\mathrm{1rsb}} = (\beta\sigma)^2 \left[1 - (\beta\sigma)^2 \overline{\langle \left(\langle N^2 \rangle_{\mathrm{1r}} - \langle N \rangle_{\mathrm{1r}}^2 \right)^2 \rangle_{m\text{-r}}}\right] = 0 \tag{6.7}$$

where the two different averages correspond to the intra-state average $\langle\cdot\rangle_{\mathrm{1r}}$ and the inter-state average, $\langle\cdot\rangle_{m\text{-r}}$. All technical details of the calculation are in the Appendix of [63]. The critical temperature that results from the equation above leads to the orange line in Fig. 6.1. Crossing this line results in a fragmentation of each state into a fractal structure of sub-basins [121] (see the landscape on the bottom in Fig. 6.1): each state becomes a meta-basin that contains many equilibria, all of them marginally stable, i.e. poised at the edge of stability [47], and organized in configuration space in a hierarchical way, as in the case of mean-field spin glasses [75]. This phase, which is called *Gardner*, plays an important role in the physics of jamming and amorphous materials [122, 123]. Our results unveil its relevance in theoretical ecology by showing that it describes the organization of equilibria in the symmetric disordered LV-model at low enough demographic noise and for highly heterogeneous couplings.

6.4. Numerical results

We now present numerical simulation results that confirm and complement our analytical study. We numerically integrate the stochastic equation Eq. (6.1) using a specifically designed method detailed in section 6.5. The initial abundance for each species is drawn independently in $[0, 1]$. The exact numerical protocol is presented in Appendix F.1. In this section, we will refer to the One Equilibrium phase, and the Multiple Equilibria phase identified on figure 6.1 (we do not consider here the Gardner phase). They are separated by a critical temperature that we denote $T_{1RSB}(\sigma)$.

6.4.1. Observables' definition

In order to compare with the theory, we need to decide which observables to focus on. So far, there are four sources of fluctuations in the process: the three random parts (interactions, initial conditions and demographic noise) that we labelled with $r = 1..N_{sample}$, and the species themselves $i = 1..S$. In the following, we will denote $\mathbb{E}[X]$ the average over all those contributions. For example:

$$\mathbb{E}[N(t)N(t')] = S^{-1}N_{sample}^{-1} \sum_{i=1}^{S} \sum_{r=1}^{N_{sample}} N_i^r(t) N_i^r(t')$$

It can be shown [77] that if the system is large enough ($S \gg 1$) and the sampling thorough enough ($N_{sample} \gg 1$), there is a convergence in law of the process. Mainly, there is a well defined limit ($S, N_{sample} \to \infty$) that we can compare with the theory.

To fix ideas, we generically use $S \sim 500$ and $N_{sample} \sim 50$, and we checked there is no (S, N_{sample}) dependency at this scale. More precisely, in the $S \to \infty$ limit, the free energy is self-averaging, so results should typically not depend on the realization of the sampling. Here for the numerics, as $1 \ll S < \infty$, we still use some averaging over the samples to get cleaner data.

We will first assume that if we wait for a long-enough time t_{wait}, the system will reach a time-translationally invariant (TTI) state, at least for high-enough temperatures. For instance, the two-time correlation C is a function of the time difference:

$$\forall\, t \geq t' > t_{wait}, \qquad \mathbb{E}[N(t)N(t')] = C(t,t') = C(t-t')$$

We check this numerically, see figures 6.3a and 6.3b. The waiting-time depends on the parameters, mainly (σ, T). However, if we lie in the One Equilibrium phase, we can always find the TTI state, for rather small waiting times $t_{wait} \sim 10^2$.

All the comparisons we will be making are in this state ($t \geq t_{wait}$), for the One Equilibrium phase. We will now use a mapping between thermodynamics properties, and dynamical ones. Our observables are the following:

$$h = \mathbb{E}\left[N(t)\right]$$
$$q_d = C(0) = \mathbb{E}\left[N(t)^2\right]$$
$$q_0 = \lim_{\tau\to\infty} C(\tau) = \lim_{\tau\to\infty} \mathbb{E}\left[N(t)N(t+\tau)\right] \sim \mathbb{E}\left[N(t)N(t_{max})\right]$$

The *lhs* is predicted by the theory, and the *rhs* are numerical observables.

6.4.2. One example of numerical results in the One Equilibrium phase

On figure 6.3a, we show that one time observables such as $\mathbb{E}\left[N(t)\right]$ or $\mathbb{E}\left[N(t)^2\right]$ converge to a constant value in time. This indicates the reach of a TTI state. It can be confirmed by the collapse of two-time observables such as the correlation $\mathbb{E}[N(t)N(t')] = C(t,t')$, that we plot as $C(t-t',t')$ for different t' on figure 6.3b. The long-time limit of $C(t-t')$ is the overlap between two generic configurations belonging to the single equilibrium state.

We can see that for $t > t_{wait} \sim 20$ here, the system is indeed TTI, at least regarding these observables. We then read the values of $h = \mathbb{E}\left[N(t)\right]_{TTI}$ and $q_d = \mathbb{E}\left[N(t)^2\right]_{TTI}$ when they stabilize. And we read $q_0 = \mathbb{E}\left[N(t)N(t_{max})\right]_{TTI}$ on the collapse of figure 6.3b.

From the time-dependence of $C(t-t')$ one can also estimate the typical time-scale characterizing dynamical fluctuations within the single equilibrium phase. Formally, we define $\tau_{decorrel}$ by the identity:

$$\frac{C(\tau_{decorrel}) - C(\infty)}{C(0) - C(\infty)} = 0.3 \tag{6.8}$$

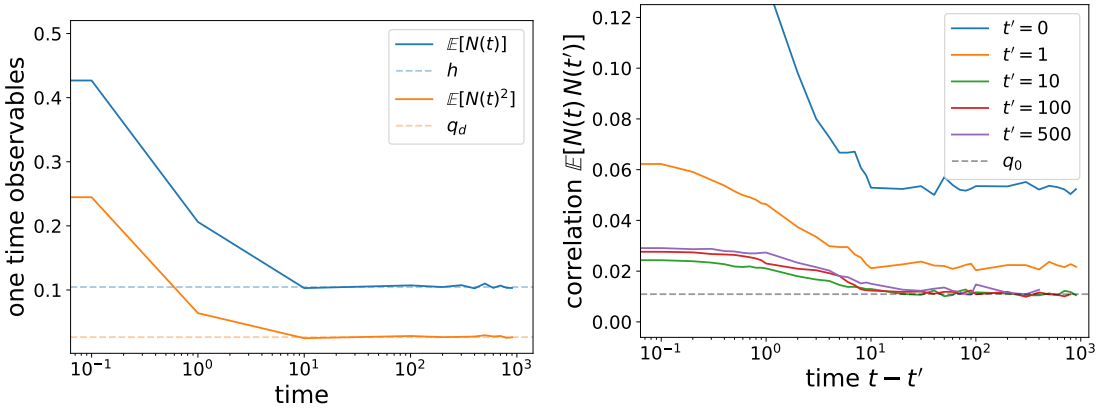

(a) One time observables converge in time.

(b) Correlation $\mathbb{E}[N(t)N(t')] = C(t, t')$, plotted as a function of $t - t'$ for different t'.

Figure 6.3. The system reaches a TTI state in the One Equilibrium phase. (a) The dashed lines correspond to the read TTI value of h and q_d. (b) We see that, up to fluctuations, the correlation collapse as a function of $t - t'$ for $t' > t_{wait} \sim 20$. The dashed line correspond to the read TTI value of q_0. Here, the timescale for decorrelation is around $\tau_{decorrel} \sim 10$. The data for both plots comes from only one sample of the process, with discrete timestep $dt = 10^{-1}$, and parameters $(S, \mu, \sigma, \lambda, T) = (500, 10, 1, 10^{-2}, 10^{-1})$.

6.4.3. Comparison with analytical results in the One Equilibrium phase

The results are presented on figure 6.4: the theory matches beautifully the numerics.

In Fig. 6.5, we plot $\tau_{decorrel}$ as a function of $(T - T_{\mathrm{1RSB}})$, where T_{1RSB} is the critical value of T at which the single equilibrium phase becomes unstable (blue line in Fig. 6.1). We find that the thermodynamic instability is accompanied by a dynamical transition at which $\tau_{decorrel}$ diverges as a power law with an exponent close to 0.5, see Fig. 6.5.

6.4.4. Results in the Multiple Equilibria phase

For small demographic noise, *i.e* when T is below the blue line of Fig. 6.1, previous results on the dynamics of mean-field spin glasses [124, 125, 65] suggest that the LV-model should never reach an equilibrium stationary state, and instead it should display *aging* [84, 126]. In fact, one expects that, among the very many equilibria, the dynamics starting from high-temperature-like initial conditions falls in the basin of attraction of the most numerous and marginally stable equilibria, and display aging behavior. This is indeed what we report in Fig. 6.6 which shows that older the system is, the longer it takes to decorrelate. The landscape interpretation of this phenomenon is that the system approaches at long times a part of configuration space with many marginally stable equilibria. This leads to aging because the longer the time, the smaller the fraction of unstable directions to move, hence the slowing down of the dynamics, but the

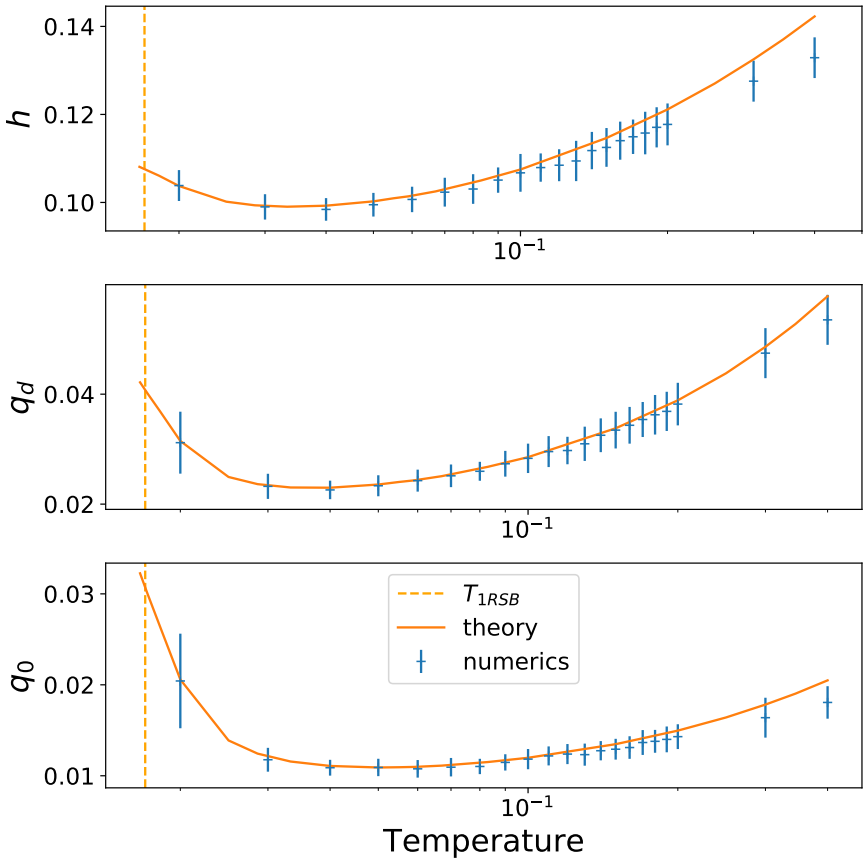

Figure 6.4. Comparison with the theory in the One Equilibrium phase. Parameters are $(S, \mu, \sigma, \lambda) = (500, 10, 1, 10^{-2})$. We consider the observables (h, q_D, q_0) as a function of temperature. The orange full line is the theory predictions. Blue crosses are numerical results, error bars are taken with respects to the $N_{sample} = 50$ different samples of the ecosystem. We found $t_{wait} \sim 200$ to be enough to observe TTI state in all these values of temperature, except for the last point on the left ($T = 2.10^2$): due to slowing down of the dynamics, we had to increase the extent of the simulation and found $t_{wait} \sim 3000$. the orange dashed line correspond to the critical temperature at which the theory enters the Multiple Equilibria phase (it becomes 1RSB). Indeed, numerically we can't observe TTI state below this temperature, even increasing t_{max} to 10^7.

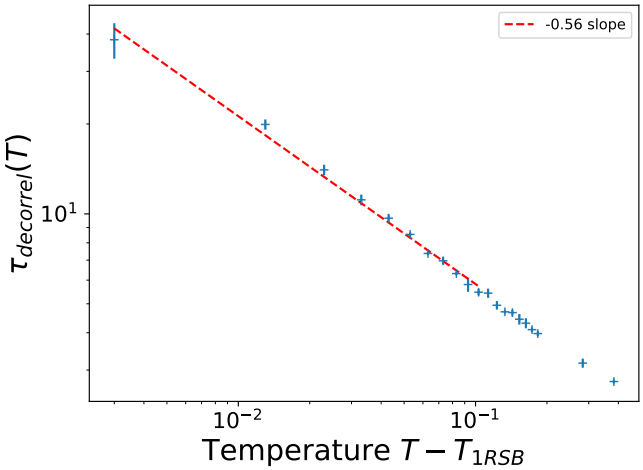

Figure 6.5. Critical slowing down of the dynamics. We plot the decorrelation time $\tau_{decorrel}(T)$ as a function of $T - T_{1RSB}$, in a log-log scale. Blues crosses come from the same numerical data as figure 6.4. Red dashed line is a simple fit. As we approach the transition, the system becomes slower and slower, and the dynamical timescale diverges.

exploration never stops and eventually the system never settles down in any equilibrium [83, 127, 128]. The two dashed lines in Fig. 6.6 correspond to our analytical prediction for the intra-state and the inter-state overlaps of the marginally stable equilibria. The agreement is satisfactory but larger times would be needed to fully confirm it.

6.5. Numerical scheme to sample demographic noise

In this section, we present in details our numerical scheme for integration of the stochastic equation Eq. (6.1). As detailed in Appendix F.2, the immigration has to be treated carefully. Indeed, a generic constant immigration rate is not strong enough to prevent populations from reaching very low values. We first perform a quick literature review of the different existing schemes, before introducing ours.

6.5.1. Literature review

Numerical simulations need discrete time. However, when discretizing time with bounded random processes, one often encounters a non-zero probability that during one time-step the system will cross the boundary of the system (for example the $N \geq 0$ boundary in our case), and become numerically unstable. We review different solutions that have been proposed to solve this issue, and check how they deal with our Lotka-Volterra (LV) system. A more thorough review can be found in [119].

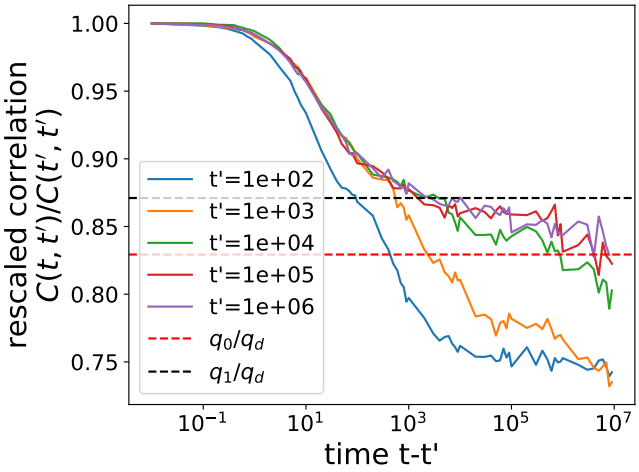

Figure 6.6. Aging behavior. Parameters are $(S, \mu, \sigma, \lambda, T, N_{sample}) = (2000, 10, 1, 10^{-2}, 1/80, 40)$. We plot the rescaled correlation $C(t,t')/C(t',t')$ as a function of $t - t'$, for different t'. The different curves no longer collapse, there is no TTI state anymore. In dotted black and red lines, we respectively show the predictions for the intermediate and final plateau values. They do not coincide exactly with the data, but the trends correspond.

A first naive way to go around the difficulty is to change variable (sqrt, ln...). But this won't work because if the noise becomes treatable, the deterministic part becomes numerically unstable. Most articles then study the numerical integration of processes such as $\dot{N} = \alpha + \beta N + \eta$, where η has correlation $\langle \eta_t \eta_{t'} \rangle = 2TN_t\,\delta(t - t')$.

Reference [129] proposes Balanced Implicit Method: they implement a clever discretization scheme so that the boundaries (positivity) are respected. The scheme amounts to Euler's for small time step. It needs a small regularization. It does not work for LV, because it needs very small regularization parameter and time-step to give good results. This is too heavy numerically. Reference [130] derives the exact Fokker Planck solution of a simpler system. But sampling is inefficient (rejection method). Reference [131] builds on this method by improving the sampling method, but this still isn't satisfactory. Eventually, Reference [132] improves again the method, by exactly solving (Fokker-Planck) the full process. The sampling is clever, with Poisson variables. They also indicate a way to solve more elaborate processes, which we will detail in the following section. Our strategy is heavily based on Reference [132].

6.5.2. Our implementation

The idea from [132] is to separate the process into solvable ones. More precisely, we want to solve:

$$\dot{N}_i = \eta_i \; -N_i^2 \; -N_i \left(\sum \alpha_{ij} N_j - 1\right) \qquad ...+hardWall(\lambda) \tag{6.9}$$

where $hardWall(\lambda)$ implements the hard wall boundary at $N = \lambda$. We will discretize time with a timestep dt, and further subdivide it into three timesteps $dt' = dt/3$. We consider that only one part of the process is active during a subtimestep dt'. So the final scheme is the following:

1. From [130], we know how to sample efficiently the demographic noise only

$$\tilde{N}_i(t + dt') = \text{Gamma}\left[\text{Poisson}[\frac{N_i(t)}{T\, dt'}]\right] T\, dt'$$

   This corresponds to a process which only feels the demographic noise $\dot{N}_i = \eta_i$ during $[0, dt']$. We respectively used the notation Poisson$[\omega]$ (Gamma$[\omega]$) for random Poisson (Gamma) variables, with parameter ω.

2. Treating immigration as a reflecting wall. The particle wishes to go to $\tilde{N}_i$ but bounces on the wall.

$$N_i(t + dt') = \lambda + |\tilde{N}_i(t + dt') - \lambda|$$

3. During $[dt', 2dt']$, only integrate the blue process $\dot{N}_i = -N_i^2$:

$$N_i(t + 2dt') = \frac{N_i(t + dt')}{1 + dt'\, N_i(t + dt')}$$

4. During $[2dt', 3dt']$, only integrate the pink process $\dot{N}_i = -N_i \left(\sum \alpha_{ij} N_j - 1\right)$:

$$N_i(t + 3dt') = N_i(t + 2dt') \exp dt' \left(1 - \sum \alpha_{ij} N_j(t)\right)$$

There are a lot of different combinations of this kind of schemes. We tried some, and chose this one after a lot of checks on simpler models for which we know the distributions at all times. In Appendix F.3, we review the issues and possible improvements of our current scheme.

6.6. Analytical results on other models

In this section, we apply our analytical treatment to a close-related model, and discuss the behavior we expect from the relaxation of the perfect symmetry hypothesis in the interactions.

Our characterization of the phases and the dynamics of the LV-model has important consequences on related systems, in particular on the so-called random replicant models (RRMs) that consist of an ensemble of replicants evolving according to random interactions. Given their numerous applications in biology, optimization problems [133, 134] as

well as evolutionary game theory [135, 136], RRMs still attract great theoretical interest. The RRM, which was introduced in [134] and further studied in [116], is remarkably similar to the disordered LV-model we studied. In the case of symmetric interactions, one can similarly map the problem onto an equilibrium statistical physics one with the following Hamiltonian:

$$H_R = -\sum_{i<j=1}^{S} J_{ij} x_i x_j - a \sum_{i=1}^{S} x_i^2 \tag{6.10}$$

where x_i/S is the concentration of the ith family in the species pool subject to the global constraint $\sum_i x_i = S$ for all $x_i \geq 0$. The couplings J_{ij} are i.i.d. Gaussian variable with variance J^2/S. Provided an appropriate rescaling of the interaction matrix of the two models, we can show that the average interaction term μ for LV – standing for a purely competitive environment – plays the same role as the Lagrange multiplier that is introduced in RRM to enforce the sum of all concentrations to be fixed. The main differences with respect to Eq. (6.4) is the absence of the logarithmic term. Our analysis can be fully extended to the RRM, as we show in the Appendix. The main result is that the three phases we found for the LV-model are present also for the RRM, and organized in a phase diagram (see Fig. 8) that is remarkably similar to the one in Fig. 6.1. This strengthens the generality of our results, and clarifies the nature of the glassy phase of the RRM that was first investigated in [116].

Let us finally discuss how we expect our results to change if the interactions contain a small random asymmetric component. The multiple basins structure associated with the 1RSB phase should not be affected because its basins correspond to stable stationary states, and a small non-conservative random force should not destabilize them [137]. On the contrary, the fractal structure and the decomposition into sub-basins are expected to be wiped out because of the marginal stability of the equilibria associated with it [138, 139, 115]. In absence of demographic noise, one therefore expects a single equilibrium at small σ, which is replaced by an exponential number of chaotic attractors at large σ. The demographic noise adds additional dynamical fluctuations to these multiple equilibria and eventually makes them merge in a single equilibrium, thus leading to a phase diagram similar to Fig.1 but with only the blue line and two phases (single and multiple equilibria).

6.7. Conclusion

In conclusion, we have unveiled a complex and rich structure for the organization of equilibria in a central model for ecological communities. Our results, supported by dynamic simulations, highlight the relevance of multiple equilibria phases for the dynamics of many strongly interacting species. Moreover, our findings clarify the glassy nature of the equilibria previously studied in [42, 45, 47, 38, 140]. As we have shown, our results carry out to more general contexts, in particular to models originating from evolutionary game theory. We expect that the collective dynamical behaviors — the phases — found in this work go beyond the LV-model itself and may play an important role in a

variety of contexts from biology to economy, which can be modeled by high-dimensional dynamical systems with random couplings.

7. Conclusion[1]

Complex ecological interactions can give rise to long-lasting fluctuating states, which both require and allow the maintenance of high species diversity. This can happen under a wide range of conditions, which we have illustrated in simulated experiments, and identified through an analytical treatment based on disordered system techniques: the Dynamical Mean Field Theory.
While we have drawn parallels with the theory of stability and coexistence in externally-perturbed ecosystems [27, 25, 26, 20], our approach also highlights essential differences between environmentally-driven and endogenous fluctuations. We show that many-species dynamics induce feedback loops between perturbation and response, and in particular a tight relationship between fluctuation strength and species diversity, which are absent from externally-perturbed ecosystems. Moreover, while similar species can display correlated responses to environmental stochasticity [97], we expect here that their trajectories will be starkly different and unpredictable, due to high-dimensional interactions which lead to complex dynamics. The resulting picture from DMFT is that the abundance of any given species undergoes stochastic dynamics with a finite correlation time. This means that the trajectory of the species abundance cannot be predicted after a time that is large compared to the correlation time – a hallmark of chaos, also found in other models of high-dimensional systems [52].
In a counterpoint to classic results [3], we have shown that, while highly diverse ecosystems are unstable, they might still persist: extinctions can be avoided and biodiversity maintained, despite species abundances fluctuating over multiple orders of magnitude. We do observe a negative feedback loop, in which endogenous fluctuations cause extinctions, and eventually lead to their own disappearance as the ecosystem reaches a lower-diversity stable equilibrium. But this self-suppression of fluctuations can be mitigated by a number of factors, among which space is particularly important.

[1] So that each chapter may be read separately, I decided to preserve all specific chapters' full conclusion, even though it may overlap with the global conclusion from here. The overlapping parts are presented in the box and can be skipped.

Conclusive remarks on my work

Summary

I will now conclude in more details on my work in particular. During my PhD, I worked on the chaotic population dynamics in large ecosystems. I tried to show that chaos is much more present in ecological setups than what is usually considered – at least from a theoretical point of view. Non-equilibrium fluctuating states might be more common than suggested by experiments and theory for well-mixed communities. And since these fluctuations permit the persistence of more species than could coexist at equilibrium, we might also expect significantly higher biodiversity in natural environments.

In order to study this phenomenon, I applied a powerful theoretical framework relying on disordered system techniques: the Dynamical Mean Field Theory. In chapter 2, I have presented a general derivation of DMFT for models of ecosystems based on the dynamical cavity method. I developed a numerical method to solve DMFT that can be used for many different systems characterized by stochastic dynamics and by a large number of degrees of freedom. One important application concerns the dynamics of interacting particle glassy systems in the limit of infinite dimensions [79, 80, 81]. In a more ecological context, I have implemented and tested our numerical method for the generalized Lotka-Volterra model of ecosystems and showed that it can capture complex dynamics such as chaos and aging.

In the following chapters, I focused on the aging dynamics: without immigration, the chaotic dynamics in an isolated ecosystem become slower and slower. In chapter 3, I presented the basic properties of the fixed points of the dynamics, and numerically showed that the ecosystem chooses marginally stable fixed points at long times. In chapter 4, I made various assumptions in order to solve analytically the DMFT equations, proposed a simpler model to understand aging dynamics within DMFT, and derived the Kac-Rice complexity of fixed points as an alternative method to study the dynamics. Both chapters 3 and 4 are still ongoing studies. More precisely, I am currently investigating if the fixed points metadynamics can be a predictive approach; I want to solve DMFT with a triangular potential in order to check the closure in temperature and the self-consistency of stable chaotic dynamics; and I would like to solve the aging toy-model. I reckon that the current state of these studies already gives relevant insights on the disappearance of the chaotic behavior, but also that a more complete view could be reached with a little bit more work.

In chapter 5, I used the DMFT framework to study how the spatial structure of an ecosystem stabilizes the chaotic dynamics. In a single well-mixed community, persistent fluctuations might not be observed in practice: while theoretically possible, they may require unrealistic population sizes and species numbers. But spatial extension and heterogeneity can dramatically reduce these requirements, in a way that parallels the insurance effect against exogenous perturbations. When fluctuations are not synchronized across space, some patches can act as sources, from which failing populations will be rescued through migration [20, 27].

Eventually, in chapter 6, I considered how demographic noise can affect the dynamics

of the single well-mixed community. Analytical results, supported by dynamic simulations, highlight the relevance of multiple equilibria phases for the dynamics of many strongly interacting species. Moreover, the findings clarify the glassy nature of the equilibria previously studied in [42, 45, 47, 38, 140]. The results carry out to more general contexts, in particular to models originating from evolutionary game theory. It is expected that the collective dynamical behaviors found in this work go beyond the general Lotka-Volterra model itself and may play an important role in a variety of contexts from biology to economy, which can be modeled by high-dimensional dynamical systems with random couplings.

Future directions of research

One aspect which is clearly missing from my PhD consists in the application to real ecological data obtained monitoring well-mixed ecosystems, such as microbiota or plant experiments [51, 39, 46]. Even though precise time-series of populations are challenging to obtain in field ecology, new techniques [59, 141] should allow the comparison to our theoretical predictions.

From a more theoretical aspect, my PhD raises many interesting directions for future work, including the role of finite-dimensional space, where spatial patches are only connected to their neighbors. Comparison with experiments could also be done in this context, for example on the role of asynchrony [100].

A few related directions of research are already under investigation at the moment: how does the analysis extend to ecological interactions that do not scale with the number of species, and how to integrate the theory of evolution into the ecological predictions. These two directions should provide a more general picture of the natural dynamics in real ecosystems.

On a more specific subject, one crucial theoretical key-point is still missing from my study: the time-scale needed for chaotic dynamics to disappear, in an isolated ecosystem with a population cut-off. This is related to the ongoing study, both numerical and analytical, that was presented in chapters 3 and 4. Even though a relevant advancement towards this scaling was hinted at in [49], a full theory for this time-scale is still missing. I reckon that this theory is the missing step for chaotic dynamics to be considered seriously in data analysis.

Nevertheless, I consider that this PhD can provide a strong theoretical base to pursue further analysis, and I am glad that I could contribute in this way.

From a more personal point of view, I reckon that, while research can always improve our understanding of ecosystems, the emergency of the global ecological situation should trigger a different kind of involvement. Indeed, it seems to me that the priority now lies in scientific vulgarization and political commitment. Along these lines, I was lucky enough to be invited to contribute to a national radio broadcast on France Culture [142], and I do intend to keep on being active in these domains.

A. Dynamical Mean Field Theory (chapter 2)

A.1. Immigration as a mathematical regularization of the problem

In this section, we consider why a regularization is needed in the general Lotka-Volterra model and how it is performed by immigration.

We recall the general Lotka-Volterra model from equation 1.7:

$$\forall i = 1, ..., S, \quad \frac{dN_i}{dt} = \frac{r_i}{K_i} N_i (K_i - N_i) - N_i \sum_{j \neq i} \alpha_{ij} N_j + \lambda_i$$

Without immigration λ_i, there are two main issues:

- the abundances are considered continuous, but they come from individual-based processes. Therefore there should be a cut-off below which an abundance is set to 0, as there is no longer any alive individual of the species. Without such a cut-off, the species that should go extinct only do so in the limit of infinite time, which is unphysical;
- in the absence of immigration, the final state of the system can depend strongly on initial conditions. For example, if a species population is set to 0 at time $t = 0$, it cannot appear in the ecosystem, even though the Unique Equilibrium might allow it to coexist with the others.

Putting a small parameter λ_i which corresponds to an individual of species i arriving in the ecosystem from time to time solves both issues: a species will be considered dead if its population stays at the minimal level λ_i, and it will always be given the chance to invade the ecosystem.

Therefore immigration regularizes the problem. We then consider the limit $\lambda \to 0$ so that the analytical solutions are simpler.

A.2. Scaling of the cross response function and cross correlation

In this section, we detail rough arguments to show two mathematical results used in the main text:

- the response from the population of species i to an infinitesimal perturbation in the population of species $j \neq i$ is subleading: $\chi_{ij} = \frac{\delta N_i}{\delta h_j} \sim 1/\sqrt{S}$;
- the correlation between two distinct species is subleading: $\langle N_i N_j \rangle - \langle N_i \rangle \langle N_j \rangle \sim 1/\sqrt{S}$.

A.2.1. Cross response function

We start from the simplified rLV case:

$$\forall i = 1, ..., S, \qquad \dot{N}_i = N_i(1 - N_i - \sum_{j \neq i} \alpha_{ij} N_j + h_i(t))$$

We differentiate this equation with respect to $h_l(t')$, in the functional sense. We'll denote $\chi_{il}(t, t') = \frac{\delta N_i(t)}{\delta h_l(t')}$. We obtain:

$$\frac{\partial}{\partial t}\chi_{il}(t,t') = \chi_{il}(t,t') \left[\frac{d}{dt}\log N_i(t) - N_i(t)\right] + N_i(t) \left[\delta(t-t')\delta_{il} - \sum_j \alpha_{ij}\chi_{jl}(t,t')\right]$$

From this equation, and considering that $\chi_{il}(t < t') = 0$ from causality, it can be shown that $\chi_{il}(t', t') = N_i(t')\delta_{il}$. Therefore the diagonal response is of order one at short time, and we know from simulations and simpler cases that it is decaying when increasing t at fixed t', see for instance A.4. We expect that the response conveyed through correlation loop will be subleading compared to the diagonal response: $\chi_{ii} \gg \chi_{i \neq l}$. Therefore, its scaling can be inferred by considering only the contribution from the diagonal in its time evolution:

$$\frac{\partial}{\partial t}\chi_{i\neq l}(t,t') \sim -N_i(t)\ \alpha_{il}\ \chi_{ll}(t,t') \rightarrow \chi_{i\neq l} \sim \alpha_{il} \sim S^{-1/2}.$$

A.2.2. Cross correlation

If we had the Fluctuation-Dissipation theorem, we would directly get the scaling of the cross correlation $C_{i \neq l} \sim \chi_{i \neq l} \sim S^{-1/2}$. The theorem cannot be applied here, but we show that the scaling relation still holds here. We start again from the simplified rLV case:

$$\dot{N}_i = f(N_i) - N_i \sum_j \alpha_{ij} N_j$$

where $f(N_i) = N_i(1 - N_i)$, and remember that $\alpha_{ii} = 0$. We use perturbation theory in the interaction matrix $\alpha = ||\alpha||$. Denoting the solution of the equation N_i^0 when $\alpha = 0$ and introducing $N_i = N_i^0 + \alpha \delta N_i + \alpha^2 ...$, we obtain the first order correction for two different species $i \neq l$ through linear response:

$$\delta N_i(t) = -\int dt_1 \chi_{ii}(t, t_1) \sum_j \alpha_{ij} N_j^0(t_1)$$

$$\delta N_l(t') = -\int dt_2 \chi_{ll}(t', t_2) \sum_{j'} \alpha_{lj'} N^0_{j'}(t_2)$$

From this relation, we compute the connected averages:

$$\begin{aligned}\langle N_i(t) N_l(t')\rangle_{con} &= \langle \delta N_i(t) \delta N_l(t')\rangle_{con} \\ &= \int dt_1 dt_2 \chi_{ii}(t, t_1)\chi_{ll}(t', t_2) \textstyle\sum_{jj'} \alpha_{ij}\alpha_{lj'} \langle N^0_j(t_1) N^0_{j'}(t_2)\rangle_{con}\end{aligned}$$

We remark that the last term $\langle N^0_j(t_1) N^0_{j'}(t_2)\rangle_{con}$ corresponds to the connected correlation $C_{jj',con}(t_1, t_2)$. Then, from the same argument as the cross response function, we expect the cross correlation to be subleading compared to the diagonal one: $C_{ii,con} \gg C_{i\neq l,con}$. Therefore we only consider the diagonal contributions:

$$\begin{aligned}\langle \delta N_i(t) \delta N_l(t')\rangle_{con} &= \int dt_1 dt_2 \chi_{ii}(t, t_1)\chi_{ll}(t', t_2) \textstyle\sum_j \alpha_{ij}\alpha_{lj} C_{jj,con}(t_1, t_2) \\ &\sim \textstyle\sum_j \alpha_{ij}\alpha_{lj}\end{aligned}$$

The last term is a random variable with average μ^2/S, and variance σ^4/S, therefore we obtain $C_{i\neq l} \sim S^{-1/2}$.

A.3. Novikov's theorem and generating functional formalism

In this section, we detail how to derive equation 2.8 introduced in section 2.2.3.

We want to evaluate: $\chi(t, t') = \mathbb{E}[J'(N_t) \left.\frac{\delta N_t}{\delta h_{t'}}\right|_{h=0}]$. For simplicity, we do not take into account the averaging over initial conditions and thermal noises, since it does not change the proof. Also, without any loss of generality we will focus on parameters $\mu = \gamma = 0$. In this case the general DMFT equation 2.6 writes:

$$\dot{N}_t = R(N_t) + I(N_t)\,(\sigma\eta_t + h_t) + f(N_t)\xi_t \tag{A.1}$$

We introduce the distribution of the population trajectories:

$$\mathbb{P}\{N\} = \int D\eta\, \mathbb{P}\{\eta\}\, \mathbb{P}\{N|\eta, h\}$$

where the brackets denotes functional distributions. η is a Gaussian noise, so its probability measure is given up to a normalization factor by:

$$\mathbb{P}\{\eta\} \quad \alpha \quad \exp\left(-\frac{1}{2}\int dt\, ds\, \eta(t)\, C_\eta^{-1}(t, s)\, \eta(s)\right)$$

Furthermore, the $\mathbb{P}\{N|\eta\}$ distribution is deterministic and follows the DMFT dynamics from equation A.1. It is therefore a Dirac-distribution:

$$\mathbb{P}\{N|\eta, h\} = \prod_t \delta\left(\dot{N}_t - R(N_t) - I(N_t)\,(\sigma\eta_t + h_t) + f(N_t)\xi_t\right)$$

We now have everything to write down the average:

$$\begin{aligned}\chi(t,t') &= \mathbb{E}[J'(N_t)\ \tfrac{\delta N_t}{\delta h_{t'}}\Big|_{h=0}] \\ &= \tfrac{\delta}{\delta h_{t'}}\mathbb{E}[J(N_t)] \\ &= \tfrac{\delta}{\delta h_{t'}}\int DN\ D\eta\ \mathbb{P}\{\eta\}\ \mathbb{P}\{N|\eta,h\}\ J(N_t) \\ &= \int DN\ D\eta\ J(N_t)\ \mathbb{P}\{\eta\}\ \tfrac{\delta}{\delta h_{t'}}\ \mathbb{P}\{N|\eta,h\}\end{aligned}$$

When we write the average as an integration over the different paths, they become non-correlated variables. The correlation aspect is taken care of in the distributions. In addition, the distribution $\mathbb{P}\{N|\eta,h\}$ is symmetric in $h(t')$ and $\sigma\eta(t')$. We also perform an integration by part and find:

$$\begin{aligned}\chi(t,t') &= \int DN\ D\eta\ J(N_t)\ \mathbb{P}\{\eta\}\ \tfrac{\delta}{\sigma\delta\eta_{t'}}\ \mathbb{P}\{N|\eta,h\} \\ &= -\int DN\ D\eta\ J(N_t)\ \mathbb{P}\{N|\eta,h\}\ \tfrac{\delta}{\sigma\delta\eta_{t'}}\ \mathbb{P}\{\eta\} \\ &= \tfrac{1}{\sigma}\int DN\ D\eta\ J(N_t)\ \mathbb{P}\{N|\eta,h\}\ \left(\int ds\ C_\eta^{-1}(t',s)\ \eta(s)\right)\mathbb{P}\{\eta\} \\ &= \tfrac{1}{\sigma}\mathbb{E}[J(N_t)\left(\int ds\ C_\eta^{-1}(t',s)\ \eta(s)\right)]\end{aligned}$$

A.4. Temporal integration of the response function

In this section, we present an alternate way to compute the response function $\chi(t,t')$ that was briefly presented at the end of section 2.2.3.

We remind the DMFT equation 2.6 for a general class of models here, and we will consider each trajectory (denoted with i) simulated through this equation:

$$\dot{N}_i = R_i(N_i) + I_i(N_i)\left(\mu m + \sigma\eta_i + \gamma\sigma^2\frac{p(p-1)}{2}\int_0^t \chi(t,s)C(t,s)^{p-2}J(N_i(s))ds + h_i\right) + f_i(N_i)\xi_i \quad \text{(A.2)}$$

We now apply $\frac{\delta}{\delta h_i(t')}$. In this way, for each trajectory i, we can compute the response function $\chi_i(t,t') = \frac{\delta N_i(t)}{\delta h_i(t')}$ *via* temporal integration:

$$\begin{aligned}\frac{\partial}{\partial t}\chi_i(t,t') &= \chi_i(t,t')I_i'(N_i(t))\left\{\mu m(t) + \sigma\eta_i(t)\right\} \\ &+\chi_i(t,t')I_i'(N_i(t))\gamma\sigma^2\frac{p(p-1)}{2}\int_0^t \chi(t,s)C(t,s)^{p-2}J(N_i(s))ds \\ &+\chi_i(t,t')\left\{R_i'(N_i(t)) + f_i'(N_i(t))\xi_i(t)\right\} \\ &+I_i(N_i(t))\gamma\sigma^2\frac{p(p-1)}{2}\int_0^t \chi(t,s)C(t,s)^{p-2}J'(N_i(s))\chi_i(s,t')ds \\ &+I_i(N_i(t))\delta(t-t')\end{aligned}$$

We thus construct χ_i by temporal integration in t at fixed t', using the initial conditions $\chi_i(t,t') = 0$ for $t < t'$ from causality. Eventually, we get:

$$\chi(t,t') = \mathbb{E}[\chi_i(t,t')] \sim \frac{1}{\#_{traj}} \sum_{i=1}^{\#_{traj}} \chi_i(t,t')$$

A.5. Comparison of the different methods for the response function

Method	**Novikov**	**Temporal integration**
Formulation	$\frac{1}{\#_{traj}} \sum_{i=1}^{\#_{traj}} \frac{1}{\sigma} J(N_i(t)) \int ds C^{-1}_{t',s}\, \eta_i(s)$	$\frac{1}{\#_{traj}} \sum_{i=1}^{\#_{traj}} \chi_i(t,t')$
Needed $\#_{traj}$	Non-linearity dependent	Low
Complexity	$\mathcal{O}(\#_{traj}\ \#^3_{time})$	$\mathcal{O}(\#_{traj}\ \#^3_{time})$
Parallelizable	Fully	Not fully
Adequacy	Linear problems	Non linear, but short range

A.6. Closure in the Unique Equilibrium phase

In this section, we derive the Unique Equilibrium population distribution presented in section 2.3.1.

A.6.1. Linear stability of dead species

We consider the rLV system of equations 2.1. For each species, there are two possible equilibria 0 or $N_i^* = 1 - \sum_{j\neq i} \alpha_{ij} N_j$. In total, assuming the reduced matrix is almost always invertible (which is reasonable), this gives 2^S possible equilibria for the ecosystem, from which we would have to subtract the unreachable ones with negative populations. We can linearize the equation around both possible choices for one species:

$$\delta \dot{N}_i = \begin{cases} N_i^*\ \delta N_i & \text{if the fixed point is 0,} \\ -N_i^* \left(\delta N_i + \sum_{j\neq i} \alpha_{ij}\, \delta N_j \right) & \text{if the fixed point is } N_i^*. \end{cases}$$

From this, we see that if $N_i^* > 0$, the fixed point $N_i = 0$ is linearly unstable. Therefore the system will dynamically prevent this species i from going extinct ($N_i = 0$) in this case.

We now use the stationary cavity solution from equation 2.12. The species population distribution is a truncated Gaussian: $p(n) = \phi p_+(n) + (1-\phi)\delta(n)$ where $\phi = w_o(\Delta)$ is the fraction of surviving species, and p_+ is a Gaussian distribution whose parameters need to be determined. We inject this form in the closure system of equations 2.11.

We introduce the parameters $q = \mathbb{E}[N_\infty^2]$, $\Delta = (1 - \mu m_\infty)\sigma^{-1}\sqrt{q}^{-1}$ and the functions $w_k(\Delta) = \int_{-\infty}^{\Delta}(\Delta - s)^k Ds$ where Ds is the standard Gaussian measure, and eventually obtain:

$$\begin{cases} \dfrac{1 - \sigma\sqrt{q}\Delta}{\mu} = \dfrac{\sigma\sqrt{q}}{1 - \gamma\sigma^2\chi_{int}} w_1(\Delta) \\ \chi_{int} = \dfrac{1}{1 - \gamma\sigma^2\chi_{int}} w_0(\Delta) \\ 1 = \dfrac{\sigma^2}{(1 - \gamma\sigma^2\chi_{int})^2} w_2(\Delta) \end{cases} \tag{A.3}$$

These equations have also been obtained by several methods [48, 87]. It is worth noting that, with the implicit dependence $w_n = w_n(\Delta)$, the system can be rewritten as:

$$\begin{cases} \sigma^2 (w_2 + \gamma w_0)^2 = w_2 \\ 1 - \gamma\sigma^2\chi_{int} = \sigma^2 (w_2 + \gamma w_0) \\ \sigma\sqrt{q} = \dfrac{\sigma^2 (w_2 + \gamma w_0)}{\mu w_1 + \Delta\sigma^2 (w_2 + \gamma w_0)} \end{cases} \tag{A.4}$$

Under this form, the first line of system A.4 gives $\Delta(\sigma, \gamma)$. Afterwards, we directly have $\chi_{int}(\sigma, \gamma, \Delta)$ and $q(\mu, \sigma, \gamma, \Delta)$.

This system can be numerically solved in the variables (χ_{int}, Δ, q) as functions of the parameters (μ, σ, γ). All observables can then be computed from the solution. For example, the proportion of alive species $\phi = w_0(\Delta)$. On figure A.1, we detail some analysis on $\phi(\sigma, \gamma)$, and the response to an environmental press $\chi_{int}(\sigma, \gamma)$. See also [45, 48, 87] for an analysis of the system.

A.7. Linear stability analysis of the Unique Equilibrium solution

In this section, we perform the linear stability analysis sketched in section 2.3.2, and show how to recover the expansions in equations 2.13 and 2.14.

A.7.1. Context reminder

We recall the protocol [53]: starting in the Unique Equilibrium phase, we let the system reach an equilibrium point, then add some small field $h(t)$ which we will take as a Gaussian white noise with covariance $\overline{h(t)h(s)} = \sigma_h^2\delta(t - s)$, and see how the system responds in perturbation theory. In order to do so, we consider the DMFT equation 2.9, and linearize it around a stationary solution. We introduce the relative amplitudes $\delta N(t) = N(t) - N_\infty$, $\delta m(t) = m(t) - m_\infty$ and $\delta\eta(t) = \eta(t) - \eta_\infty$, respectively corresponding to the population, average population and interaction noise. These amplitudes are supposed to go to zero, at least in the Unique Equilibrium phase. The self-consistent relation also holds for these relative amplitudes. Indeed, if we denote $C_c(t, s)$ the connected correlator, it verifies:

$$C_c(t, s) = \mathbb{E}[\delta\eta(t)\delta\eta(s)] = \mathbb{E}[\delta N(t)\delta N(s)]$$

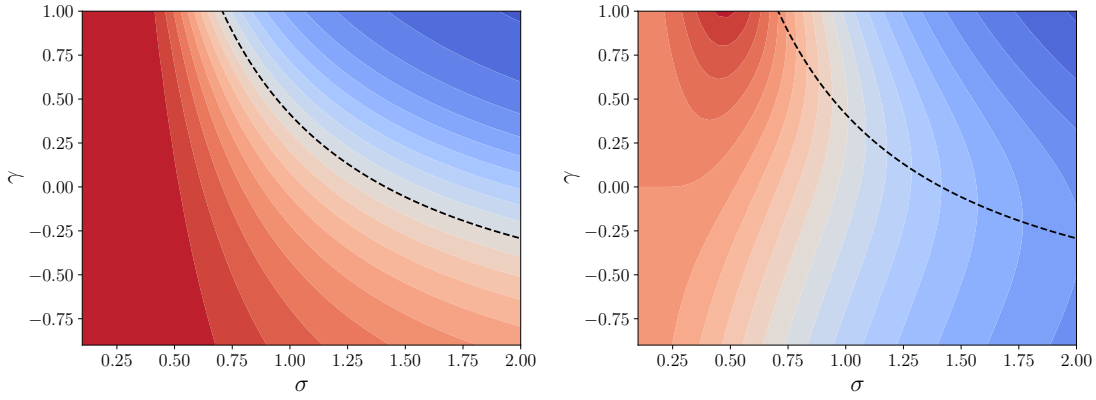

Figure A.1. Contour plots of the proportion of alive species ϕ and the integrated response kernel χ_{int}, with parameters σ and γ. Both of them are independent from μ. In dotted black line is the chaotic transition. In the Multiple Attractors phase (upper right side of the black line), the stationary cavity analysis is only approximate. The color scale starts at 1 in bright red, then each level corresponds to a 0.05 decrease. Left: Proportion of alive species $\phi(\sigma, \gamma)$. It can be shown that the chaotic transition corresponds to an isocline $\phi = 1/2$: half the species survive. Right: Integrated response kernel $\chi_{int}(\sigma, \gamma)$. It can be shown that the chaotic transition corresponds to a saddle line: $\partial_\gamma \chi_{int}|_{transition} = 0$.

From now on, $\mathbb{E}$ denotes the average over the static noise η_∞, the dynamical noise $\delta\eta$ and the perturbation field $h(t)$.

A.7.2. Linearization around the fixed point

The cases when $N_\infty = 0$ will just give a relaxing exponential and not influence relevantly the correlator nor the response function at large times. Therefore, we will focus on the cases $N_\infty > 0$, and write the corresponding average $\mathbb{E}_+$. The linearization reads:

$$\delta\dot{N} = N_\infty(-\delta N - \mu\delta m - \sigma\delta\eta + \gamma\sigma^2 \int_0^t ds\chi(t,s)\delta N(s) + h) \tag{A.5}$$

where the statistics of N_∞ is not perturbed by h at linear order. We focus on long times, and we assume time-translational invariance for the system: $C_c(t,s) = C(t-s)$ and $\chi(t,s) = \chi(t-s)$. This assumption has two consequences. First it transforms the integral term in equation A.5 into a convolution product. Secondly, denoting $\tilde{f}(\omega)$ the Fourier transform of f, the closure relations become:

$$\tilde{C}_{c,alive}(\omega) = \mathbb{E}_+\left[|\delta\tilde{N}(\omega)|^2\right] = \mathbb{E}_+\left[|\tilde{\delta\eta}(\omega)|^2\right] \qquad \tilde{\chi}_{alive}(\omega) = \mathbb{E}_+\left[\frac{\delta\tilde{N}(\omega)}{\delta\tilde{h}(\omega)}\right] \tag{A.6}$$

We are computing observables X for alive species only; the global average should be:

$$\mathbb{E}[X] = \phi\mathbb{E}_+[X] + (1-\phi)\mathbb{E}_{dead}[X]$$

where for relevant observables, the dead species contribution $\mathbb{E}_{dead}[X]$ vanishes in the large-S limit. ϕ denotes the fraction of alive species in the Unique Equilibrium around which we are linearizing. It can be computed from the Unique Equilibrium distribution detailed in appendix A.6.1.

A.7.3. Getting closed equations for the response and correlation

We consider the linearized cavity equation A.5 in Fourier space:

$$\delta\tilde{N} = (-\mu\,\tilde{\delta m} - \sigma\tilde{\delta\eta} + \tilde{h})\left(\frac{i\omega}{N_\infty} + 1 - \gamma\sigma^2\tilde{\chi}\right)^{-1} \tag{A.7}$$

Averaging directly equation A.7, and as the perturbation is of zero mean $\overline{h(t)} = 0$, we get that the perturbation of the mean population is $\delta m = 0$. At this point, we can directly apply the relation in equation A.6 for the response function and get the closed equation:

$$\tilde{\chi}(\omega) = \phi\mathbb{E}_+\left[\left(\frac{i\omega}{N_\infty} + 1 - \gamma\sigma^2\tilde{\chi}(\omega)\right)^{-1}\right] \tag{A.8}$$

Now we want to apply the relation in equation A.6 for the correlation. In order to do so, we take the modulus of equation A.7 (remember that $\delta m = 0$):

$$|\delta\tilde{N}|^2 = |\frac{i\omega}{N_\infty} + 1 - \gamma\sigma^2\tilde{\chi}|^{-2} \left\{ |\tilde{h}|^2 + \sigma^2|\tilde{\delta\eta}|^2 + 2\sigma Re(\tilde{h}\ \tilde{\delta\eta}^*) \right\} \tag{A.9}$$

where X^* denotes the complex conjugate of X, and $Re(X)$ its real part. At this stage, we want to take the average of the l.h.s., whereas there are three random variables on the r.h.s.: N_∞, $\tilde{h}$ and $\tilde{\delta\eta}$. They verify independence relations for different reasons:

- $\tilde{h}$ is independent of N_∞ by construction, because we added the perturbation once the steady-state had already been reached;
- $\delta\eta$ and N_∞ are uncorrelated since at linear order in equation A.7 we only need to consider the unperturbed statistics for N_∞;
- h and $\delta\eta$ are directly uncorrelated, as the noise is sampled from a given covariance C.

We can then average equation A.9;

$$\mathbb{E}_+\left[|\delta\tilde{N}|^2\right] = \mathbb{E}_+\left[|\frac{i\omega}{N_\infty} + 1 - \gamma\sigma^2\tilde{\chi}|^{-2}\right] \left\{ \mathbb{E}_+\left[|\tilde{h}|^2\right] + \sigma^2\mathbb{E}_+\left[|\tilde{\delta\eta}|^2\right] \right\}$$

Finally, we apply the closure relation in equation A.6 for the correlation, and rearrange the terms so that we obtain:

$$\tilde{C}_c(\omega) = \left(\left\{ \phi\mathbb{E}_+\left[|\frac{i\omega}{N_\infty} + 1 - \gamma\sigma^2\tilde{\chi}(\omega)|^{-2}\right] \right\}^{-1} - \sigma^2 \right)^{-1} \sigma_h^2 \tag{A.10}$$

A.7.4. Compute the small-ω expansions

As we are interested in the large time behavior of the system, we perform a small-ω expansion of the equations A.10 and A.8. This limit needs to be taken carefully because there is a competitive effect in the average between ω and $\frac{1}{N_\infty}$. We recall that:

$$\mathbb{E}_+\left[f(N_\infty)\right] = \int_0^\infty dn\ p_+(n)\ f(n)$$

where $p_+(n)$ is the truncated Gaussian computed from the Unique Equilibrium analysis in appendix A.6.1.

Let's first focus on the expansion for the response function in equation A.8. We first take the limit $\omega = 0$ to obtain:

$$\tilde{\chi}(0) = \frac{\phi}{1 - \gamma\sigma^2\tilde{\chi}(0)}$$

which consistently shows that the integral of the response function is the same as the response to a press perturbation from appendix A.6.1: $\tilde{\chi}(0) = \chi_{int}$. We introduce $\chi'(\omega) = \tilde{\chi}(\omega) - \tilde{\chi}(0)$, and develop equation A.8:

$$\chi'(\omega) = \left(1 - \gamma\sigma^2\tilde{\chi}(0)\right)^{-1} \int_0^\infty dn\; p_+(n) \frac{-i\omega + n\,\gamma\sigma^2\chi'}{i\omega + n\,(1 - \gamma\sigma^2\tilde{\chi}(\omega))}$$

We introduce the constant $B = 1 - \gamma\sigma^2\tilde{\chi}(0)$, and the denominator $d(n,\omega) = i\omega + n\,(B - \gamma\sigma^2\chi'(\omega))$. We now consider independently the two terms in the integral:

$$B\chi'(\omega) = -i\omega \int_0^\infty dn\; p_+(n)\; d(n,\omega)^{-1} + \gamma\sigma^2\chi'(\omega) \int_0^\infty dn\; p_+(n)\; n\; d(n,\omega)^{-1}$$

Because of the strong behavior of the Gaussian $p_+(n)$ at large n, we know that the integrals will be dominated by the behavior at small n. We focus on the first integral. We introduce a cut-off A, and the contribution from $-i\omega$ reads:

$$\int_0^\infty dn\; p_+(n)\; d(n,\omega)^{-1} \sim p_+(0) \int_0^A dn \frac{1}{i\omega + nB} + \int_A^\infty dn\; p_+(n)\; d(n,\omega)^{-1}$$

$$= -p_+(0)\, B^{-1} \log(\omega) + o_{\omega\to 0}(\log(\omega))$$

Now we can get the proper coefficient by considering also the second term. We eventually obtain the expansion:

$$\tilde{\chi}(\omega) = \frac{\phi}{B} + i\omega\log(\omega)\frac{p_+(0)}{B^2 - \gamma\sigma^2\phi}$$

The correlation function integral is slightly simpler. We denote this integral:

$$\begin{aligned} I_2(\omega) &= \phi\,\mathbb{E}_+\left[\left|\tfrac{i\omega}{N_\infty} + 1 - \gamma\sigma^2\tilde{\chi}(\omega)\right|^{-2}\right] \\ &= \int_0^\infty \tfrac{dn\; p_+(n)}{|i\omega/n + B - \gamma\sigma^2\tilde{\chi}'(\omega))|^2} \end{aligned}$$

The $\omega = 0$ contribution is directly $I_2(0) = \phi/B^2$. We remember that the dominant term in χ' is $iK\omega\,\log(\omega)$. We this in mind we expand:

$$I_2(\omega) - I(0) = -B^{-2} \int_0^\infty dn\; p_+(n)\; \frac{\omega^2\,(1/n - \gamma\sigma^2 K\log(\omega))^2}{B^2 + \omega^2\,(1/n - \gamma\sigma^2 K\log(\omega))^2}$$

We focus on small n such that $1/n \gg \log(\omega)$. It can be shown that the remaining integral is subleading ($\omega^2\log(\omega)^{-2}$).

$$I_2(\omega) - I(0) \sim -\omega\, B^{-2} \int_0^A dn\; p_+(n)\; \frac{\omega}{B^2\, n^2 + \omega^2}$$

$$\begin{aligned} I_2(\omega) - I(0) &\sim -\omega\, B^{-2} \textstyle\int_0^A dn\; p_+(n)\; \frac{\omega}{B^2\, n^2 + \omega^2} \\ &\sim -\omega\, B^{-3}\, \tfrac{\pi}{2}\, p_+(0) \end{aligned}$$

where we used the fact that the Lorentzian function converges to a Dirac: $\frac{1}{\pi}\frac{\omega}{\omega^2+n^2} \to_{\omega\to 0} \delta(n)$. The 1/2 factor comes from limiting the integral to positive values. Eventually, we obtain the expansion:

$$\tilde{C}_c(\omega)/\sigma_h^2 \quad = \quad \left(\frac{B^2}{\phi} - \sigma^2 + \omega\frac{B}{\phi^2}\frac{\pi}{2}p_+(0)\right)^{-1}$$

In order to get the cleaner expressions in equations 2.13 and 2.14, we simply use the relation $B = \phi/\chi_{int}$ from the second line of the system of equations A.3.

A.8. Details of the numerical strategy for the DMFT solver

In this section, we provide more details about the numerical strategy presented in section 2.2.3: how to sample the noise, integrate the trajectories, iterate the observables. Eventually, we show an example of convergence, and we make explicit what initialization was used.

We made a gitHub repository with the Python programs we wrote [74]. There is also a runMe.py file which can be directly run in order to produce DMFT solutions and figures such as 2.2 or 2.4. In this section, we write down in details the methodology of the algorithm.

We discretize time in equal units of dt such that $t_k = k\ dt$. We also fix the final time we're interested in as $t_{max} = \#_{time}\ dt$. We usually take $dt = 0.1$. The two-dimensional functions then become matrices, and the one-dimensional ones are vectors:

$$m_k = m(t_k) \qquad C_{kl} = C(t_k, t_l) \qquad \chi_{kl} = \chi(t_k, t_l)$$

We will now describe how one iteration of the algorithm is computed numerically. We start from the observables m_k, C_{kl} and χ_{kl}, and we want to compute the new ones m_k^{new}, C_{kl}^{new} and χ_{kl}^{new} after one iteration.

A.8.1. Sampling of the noise

We will simulate $\#_{traj}$ trajectories that we will refer to as "species". Remember that they are independent in DMFT setting. We will then detail the procedure for one species only. For each species, we need a given realization of the Gaussian noise at all times $\{\eta_k\}_{k=1,\dots,\#_{time}} = \{\eta(t = t_k)\}_{k=1,\dots,\#_{time}}$, sampled according to the correlator C. Given the discretization, we sample $\{\eta_k\}_{k=1,\dots,\#_{time}}$ as a multivariate Gaussian vector with covariance C_{kl}. One way to do this is to diagonalize the matrix C_{kl}, then in the proper basis all components are independent.

A.8.2. Numerical integration of the trajectory

For the trajectory of the species, the integration of the differential equation is done with a basic Euler scheme. The Lotka-Volterra system is better simulated in log space. Therefore, if we denote $N_k = N(t_k)$, we implement the scheme:

$$\log N_{k+1} = \log N_k + dt\ \mathcal{F}(N_k|m,\eta,\chi) + dt\ \mathcal{G}(N_k|\lambda)$$

with:

$$\begin{cases} \mathcal{F}(N_k|m,\eta,\chi) = 1 - N_k - \mu m_k - \sigma\eta_k + \gamma\sigma^2 dt \sum_{l=0}^{k} \chi_{kl}\ N_l \\ \mathcal{G}(N_k|\lambda) = \begin{cases} 0 & \text{for } \lambda = 0 \\ \exp\left[\log(\lambda) - \log N_k\right] & \text{for } \lambda > 0 \end{cases} \end{cases}$$

The last λ-dependent scheme is for numerical stability whenever there is immigration in the system. Using this scheme, we compute the trajectory $\{N_k\}_{k=1..\#_{time}}$.

A.8.3. Computing the new observables from the trajectories

We sample and integrate the trajectories for $\#_{traj}$ species following the previous procedure. We end up with an array of trajectories:

$$\left\{N_k^i\right\}_{k=1,\ldots,\#_{time}}^{i=1,\ldots,\#_{traj}}$$

From them we can compute the new observables m and C by direct averages:

$$\begin{cases} m_k^{new} = \dfrac{1}{\#_{traj}} \displaystyle\sum_{i=1}^{\#_{traj}} N_k^i \\ C_{kl}^{new} = \dfrac{1}{\#_{traj}} \displaystyle\sum_{i=1}^{\#_{traj}} N_k^i N_l^i \end{cases}$$

As stated in appendix A.5 and section 2.2.3, the response function χ is more difficult to compute. The two methods can be used:

$$\chi_{kl}^{new} = \begin{cases} \frac{1}{\#_{traj}} \sum_{i=1}^{\#_{traj}} \frac{1}{\sigma} N_k^i\ dt\ \sum_{l'=1}^{\#_{time}} C_{ll'}^{-1} \eta_{l'}^i & \text{for Novikov} \\ \frac{1}{\#_{traj}} \sum_{i=1}^{\#_{traj}} \chi_{kl}^i & \text{for temporal integration} \end{cases}$$

In the last line of the equation χ_{kl}^i is integrated for each species according to appendix A.4. Eventually, we will start a new iteration of the algorithm, with a soft update:

$$\begin{cases} m^{updated} = (1-a)\ m + a\ m^{new} \\ C^{updated} = (1-a)\ C + a\ C^{new} \\ \chi^{updated} = (1-a)\ \chi + a\ \chi^{new} \end{cases}$$

After some trials, a reinjection parameter $a = 0.3$ is a good value.

A.8.4. Convergence and the iterative strategy

After one iteration of the algorithm, the new results always present some statistical noise, due to the fact that we average over a finite number $\#_{traj}$ of trajectories. To get a good convergence, we increase the number of trajectories as the iteration goes on. The first iterations are performed with few trajectories; they correspond to rough steps in the configurational space. As the observables get closer to the real solution, we refine the iterations by using more trajectories.

All results are shown with the following scheme: 30 iterations with 10^3 trajectories each, then 10 iterations with 10^4 each, and 20 iterations with 10^5 each. The convergence is considered to be reached when the iteration step becomes lower than a given threshold. More precisely, labeling C^i_{kl} the correlator after iteration i, we have reached convergence when:

$$\|C^{i+1} - C^i\|_F < 10^{-9}$$

where $\|M\|_F = \#^{-2}_{time} \sum_{kl} M^2_{kls}$ is the rescaled Frobenius norm. We use the threshold on the correlator, because we found that it is the most difficult observable to converge. A mixed criterion in all three observables would work as well. On figure A.2 we show the convergence in terms of iteration steps.

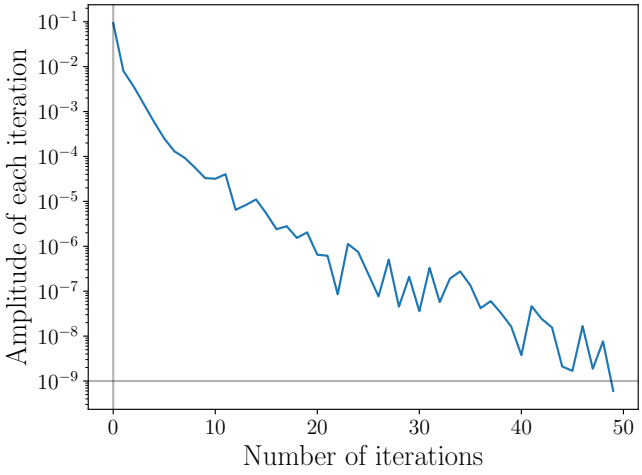

Figure A.2. Amplitude of each iteration step as a function of the number of iterations. The amplitude is computed as the matrix norm of the difference in the correlator before and after iteration. It is plotted on a semi-log scale. This computation was done with parameters $(\mu, \sigma, \gamma, \lambda) = (10, 4, -1, 10^{-4})$ in the Unique Equilibrium phase.

A.8.5. Initialization

At the beginning of the algorithm, we need to give as input initial guesses for the correlator matrix $C(t, s)$, the average abundance vector $m(t)$, and the response matrix

$\chi(t,s)$. The results are found to be independent on the initial guesses. We consider for example random initial guesses: a random vector for m, diagonal or random positive symmetric matrices for C, and lower triangular random matrices for χ (since χ is a causal function).

A.9. Some examples of numerical solutions

In this section, we show some more examples of numerical solutions for the correlator and the response function.

On figure A.3, we show an example of a chaotic correlator $C(t,t')$. It is to be put in contrast with figure 2.4, which depicted the Unique Equilibrium plateau type correlator. On A.4, we show an example of a response numerical solution $\chi(t,t')$. The behavior of χ does not seem to change drastically between Unique Equilibrium phase and the Multiple Attractors phase.

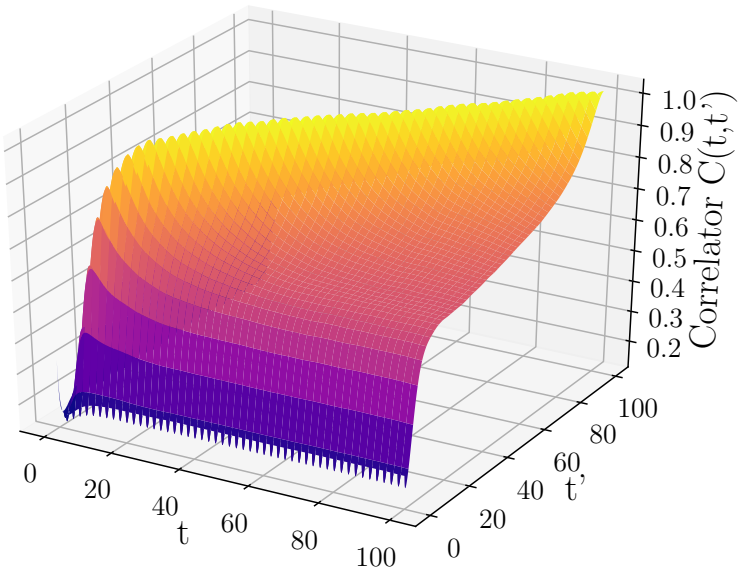

Figure A.3. Numerical correlator, for rLV DMFT with parameters $(\mu,\sigma,\gamma,\lambda) = (4,2,0,10^{-4})$ in the Multiple Attractors phase. The parameters of the program are the same as in figure 2.2. Contrary to the Unique Equilibrium case in figure 2.4, there is no convergence towards a plateau. However, after a transient, the systems becomes TTI.

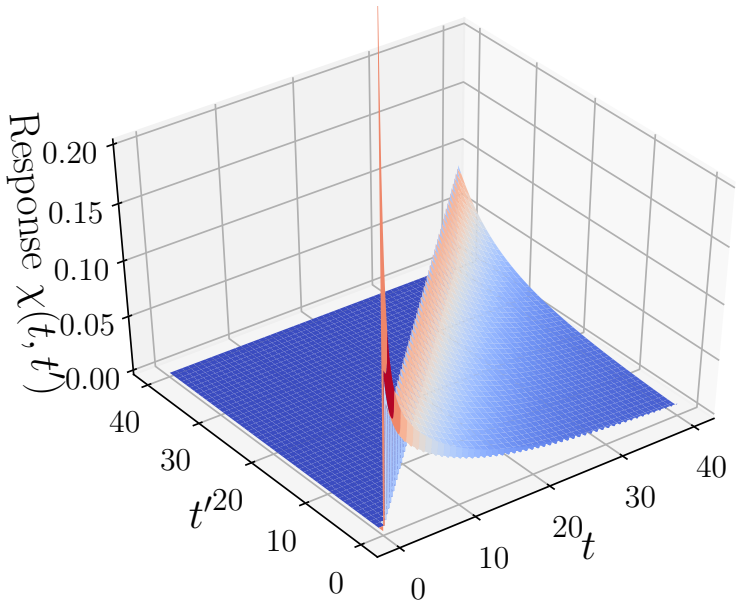

Figure A.4. Numerical response function, for rLV DMFT with parameters $(\mu, \sigma, \gamma, \lambda) = (10, 1/2, 1/2, 10^{-4})$ below the onset of chaos. The parameters of the program are the same as in figure 2.2. From causality, $\chi(t, t') = 0$ for $t < t'$. It can be shown analytically that $\chi(t, t) = m(t)$. Then, for $t > t'$, there is a relaxation towards 0, as the perturbation is absorbed.

B. Analytical closure of DMFT (chapter 4)

B.1. Stationary distribution with the real potential

B.1.1. Stationary distribution conditioned on N^*

Here we assume that the dynamical noise is white: $C_\xi(t,t') = 2T\delta(t-t')$. The first consequence is that we know:

$$\mathbb{P}_{t=\infty}(x|N^*) = Z^{-1}\exp(-\beta V(x))$$

$$\Rightarrow \qquad \mathbb{P}_{t=\infty}(N|N^*) = \frac{\beta^{\beta N^*}}{\Gamma(\beta N^*)} N^{-1+\beta N^*} e^{-\beta N}\, \mathbf{1}_{N^*>0} + \delta(N)\mathbb{P}(N^*<0)$$

which is a usual Gamma distribution. We use rescaled variables for convenience $n = \beta N$ and $n^* = \beta N^*$. Then:

$$\mathbb{P}^{alive}_{t=\infty}(n|n^*) = \Gamma(n^*)^{-1}\, n^{n^*-1}\, e^{-n}$$

from which it is easy to compute (using $\Gamma(x+1) = x\,\Gamma(x)$):

$$\langle n^m \rangle_{|n^*} = n^*(n^*+1)...(n^*+m-1)$$

It yields in particular:

$$\langle N \rangle_{|N^*} = N^* \qquad\qquad \langle N^2 \rangle_{|N^*} = (N^*)^2 + N^*/\beta$$

B.1.2. Consequent stationary distribution on N

We need to integrate against the distribution $P(N^*)$, which we know is a truncated Gaussian. In particular, $P(N^*) = \mathcal{O}_{N^*\to 0}(1)$.

$$P_{alive}(n) = \int_0^\infty dn^*\, P(n|n^*)P(n^*) = e^{-n}/n \int_0^\infty dn^*\, \Gamma(n^*)^{-1}\, e^{n^*\log(n)} P(n^*)$$

For small abundances $n \ll 1$, the integral is dominated by $n^* \ll 1$. There, using again $\Gamma(x+1) = x\,\Gamma(x)$ (and $\Gamma(1)=1$), we know that $\Gamma(x)^{-1} = x + o_{x\to 0}(x)$. Therefore, the integral is roughly:

$$\int_0^A dx\, x\, e^{x\log(n)} P(n^*\to 0) \simeq P(n^*\to 0)\log(n)^{-2}$$

Eventually:

$$P_{alive}(0 < N \ll 1) \simeq \frac{1}{n\,\log(n)^2}$$

which is barely integrable $\int_\epsilon^A dx\, x^{-1}\,\log(x)^{-2} \simeq \log(\epsilon)^{-1} \to_{\epsilon\to 0} 0$.

B.1.3. Relax the white noise assumption

Here we show that we can relax the white noise assumption into 'integrable correlation C' only, for the small values $x_f \ll -1$. We denote $2T = \int_{-\infty}^{\infty} dt\, C(t)$. Then, we introduce the large deviation formalism:

$$\begin{aligned} P_{N^*}(x_f, t_f | x_0, t_0) &= \int Dx\, D\xi\, P(\xi)\, \prod_t \delta(\dot{x}_t + V(x_t) - \xi_t) \\ &= \int Dx\, D\hat{x}\, D\xi\, P(\xi)\, \exp\left(\int_{t_0}^{t_f} dt\, \hat{x}_t(\dot{x}_t + V'(x_t) - \xi_t)\right) \\ &= \int Dx\, D\hat{x}\, \exp\left(S\{x, \hat{x}\}\right) \end{aligned}$$

with

$$S\{x,\hat{x}\} = \int_{t_0}^{t_f} dt\, \hat{x}_t(\dot{x}_t + V'(x_t)) + 1/2 \int_{t_0}^{t_f} dt\, dt'\, \hat{x}_t\, C(t-t')\, \hat{x}_{t'}$$

Now we assume that the distribution of path is dominated by a saddle point. Maybe it can be justified because $|x_f| \gg 1$. The saddle point equation $0 = \frac{\delta S}{\delta x} = \frac{\delta S}{\delta \hat{x}}$ yields:

$$\begin{cases} \dot{\hat{x}}_t &= \hat{x}_t\, V''(x_t) \\ \dot{x}_t &= -V'(x_t) - \int_{t_0}^{t_f} dt'\, C(t-t')\, \hat{x}_{t'} \end{cases} \tag{B.1}$$

Now, as $|x_f| \gg 1$, we can say that for a long portion of the trajectory near its end, $\dot{\hat{x}}_t \simeq \hat{x}_t\, e^{x_f} \simeq 0$. We will therefore consider $\hat{x}_t$ roughly constant. More precisely, we use the adiabatic approximation: the dynamics of $\hat{x}_t$ is slower than the one of C. In the second line, we then take it out of the integral. What remains is twice the temperature, if we consider $t_0 \ll t \ll t_f$:

$$\dot{x}_t \simeq -V'(x_t) - 2T\,\hat{x}_t \qquad \Rightarrow \qquad \hat{x}_t = -\frac{\dot{x}_t + V'(x_t)}{2T}$$

Now we show that the solution $\dot{x}_t = V'(x_t)$ satisfies the system:

$$\dot{\hat{x}}_t = -\frac{1}{T}\dot{x}_t V''(x_t) = \hat{x}_t\, V''(x_t)$$

(The trick is to use alternatively sometimes $\hat{x}_t = -T^{-1}V'(x_t)$ and $\hat{x}_t = -T^{-1}\dot{x}_t$.)

We inject the saddle point path into the action:

$$\begin{aligned} S\{x_{SP}, \hat{x}_{SP}\} &= [-2V(x_t)/T]_{t_0}^{t_f} + 1/2 \int_{t_0}^{t_f} dt\, \hat{x}_t\, \hat{x}_t\, 2T \\ &= [V(x_t)/T]_{t_0}^{t_f}\,(-2 + 2/2) \\ &\simeq -\beta V(x_f) \end{aligned} \tag{B.2}$$

And eventually:

$$P_{N^*}(x_f, t_f | x_0, t_0) \simeq \exp -\beta V(x_f)$$

B.2. Dynamics with the harmonic potential

In this section, we'll use the variable $u = x - x_{min}$. The Langevin equation for the harmonic approximation is:

$$\dot{u} = -N^* u + \xi \qquad \Rightarrow \qquad \overline{e^{u_t}} = \exp\left(u_0 e^{-N^* t} + \frac{T}{2N^*}(1 - e^{-2N^* t})\right)$$

Then, we directly obtain by Gaussian (stationary distribution) integration:

$$\mathbb{E}_{ICTTI}[\overline{e^{x_t}}] = N^* \, e^{\frac{T}{2N^*}} \qquad \mathbb{E}_{ICTTI}[\overline{e^{x_t + x_0}}] = (N^*)^2 \, \exp\left(\frac{T}{N^*}(1 + e^{-N^* t})\right)$$

We see that it does satisfy $\overline{e^{x_t}} \sim N^*$, for $T \ll N^*$ which is the validity domain of the harmonic approximation. We can close the equation on m_{N^*} and q_{N^*}. Switching the $\mathbb{E}_z$ and $\lim_{t\to\infty}$, we obtain:

$$m_{N^*} = N^* e^{\frac{T}{2N^*}} \qquad q_{N^*} = (N^*)^2 e^{\frac{T}{N^*}}$$

This is diverging for $N^* \ll T$. In this regime, it is not a good approximation, as expected. However it can give some relevant insights for species with $N^* \gg T$. We also see that $q_{N^*} = m_{N^*}^2$ logically holds, because of ergodicity. Using equations 4.6 and 4.8, we can compute the self-consistent temperature for a given bias:

$$\boxed{T_{N^*}^{harm}(T)/\sigma^2 = N^* \exp(T/N^*) \int_0^{T/N^*} \frac{e^x - 1}{x} dx} \tag{B.3}$$

The self-consistent temperature is logically an increasing function of T/N^*, because the log variable can explore a larger space. The small temperature expansion can be written:

$$T_{N^*}^{harm}(T)/\sigma^2 = T\left(1 + \frac{5}{4}\frac{T}{N^*} + o_{T\ll N^*}\left(\frac{T}{N^*}\right)\right) \tag{B.4}$$

B.3. Dynamics with the box potential

B.3.1. Solve the diffusion in a box

We'll consider the Fokker-Planck equation, which in this case is simply the diffusion equation for $P(x,t)$, inside a box of length L, with right wall in 0. We can solve it exactly.

$$\partial_t P = D\,\partial_x^2 P \qquad | \qquad P(x, t=0) = \delta(x - x_0) \quad \& \quad \partial_x P(\{-L, 0\}, t) = 0$$

Thanks to the hard boundary, we can construct by reflection a periodicity of $2L$, and P is now even in x. Therefore we analyze the system on the Fourier basis, with frequency $\omega = 2\pi/(2L)$:

$$P(x,t) = \sum_{n=0}^{\infty} a_n(t)\,\cos(n\omega x)$$

For now, we write the Fourier series in complex form $P(x,t) = \sum_{n=-\infty}^{\infty} c_n(t)\,e^{in\omega x}$. As this is a free family, this yields the differential equation for all Fourier coefficients: $\forall n, c_n'(t) = (in\omega)^2 c_n(t)$. We then determine $c_n(0)$ with the symmetrized IC: $\forall n, c_n(0) = (2L)^{-1}(e^{in\omega x_0} + e^{-in\omega x_0})$. Eventually we obtain:

$$P(x,t) = \frac{1}{L} + \frac{2}{L}\sum_{n=1}^{\infty} e^{-D(n\omega)^2 t}\cos(n\omega x_0)\,\cos(n\omega x) \tag{B.5}$$

This equation is properly normalized. $P(x,t)$ can also be computed by the image method technique, yielding:

$$P(x,t) = \frac{1}{4\pi D t}\sum_{m=-\infty}^{+\infty} e^{-\frac{(x-2mL-x_0)^2}{4Dt}} + e^{-\frac{(x-2mL+x_0)^2}{4Dt}}$$

And this expression can be recovered from eq (B.5), by writing $e^{-D(n\omega)^2 t}$ as a Gaussian integral, switching sum and integral, and computing the poles of the expression.

Now, we want to compute the closure relation in temperature. For this we need $\overline{e^{x_t}}$, for which we will need the basic integrals:

$$\int_{-L}^{0} dx\, e^x \cos(n\omega x) = \frac{1 - e^{-L}(-1)^n}{1 + (n\omega)^2}$$

From them, we compute directly:

$$\begin{aligned} L\,\overline{e^{x_t}} &= \left(1 - e^{-L}\right) + 2\sum_{n=1}^{\infty} e^{-D(n\omega)^2 t}\cos(n\omega x_0)\,\tfrac{1-e^{-L}(-1)^n}{1+(n\omega)^2} \\ &= \left(1 + 2\sum_{n=1}^{\infty} e^{-D(n\omega)^2 t}\,\tfrac{\cos(n\omega x_0)}{1+(n\omega)^2}\right)\left(1 + \mathcal{O}_{L\to\infty}(e^{-L})\right) \end{aligned}$$

Then we average against the initial distribution, sampling x_0 from the stationary distribution: the uniform one.

$$L^2\,\mathbb{E}_{ICTTI}[\overline{e^{x_t + x_0}}] = \left(1 - e^{-L}\right)^2 + 2\sum_{n=1}^{\infty} e^{-D(n\omega)^2 t}\left(\tfrac{1-e^{-L}(-1)^n}{1+(n\omega)^2}\right)^2 \tag{B.6}$$

$$= \left(1 + 2\sum_{n=1}^{\infty}\tfrac{e^{-D(n\omega)^2 t}}{(1+(n\omega)^2)^2}\right)\left(1 + \mathcal{O}_{L\to\infty}(e^{-L})\right) \tag{B.7}$$

B.3.2. Closure in temperature

In order to apply the last result in equation B.6 to our problem, we need to remember that in our case, the right limit of the box is in $x_{right} \neq 0$. Therefore:

$$L^2\,\mathbb{E}_{ICTTI}[\overline{e^{x_t+x_0}}] = e^{2x_{right}}\left(1+2\sum_{n=1}^{\infty}\frac{e^{-D(n\omega)^2 t}}{\left(1+(n\omega)^2\right)^2}\right)\left(1+\mathcal{O}_{L\to\infty}(e^{-L})\right) \tag{B.8}$$

We integrate equation (B.8) in time, between $t=0$ and $+\infty$:

$$\begin{aligned}\frac{D\,L^2}{2}\,e^{-2x_{right}}\,T_L &= D^2\left(\textstyle\sum_{n=1}^{\infty}\frac{1}{(n\omega)^2(1+(n\omega)^2)^2}\right)\left(1+\mathcal{O}_{L\to\infty}(e^{-L})\right)\\ &= D^2\left(\tfrac{1}{6}\,L^2-\tfrac{3}{4}L\,\coth(L)+1-\tfrac{1}{4}\left(\tfrac{L}{\sinh(L)}\right)^2\right)\left(1+\mathcal{O}_{L\to\infty}(e^{-L})\right)\end{aligned}$$

Eventually:

$$D\,T_L\,e^{-2x_{right}} = 1/3-(3/2)\,L^{-1}+2\,L^{-2}+\mathcal{O}_{L\to\infty}(e^{-L}) \tag{B.9}$$

B.4. Dynamics with the triangular potential

B.4.1. Solve the drifted diffusion

We'll consider the Fokker-Planck equation, which in this case is simply the drifted diffusion equation for $P(x,t)$, for $x<0$, and with a right wall in $x=0$. We can solve it exactly. The differential equation reads:

$$\partial_t P = -vP + D\,\partial_x^2 P \qquad | \qquad P(x,t=0)=\delta(x-x_0) \tag{B.10}$$

We only consider positive bias $v>0$, that pushes back the particle against the wall. Otherwise the particle escapes to $-\infty$. The no-flux boundary condition imposes:

$$-\,v\,P(x=0,t)+D\,\partial_x P(x=0,t)=0 \tag{B.11}$$

We introduce the Laplace transform in time $c(x,s)=\mathcal{L}\{P(x,t)\}$. Then the Fokker-Planck equation (B.10) becomes:

$$s\,c-\delta(x-x_0) = -v\,c+D\,\partial_x^2 c \tag{B.12}$$

We denote the rates:

$$r_\pm = \frac{v}{2D}\left(1\pm\sqrt{1+\frac{4D}{v^2}s}\right) \tag{B.13}$$

Then, equation (B.12) can be solved above and below x_0:

$$\begin{cases} c_<(x,s) = Be^{r_+ x} + B_\infty e^{r_- x} \\ c_>(x,s) = A\left(e^{r_+ x} + Re^{r_- x}\right) \end{cases} \tag{B.14}$$

where A, B, B_∞ and R are constants that depend on s and x_0. To determine them, we use:

- the fact that the probability should decay at $x == \infty$:

$$B_\infty = 0$$

- the continuity of c in x_0:

$$Be^{r_+ x_0} = A\left(e^{r_+ x_0} + Re^{r_- x_0}\right)$$

- the no flux boundary condition at $x = 0$:

$$-v(1+R) + D(r_+ + Rr_-) = 0$$

- the junction equation in x_0, obtained by integrating equation (B.12) between $x_0 \pm \epsilon$:

$$-D^{-1} = A(r_+ e^{r_+ x_0} + Rr_- e^{r_- x_0}) - Br_+ e^{r_+ x_0}$$

This determines all constants. The quantity that we are interested in is $\langle e^{x_t} \rangle$, where the average is over the white noise, at given x_0. Therefore, we introduce another Laplace transform: $g(s) = \mathcal{L}\{\langle e^{x_t} \rangle\}$. After some computation, we obtain:

$$g(s) = \frac{D^{-1}}{(1+r_+)(1+r_-)} \left(-e^{x_0} - \frac{e^{-r_- x_0}}{r_-} \right) \tag{B.15}$$

From this, we can already obtain the interesting quantity:

$$\lim_{t\to\infty} \langle e^{x_t} \rangle = \lim_{s\to 0} s g(s) = \frac{v}{D+v} \tag{B.16}$$

In order to obtain the self-consistent temperature, we will need:

$$\mathbb{E}_{x_0} \left[e^{x_0} \int_0^{+\infty} dt \, \left(\langle e^{x_t} \rangle - \lim_{t\to\infty} \langle e^{x_t} \rangle \right) \right] \tag{B.17}$$

We first compute the integral part, using Laplace properties:

$$\lim_{s\to 0} \left[g(s) - s^{-1} \lim_{s'\to 0} s' g(s') \right] = \frac{1}{D+v} \left[-e^{x_0} + x_0 + \frac{D}{v} + \frac{v}{D+v} \right] \tag{B.18}$$

Eventually, we average against the stationary distribution for x_0, which we recall here:

$$\mathbb{P}(x_0) = \frac{v}{D} e^{\frac{v}{D} x_0} \, \mathbf{1}\{x_0 \leq 0\} \tag{B.19}$$

We then obtain for equation (B.17):

$$\frac{2}{D} \frac{1}{(1+\frac{v}{D})^3 (2+\frac{v}{D})} \tag{B.20}$$

B.4.2. Back to the ecological problem

In the previous section, we solve the drifted diffusion with a hard-wall in $x = 0$, a bias v, and temperature D. In the ecological set-up, the bias is N^*, the temperature is denotes T, and the hard-wall is located at $x_{right} = \log T$, as for the box potential. We obtain the average abundance at given bias N^* using equation (B.16):

$$m_{N^*} = N^* \frac{T}{T + N^*} < N^* \tag{B.21}$$

This is an underestimation as for the box potential, and it becomes exact in the expected limit $T \gg N^*$. Eventually, using equations (B.17) and (B.20), we obtain the self-consistent triangular temperature:

$$T^{tri}_{N^*}(T)/\sigma^2 = \frac{2T}{(1 + \frac{N^*}{T})^3(2 + \frac{N^*}{T})} \tag{B.22}$$

C. A tentative toy model for aging (chapter 4)

We know from simulations that the chaotic state is unstable, and the system displays aging dynamics. Therefore, in this section we propose a model to analyze the aging behavior that slows down the chaotic dynamics. We do not have results for this model yet, this is also ongoing work.

We start again from the DMFT equation with $\gamma = 0$:

$$\dot{N} = N\,(1 - \mu\, m_t - N + \sigma\, \eta_t)$$

and the closure writes:

$$\begin{cases} m(t) &= \mathbb{E}[N(t)] \\ C_\eta(t,s) &= \mathbb{E}[N(t)N(s)] \end{cases}$$

We will now simplify the dynamics step-by-step, in order to obtain a tractable model. Based on numerical simulations, we will assume that some one-time properties are constant in time: the average population $m_t = m$, the equal-time correlation $C_\eta(t,t) = q_d$, and the left-over correlation $C_\eta(+\infty, t) = q_0$. What we are interested in is the timescale $\tau(t_w)$ it takes to decorrelate populations starting from a given age t_w (for "waiting time") of the system. From simulations, it seems this timescale behaves as $\tau(t_w) \sim t_w$, which is consistent with stationary dynamics in log time. We would like to catch the aging scaling by a simple self-consistent argument.

We perform the usual decomposition of the dynamical noise into two independent parts $\sigma\eta_t = z + \xi_t$, such that $\langle z^2 \rangle = \sigma^2 q_0$, and $C_\xi(t, t_w) = C(\frac{t-t_w}{\tau(t_w)})$ with $C(0) = \sigma^2(q_d - q_0)$, and $C(\infty) = 0$. Reformulating, we have the following simple dynamics:

$$\dot{N} = N\,(N^* - N + \xi_t)$$

where $N^* = 1 - \mu m + z$ is a static Gaussian, ξ_t is a Gaussian noise. The full problem would be to close equations on the moments of the Gaussians, and the timescale of the noise. This is too difficult. We will assume that the moments are given (from simulations for example), and try to catch the timescale.

As the noise is colored (so everything is continuous), it makes no difference to consider Ito or Stratonovich discretization. We can change to the natural log variables:

$$\dot{x} = N^* - e^x + \xi_t = -V'(x) + \xi_t$$

with $V(x) = -N^* x + e^x$. This potential is strongly restraining on the right side, the left side depends on the species. We can already forget about species that have $N^* < -1$, because they will never contribute to the dynamics. We add the following assumptions:

- For a species to contribute to the correlation $C_\xi(t, t_w) \sim \langle e^{l_t + l_{t_w}} \rangle$, it needs to have its log-population around 0 at both times. Mathematically:

$$C_\xi(t, t_w) \sim \langle \mathbf{1}[l_t = 0,\, l_{t_w} = 0] \rangle$$

- The time-evolution for low-abundance species is linear by parts in log-population: their dynamics can be approximated by linear dives and blooms at various depths.

Until now, all hypothesis are well-funded. Starting here, we make further wrong assumptions to try to close the problem:

- We assume that the dynamical noise ξ_t is constant by parts $\tau(t)$. More precisely, we will discretize time t_n, such that $t_{n+1} - t_n = \tau_n = \tau(t_n)$ is the decorrelation time. The time index will be n, the species index i.

- We feel more comfortable working with positive values, so we introduce $x = -l$. We further simplify the dynamics during one timestep. During the decorrelation time, every species feels a constant random growth-rate $g_{in} = N_i^* + \xi_{in}$. We assume that the non-linearity in the potential can be treated as follows: in log-space, all species perform a linear jump of length g_{in} and with sticky boundary conditions at 0.

$$x_{i,n+1} = \max\left(x_{i,n} - g_{in}\,\tau_n,\, 0\right)$$

  We will denote the jumps $j_{in} = -g_{in}\,\tau_n$ in the following. Let's recall $j_{in} = -(N_i^* + \xi_{in})\,\tau_n$.

It still seems too difficult to obtain the series $\tau_n(m, q_d, q_0)$. We will focus on a more specific aspect of the problem, which we find crucial to understand the aging phenomenon. We consider a given species, with bias N^*. For it to contribute to the correlation decay, we assume that it starts at $\mathcal{O}(1)$ abundance, so $x_0 = 0$. We consider the correlation length of the noise constant τ. We perform the above dynamics for the species:

$$x_{n+1} = \max\left(x_n + j_n,\, 0\right)$$

where $j_n = -(N^* + \xi_n)\,\tau$ is a static Gaussian variable, with given mean $-N^*$ and variance $\sigma^2(q_0 + q_D)$. Then, we consider that this species will contribute to the correlation at time n *if and only if* $x_n = 0$. This amounts to the contribution for a given bias N^*:

$$C_n^{N^*} = \mathbb{P}_{N^*}(x_n = 0 \,|\, x_0 = 0)\mathbb{P}_{N^*}(x_0 = 0) \tag{C.1}$$

Eventually, the full correlation is recovered by $C_n = \mathbb{E}_{N^*}[C_n^{N^*}]$. This correlation should be decaying with n, and reaching a constant left-over correlation plateau C_∞. From this decorrelation, we will be able to infer a timescale $\tau_{decor}(\tau, m, q_D, q_0)$.

The first *rhs* term of equation (C.1) roughly amounts to computing the distribution of the first return time in 0 of a discrete-time random walk with a sticky boundary condition. Actually, this weird boundary condition can be taken care of by also discretizing space with step a, using a smaller time step $\tau/2$, and enforcing a hard-wall reflection in $x = -a$.

If we denote $\phi_n = \mathbb{P}_{N^*}(x_n = 0 \,|\, x_0 = 0)$, and $r(t)$ the first return time distribution in 0, we can condition on this return time:

$$\phi_t = \sum_{t'>t} r(t') \,.\, 0 + \sum_{t' \leq t} r(t')\phi_{t'} = \sum_{t' \leq t} r(t')\phi_{t'} \tag{C.2}$$

There are probably some issues of taking the first step to the right, but we would say that this is manageable. We still have to:

1. Derive, or find in the literature $r(t)$ the distribution of the first return time in 0;
2. Solve ϕ_t the generic return time to 0, using equation (C.2) or something similar;
3. Use an ansatz for the probability $\mathbb{P}_{N^*}(x_0 = 0)$ to start from $x_0 = 0$ at a given bias N^*;
4. Average equation (C.1) over the bias N^* to obtain the correlation decay;
5. Study the behavior of the decorrelation time as a function of the input parameters $\tau_{decor}(\tau, m, q_D, q_0)$.

D. Kac-Rice computation of fixed points (chapter 4)

I recall the setup of the computation of fixed-points, and its derivation. I start from the usual LV system:

$$\forall i \in \{1...S\}, \qquad \dot{N}_i = N_i F_i(N_i)$$

where I used $F_i(N_i) = \left(1 - N_i - \sum_j \alpha_{ij} N_j\right)$, I introduced $\underline{\underline{\alpha}} = \mu/S + \sigma/\sqrt{S}\,\underline{\underline{a}}$, and the matrix $\underline{\underline{a}}$ follows a Gaussian distribution with:

$$a_{ii} = 0 \qquad \langle a_{ij} \rangle = 0 \qquad \langle a_{ij} a_{kl} \rangle = \delta_{ik}\delta_{jl} + \gamma \delta_{il}\delta_{jk}$$

To simplify notations, we also introduce the matrix $\tilde{\underline{\underline{\alpha}}} = \underline{\underline{I}}(1 - \frac{\mu}{S}) + \frac{\mu}{S}\,\underline{\underline{1}} + \frac{\sigma}{\sqrt{S}}\,\underline{\underline{a}}$, so that we can express $\vec{F}(\vec{N}) = \vec{1} - \tilde{\underline{\underline{\alpha}}}\vec{N}$.

First, I choose which species are alive: $i = 1...\phi\, S$ will be alive. Then I fix the disorder (the matrix $\underline{\underline{a}}$). Then the number of (possibly invadable) fixed points is:

$$\mathcal{N}_{givenAlive|disorder} = \left|\det \tilde{\underline{\underline{\alpha}}}^*\right| \int_0^\infty \prod_{i=1}^{\phi S} dN_i \prod_i \delta(F_i(N_i))$$

I introduced the * in $\tilde{\underline{\underline{\alpha}}}^*$ to remind that this matrix is of size ϕS. In the following, I will neglect the subdominant diagonal effects: the μ/S term in $\underline{\underline{I}}(1 - \mu/S)$, and the fact that $a_{ii} = 0$. I average over the disorder:

$$\begin{aligned}
\mathcal{N}_{givenAlive} &= \mathbb{E}\left[\mathcal{N}_{givenAlive|disorder}\right] \\
&= \int d^{(\phi S)^2}\underline{\underline{a}}\ \ \mathbb{P}(\underline{\underline{a}})\ \ \left|\det \tilde{\underline{\underline{\alpha}}}^*\right| \int_0^\infty d^{\phi S}\vec{N}\, \delta^{\phi S}(\vec{F}(\vec{N})) \\
&= \int_0^\infty d^{\phi S}\vec{N}\ \mathbb{P}\left(\vec{F}_{\vec{N}} = \vec{0}\right)\ \mathbb{E}\left[\left|\det \tilde{\underline{\underline{\alpha}}}^*\right| |\vec{F}\right]
\end{aligned}$$

From now on, I will assume that the conditioning on $\vec{F}$ in the average of the determinant is subdominant. This can be checked tediously, it holds.

D.1. Compute $\mathbb{P}\left(\vec{F}_{\vec{N}} = \vec{0}\right)$

The main point is to compute $\mathbb{P}\left(\vec{F}_{\vec{N}} = \vec{0}\right)$. It has Gaussian statistics, which can be made explicit:

$$|\mathbb{E}[F]\rangle = (1-\mu m)|1\rangle - |N\rangle$$
$$Cov_{ij} = \mathrm{Cov}\left[F_i, F_j\right] = \frac{\sigma^2}{S}\sum_{i',j'}\mathbb{E}\left[a_{ii'}a_{jj'}\right]N_{i'}N_{j'}$$
$$\underline{\underline{Cov}} = \sigma^2 q\left(\underline{\underline{I}} + \frac{\gamma}{qS}|N\rangle\langle N|\right) \qquad \Rightarrow \qquad \underline{\underline{Cov}}^{-1} = \frac{1}{\sigma^2 q}\left(\underline{\underline{I}} - \frac{\Gamma}{qS}|N\rangle\langle N|\right)$$

where I introduced the bracket notations for vectors. I also introduced the order parameters $Sm = \langle N|1\rangle$, $Sq = \langle N|N\rangle$, and $\Gamma = \frac{\gamma}{1+\gamma}$. For convenience, I label $A = 1-\mu m$. With these conventions, the Gaussian probability can be computed exactly:

$$\mathbb{P}\left(\vec{F}_{\vec{N}} = \vec{0}\right) = \det\left(2\pi\underline{\underline{Cov}}\right)^{-1}\exp -\frac{1}{2}\langle\mathbb{E}[F]|Cov^{-1}|\mathbb{E}[F]\rangle$$

We use the bilinearity, and the intermediate computations:

$$\sigma^2 q\, Cov^{-1}|1\rangle = |1\rangle - \frac{\Gamma m}{q}|N\rangle$$
$$\sigma^2 q\, Cov^{-1}|N\rangle = |N\rangle - \Gamma|N\rangle$$

to obtain:

$$\mathbb{P}\left(\vec{F}_{\vec{N}} = \vec{0}\right) = (1+\gamma)^{-1}\exp -S\mathcal{P}$$
$$\mathcal{P} = \frac{\phi}{2}\log(2\pi\sigma^2 q) + \frac{1}{2\sigma^2 q}\left(A^2\left[\phi - \frac{\Gamma m^2}{q}\right] + (q-2Am)(1-\Gamma)\right)$$

D.2. Compute the average determinant

The missing part is now $\mathbb{E}\left[\left|\det\underline{\underline{\tilde{\alpha}}}\right|\right]$. Matrix theory tells me that the spectrum of $\underline{\underline{a}}/\sqrt{S}$ converges to the uniform distribution over the ellipse E_γ in complex plane, with real semi-axis $1+\gamma$ and imaginary semi-axis $1-\gamma$. The same convergence holds for $\underline{\underline{a^*}}/\sqrt{\phi S}$

I recall that $\underline{\underline{\tilde{\alpha}^*}} = \underline{\underline{I^*}} + \frac{\mu}{S}\underline{\underline{1}}^* + \frac{\sigma\sqrt{\phi}}{\sqrt{S^*}}\underline{\underline{a^*}}$. The $\underline{\underline{I}}$ adds 1 to all eigenvalues. The $\underline{\underline{1}}$ part will only give a contribution for one high eigenvalue, I will forget about it in the following. So I write:

$$\begin{aligned}\mathbb{E}\left[\left|\det\underline{\underline{\tilde{\alpha}}}\right|\right] &= \mathbb{E}\left[\exp\left(\sum_i \log|\tilde{\lambda}_i|\right)\right] \\ &= \mathbb{E}\left[\exp\phi\, S\int d\lambda\,\rho(\lambda)\log|1+\sigma\sqrt{\phi}\lambda|\right] \\ &\sim \exp\phi\, S\int_{\mathrm{E}_\gamma}\frac{d\lambda}{\pi(1-\gamma^2)}\,\log|1+\sigma\sqrt{\phi}\lambda|\end{aligned}$$

where ρ is the uniform distribution in the ellipse E_γ. I change variables to go to the unit circle C, and I use the complex conjugate of each eigenvalue to write the integral:

$$\begin{aligned}\frac{1}{S}\log\mathbb{E}\left[\left|\det\tilde{\underline{\underline{\alpha}}}\right|\right] &= \mathcal{D}_{\gamma,\sigma}(\phi)\\ &= \frac{\phi}{\pi}\int_{-1}^{1}dx\int_{0}^{\sqrt{1-x^2}}dy\,\log\left[(1+ax)^2+(by)^2\right]\end{aligned}$$

where $a=\sigma\sqrt{\phi}(1+\gamma)$ and $b=\sigma\sqrt{\phi}(1-\gamma)$. One of the integral can be computed analytically.

Putting everything together, we find:

$$\begin{aligned}\mathcal{N}_{givenAlive} &= \frac{e^{S\,\mathcal{D}_{\gamma,\sigma}(\phi)}}{1+\gamma}\int_0^\infty d^{\phi S}\vec{N}\;e^{-S\,\mathcal{P}_{\mu,\gamma,\sigma}(\phi,m,q)}\\ &= \frac{e^{S\,\mathcal{D}_{\gamma,\sigma}(\phi)}}{1+\gamma}\int_0^\infty dm\,dq\;e^{-S\,\mathcal{P}_{\mu,\gamma,\sigma}(\phi,m,q)+S\mathcal{V}(\phi,m,q)}\end{aligned}$$

D.3. The volume term

D.3.1. Intuitive derivation

The dependence on the species abundances only comes through ϕ, m and q. To compute the volume term of the change of variables , we will use the saddle point approximation.

$$\begin{aligned}e^{S\mathcal{V}(\phi,m,q)} &= \int_0^\infty d^{\phi S}\vec{N}\;\delta(m_{\vec{N}}-m)\;\delta(q_{\vec{N}}-q)\\ &= \int_0^\infty d^{\phi S}\vec{N}\;S^2\delta(\vec{1}.\vec{N}-mS)\;\delta(\vec{N}^2-qS)\\ &= S^2\int_{i\mathbb{R}}d\hat{m}\,d\hat{q}\,e^{S(\hat{m}m+\hat{q}q)}\int_0^\infty d^{\phi S}\vec{N}\exp\left[-\hat{m}\sum_i N_i-\hat{q}\sum_i N_i^2\right]\\ &= S^2\int_{i\mathbb{R}}d\hat{m}\,d\hat{q}\,e^{S(\hat{m}m+\hat{q}q)+\phi S v(\hat{m},\hat{q})}\end{aligned}$$

Where we introduced:

$$\begin{aligned}v(\hat{m},\hat{q}) &= \log\left(\int_0^\infty dN\,e^{-\hat{m}N-\hat{q}N^2}\right)\\ &= \frac{1}{2}(\frac{\hat{m}}{\sqrt{2\hat{q}}})^2+\log cdf(-\frac{\hat{m}}{\sqrt{2\hat{q}}})-\log(\sqrt{2\hat{q}})+\frac{1}{2}\log(2\pi)\end{aligned}$$

where $cdf(x) = \int_{-\infty}^{x} Dz$ where Dz is the centered Gaussian measure.

Now we consider the saddle point approximation:

$$\begin{aligned}\mathcal{V}(\phi, m, q) &= \max_{\hat{m},\hat{q}} \ \hat{m}m + \hat{q}q + \phi\left\{ -\log(\sqrt{2\hat{q}}) + \frac{1}{2}\left(\frac{\hat{m}}{\sqrt{2\hat{q}}}\right)^2 + \log cdf(-\frac{\hat{m}}{\sqrt{2\hat{q}}}) + \frac{1}{2}\log(2\pi)\right\} \\ &= \frac{\phi}{2}\log(2\pi) + \phi \max_{x,y}\left\{ \frac{m}{\phi}xy + \frac{q}{\phi}\frac{y^2}{2} - \log(y) + \frac{1}{2}x^2 + \log cdf(-x)\right\}\end{aligned}$$

Where I introduced $x = \frac{\hat{m}}{\sqrt{2\hat{q}}}$ and $y = \sqrt{2\hat{q}}$. I now take the derivatives of the function $\mathcal{H}$ in the max:

$$\begin{cases} \frac{\partial \mathcal{H}}{\partial x} = \frac{m}{\phi}y + x - \frac{pdf(-x)}{cdf(-x)} \\ \frac{\partial \mathcal{H}}{\partial y} = \frac{m}{\phi}x + \frac{q}{\phi}y - \frac{1}{y} \end{cases}$$

I can solve $\partial_y H = 0$, considering $\phi, m, q, y > 0$. I introduce $\alpha = \frac{m^2}{\phi q}$.

$$y_{SP} = \frac{\phi}{m}\frac{\alpha}{2}\left(\sqrt{x^2 + 4/\alpha} - x\right)$$

Then $\partial_x H = 0$ can be rewritten:

$$\frac{\alpha}{2}\left(\sqrt{x^2 + 4/\alpha} - x\right) = \frac{pdf(-x)}{cdf(-x)} - x$$

Or equivalently:

$$\frac{\alpha}{2}\left(\sqrt{x^2 + 4/\alpha} - x\right) = \sqrt{\frac{2}{\pi}}\left(\text{erfcx}(x/\sqrt{2})\right)^{-1} - x$$

D.3.2. Probabilistic derivation

The saddle point can also be seen as a probabilistic interpretation. The final formulas are the same, but the geometric one is faster numerically.

$$\mathcal{V}(\phi, m, q) = \max_{\hat{m},\hat{q}} \ \hat{m}m + \hat{q}q + \phi \log \int_0^\infty dN\, e^{-\hat{q}N^2 - \hat{m}N}$$

And now I take the saddle point equations in $(\hat{q}, \hat{m})$.

$$\begin{cases} \partial_{\hat{m}}\mathcal{H} = m - \phi \langle N \rangle_{trunc} \\ \partial_{\hat{q}}\mathcal{H} = q - \phi \langle N^2 \rangle_{trunc} \end{cases}$$

Where I introduced the average $\langle . \rangle_{trunc}$, with regards to the truncated Gaussian density:

$$\rho_{trunc}(N) = \frac{\Theta(N)}{Z}\exp\left(-\hat{q}(N + \frac{\hat{m}}{2\hat{q}})^2 + \frac{\hat{m}^2}{4\hat{q}}\right)$$

The last term in the exponential is just a proportionality factor that will drop out in the normalization. I introduce the cumulants of the non-truncated Gaussian $\mu = -\frac{\hat{m}}{2\hat{q}}$ and $\sigma = 1/\sqrt{2\hat{q}}$. Then it becomes quite close to the static cavity equations! In fact, I introduce $\Delta = \mu/\sigma = -\frac{\hat{m}}{\sqrt{2\hat{q}}} = -x$, and $N = \sigma(\Delta + z)$. Then the saddle point on $(\hat{q}, \hat{m})$ rewrites:

$$\begin{cases} \frac{m}{\phi} = \sigma w_1/w_0(\Delta) \\ \frac{q}{\phi} = \sigma^2 w_2/w_0(\Delta) \end{cases}$$

where $w_i(\Delta) = \int_{-\Delta}^{\infty} Dz(\Delta + z)^i$. I eliminate easily the variable σ, and get back the adimensionned parameter $\alpha = \frac{m^2}{q\phi}$:

$$\alpha = \frac{w_1^2}{w_2 w_0}(\Delta)$$

And then:

$$y = \sigma^{-1} = \frac{\phi}{m}\frac{w_1}{w_0}(\Delta)$$

D.3.3. Bounds on $\alpha = \frac{m^2}{q\phi}$

It can be shown that:

$$(S^*)^{-1} \leq \alpha \leq 1$$

The upper bound comes from Cauchy-Schwartz, and is therefore saturated by a uniform ecosystem $\forall i$, $N_i = 1$. The lower bound comes from developing m^2, and is saturated by $N_1 = 1$, $N_{i\neq 1} = \epsilon$ and taking $\epsilon \to 0$ at fixed S.

However, there is a numerical bound $1/2 < \alpha$ below which I cannot find solutions.

The only complication arises from the $\{N_i \geq 0\}$ boundaries. Indeed, without these boundaries, the volume term becomes a simple high-dimensional sphere. I computed this simple approximation twice, once with the saddle point, and once with exact geometry. I obtain:

$$\mathcal{V}_{sph}(\phi, m, q) = \frac{\phi}{2}\left(1 + \log 2\pi + \log\frac{q\phi - m^2}{\phi^2}\right)$$

Going back to the complete volume term, I can find a solution only if $1/2 < \alpha < 1$. If I visualize the problem in ϕS-dimensional space, imposing q fixes the $\vec{N}$ vector on the sphere of radius $\sqrt{Sq}$. Imposing m fixes its projection on the unit vector colinear to $\vec{1}$. More specifically, if I call θ the angle between $\vec{N}$ and $\vec{1}$, I get $\cos^2\theta = \alpha$.

Therefore, I start to have issues numerically when $\theta = 45^o$. This is not the angle for which the allowed space start to touch the boundary (that would be $\cos\theta^* = \sqrt{1 - d^{-1}}$, with $d = \phi S$ the dimension of the problem).

$1/2$ is the moment almost all the volume starts to concentrate at the $\{N_i \geq 0\}$ boundary, and the saddle point collapses: the volume term becomes sub-exponential in S.

In the probabilistic interpretation, it comes from the fact that with a truncated Gaussian distribution and playing with its two moments, it is not possible to obtain $\alpha = \langle N\rangle^2/\langle N^2\rangle < 1/2$.

D.4. Add uninvadability constraint

For the dead species $j = \phi S + 1..S$, I want to impose that $F_j(\vec{N}) < 0$. This can be written as:

$$\mathcal{N}_{givenAlive} = \mathbb{E}\left[\left|\det \underline{\underline{\tilde{\alpha}}}^*\right|\right] \int_0^\infty d^{\phi S}\vec{N} \int_{-\infty}^0 d^{(1-\phi)S}\vec{G}\, \mathbb{P}\left(\vec{F}_{\vec{N}} = \vec{G}\right)$$

where $\underline{\underline{\tilde{\alpha}}}^*$ is the same matrix as before, I just added the * to make clear that this is an S^*-size matrix. However, now the vectors are slightly different. Indeed, $\vec{N}$ has its first ϕS components positive and free, but the $(1-\phi)S$ last ones are set to 0. Similarly, $\vec{G}$ has its first ϕS components set to 0, but the $(1-\phi)S$ last ones are negative and free. I recall $\vec{F}(\vec{N}) = \vec{1} - \underline{\underline{\tilde{\alpha}}}\vec{N}$. We can rederive the exact same steps:

$$\begin{aligned} |\mathbb{E}[F]\rangle &= (1-\mu m)|1\rangle - |N\rangle \\ \underline{\underline{Cov}} &= \sigma^2 q\left(\underline{\underline{I}} + \frac{\gamma}{qS}|N\rangle\langle N|\right) \qquad \Rightarrow \qquad \underline{\underline{Cov}}^{-1} = \frac{1}{\sigma^2 q}\left(\underline{\underline{I}} - \frac{\Gamma}{qS}|N\rangle\langle N|\right) \end{aligned}$$

but now, $|1\rangle$ is the S-dimensional $\vec{1}$, whereas $|N\rangle$ has 0 on its last $(1-\phi)S$ components.

D.4.1. Normalization

The normalization is slightly different from before because the matrix is bigger. Before I had $\det(2\pi\underline{\underline{Cov}}) = (2\pi\sigma^2 q)^{\phi S}(1+\gamma)$, and now it becomes $\det(2\pi\underline{\underline{Cov}}) = (2\pi\sigma^2 q)^{S}(1+\gamma)$. But actually, I will keep the extra term for the contribution of the uninvadability.

D.4.2. Bilinear form

We need to compute the bilinear form for the Gaussian probability:

$$\begin{aligned} (\langle G| - \mathbb{E}[\langle F|])\underline{\underline{Cov}}^{-1}(|G\rangle - \mathbb{E}[|F\rangle]) &= \sum_{i,j=1}^{S} V_i C_{ij} V_j \\ &= \left(\sum_{i,j=1}^{\phi S} + 2\sum_{i=1}^{\phi S}\sum_{j=\phi S+1}^{S} + \sum_{i,j=\phi S+1}^{S}\right) V_i C_{ij} V_j \end{aligned}$$

I introduced $\vec{V} = \mathbb{E}[\vec{F}] - \vec{G}$. More precisely:

$$V_i = \begin{cases} (1-\mu m) - N_i, & \text{if } i \leq \phi S \\ (1-\mu m) - G_i, & \text{if } i > \phi S \end{cases}$$

The first sum gives the same contribution as before. But actually the block decomposition of the matrix $\underline{\underline{Cov}}$ is $\underset{=\phi.(1-\phi)}{0}$ in the upper right corner, and $\underset{=(1-\phi)^2}{I}$ in the lower right corner. So the only extra-term is:

$$\int_{-\infty}^{0} \frac{d^{(1-\phi)S}\vec{G}}{\sqrt{2\pi\sigma^2 q}^{(1-\phi)S}} \exp\left(-\frac{1}{2\sigma^2 q}\sum_{j=\phi S+1}^{S}(A-G_j)^2\right) = \left(\int_{-\infty}^{0}\frac{dG}{\sqrt{2\pi\sigma^2 q}}\, e^{-\frac{1}{2\sigma^2 q}(A-G)^2}\right)^{(1-\phi)S}$$
$$= \left(\int_{-\infty}^{-A/\sqrt{\sigma^2 q}} Dz\right)^{(1-\phi)S} = \left(cdf(-A/\sqrt{\sigma^2 q})\right)^{(1-\phi)S}$$

Eventually, the contribution to the complexity is to add a negative term:

$$\mathcal{U}(\phi, m, q) = (1-\phi)\log cdf(-A/\sqrt{\sigma^2 q})$$

E. Stabilization of chaos by a spatial structure (chapter 5)

E.1. Model parameters used in simulations, definitions of quantities in figures

For convenient reference, this Appendix includes the parameters for all simulations. The model is given in Eq. (5.1). All $B_{i,u} = 1$ and all $D_{i,uv} = d/(M-1)$. The $A_{ij,u}$ are independent for different (i,j) pairs (except in Appendix E.3).

In Fig. 5.3, the probability of $A_{ij,u}$ to be non-zero is $c = 1/8$, and the non-zero elements are sampled from a normal distribution with $\text{mean}(A_{ij,u}) = 0.3$, $\text{std}(A_{ij,u}) = 0.45$. The same elements $A_{ij,u}$ are non-zero across all patches u. The correlation coefficient between non-zero $A_{ij,u}$ in different patches is $\rho = \text{corr}[A_{ij,u}, A_{ij,v}] = 0.95$ for $u \neq v$. (The correlation is 0.964 when interactions with $A_{ij,u} = 0$ are also counted.) The initial (pool) diversity is $S = 250$. In Fig. 5.3(A), $M = 1$. In Fig. 5.3(B), $M = 8$ patches and $d = 10^{-3}$. The cutoff is $N_c = 10^{-15}$. For each i,j, the M values $A_{ij,u=1..M}$ are drawn simultaneously from a multi-variate normal distribution with correlation matrix $C_{uv} = \rho + (1-\rho)\delta_{uv}$, using standard numerical methods (e.g., as implemented in the Matlab function `mvnrnd`).

Fig. 5.4(bottom), uses the same parameters as Fig. 5.3, but with a range of values for d, S and N_c.

Fig. 5.8 uses the runs shown in Fig. 5.3(B). Standard deviation and mean are estimated from 1601 time points during the time period $t = [10^4, 2 \cdot 10^5]$.

Fig. 5.10(a) uses multiple runs, with the same parameters as 5.3, except for $d = 10^{-4}$ and $N_c = 10^{-15}$. Fig. 5.10(c), shows the line where half of the runs are fixed points, and half continue to fluctuate until $t = 2 \cdot 10^5$. It uses same parameters as Fig. 5.10(a), except with $D = d/(M-1) = 10^{-4}$.

In Fig. 5.10(a), the size of the fluctuations are calculated from $\text{var}(\xi_u) = \langle \xi_u^2(t) \rangle = \sigma^2 C_{N,u}(t,t)$, with $C_{N,u}(t,t) = \langle N_u^2(t) \rangle - \lim_{t-t' \to \infty} \langle N_u(t) N_u(t') \rangle$. For more details on the averaging, see section 5.3 and Fig. 5.5.

Fig. 5.10(a) shows the strength of noise at different diversities. Extinctions beyond the time shown in simulations ($t = 2 \cdot 10^5$) take extremely long times to happen, so reaching these lower diversities in simulations is unfeasible. Instead, we remove species that are most likely to go extinct. Recalling that the time to extinction is $\tau (1/N_c)^{2MN^*_{\text{eff}}/W}$, we remove species with the lowest N_{eff}. This is done by running the system for time $\Delta t = 15 \cdot 10^3$, calculating N_{eff}, and removing the 5 species with the lowest values of N_{eff}. This process is repeated. Other protocols for species removal where attempted, such as

increasing N_c in time; they give similar results. The results are averaged over 3 runs, with independent sampling of interactions and initial conditions.

E.2. General validity of DMFT equations

As explained above, DMFT can be implemented as an approximation for a large variety of systems. In this case one has to infer the average μ, the standard deviation σ of interactions, and the distribution $\mathbb{P}(X^u)$ from the data (we remind that $X^u = \{N_u(0),\, B_u,\, D_{uv}\}$) and use them as an input to define an effective model. The generalization to patch-dependent cumulants μ_u and σ_u is quite straightforward. So is the generalization to patch-dependent correlation ρ_{uv}. With the assumptions described below, the fraction of coexisting species S^*/S is finite when S is large, so that resident diversity S^* in each community is also large.

We have derived DMFT for a completely connected set of interactions A_{ij}. A different way to obtain DMFT is considering a finite connectivity network of interactions A_{ij}, e.g. the one produced by a Erdos-Renyi random graph with average connectivity per species C or a regular random graph with connectivity C. In these cases, for each link ij one generates a random variable with average μ/C and variance σ^2/C and set it to A_{ij}. In the large connectivity limit, $C \to \infty$, each species interacts with a very large number of species and one can replace the deterministic interaction with an effective stochastic noise, as done for a completely connected lattice. Although the resulting DMFT equations are the same, the two cases are quite different: in the former a species interact with $C \ll S$ species whereas in the latter a species interacts with $C = S$ species. The equivalence of DMFT for completely connected lattices and finite connectivity ones in the $C \to \infty$ limit has been thoroughly studied in physics of disordered systems in the last twenty years [143].

In addition, this chapter focuses on the case where migration connects all patches to one another. But the basic DMFT framework, Eq. (5.2), is valid even if only certain patches are connected, and migration is zero otherwise. This can allow for analysis of different spatial connectivities, such as lattices representing finite-dimensional space, and is an interesting direction for future work.

E.3. Derivation of the multivariate Gaussian distribution for diversity

We use notations from section 5.3. Within the time-translational-invariant state:

$$\frac{1}{N_u}\frac{dN_u}{dt} = N_u^* - N_u + \xi_u\left(t\right) + \sum_{v\sim u} D_{uv}\left(\frac{N_v}{N_u} - 1\right)$$

Consider the case of low migration, $D \to 0^+$. We now develop a theory assuming that the amplitude of the endogenous fluctuations,

$$W \equiv \int dt\, C_\xi\left(t, t'\right) \ ,$$

remains finite in the limit $D \to 0^+$. Assume the species survives, i.e. there is at least one patch with $N_u^* > 0$. If $N_u^* < 0$ then $N_u = O(D)$. If $N_u^* > 0$ then $N_u = O(1)$ and therefore $\sum_{v\sim u} D_{uv}\left(\frac{N_v}{N_u} - 1\right) = O(D)$. Taking the time average of the above equation

$$0 = \overline{\frac{1}{N_u}\frac{dN_u}{dt}} = N_u^* - \overline{N_u} + O(D)$$

and therefore $\overline{N_u} = N_u^* + O(D)$.

The previous arguments lead to the conclusion that in the $D \to 0^+$ limit $\overline{N_u} = N_u^*$ if $N_u^* > 0$ and is equal to zero otherwise. In the following we provide more detail about this argument and its possible limitations. For this last equality to be valid, we need that $\sum_{v\sim u}\left(\frac{N_v}{N_u} - 1\right)$ will be finite, so that $D\sum_{v\sim u}\left(\frac{N_v}{N_u} - 1\right)$ will indeed be small. This might break if N_u can be small while some other N_v remains $O(1)$. An estimate for that proceeds by noting that the carrying capacity of patch u in the presence of other patches is larger or equal to $N_u^* - MD \simeq N_u^*$, its carrying capacity alone. If patch u fluctuates alone, then

$$\frac{dx_u}{dt} = N_u^* + \xi(t) \Rightarrow P(x) \sim e^{\frac{2N^* x}{\sigma^2 W}}$$

This gives for $\overline{1/N_u}$

$$\overline{e^{-x_u}} \sim \frac{\int_{-\infty}^0 e^{x\left(\frac{N_u^*}{W}-1\right)}dx}{\int_{-\infty}^0 e^{x\frac{N_u^*}{W}}dx} = \frac{\frac{N_u^*}{W}+1}{\frac{N_u^*}{W}} = 1 + \frac{W}{N_u^*}$$

For any given N_u^* this is finite. It diverges as $N_u^* \to 0$. Therefore the migration term is negligible only if $\frac{DW}{1-D} \simeq DW \ll N_u^*$. (Note that migration itself would limit N_u going below much below DN_v, which would make this term smaller.) The main approximation (or limitation) of our approach is the assumption that W remains finite in the small D limit. This is shown to hold in simulations presented in section 5.3 and Fig. 5.5. It breaks down if the noise develops long-lasting correlations in time. Our approximation will be nevertheless good for large $|N_u^*|$ and for weak endogenous fluctuations.

We now used the relationship discussed above between $\overline{N_u}$ and N_u^* to determine the statistics of N_u^*. We shall use the term "source" for patches where $N_u^* > 0$, and "sink" otherwise[1]. In order to understand the correlation between the sources in the different communities, we unpack N_u^* using section 5.3. Taking the time-average is equivalent to averaging over the dynamical noise ξ. Therefore, in patch u for species i, $z_{i,u} = -\sigma S^{-1/2}\sum_j a_{ij,u}\overline{N_{j,u}} = -\sigma S^{-1/2}\sum_{j,+} a_{ij,u} N_{j,u}^*$. The sum $\sum_{j,+}$ means that we only sum over $N_{j,u}^* > 0$. Here, we recall that $a_{ij,u}$ are standard random variables with mean zero, variance one, and correlation between patches:

$$\mathbb{E}\left[a_{ij,u}\, a_{kl,v}\right] = \delta_{ik}\,\delta_{jl}\,\rho_{uv}$$

[1]The term "source" is used here so as to include patches (sometimes referred to as pseudo-sinks) where a species might still receive migration from patches with even larger N_u^*. But the contribution of this migration is small and not required for its persistence.

where we used the Kronecker symbol δ_{ik}.

Therefore:

$$N^*_{i,u} = 1 - \mu\, m_u - \sigma S^{-1/2} \sum_{j,+} a_{ij,u}\, N^*_{j,u} \tag{E.1}$$

where we recall $m_u = \langle \overline{N_{i,u}} \rangle = \left\langle N^*_{i,u} \right\rangle_+$. We can now compute the different moments of the multivariate Gaussian random variable N^*_u, using equation (E.1). We obtain the closure:

$$\begin{cases} \text{mean}\,[N^*_u] = 1 - \mu \left\langle N^*_{i,u} \right\rangle_+ \\ \text{covariance}\,[N^*_u, N^*_v] = \sigma^2 \rho_{uv} \left\langle N^*_{i,u} N^*_{i,v} \right\rangle_+ \end{cases}$$

When $u = v$, as $\rho_{uu} = 1$, we find the expected single community result. In particular, mean $[N^*_u]$ and variance $[N^*_u]$ do not depend on the patch u.

We numerically solve the closure in a self-consistent way: start with a guess for $\left\langle N^*_{i,u} N^*_{i,v} \right\rangle_+$, and then (1) Produce many samples of the vector $N^*_{u=1..M}$ and (2) calculate the next estimate for $\left\langle N^*_{i,u} N^*_{i,v} \right\rangle_+$, by averaging only over $N^*_{i,u}$ and $N^*_{i,v}$ that are both positive. For stability of this numerical scheme, we only replace half the samples at each iteration. We use 10^5 samples and 1000 iterations. The algorithm is always found to converge to the same solution.

E.4. Single patch ($M = 1$)

Here we show that in principle a single patch can reach and maintain a dynamically fluctuating state. However, this requires prohibitively large S, not attainable in practice. In Fig. E.1 and Fig. E.2 we show results of a numerical solution [61] to the DMFT equations detailed in section 5.3. At extremely low values of N_c the system appears to reach a final diversity above the May bound and, hence, to be chaotic. DMFT however describes the behavior in the $S \gg 1$ limit. When full simulations of the model in Eq. (5.1) are carried out at finite S, they diversity falls somewhat below the DMFT final diversity, leading to a fixed point, rather than a chaotic state, see Fig. E.2. This finite-size correction to the DMFT result are important since they show that maintaining a dynamically fluctuating state for realistic values of S is not possible for $M = 1$.

E.5. Correlations of interactions in a pair of species

In the main text we assumed that $A_{ij,u}$ is sampled independently from $A_{ji,u}$. Here we show that the long-lived endogenous fluctuations can be found even if this assumption is relaxed. For this purpose, we consider a symmetric network of non-zero $A_{ij,u}$, namely $A_{ij,u} \neq 0$ if and only if $A_{ji,u}$. We define γ the correlation of the non-zero elements $\gamma = \text{corr}\,[A_{ij,u}, A_{ji,u}]_{A_{ij,u} \neq 0}$. Fig. E.3 shows two simulations, one with $\gamma > 0$ and the other with $\gamma < 0$. In both cases the system relaxes to a long-lived state with fluctuating

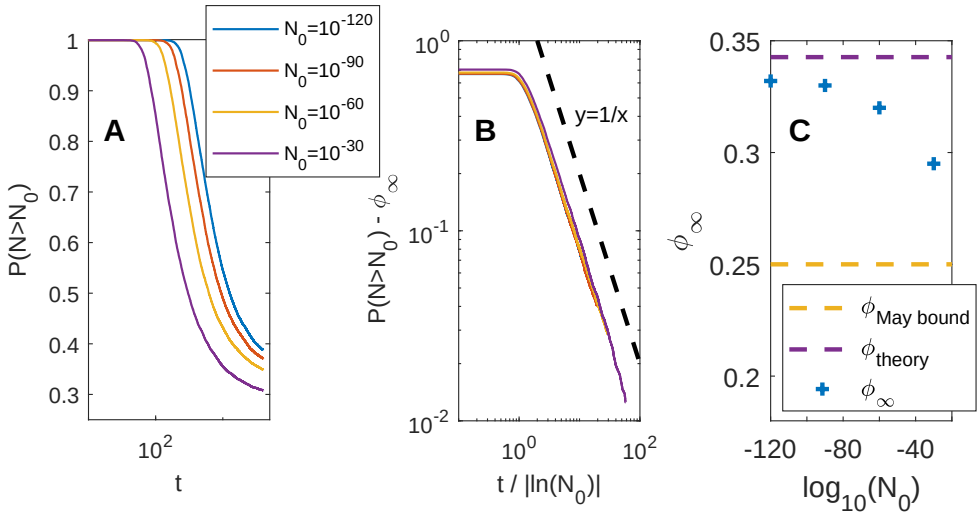

Figure E.1. DMFT numerics for a single patch, $M = 1$, showing that chaos is in principle possible here, although for unrealistic values of model parameters. (A) The fraction of species above different values of N_0, $P(N > N_0)$ is plotted as a function of time, for different values of N_0. (B) The curves for different N_0 collapse when $P(N > N_0) - \phi_\infty(N_0) \sim |\ln N_0| / t$. Here $\phi_\infty(N_0)$ is a fitted parameter, the extrapolated value of $P(N > N_0)$ at long times. (C) The values of $\phi_\infty(N_0)$ are well above the linear stability bound ("May bound"), and at (very) low N_0 come quite close to the theoretical maximal value for $\phi_\infty(N_0)$, predicted in section 5.4.1. Here $\sigma = 2, \mu = 10, N_c = 10^{-120}$.

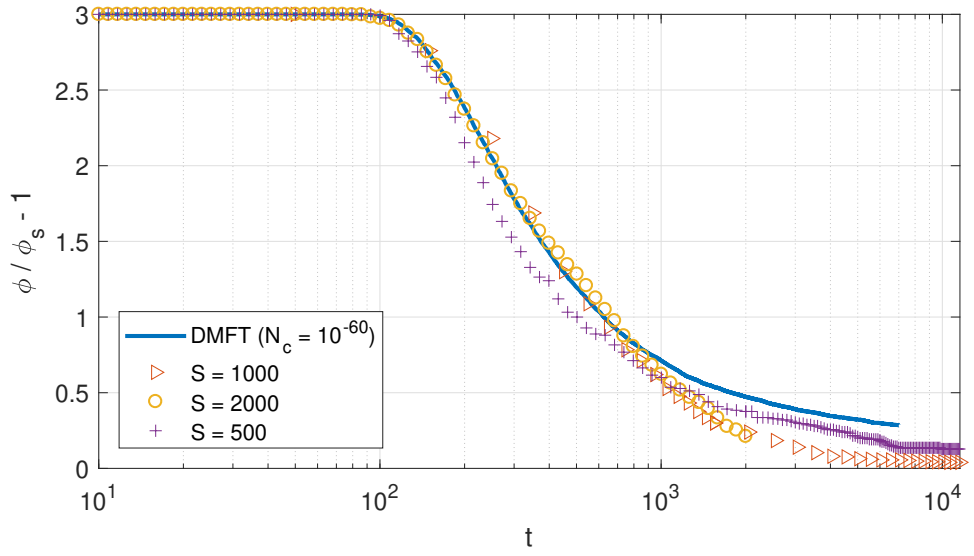

Figure E.2. The DMFT solution and the simulations only agree up to times $t \sim 10^3$, after which the diversity in the simulations reduces more rapidly and reaches a fixed point. This means that the convergence to the DMFT solution is slow with S.

abundances, without further loss of diversity up to time $2 \cdot 10^5$. They are intended solely to demonstrate that conditions with $\gamma \neq 0$ exist, rather than a systematic exploration of such cases.

The parameters for the simulations (using the notation of Appendix E.1) are the following:

Run with positive γ: $\gamma = 1/4$, $S = 350$, mean $(A_{ij,u}) = 0.075$, std $(A_{ij,u}) = 0.175$, $c = 0.357$, $M = 8$, $d = 10^{-3}$, $\rho = 0$, $N_c = 10^{-15}$.

Run with negative γ: $\gamma = -1/2$, $S = 250$, mean $(A_{ij,u}) = 0.075$, std $(A_{ij,u}) = 0.358$, $c = 0.5$, $M = 8$, $d = 10^{-3}$, $\rho = 0$, $N_c = 10^{-15}$.

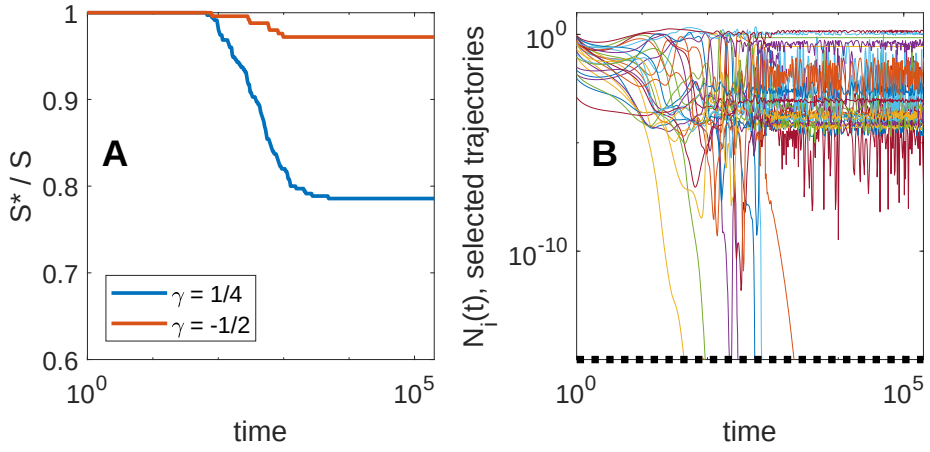

Figure E.3. (A) The diversity $S^{*}(t)/S$ for two runs with $\gamma \equiv \mathrm{corr}\left[A_{ij,u}, A_{ji,u}\right] \neq 0$. (B) Selected trajectories of $N_{i,u}(t)$ for the run with $\gamma = 1/4$.

F. Impact of demographic noise (chapter 6)

F.1. Protocol for the numerical samples

For comparing with the theoretical results, we sample the dynamical system presented in Equation (6.1). The input parameters of a sample are the system size S, the interaction matrix parameters (μ, σ), the immigration λ, the strength of the demographic noise T (temperature), and the initial condition distribution $\mathbb{P}[\{N_i(0)\}_{i=1..S}]$. In order to sample one realization of the ecosystem, we perform the following steps:

1. We sample the S-sized symmetric interaction matrix α, from the Gaussian distribution with scaled parameters (μ, σ).

2. We sample the initial conditions $N_i(t=0)$ from the distribution $\mathbb{P}[\{N_i(0)\}_{i=1..S}]$. For instance, we use a factorized uniform distribution in $[0,1]$:

$$\mathbb{P}[\{N_i(0)\}_{i=1..S}] = \prod_{i=1}^{S} \mathbf{1}\{N_i(0) \in [0,1]\}$$

   where $\mathbf{1}\{.\}$ is the indicator function.

3. We sample the demographic noise $\{\eta_i(t)\}_{i=1..S}^{t=0..t_{max}}$, from the white-noise distribution, with temperature T.

4. Then, all three random contributions (interactions, initial conditions and demographic noise) have been dealt with. We can then integrate deterministically the system, to end up with $\{N_i(t)\}_{i=1..S}^{t=0..t_{max}}$, where t_{max} is the temporal extent for the simulation.

Actually, the above 3 and 4 points are a bit more involved: the implementation of immigration is detailed in Appendix F.2, and the exact numerical scheme we used is presented in Appendix 6.5. But for simplicity's sake, let's focus on this framework: we fix parameters $(S, \mu, \sigma, \lambda, T)$, we sample the three random contributions, we integrate, and we obtain the species populations over time $\{N_i(t)\}_{i=1..S}^{t=0..t_{max}}$.

When we reproduce different sets of data by keeping the same parameters, but sampling different randomness, we obtain $\{N_i^r(t)\}_{i=1..S,\, r=1..N_{sample}}^{t=0..t_{max}}$.

F.2. Mathematical issues for immigration implementation

In this part, we detail the mathematical issue for immigration implementation. This problem is independent on the interactions, so we drop them ($\alpha = 0$ here). We consider the following one-species Ito-stochastic process:

$$\frac{dN}{dt} = N(1-N) + \sqrt{2TN}\,\eta + \lambda I(N) \tag{F.1}$$

with white noise $\langle \eta(t)\eta(t')\rangle = \delta(t-t')$, and immigration function $I(N)$. Immigration is generically implemented so that the populations do not go too close to 0. In the usual immigration, $I(N) = 1$, but we will see that this is problematic.

We want to have a hint at the stationary distribution of population $P_\infty(N) = P(N, t = \infty)$. In order to obtain it, we change variables so that the noise becomes additive, and not multiplicative any more. Here the relevant change of variables is $s(t) = \sqrt{N}(t)$, and Ito's lemma gives:

$$\frac{ds}{dt} = \frac{s^2 - s^4 + \lambda I(N)}{2s} - \frac{T/4}{s} + \sqrt{2T/4}\,\eta$$

Then we use Langevin-Boltzmann to read the stationary distribution.

In the usual immigration $I(N) = 1$ case, the stationary distribution is always integrable:

$$\mathcal{P}_\infty(N) = Z^{-1} N^{\lambda/T-1} \exp \frac{1}{T}(N - \frac{N^2}{2})$$

However, the corresponding effective potential $V_{eff}(N)$ behaves repulsively around $N = 0$ only if $\lambda > T$:

$$V_{eff}(N) = -N + \frac{N^2}{2} - (\lambda - T)\ln N$$

Indeed, if we introduce an approximate induced cut-off value $N_{cut}(b)$ such that $\mathcal{P}_\infty(N < N_{cut}) \sim e^{-b} \ll 1$, the scaling yields $N_{cut}(b) \sim e^{-bT/\lambda}$, which means that the density is still relevant up to $e^{-bT/\lambda} \ll 1$.

Basically, this means that demographic noise with usual immigration will not prevent populations from reaching very low values. The usual immigration is not strong enough when facing demographic noise. This is indeed problematic, because whenever we will want to actually compute observables, the integrals will be dominated by the domain $N \sim 0$. This is wrong physically (important species should be the high population ones), and difficult numerically (integration is ill-defined).

In order to solve this, we can implement stronger immigration such as $I(N) = N^{-\alpha}$ with $\alpha > 0$. However, another even simpler physical solution is to impose a hard repulsive boundary condition on the problem: an infinite potential at $N = \lambda$. In this case, the same steps can be performed and we obtain the stationary distribution:

$$\mathcal{P}_\infty(N) = Z^{-1} N^{-1} \exp\left[\frac{1}{T}(N - \frac{N^2}{2})\right] \mathbf{1}\{N > \lambda\}$$

which is well-behaved. This is the solution we chose for both the theory predictions and the numerics. We will now detail in the next section how to integrate this process numerically.

F.3. Issues of our numerical scheme

After careful tests on simpler models, we used this scheme to compare with the theory. Initially we used a hard-wall immigration at $\lambda = 10^{-3}$. The agreement was quite good for second degree observables (q_d, q_0), but not for h. This is due to the numerical scheme. Indeed, if T is quite high ($T \gg \lambda$), the sampling of the demographic noise sends many $\mathcal{O}(1)$ species close to 0, then they bounce on the wall and end up at $N = 2\lambda$. Therefore there is an induced concentration of species at $N = 2\lambda$. Because of the 2λ peak, there is a subsampling of the $\mathcal{O}(1)$ populations.

In order to reduce this issue, we use a higher $\lambda = 10^{-2}$ in the final results that are shown on figure 6.4. We reckon the slight discrepancy at high temperature between theory and numerics comes from this issue. We are aware that the method is still in development. However, it is already enough at the moment to beautifully confirm the theory.

We detail here the ongoing improvements for the numerical scheme. In the current version, we first sample pure demographic noise then implement the hard wall immigration. When doing this, a lot of trajectories do bounce on the wall, which lowers the accuracy of the scheme. A way to solve this would be to directly solve the Fokker-Planck equation associated to the whole process "demographic noise + hard wall". We reckon this can be done adapting the proof from [132].

G. Miscellaneous

In this chapter, we detail three results that are independent from all previous chapters. First, we perform a Landau-like expansion in the correlation function, close to the chaotic transition. Then, we play with the quadratic saturation in the Lotka-Volterra model. We show that there is no chaotic phase with a log saturation. And eventually, we show that there is an aging chaotic behavior with a cubic saturation; just like with the usual quadratic one.

G.1. Perturbation expansion in the correlation close to the chaotic transition

In this section, we present an expansion for the correlation function, close to the chaotic transition.

I wait for a steady state to be reached, either a chaotic one or a stable equilibrium. Starting here, I'll perform a perturbation expansion over the noise.

The details of the computation can be found in Appendix H. This result involved quite tedious computations, so any application should check the second order coefficients. In theory, it could also be obtained by using Martin-Siggia-Rose field theory.

G.1.1. Result

Using Wick's theorem, the evenness of the correlation and assuming time-translation invariance, I obtain a second-order closed equation on the correlation function $C(\tau)$:

$$\forall \tau, \qquad C(\tau) = \int dt_1 \; M_1^C(\tau; t_1) \; C(t_1) + \int dt_1 \; dt_2 \; M_2^C(\tau; t_1, t_2) \; C(t_1) \; C(t_2) \tag{G.1}$$

It is easier to simplify the diagrams in Fourier space, where the nodes' law from electronics applies. After tedious classifications, and writing $c(\omega)$ the direct Fourier transform of $C(\tau)$ I obtain:

$$
\begin{aligned}
c(\omega) &= \sigma^2 c(\omega)\langle \frac{N^2}{N^2+\omega^2}\rangle_+ \\
&+ 2\pi\sigma^4\delta(\omega)\langle\{\int \frac{d\Omega}{2\pi} c(\Omega)\frac{i\Omega}{N^2+\Omega^2}\}^2\rangle_+ \\
&+ \sigma^4 \int \frac{d\Omega}{2\pi} c(\Omega)c(\omega-\Omega)\langle N^2 \frac{N(-2i\Omega+3i\omega)+\omega\Omega}{(N^2+\omega^2)(N^2+(\omega-\Omega)^2)(N^2+\Omega^2)}\rangle_+ \\
&+ \sigma^4 c(\omega)\int \frac{d\Omega}{2\pi} c(\Omega)\langle N \frac{P(N,\omega,\Omega)}{(N^2+\omega^2)(N+i\omega)(N+i(\omega-\Omega))(N^2+\Omega^2)}\rangle_+
\end{aligned}
\tag{G.2}
$$

In what I wrote, $\langle . \rangle_+$ denotes the average over the stationary solution. I also introduced $P(N,\omega,\Omega)$, which is the polynomial expression:

$$P(N,\omega,\Omega) = 8N^4 + N^3(-9-8i\Omega) + N^2(5i\Omega-4i\omega) + N(-2\Omega\omega-4\Omega^2) + i\omega\Omega(\omega-\Omega)$$

The second line with the $\delta(\omega)$ in equation (G.2) should probably be omitted, because it comes from non-connected diagrams.

G.1.2. First order

If I keep only the first order, I recover the usual transition line to chaotic behavior. Let's detail this result a little bit more. If I keep only the first order in equation (G.2), it reads:

$$\forall\tau, 0 = \int dt_1\ \mathcal{L}(\tau;t_1)\ C(t_1) \tag{G.3}$$

where I introduced the linear operator $\mathcal{L}(\tau;t_1) = M_1^C(\tau;t_1) - \delta(\tau-t_1)$. When the operator $\mathcal{L}$ is invertible, there is only one solution to equation (G.3): $\forall\tau,\ C(\tau) = 0$. This is the case in the One Equilibrium phase. For a chaotic state to exist, it is therefore needed that the linear operator $\mathcal{L}$ becomes non-invertible. This operator happens to be time-translationally invariant, and it can thus be diagonalized in Fourier space. It starts to be non-invertible when its lowest eigenvalue touches zeros. The corresponding eigenvector is the small frequency one, and the transition happens when $\sigma = \sqrt{2}$. More precisely, the Fourier representation of the operator is:

$$\lim_{\omega\to 0} \tilde{\mathcal{L}}(\omega) = \phi(\phi^{-1} - \sigma^2) \tag{G.4}$$

It can then be shown that the condition that indicates the appearance of chaos (*i.e.* $0 = \lim_{\omega\to 0}\tilde{\mathcal{L}}(\omega)$) is exactly the same condition as the one from section 2.3.2 (for $\gamma = 0$).

G.1.3. Second order

The second order analysis of equation (G.2) should be able to tell us how the transition to chaos occurs: what is the correlation function just above the chaotic threshold. we haven't done it yet.

G.2. Different functional responses

In this section, we broaden the study of the model to different saturations (which are called functional responses in ecology). We do know that they are essential to the different phases the ecosystem can present. For instance, the Unbounded Growth phase can be suppressed by implementing a stronger limitation from the environment. Here, we present the analytical study of a logarithmic saturation, followed by the numerical investigation of a cubic saturation.

G.2.1. Log saturation

In this section, we study a slightly different model, where the saturation from the environment isn't quadratic but rather logarithmic:

$$\forall i = 1, ..., S, \quad \frac{dN_i}{dt} = N_i \left(-\log(N_i) - \sum_{j \neq i} \alpha_{ij} N_j \right) \tag{G.5}$$

The logarithmic saturation simplifies the analytical treatment, because the natural variables of the dynamics are indeed the log of the populations. Due to the saturation, the extinct-state of a species can never be stable: all species stay present. A previous study [144], showed that there was no chaotic dynamics in the case $\mu = 0$. However, we hoped to observe them with this saturation for $\mu \neq 0$, and DMFT would be easier to tackle (at least for $\gamma = 0$). However, we show here that there is no Multiple Attractor phase in the phase space of the model.

We will only deal with the purely asymmetric $\gamma = 0$ case. We write the static cavity equations:

$$\begin{cases} q = m^2 e^{\sigma^2 q} \\ m\, e^{\mu m} = e^{\sigma^2 q/2} \end{cases} \tag{G.6}$$

We perform the stability analysis of the static cavity solution, just like in Appendix A.7. We end up with the correlation closure (similar to equation 2.13 with a different saturation):

$$\tilde{C}_c(\omega)/\sigma_h^2 \quad = \frac{q}{1 - \sigma^2 q + \omega^2} \tag{G.7}$$

From it, we see that the instability occurs again at zero mode ($\omega = 0$), but that this time it is inversely quadratic in the frequency instead of inversely linear. This instability transition occurs at $\sigma^2 q = 1$, which in the phase portrait means:

$$\frac{\mu}{\sqrt{e}} = \sigma(1 + \log \sigma)$$

This would usually mark the boundary between the One Equilibrium phase and the Multiple Attractors one. However, we can also check when does the Unbounded Growth

transition occurs. We now focus on the system of equations G.6, we want to understand when does the solution explodes.

The first equation is of the type $e^X = aX$, with $X = \sigma^2 q$ and $a = \{\sigma m\}^{-2}$. This equation admits two solutions when $a > e$, that merge and disappear at $X = 1$ when $a = e$. A quick stability analysis of the system shows that the stable (in terms of flow) solution is the $X < 1$ one.

The second equation is always well-behaved, because it is of the type $e^{-Y} = bY$ with $Y = \mu m$, and $b = \mu^{-1} e^{-\sigma^2 q/2}$. There is always one unique solution $Y(b)$.

This analysis shows that the static cavity solution disappears when $a \to e$ from above. But interestingly, the limit $a = e$ exactly corresponds to the Multiple Attractors phase transition. Therefore, we showed that the system cannot exhibit chaotic dynamics, because the instability directly ends up in the Unbounded Growth phase: there is no Multiple Attractors phase. We confirmed this result numerically, it was not possible to find a chaotic simulation with log saturation.

G.2.2. Cubic saturation

In this section, we change again the saturation in the model, and use a cubic one. The model then becomes:

$$\forall i = 1, ..., S, \quad \frac{dN_i}{dt} = N_i \left(1 - N_i^2 - \sum_{j \neq i} \alpha_{ij} N_j \right) \tag{G.8}$$

Based on the work of [49], it was suspected that the cubic saturation might prevent the chaotic behavior from aging and disappearing. However, we performed a numerical study to show that this is not the case. Indeed, it can be seen on figure G.1 that the system does exhibit chaotic aging dynamics; just like the usual quadratic saturation model.

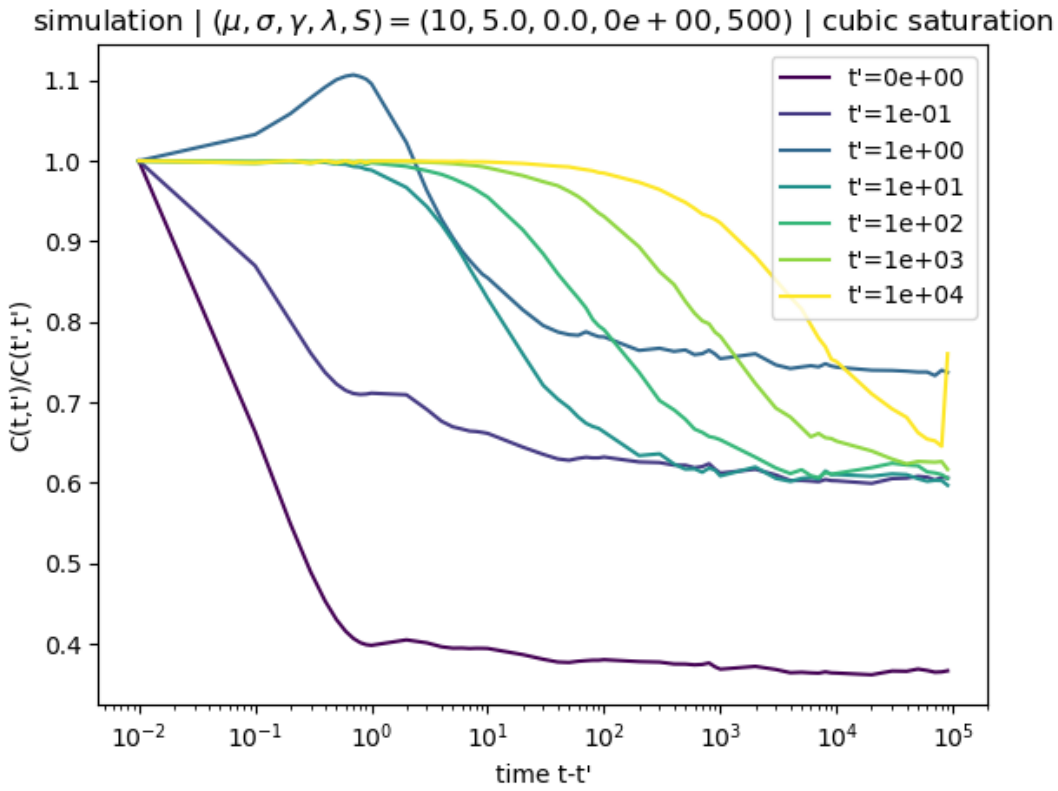

Figure G.1. Chaotic aging with cubic saturation

H. Perturbation expansion in the correlation (Appendix G)

H.1. Setup

I wait for a steady state to be reached, either a chaotic one or a stable equilibrium. Starting here, I'll perform a perturbation expansion over the noise.

In all this section, I'll focus first on the $\gamma = 0$ case. I consider the interactions from all species as a noise $\eta_i = \sum_j a_{ij} N_j(t)$ without going through the cavity derivation. I introduce the notation $\overline{X_j} = \frac{1}{S}\sum_j X_j$, and $\langle . \rangle$ denotes the average over the noise.

$$\dot{N}_i = N_i(1 - N_i - \mu\overline{N_j} - \sigma\eta_i)$$

From the cavity derivation, I know that η_i is Gaussian with covariance

$$\langle \eta_i(t)\eta_i(t')\rangle = \langle \overline{N_j(t)N_j(t')}\rangle$$

Now I will separate the noise into two independent contributions: $\eta_i(t) = \eta_\infty + \delta\eta(t)$, and their variance:

$$\langle \eta_\infty^2 \rangle = \overline{\langle N_j \rangle^2}$$
$$\langle \delta\eta(t)\delta\eta(t')\rangle = \overline{\langle N_j(t)N_j(t')\rangle} - \overline{\langle N_j\rangle^2}$$

The idea is that in the chaotic regime, $N_j(t)$ and $N_j(t')$ will decorrelate when $t - t'$ becomes large enough. The ergodic hypothesis should hold. In addition, in small chaos, I should also have that the time average of a trajectory $\langle N_i(t)\rangle_T = N_i^\infty$ (I checked it with Giulio at some point). Therefore the noise $\delta\eta$ will disappear

I need to be careful, because the stationary noise I introduce is not the one the system converges to in the 1eq phase. Maybe it would be better to introduce three independent noises to be clear. I'll keep on with the computations I had started.

I can rewrite:

$$\dot{N}_i = N_i(H_i - N_i - \sigma\delta\eta_i)$$

H.2. Diagrammatic expansion

First I rule out the extinct species. For them, $H_i < 0$ and at first order in δN_i and $\delta\eta_i$: $\delta N_i(t) = N_i(t) = N_i(0)\exp(-|H_i|t - \int_0^t \delta\eta_i)$. The integral term scales as $\sqrt{t}$ and therefore at long times $|H_i|$ always wins.

Now I focus on the remaining species, for which $H_i > 0$ and I introduce $n_i(t) = \delta N_i(t) = N_i(t) - H_i$. I'll drop the i index, the δs and the $*$.

$$\dot{n} = -(N+n)(n+\sigma\eta) \tag{H.1}$$

I know from the self-consistent relation that η and n are of the same order, supposed to be small. If I forget about the transient (exponential relaxation) by sending the initial condition to $-\infty$, I get the perturbative expansion:

$$n(t) = \int dt_1 M_1(t;t_1)\eta(t_1) + \int dt_1 dt_2 M_2(t;t_1,t_2)\eta(t_1)\eta(t_2)$$
$$+ \int dt_1 dt_2 dt_3 M_3(t;t_1,t_2,t_3)\eta(t_1)\eta(t_2)\eta(t_3) + ...$$

I define the operator $M(t,t_1) = \theta(t-t_1)e^{-N(t-t_1)}$ where θ is the Heavyside function. Then I can define the M_i operators from above as diagrams. Eventually, I'm interested in the second order for the correlation function, so I need to go up to third order in η:

$$C(t,t') = \langle n(t)n(t')\rangle = ... \tag{H.2}$$

Using Wick's theorem, the evenness of C and assuming time-translation invariance, I obtain a closed equation on C. It is easier to simplify the diagrams in Fourier space, where the nodes' law from electronics applies. After tedious classifications, and writing $c(\omega)$ the direct Fourier transform of $C(\tau)$ I obtain:

$$c(\omega) = \sigma^2 c(\omega)\langle\frac{N^2}{N^2+\omega^2}\rangle_+ \tag{H.3}$$
$$+2\pi\sigma^4\delta(\omega)\langle\{\int\frac{d\Omega}{2\pi}c(\Omega)\frac{i\Omega}{N^2+\Omega^2}\}^2\rangle_+$$
$$+\sigma^4\int\frac{d\Omega}{2\pi}c(\Omega)c(\omega-\Omega)\langle N^2\frac{N(-2i\Omega+3i\omega)+\omega\Omega}{(N^2+\omega^2)(N^2+(\omega-\Omega)^2)(N^2+\Omega^2)}\rangle_+$$
$$+\sigma^4 c(\omega)\int\frac{d\Omega}{2\pi}c(\Omega)\langle N\frac{P(N,\omega,\Omega)}{(N^2+\omega^2)(N+i\omega)(N+i(\omega-\Omega))(N^2+\Omega^2)}\rangle_+$$
$$P(N,\omega,\Omega) = 8N^4 + N^3(-9-8i\Omega) + N^2(5i\Omega-4i\omega) + N(-2\Omega\omega-4\Omega^2) + i\omega\Omega(\omega-\Omega)$$

In what I wrote, $\langle.\rangle_+$ denotes the average over the stationary solution. I should be careful with the decomposition of the noise, but so far I considered it was the usual truncated Gaussian.

I present the blackboard notes of the derivation in figure H.1.

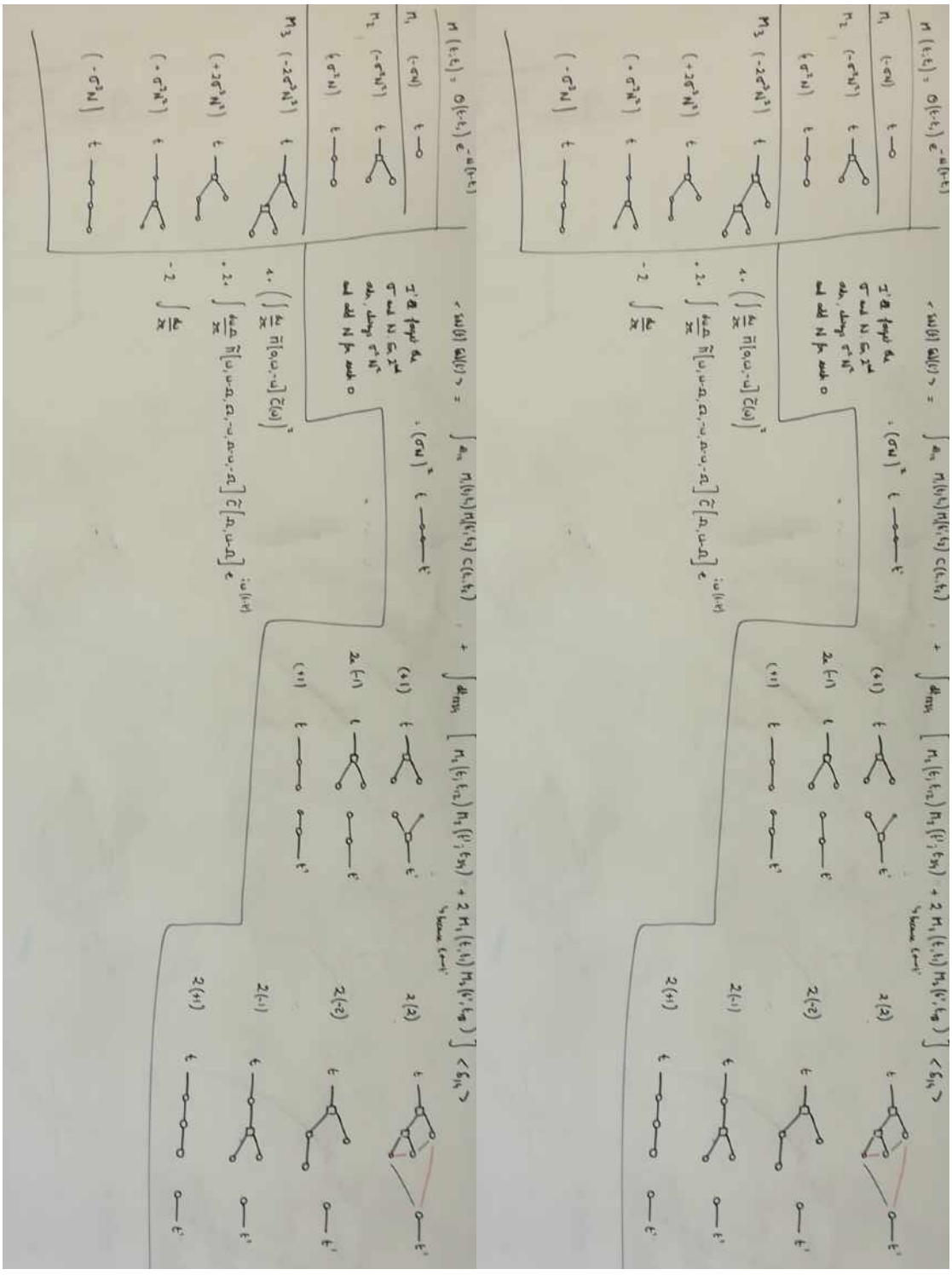

Figure H.1. Diagrammatic expansion: definitions and closure in Fourier space

Bibliography

[1] Robert MacArthur. Species packing and competitive equilibrium for many species. *Theoretical Population Biology*, 1(1), May 1970.

[2] Peter Chesson. MacArthur's consumer-resource model. *Theoretical Population Biology*, 37(1), February 1990.

[3] Robert May. Will a large complex system be stable. *Nature*, 238:413–4, 09 1972.

[4] Stephen P. Hubbell. *The Unified Neutral Theory of Biodiversity and Biogeography (MPB-32)*. Princeton University Press, April 2001.

[5] James Rosindell, Stephen P. Hubbell, and Rampal S. Etienne. The Unified Neutral Theory of Biodiversity and Biogeography at Age Ten. *Trends in Ecology & Evolution*, 26(7), July 2011.

[6] Sandro Azaele, Samir Suweis, Jacopo Grilli, Igor Volkov, Jayanth R. Banavar, and Amos Maritan. Statistical mechanics of ecological systems: Neutral theory and beyond. *Rev. Mod. Phys.*, 88:035003, Jul 2016.

[7] Charles S. Elton. *The Ecology of Invasions by Animals and Plants*. Springer US, 1958.

[8] Robert MacArthur. Fluctuations of Animal Populations and a Measure of Community Stability. *Ecology*, 36(3), 1955.

[9] Mark R. Gardner and W. Ross Ashby. Connectance of Large Dynamic (Cybernetic) Systems: Critical Values for Stability. *Nature*, 228(5273), November 1970.

[10] Garrett Hardin. The competitive exclusion principle. *Science*, 131(3409):1292–1297, 1960.

[11] Maayke Stomp, Jef Huisman, Gary G. Mittelbach, Elena Litchman, and Christopher A. Klausmeier. Large-scale biodiversity patterns in freshwater phytoplankton. *Ecology*, 92(11), 2011.

[12] G. E. Hutchinson. The Paradox of the Plankton. *The American Naturalist*, 95(882), May 1961.

[13] Karoline Faust and Jeroen Raes. Microbial interactions: from networks to models. *Nat Rev Micro*, 10(8):538–550, Aug 2012.

[14] Elizabeth Pennisi. How Did Cooperative Behavior Evolve? *Science*, 309(5731), July 2005.

[15] Per Lundberg, Esa Ranta, Jörgen Ripa, and Veijo Kaitala. Population variability in space and time. *Trends in Ecology & Evolution*, 15(11), November 2000.

[16] Pablo Inchausti and John Halley. On the relation between temporal variability and persistence time in animal populations. *Journal of Animal Ecology*, 72(6), 2003.

[17] Stephen Ellner and Peter Turchin. Chaos in a Noisy World: New Methods and Evidence from Time-Series Analysis. *The American Naturalist*, 145(3), March 1995.

[18] Marten Scheffer, Sergio Rinaldi, Jef Huisman, and Franz J. Weissing. Why plankton communities have no equilibrium: solutions to the paradox. *Hydrobiologia*, 491(1), January 2003.

[19] Robert M. May. Biological Populations with Nonoverlapping Generations: Stable Points, Stable Cycles, and Chaos. *Science*, 186(4164), November 1974.

[20] J. C. Allen, W. M. Schaffer, and D. Rosko. Chaos reduces species extinction by amplifying local population noise. *Nature*, 364(6434), July 1993.

[21] Jean P. Gibert and Justin D. Yeakel. Laplacian matrices and Turing bifurcations: revisiting Levin 1974 and the consequences of spatial structure and movement for ecological dynamics. *Theoretical Ecology*, 12(3), September 2019.

[22] A. A. Berryman and J. A. Millstein. Are ecological systems chaotic — And if not, why not? *Trends in Ecology & Evolution*, 4(1), January 1989.

[23] Roger Nisbet, Steve Blythe, Bill Gurney, Hans Metz, Kevin Stokes, Adam Lomnicki, and G. S. Mani. Avoiding chaos. *Trends in Ecology & Evolution*, 4(8), August 1989.

[24] Dominique Gravel, François Massol, and Mathew A. Leibold. Stability and complexity in model meta-ecosystems. *Nature Communications*, 7(1), August 2016.

[25] Egbert Giles Leigh. The average lifetime of a population in a varying environment. *Journal of Theoretical Biology*, 90(2), May 1981.

[26] Russell Lande. Risks of Population Extinction from Demographic and Environmental Stochasticity and Random Catastrophes. *The American Naturalist*, 142(6), December 1993.

[27] Michel Loreau, Nicolas Mouquet, and Andrew Gonzalez. Biodiversity as spatial insurance in heterogeneous landscapes. *Proceedings of the National Academy of Sciences*, 100(22), October 2003.

[28] Jörgen Ripa and Per Lundberg. Noise colour and the risk of population extinctions. *Proceedings of the Royal Society of London. Series B: Biological Sciences*, 263(1377), December 1996.

[29] Alan Hastings, Carole L. Hom, Stephen Ellner, Peter Turchin, and H. Charles J. Godfray. Chaos in Ecology: Is Mother Nature a Strange Attractor? *Annual Review of Ecology and Systematics*, 24(1), 1993.

[30] Marten Scheffer. Should we expect strange attractors behind plankton dynamics – and if so, should we bother? *Journal of Plankton Research*, 13(6), January 1991.

[31] Jef Huisman and Franz J. Weissing. Biodiversity of plankton by species oscillations and chaos. *Nature*, 402(6760), November 1999.

[32] Elisa Benincà, Jef Huisman, Reinhard Heerkloss, Klaus D. Jöhnk, Pedro Branco, Egbert H. Van Nes, Marten Scheffer, and Stephen P. Ellner. Chaos in a long-term experiment with a plankton community. *Nature*, 451(7180), February 2008.

[33] Iaroslav Ispolatov, Vaibhav Madhok, Sebastian Allende, and Michael Doebeli. Chaos in high-dimensional dissipative dynamical systems. *Scientific Reports*, 5(1), July 2015.

[34] James BT Sanders, J Doyne Farmer, and Tobias Galla. The prevalence of chaotic dynamics in games with many players. *Scientific reports*, 8(1):1–13, 2018.

[35] Stefano Allesina and Si Tang. Stability criteria for complex ecosystems. *Nature*, 483(7388), March 2012.

[36] Mikhail Tikhonov and Remi Monasson. Collective phase in resource competition in a highly diverse ecosystem. *Phys. Rev. Lett.*, 118:048103, Jan 2017.

[37] Madhu Advani, Guy Bunin, and Pankaj Mehta. Statistical physics of community ecology: a cavity solution to MacArthur's consumer resource model. *Journal of Statistical Mechanics: Theory and Experiment*, 2018(3), March 2018.

[38] Ada Altieri and Silvio Franz. Constraint satisfaction mechanisms for marginal stability and criticality in large ecosystems. *Physical Review E*, 99(1):010401, 2019.

[39] Joshua E. Goldford, Nanxi Lu, Djordje Bajić, Sylvie Estrela, Mikhail Tikhonov, Alicia Sanchez-Gorostiaga, Daniel Segrè, Pankaj Mehta, and Alvaro Sanchez. Emergent simplicity in microbial community assembly. *Science*, 361(6401), August 2018.

[40] Robert Marsland Iii, Wenping Cui, Joshua Goldford, Alvaro Sanchez, Kirill Korolev, and Pankaj Mehta. Available energy fluxes drive a transition in the diversity, stability, and functional structure of microbial communities. *PLOS Computational Biology*, 15(2), February 2019.

[41] C. K. Fisher and P. Mehta. The transition between the niche and neutral regimes in ecology. *Proceedings of the National Academy of Sciences*, 111(36):13111–13116, September 2014.

[42] David A. Kessler and Nadav M. Shnerb. Generalized model of island biodiversity. *Physical Review E*, 91(4):042705, April 2015.

[43] Yael Fried, David A. Kessler, and Nadav M. Shnerb. Communities as cliques. *Scientific Reports*, 6(1), October 2016.

[44] Matthieu Barbier, Jean-François Arnoldi, Guy Bunin, and Michel Loreau. Generic assembly patterns in complex ecological communities. *Proceedings of the National Academy of Sciences*, 115(9):2156–2161, 2018.

[45] Guy Bunin. Ecological communities with lotka-volterra dynamics. *Physical Review E*, 95(4):042414, 2017.

[46] Matthieu Barbier, Claire de Mazancourt, Michel Loreau, and Guy Bunin. Fingerprints of high-dimensional coexistence in complex ecosystems. *bioRxiv*, March 2020.

[47] Giulio Biroli, Guy Bunin, and Chiara Cammarota. Marginally stable equilibria in critical ecosystems. *New Journal of Physics*, 20(8):083051, 2018.

[48] Tobias Galla. Dynamically evolved community size and stability of random Lotka-Volterra ecosystems. *EPL (Europhysics Letters)*, 123(4):48004, September 2018. arXiv: 1808.06660.

[49] Michael T. Pearce, Atish Agarwala, and Daniel S. Fisher. Stabilization of extensive fine-scale diversity by ecologically driven spatiotemporal chaos. *Proceedings of the National Academy of Sciences*, 117(25), June 2020.

[50] Narendra S. Goel, Samaresh C. Maitra, and Elliott W. Montroll. On the volterra and other nonlinear models of interacting populations. *Rev. Mod. Phys.*, 43:231–276, Apr 1971.

[51] William R. Harcombe, William J. Riehl, Ilija Dukovski, Brian R. Granger, Alex Betts, Alex H. Lang, Gracia Bonilla, Amrita Kar, Nicholas Leiby, Pankaj Mehta, Christopher J. Marx, and Daniel Segrè. Metabolic Resource Allocation in Individual Microbes Determines Ecosystem Interactions and Spatial Dynamics. *Cell Reports*, 7(4), May 2014.

[52] H. Sompolinsky, A. Crisanti, and H. J. Sommers. Chaos in random neural networks. *Phys. Rev. Lett.*, 61:259–262, Jul 1988.

[53] Manfred Opper and Sigurd Diederich. Phase transition and 1/f noise in a game dynamical model. *Phys. Rev. Lett.*, 69:1616–1619, Sep 1992.

[54] Richard M Goodwin. *Chaotic economic dynamics*. Oxford University Press, 2003.

[55] Systemic Financial Risk. Oecd reviews of risk management policies this series presents a series of books examining the management of risk by governments in such areas as natural disasters, climate change, information security, nuclear energy, biotechnology and financial services. english. *OECD Economic Outlook*, 2012(1), 2012.

[56] Stefan Thurner. Systemic financial risk: agent based models to understand the leverage cycle on national scales and its consequences. *IFP/FGS Working Paper*, 14, 2011.

[57] José Moran and Jean-Philippe Bouchaud. May's instability in large economies. *Physical Review E*, 100(3):032307, 2019.

[58] Vanni Bucci and Joao B Xavier. Towards predictive models of the human gut microbiome. *Journal of molecular biology*, 426(23):3907–3916, 2014.

[59] Richard R. Stein, Vanni Bucci, Nora C. Toussaint, Charlie G. Buffie, Gunnar Rätsch, Eric G. Pamer, Chris Sander, and João B. Xavier. Ecological modeling from time-series inference: Insight into dynamics and stability of intestinal microbiota. *PLOS Computational Biology*, 9(12):1–11, 12 2013.

[60] Tommaso Castellani and Andrea Cavagna. Spin-glass theory for pedestrians. *Journal of Statistical Mechanics: Theory and Experiment*, 2005(05):P05012, may 2005.

[61] F. Roy, G. Biroli, G. Bunin, and C. Cammarota. Numerical implementation of dynamical mean field theory for disordered systems: application to the Lotka–Volterra model of ecosystems. *Journal of Physics A: Mathematical and Theoretical*, 52(48), November 2019.

[62] Felix Roy, Matthieu Barbier, Giulio Biroli, and Guy Bunin. Complex interactions can create persistent fluctuations in high-diversity ecosystems. *PLOS Computational Biology*, 16(5), May 2020.

[63] Ada Altieri, Felix Roy, Chiara Cammarota, and Giulio Biroli. Properties of equilibria and glassy phases of the random Lotka-Volterra model with demographic noise. *arXiv:2009.10565 [cond-mat]*, September 2020.

[64] H. Sompolinsky and Annette Zippelius. Dynamic theory of the spin-glass phase. *Phys. Rev. Lett.*, 47:359–362, Aug 1981.

[65] Leticia F Cugliandolo and Jorge Kurchan. Analytical solution of the off-equilibrium dynamics of a long-range spin-glass model. *Physical Review Letters*, 71(1):173, 1993.

[66] Tobias Galla. Random replicators with asymmetric couplings. *Journal of Physics A: Mathematical and General*, 39(15), March 2006.

[67] Robert May, Angela R McLean, et al. *Theoretical ecology: principles and applications*. Oxford University Press on Demand, 2007.

[68] Ludovic Berthier, Jean-Louis Barrat, and Jorge Kurchan. A two-time-scale, two-temperature scenario for nonlinear rheology. *Physical Review E*, 61(5):5464, 2000.

[69] Leticia F. Cugliandolo, Jorge Kurchan, Pierre Le Doussal, and Luca Peliti. Glassy behaviour in disordered systems with nonrelaxational dynamics. *Phys. Rev. Lett.*, 78:350–353, Jan 1997.

[70] Bongsoo Kim and Arnulf Latz. The dynamics of the spherical p-spin model: From microscopic to asymptotic. *EPL (Europhysics Letters)*, 53(5):660, 2001.

[71] H. Eissfeller and M. Opper. Mean-field Monte Carlo approach to the Sherrington-Kirkpatrick model with asymmetric couplings. *Phys. Rev. E*, 50:709–720, Aug 1994.

[72] H. Eissfeller and M. Opper. New method for studying the dynamics of disordered spin systems without finite-size effects. *Physical Review Letters*, 68:2094–2097, March 1992.

[73] Antoine Georges, Gabriel Kotliar, Werner Krauth, and Marcelo J. Rozenberg. Dynamical mean-field theory of strongly correlated fermion systems and the limit of infinite dimensions. *Rev. Mod. Phys.*, 68:13–125, Jan 1996.

[74] FelixRoy. Implements the DMFT solver, applied to the rLV model, January 2019. https://github.com/FelixRoy/dmft_rLV.

[75] Marc Mézard, Giorgio Parisi, and Miguel Virasoro. *Spin glass theory and beyond: An Introduction to the Replica Method and Its Applications*, volume 9. World Scientific Publishing Company, 1987.

[76] Robert Zwanzig. *Nonequilibrium Statistical Mechanics*. Oxford University Press, April 2001. Google-Books-ID: 4cI5136OdoMC.

[77] Gérard Ben Arous, Amir Dembo, and Alice Guionnet. Cugliandolo-kurchan equations for dynamics of spin-glasses. *Probability Theory and Related Fields*, 136(4):619–660, Dec 2006.

[78] E. A. Novikov. Functionals and the random-force method in turbulence theory. *Soviet Journal of Experimental and Theoretical Physics*, 20:1290–1294, May 1965.

[79] Jorge Kurchan, Thibaud Maimbourg, and Francesco Zamponi. Statics and dynamics of infinite-dimensional liquids and glasses: a parallel and compact derivation. *Journal of Statistical Mechanics: Theory and Experiment*, 2016(3):033210, 2016.

[80] Elisabeth Agoritsas, Thibaud Maimbourg, and Francesco Zamponi. Out-of-equilibrium dynamical equations of infinite-dimensional particle systems. I. The isotropic case. *Journal of Physics A: Mathematical and Theoretical*, 52(14):144002, April 2019. arXiv: 1808.00236 version: 2.

[81] Alessandro Manacorda, Grégory Schehr, and Francesco Zamponi. Numerical solution of the dynamical mean field theory of infinite-dimensional equilibrium liquids. *The Journal of Chemical Physics*, 152(16), April 2020.

[82] G. Biroli. Slow Relaxations and Non-Equilibrium Dynamics in Classical and Quantum Systems. *ArXiv e-prints*, July 2015.

[83] Jorge Kurchan and Laurent Laloux. Phase space geometry and slow dynamics. *Journal of Physics A: Mathematical and General*, 29(9):1929, 1996.

[84] Leticia F Cugliandolo. Course 7: Dynamics of glassy systems. In *Slow Relaxations and nonequilibrium dynamics in condensed matter*, pages 367–521. Springer, 2003.

[85] H. J. Sommers, A. Crisanti, H. Sompolinsky, and Y. Stein. Spectrum of large random asymmetric matrices. *Phys. Rev. Lett.*, 60:1895–1898, May 1988.

[86] Lewi Stone. The feasibility and stability of large complex biological networks: a random matrix approach. *Scientific Reports*, 8(1), May 2018.

[87] Guy Bunin. Interaction patterns and diversity in assembled ecological communities. *arXiv:1607.04734 [cond-mat, physics:physics, q-bio]*, July 2016. arXiv: 1607.04734.

[88] Gérard Ben Arous, Yan V Fyodorov, and Boris A Khoruzhenko. Counting equilibria of large complex systems by instability index, 2020.

[89] Yan V. Fyodorov. Complexity of random energy landscapes, glass transition, and absolute value of the spectral determinant of random matrices. *Phys. Rev. Lett.*, 92:240601, Jun 2004.

[90] Yan V Fyodorov. High-dimensional random fields and random matrix theory, 2013.

[91] Tobias Galla and J. Doyne Farmer. Complex dynamics in learning complicated games. *Proceedings of the National Academy of Sciences*, 110(4), January 2013.

[92] Jacopo Grilli, Matteo Adorisio, Samir Suweis, György Barabás, Jayanth R. Banavar, Stefano Allesina, and Amos Maritan. Feasibility and coexistence of large ecological communities. *Nature Communications*, 8(1), February 2017.

[93] Catherine H. Graham and Ben G. Weinstein. Towards a predictive model of species interaction beta diversity. *Ecology Letters*, 21(9), 2018.

[94] G. Ben Arous and A. Guionnet. Symmetric Langevin spin glass dynamics. *Annals of Probability*, 25(3), July 1997.

[95] Daniel W. Carstensen, Malena Sabatino, Kristian Trøjelsgaard, and Leonor Patricia C. Morellato. Beta Diversity of Plant-Pollinator Networks and the Spatial Turnover of Pairwise Interactions. *PLOS ONE*, 9(11), November 2014.

[96] Rebecca L. Kordas, Christopher D. G. Harley, and Mary I. O'Connor. Community ecology in a warming world: The influence of temperature on interspecific interactions in marine systems. *Journal of Experimental Marine Biology and Ecology*, 400(1), April 2011.

[97] Michel Loreau and Claire de Mazancourt. Biodiversity and ecosystem stability: a synthesis of underlying mechanisms. *Ecology Letters*, 16(s1), 2013.

[98] Yuval R. Zelnik, Jean-François Arnoldi, and Michel Loreau. The three regimes of spatial recovery. *Ecology*, 100(2), 2019.

[99] J. M. Halley. Ecology, evolution and 1 f -noise. *Trends in Ecology & Evolution*, 11(1), 1996.

[100] Kevin R. Wilcox, Andrew T. Tredennick, Sally E. Koerner, Emily Grman, Lauren M. Hallett, Meghan L. Avolio, Kimberly J. La Pierre, Gregory R. Houseman, Forest Isbell, David Samuel Johnson, Juha M. Alatalo, Andrew H. Baldwin, Edward W. Bork, Elizabeth H. Boughton, William D. Bowman, Andrea J. Britton, James F. Cahill, Scott L. Collins, Guozhen Du, Anu Eskelinen, Laura Gough, Anke Jentsch, Christel Kern, Kari Klanderud, Alan K. Knapp, Juergen Kreyling, Yiqi Luo, Jennie R. McLaren, Patrick Megonigal, Vladimir Onipchenko, Janet Prevéy, Jodi N. Price, Clare H. Robinson, Osvaldo E. Sala, Melinda D. Smith, Nadejda A. Soudzilovskaia, Lara Souza, David Tilman, Shannon R. White, Zhuwen Xu, Laura Yahdjian, Qiang Yu, Pengfei Zhang, and Yunhai Zhang. Asynchrony among local communities stabilises ecosystem function of metacommunities. *Ecology Letters*, 20(12), 2017.

[101] Daniel S Maynard, Zachary R Miller, and Stefano Allesina. Predicting coexistence in experimental ecological communities. *Nature Ecology & Evolution*, 4(1):91–100, 2020.

[102] James Angus Chandler, Jenna Morgan Lang, Srijak Bhatnagar, Jonathan A Eisen, and Artyom Kopp. Bacterial communities of diverse drosophila species: ecological context of a host–microbe model system. *PLoS genet*, 7(9):e1002272, 2011.

[103] Jason Lloyd-Price, Anup Mahurkar, Gholamali Rahnavard, Jonathan Crabtree, Joshua Orvis, A Brantley Hall, Arthur Brady, Heather H Creasy, Carrie McCracken, Michelle G Giglio, et al. Strains, functions and dynamics in the expanded human microbiome project. *Nature*, 550(7674):61–66, 2017.

[104] Luis Barreira and Claudia Valls. Low-dimensional dynamics. In *Dynamical Systems*, pages 57–86. Springer, 2013.

[105] David Tilman. *Resource competition and community structure*. Princeton university press, 1982.

[106] Shigui Ruan. Delay differential equations in single species dynamics. In *Delay differential equations and applications*, pages 477–517. Springer, 2006.

[107] JA Vano, JC Wildenberg, MB Anderson, JK Noel, and JC Sprott. Chaos in low-dimensional lotka–volterra models of competition. *Nonlinearity*, 19(10):2391, 2006.

[108] Joost HJ van Opheusden, Lia Hemerik, Mieke van Opheusden, and Wopke van der Werf. Competition for resources: complicated dynamics in the simple tilman model. *SpringerPlus*, 4(1):474, 2015.

[109] Carlos A Serván, José A Capitán, Jacopo Grilli, Kent E Morrison, and Stefano Allesina. Coexistence of many species in random ecosystems. *Nature ecology & evolution*, 2(8):1237–1242, 2018.

[110] Robert Marsland, Wenping Cui, and Pankaj Mehta. A minimal model for microbial biodiversity can reproduce experimentally observed ecological patterns. *Scientific reports*, 10(1):1–17, 2020.

[111] Laura Sidhom and Tobias Galla. Ecological communities from random generalized lotka-volterra dynamics with nonlinear feedback. *Physical Review E*, 101(3):032101, 2020.

[112] Itay Dalmedigos and Guy Bunin. Dynamical persistence in resource-consumer models. *arXiv preprint arXiv:2002.04358*, 2020.

[113] Yan V. Fyodorov and Boris A. Khoruzhenko. Nonlinear analogue of the may wigner instability transition. *Proceedings of the National Academy of Sciences*, 113(25):6827–6832, June 2016.

[114] Yan V Fyodorov and Pierre Le Doussal. Hessian spectrum at the global minimum of high-dimensional random landscapes. *Journal of Physics A: Mathematical and Theoretical*, 51(47):474002, 2018.

[115] Yan V Fyodorov, Gérard Ben Arous, and Boris A Khoruzhenko. Counting equilibria of large complex systems by instability index. *arXiv preprint arXiv:2008.00690*, 2020.

[116] Paolo Biscari and G Parisi. Replica symmetry breaking in the random replicant model. *Journal of Physics A: Mathematical and General*, 28(17):4697, 1995.

[117] Gábor Domokos and István Scheuring. Discrete and continuous state population models in a noisy world. *Journal of Theoretical Biology*, 227(4):535–545, 2004.

[118] Tim Rogers, Alan J McKane, and Axel G Rossberg. Demographic noise can lead to the spontaneous formation of species. *EPL (Europhysics Letters)*, 97(4):40008, 2012.

[119] Haim Weissmann, Nadav M. Shnerb, and David A. Kessler. Simulation of spatial systems with demographic noise. *Physical Review E*, 98(2):022131, 2018.

[120] Rémi Monasson. Structural glass transition and the entropy of the metastable states. *Physical review letters*, 75(15):2847, 1995.

[121] Patrick Charbonneau, Jorge Kurchan, Giorgio Parisi, Pierfrancesco Urbani, and Francesco Zamponi. Fractal free energy landscapes in structural glasses. *Nature communications*, 5(1):1–6, 2014.

[122] Patrick Charbonneau, Jorge Kurchan, Giorgio Parisi, Pierfrancesco Urbani, and Francesco Zamponi. Glass and jamming transitions: From exact results to finite-dimensional descriptions. *Annual Review of Condensed Matter Physics*, 8:265–288, 2017.

[123] Ludovic Berthier, Giulio Biroli, Patrick Charbonneau, Eric I Corwin, Silvio Franz, and Francesco Zamponi. Gardner physics in amorphous solids and beyond. *The Journal of chemical physics*, 151(1):010901, 2019.

[124] Haim Sompolinsky and Annette Zippelius. Relaxational dynamics of the edwards-anderson model and the mean-field theory of spin-glasses. *Physical Review B*, 25(11):6860, 1982.

[125] Silvio Franz and Marc Mézard. On mean field glassy dynamics out of equilibrium. *Physica A: Statistical Mechanics and its Applications*, 210(1-2):48–72, 1994.

[126] Giulio Biroli. A crash course on ageing. *Journal of Statistical Mechanics: Theory and Experiment*, 2005(05):P05014, 2005.

[127] Leticia F Cugliandolo, Jorge Kurchan, and Luca Peliti. Energy flow, partial equilibration, and effective temperatures in systems with slow dynamics. *Physical Review E*, 55(4):3898, 1997.

[128] Giorgio Parisi. Spin glasses and fragile glasses: Statics, dynamics, and complexity. *Proceedings of the National Academy of Sciences*, 103(21):7948–7955, 2006.

[129] G. N. Milstein, E. Platen, and H. Schurz. Balanced implicit methods for stiff stochastic systems. *SIAM Journal on Numerical Analysis*, 35(3):1010–1019, 1998.

[130] Leonid Pechenik and Herbert Levine. Interfacial velocity corrections due to multiplicative noise. *Physical Review E*, 59(4):3893–3900, 1999.

[131] Esteban Moro. Numerical schemes for continuum models of reaction-diffusion systems subject to internal noise. *Physical Review E*, 70(4):045102, 2004.

[132] Ivan Dornic, Hugues Chate, and M. A. Munoz. Integration of langevin equations with multiplicative noise and viability of field theories for absorbing phase transitions. *Physical Review Letters*, 94(10):100601, 2005.

[133] Werner Mende. *The predator-prey model: do we live in a Volterra world?* Akademie-Verlag, 1986.

[134] Sigurd Diederich and Manfred Opper. Replicators with random interactions: A solvable model. *Physical Review A*, 39(8):4333, 1989.

[135] John Maynard Smith and John Maynard Maynard Smith. *Evolution and the Theory of Games*. Cambridge university press, 1982.

[136] Karl Sigmund et al. *Evolutionary Game Dynamics: American Mathematical Society Short Course, January 4-5, 2011, New Orleans, Louisiana*, volume 69. American Mathematical Soc., 2011.

[137] Ludovic Berthier and Jorge Kurchan. Non-equilibrium glass transitions in driven and active matter. *Nature Physics*, 9(5):310–314, 2013.

[138] JA Hertz, G Grinstein, and SA Solla. Memory networks with asymmetric bonds. In *AIP Conference Proceedings*, volume 151, pages 212–218. American Institute of Physics, 1986.

[139] JA Hertz, G Grinstein, and SA Solla. Irreversible spin glasses and neural networks. In *Heidelberg colloquium on glassy dynamics*, pages 538–546. Springer, 1987.

[140] Ada Altieri. The jamming paradigm in ecology. In *Jamming and Glass Transitions*, pages 133–152. Springer, 2019.

[141] Shreyas Gokhale, Arolyn Conwill, Tanvi Ranjan, and Jeff Gore. Migration alters oscillatory dynamics and promotes survival in connected bacterial populations. *Nature Communications*, 9(1), December 2018.

[142] Nicolas Martin, José Halloy, Pablo Jensen, and Felix Roy. Systèmes complexes : un petit poisson, un petit oiseau. *La Méthode scientifique, France Culture*, February 2020.

[143] M. Mézard and G. Parisi. The Bethe lattice spin glass revisited. *The European Physical Journal B - Condensed Matter and Complex Systems*, 20(2), March 2001.

[144] H. Rieger. Solvable model of a complex ecosystem with randomly interacting species. *Journal of Physics A: Mathematical and General*, 22(17), September 1989.